CRYSTAL PLASTICITY MODELING OF THE DEFORMATION OF BCC IRON AND NIOBIUM SINGLE CRYSTALS

By

Aboozar Mapar

A DISSERTATION

Submitted to
Michigan State University
in partial fulfillment of the requirements
for the degree of

Mechanical Engineering – Doctor of Philosophy
Materials Science and Engineering – Dual Major

2017

ABSTRACT

CRYSTAL PLASTICITY MODELING OF THE DEFORMATION OF BCC IRON AND NIOBIUM SINGLE CRYSTALS

By

Aboozar Mapar

The conventional Schmid-type crystal plasticity models cannot predict the deformation of BCC polycrystals or single crystals. Therefore, in this study, a non-Schmid crystal plasticity model was developed for single crystal ferrite which has a BCC structure. The average error of this model in predicting the force-displacement response of these ferrite single crystals is 4.3%, while the average error of the Schmid-type crystal plasticity model is 10.1%.

To address the shortcomings of the conventional Hill-type hardening rule, two novel hardening models were derived, developed, and compared to the classical hardening rule. These models are named the Differential-Exponential and the Dynamic hardening rules.

The Differential-Exponential hardening rule was implemented into the non-Schmid crystal plasticity model. This model was then used to predict the deformation behavior of the single crystal ferrite micropillars that show stage I and stage II hardening. The average error of this model in predicting the force-displacement of these ferrite micropillars is 3.7%.

The Dynamic hardening rule was implemented into the Schmid-type crystal plasticity model. This enabled the crystal plasticity model to accurately predict the deformation behavior of Nb single crystals. The average error in predicting the stress-strain curves using the Schmid-type crystal plasticity model and the Dynamic hardening rule is 6.8%, while this error with the classical hardening rule is 8.9%.

Finally, the hydroforming of an oligo-crystal Nb tube with several large grains was simulated with the Schmid-type crystal plasticity model and the Dynamic hardening. The goal was to assess the accuracy of the new hardening model in simulating the tube hydroforming process where the material undergoes the more complex biaxial deformations. Qualitatively,

the model predicted the location of the crack and the areas with significant circumferential strain in the hydroformed tube effectively.

To the love of my life, Sahar.

ACKNOWLEDGMENTS

I would like to express my deepest gratitude to my advisers Dr. Farhang Pourboghrat, and Dr. Thomas Bieler, for their guidance, encouragement, support, and friendship throughout my Ph.D. program. They were available and ready to help whenever I had a question or needed advice. I appreciate their trust and the opportunity they gave me to develop my skills and become an independent researcher.

I would like to thank the members of my thesis committee Dr. Carl Boehlert and Dr. Thomas Pence for their help and guidance. I am grateful to Dr. Philip Eisenlohr for his wonderful discussions and insight. I am thankful to Dr. Martin Crimp for his valuable discussions and honest feedback.

I would like to acknowledge the help of my friends and colleagues Di Kang and Chen Zhang. Di assisted me in many of my experiments and Chen shared several pieces of his code with me.

I would like to thank Dr. Sharvan Kumar and Dr. Hassan Ghassemi-Armaki for sharing the experiments they performed at Brown University with me.

Finally, and most importantly, I would like to express my gratitude to my wife, Sahar, for her patience and love throughout the years. Her support and encouragement are what made this dissertation possible.

TABLE OF CONTENTS

LIST OF TABLES

LIST OF FIGURES

CHAPTER 1

INTRODUCTION

Computational modeling has become an integral part of the design process in the modern industry. Accurate models speed up design processes, reduce the time to commercialize products and reduce the costs. The current deformation models are generally developed for polycrystalline materials. Randomly-orientated polycrystals are less anisotropic than single crystals. This means that the dependence of physical and mechanical properties of randomly-orientated polycrystals on the direction of testing is often less evident than that of single crystals. Therefore, the behavior of these materials can be modeled with simpler models.

The available models for deformation of FCC materials are usually more accurate than the models for BCC materials. FCC materials have 12 slip systems while BCC materials have 48 slip systems. FCC materials have close-packed planes, so their active slip systems can be clearly distinguished. On the other hand, there is no close-packed plane in BCC materials, which causes ambiguity in finding the active slip system in these materials.

Crystal plasticity theory assumes that all deformation takes place because of dislocation slip on a slip plane. This theory uses Schmid law; according to which dislocations start slipping when the resolved shear stress on the dislocation plane parallel to slip direction reaches a threshold. In BCC materials, the core of a screw dislocation is non-planar and spreads on three planes. Therefore, stresses on planes other than the slip plane can affect the threshold value for initiation of dislocation slip.

The above are some of the reasons why conventional crystal plasticity models cannot predict the deformation behavior of BCC single crystals. In this study, a BCC crystal plasticity model was developed. Next, multiple approaches were used to improve the accuracy of the model for BCC materials including single crystal ferrite (α-Fe) and niobium (Nb).

A non-Schmid crystal plasticity model was developed and verified for ferrite and Nb.

This model could predict the deformation behavior of ferrite.

Each crystal plasticity model has a hardening rule that predicts the increase in flow stress (yield stress) as the strain increases. The conventional Hill-type hardening rule cannot accurately estimate the hardening of BCC materials. Therefore, two novel hardening models, the Differential-Exponential hardening rule and the Dynamic hardening rule, were developed.

The Differential-Exponential hardening rule was developed to predict the deformation behavior of ferrite micropillars that show stage I and II hardening. This model uses two distinct hardening equations to predict the rate of hardening of stage I and II of deformation of single crystals.

The Dynamic hardening rule was developed for single crystal Nb. This model reduces the rate of hardening during single slip deformation and increases the hardening when more slip systems activate. The Dynamic hardening rule increases the prediction accuracy of the Schmid-type crystal plasticity model for Nb.

Finally, a large grain Nb tube was hydroformed. The process was simulated in Abaqus® and the behavior of Nb under the loading was predicted using the Dynamic hardening model. The location of the crack and areas with the highest circumferential strain predicted by this model match with the experiment, although the magnitude of strains does not.

The rest of this dissertation is organized as follows. A review of literature is presented in Chapter 2. Chapter 3 explores some of the methods that can be used to improve the predictions of crystal plasticity models for BCC materials. Chapter 4 discusses the development of a non-Schmid crystal plasticity model and derivation of the Differential-Exponential hardening rule. Predictions of the Schmid and non-Schmid models are compared and the Differential-Exponential is verified with the experiment. Chapter 5 presents the development of the Dynamic hardening model. This chapter also compares the predictions of the Hill-type and the Dynamic hardening rules for single crystal Nb. Chapter 6 discusses the modeling of the hydroforming of a large grain Nb tube with the Dynamic hardening rule. Chapter 4 through Chapter 6 are presented as comprehensive papers. Among these, Chapter 4 has

been published. Chapter 7 discusses the findings of this dissertation. Conclusions of this dissertation and proposed future works are presented in Chapter 8.

This document has two appendices. Many of the equations in this dissertation are written using the Einstein (index) notation. Consequently, familiarity of the reader with this subject is crucial, so Appendix A briefly reviews the Einstein notation. Appendix B covers the calibration method that was used in this dissertation to find the material parameters of the crystal plasticity models.

CHAPTER 2

LITERATURE REVIEW

The material response to loading can be divided into two general categories; elastic and non-elastic. The material application determines the desirable type of response. In many applications, the part or product should only deform elastically under the loading, like the beams used in buildings, or the part or product would be useless. It is much easier to predict the elastic behavior than the plastic behavior. In the 17th century, Robert Hooke modeled the elastic deformation of materials [1]. Although Hooke's law is only a first approximation, it is what modern elasticity theory is built upon. The next step was to predict the yielding point. In 1864, Henri Édouard Tresca proposed a yield criterion to predict the onset of plastic deformation [2]. In 1913, Richard Edler von Mises [3] suggested another criterion that gave better predictions of yielding than the Tresca criterion.

Plasticity, on the other hand, is the main area of interest in manufacturing processes. One needs to know the minimum load needed for initiation and continuation of deformation. Modeling the plastic deformation is more complicated than modeling the elastic deformation. In fact, it was not until 300 years after Hooke, that John Holloman [4] proposed his well-known equation for work hardening. This equation relates the stress and strain after yielding and works for many steel alloys and nonferrous metals.

$$\sigma = K\varepsilon^n \tag{2.1}$$

In this equation, σ is the true stress and ε is the true strain after yielding. n is the slope of the stress-strain curve on a logarithmic scale, which is also known as strain-hardening exponent, and K is a material constant. Hollomon's work hardening equation gives good insight to the behavior of metals in uniaxial deformation, but it is far from sufficient for designing deformation processes. In most manufacturing processes, stress states are more complex than uniaxial deformation. Moreover, the flow stress of many metals changes when

the direction of the loading changes. While Hollomon's law works for isotropic materials, it has no means to capture changes in the deformation behavior of anisotropic materials.

Some of the physical properties of materials change with the direction in which they are measured. Materials that show this kind of directionality are called anisotropic with respect to the measured property. A material can be isotropic with respect to one property and anisotropic with respect to another [5].

Applying a stress to a polycrystal with a random grain orientation causes crystals to rotate and elongate in order to accommodate the deformation. This creates a crystallographic texture (a set of preferred crystal orientations) that can cause anisotropy in the metal. Anisotropy can also happen due to the existence of residual stress, lamellar inclusions, or cavities. Anisotropy is usually undesirable, as it causes non-uniform deformation, like earing in deep drawing [6]. This makes designing a deformation process more challenging, as one must consider the non-uniform behavior of the material under loading.

Anisotropy should be considered in designing deformation processes. Simple yield criteria like Tresca or von Mises are not accurate enough for designing an effective deformation. In fact, models capable of predicting material behavior under complex loading conditions and varying crystal orientations are needed to reduce the cost and increase the speed of designing processes. Without such models manufacturing of many of modern parts would be virtually impossible.

Numerous material models are available in the literature; ranging from the empirical models developed based on extensive experimental data to phenomenological models and crystal plasticity. Some of these models are reviewed in §2.1 through §2.2.

Over the years many researchers [7–21] have worked on modeling the deformation behavior of materials. They have used different methods to capture this behavior. One of the main features of each deformation model is the yield criteria. For a given stress state, these models define boundaries within which the material deforms elastically. If the stress state falls beyond such boundaries, the material will deform plastically.

The rest of this chapter is organized as follows. In §2.1, some phenomenological yield models are reviewed. These are the more familiar models and are often easier to use. Some of these model can even be calculated by hand. Thus, these models can be used to roughly estimate the type of deformation that an applied stress state causes.

Another category of the models is crystal plasticity which is explained in §2.2. These models are more sophisticated than the phenomenological models. In most cases, computer codes are needed to find the type of deformation these models predict for a given stress state.

§2.3 reviews the hydroforming process. Niobium and ferrite are the materials that were studied in this dissertation. §2.4 explains the motivation for investigating these materials.

2.1 Phenomenological yield models

Anisotropy affects almost all modes of deformation. Therefore, special care should be taken when using isotropic plasticity theories. These theories are only valid as an approximation to anisotropic materials. Many researchers have tried to address this issue. In 1948, Hill [7] extended the von Mises criterion and proposed a quadratic yield function for anisotropic materials. To derive this criterion, he assumed that the hydrostatic pressure does not contribute to yielding.

$$F\left(\sigma_{yy}-\sigma_{zz}\right)^2+G\left(\sigma_{zz}-\sigma_{xx}\right)^2+H\left(\sigma_{xx}-\sigma_{yy}\right)^2+2L\sigma_{yz}^2+2M\sigma_{zx}^2+2N\sigma_{xy}^2=1 \quad (2.2)$$

In this equation, F, G, H, L, M, and N are anisotropic constants, and σ_{ij} (where $i,j \in \{x,y,z\}$) are components of stress tensor. This form is useful when the principal axes of anisotropy are chosen as the reference axes. Anisotropic axes are taken as orthogonal directions on the three mutually perpendicular symmetry planes. This equation will have a different form under an arbitrary choice of axes.

The Hill 1948 criterion is, in fact, a yield surface that can be used to predict the deformation behavior of polycrystalline materials. Although this is an improvement over the von Mises criterion, it is not sufficiently accurate in predicting the onset of plastic deformation. Therefore, in 1979, Hill [22] revised his yield surface and proposed the following model for

orthotropic materials in terms of principal stresses.

$$f\,|\sigma_2-\sigma_3|^m + g\,|\sigma_3-\sigma_1|^m + h\,|\sigma_1-\sigma_2|^m + a\,|2\sigma_1-\sigma_2-\sigma_3|^m + b\,|2\sigma_2-\sigma_3-\sigma_1|^m + c\,|2\sigma_3-\sigma_1-\sigma_2|^m = \bar{\sigma}^m \quad (2.3)$$

Similarly, this equation is valid when the axis of loading and orthotropy are the same. Here σ_i (where $i = 1 \ldots 3$) are the principal stresses. The exponent $m > 1$ and f, g, h, a, b and c are material constants and $\bar{\sigma}$ is the effective stress. f, g and h are positive and if divided by σ^m they turn back to respective coefficients (F, G, H) in Hill 1948.

In 1980, Logan and Hosford [23] proposed a model similar to the Hill 1979 model and showed that it could give a good approximation of yield surfaces for anisotropic BCC metals.

The Hosford and Hill 1979 yield criteria are expressed in terms of principal stresses. In 1990, Hill proposed a generalization of his 1979 model that was expressed in a general coordinate system for a sheet.

$$\left|\sigma_x x+\sigma_y y\right|^m + \left(\frac{\sigma^m}{\tau^m}\right)\left|\left(\sigma_x x-\sigma_y y\right)^2+4\sigma_{xy}^2\right|^{\frac{m}{2}} + \left|\sigma_{xx}^2+\sigma_{yy}^2+2\sigma_{xy}^2\right|^{\frac{m}{2}-1}\left\{-2a(\sigma_x x^2-\sigma_y y^2)+b(\sigma_x x-\sigma_y y)^2\right\} = (2\sigma_b)^m \quad (2.4)$$

where σ_b and τ are the yield stress in equi-biaxial tension and pure shear parallel to orthotropic axes, a, b and m are material constants and $m > 1$. To incorporate shear stresses, in 1989, Barlat and Lian [24] expressed these yield functions in a general plane stress state (Yld89).

$$a\,|K_1+K_2|^M + a\,|K_1-K_2|^M + c\,|2K_2|^M = \bar{\sigma}^M \quad (2.5)$$

where

$$K_1 = \frac{\sigma_{xx}+h\sigma_{yy}}{2} \quad (2.6)$$

$$K_2 = \sqrt{\frac{\sigma_{xx}-h\sigma_{yy}}{2}^2 + p^2\sigma_x^2 y} \quad (2.7)$$

in which the coefficients a, c, h and p are material parameters.

In 1991, Barlat et al. [25] proposed another yield criteria (Yld91) that used all six independent components of a stress tensor. Thus, it could be used for any stress state. Habraken and Dautzenberg used Yld91 to predict the earing of an aluminum alloy in cup drawing [26].

In 2000, Barlat et al. [27] proposed another plane stress model (Yld2000-2d). Yoon et al. [28] compared this model with older Barlat yield criteria (Yld91, Yld94, and Yld96). They showed between the aforementioned criteria, Yld2000-2d is the most accurate in predicting the earing profile in aluminum cup drawing.

In 2004, Barlat et al. [29] proposed a 3D stress yield criteria (Yld2004-18p) with 18 parameters.

$$\begin{aligned}\left|S'_1 - S''_1\right|^a + \left|S'_1 - S''_2\right|^a + \left|S'_1 - S''_3\right|^a + \left|S'_2 - S''_1\right|^a + \left|S'_2 - S''_2\right|^a \\ + \left|S'_2 - S''_3\right|^a + \left|S'_3 - S''_1\right|^a + \left|S'_3 - S''_2\right|^a + \left|S'_3 - S''_3\right|^a = 4\bar{\sigma}^a \end{aligned} \tag{2.8}$$

where a is a material constant and $\bar{\sigma}$ is the effective stress. $S = [S_{11}, S_{22}, S_{33}, S_{23}, S_{31}, S_{12}]^T$ is vector containing the deviatoric stress components along the orthotropic axes of material. This vector is linearly transformed to S' and S'' with the following equations:

$$S' = C'S \tag{2.9}$$

$$S'' = C''S \tag{2.10}$$

The linear transformations C' and C'' are defined as follows:

$$C' = \begin{bmatrix} 0 & -c'_{12} & -c'_{13} & 0 & 0 & 0 \\ -c'_{21} & 0 & -c'_{23} & 0 & 0 & 0 \\ -c'_{31} & -c'_{32} & 0 & 0 & 0 & 0 \\ 0 & 0 & 0 & -c'_{44} & 0 & 0 \\ 0 & 0 & 0 & 0 & -c'_{55} & 0 \\ 0 & 0 & 0 & 0 & 0 & -c'_{66} \end{bmatrix} \tag{2.11}$$

$$C'' = \begin{bmatrix} 0 & -c''_{12} & -c''_{13} & 0 & 0 & 0 \\ -c''_{21} & 0 & -c''_{23} & 0 & 0 & 0 \\ -c''_{31} & -c''_{32} & 0 & 0 & 0 & 0 \\ 0 & 0 & 0 & -c''_{44} & 0 & 0 \\ 0 & 0 & 0 & 0 & -c''_{55} & 0 \\ 0 & 0 & 0 & 0 & 0 & -c''_{66} \end{bmatrix} \tag{2.12}$$

In these matrices c'_{ij} and c''_{ij} are constants that define the anisotropy of the material. These linear transformations are, in fact, weighting matrices that define the anisotropy of the material. S'_i and S''_i (where $i = 1 \dots 3$) are the principal values of the linearly transformed deviatoric stresses S' and S''. Each of C' and C'' has nine independent components. Therefore, the final form of this model has 18 material parameters. One needs the experimental data from a balanced biaxial tensile test and uniaxial tensile tests performed in seven directions between the rolling direction (RD) and transverse directions (TD) to find these parameters.

Grytten et al. [30] used Yld2004-18 and Voce isotropic hardening to predict the deformation of an aluminum alloy sheet. Souto et al. [31] used Yld2004-18 combined with the Chaboche isotropic-kinematic hardening law to predict the deformation response of a mild steel.

2.2 Crystal plasticity models

Crystal plasticity is a method of predicting the plastic deformation of metals which assumes that the deformation takes place only by dislocation slip on crystal planes. Crystal plasticity is mainly based on the 1938 work of Sir Geoffrey Ingram Taylor [32]. He observed that slip in FCC aluminum crystals happens on octahedral {111} planes, parallel to the $\langle 1\bar{1}0 \rangle$ edges of each plane. An octahedron has four pairs of parallel planes; hence, there are four independent slip planes and three directions on each plane. Thus, 12 slip systems will be available in each crystal.

Taylor then resolved the shear stress on these planes parallel to each direction and noticed that the slip direction with the highest resolved shear stress accommodates the deformation. He further studied the grain structure of a drawn wire and concluded that all grains had the same amount of strain as the bulk [32].

In 1928, Sachs assumed grains in a polycrystal under loading experience the same stress [33]. Taylor however, argued for all grain boundaries to remain in contact during the deformation, all grains in a polycrystal should experience the same macroscopic strain [32]. In 1964, Hutchinson [34] assumed the macroscopic plastic strain in a polycrystal is the average of strain in all grains. A shear strain γ^α on a slip system α with slip direction m^α and slip plane normal n^α causes a plastic strain ε^α that can be calculated as [34]:

$$\varepsilon^\alpha = \frac{1}{2}\left(m^\alpha \otimes n^\alpha + n^\alpha \otimes m^\alpha\right)\gamma^\alpha \tag{2.13}$$

This equation is based on the Schmid law [35] that states dislocation slip happens when the resolved shear stress on the slip plane of a dislocation and parallel to its slip direction reaches a critical value. The symmetric part of the Schmid tensor, d^α, is used in the above equation and is defined as follows:

$$d^\alpha = \frac{1}{2}\left(m^\alpha \otimes n^\alpha + n^\alpha \otimes m^\alpha\right) \tag{2.14}$$

Summation of the shear strain over all N slip systems gives the total shear strain in a grain.

$$\varepsilon = \sum_{\alpha=1}^{N} d^\alpha \gamma^\alpha \tag{2.15}$$

The dislocation motion on slip system α starts when the stress applied on this slip system reaches a critical value τ_y^α. Therefore, the yield criterion for slip system α is defined as:

$$\sigma : d^\alpha = \tau_y^\alpha \tag{2.16}$$

In this equation, the colon operator is the double dot product of tensors, which produces a scalar result. This operator is defined in Appendix A.

2.2.1 Crystal plasticity yield surface

To predict the yielding of a crystal with multiple slip systems, a yield surface is required. Toth et al. [36] proposed a yield surface based on Taylor's model that is more accurate than the yield criterion used by Hutchinson, equation (2.16). Darrieulat and Piot [37] developed a yield surface for FCC single crystals based on the Toth model. This model includes an exponent n, and reduces to Hill's 1948 yield model when $n = 2$. The yield surface for a FCC single crystal proposed by Darrieulat and Piot [37] is defined as follows:

$$f_n(s) = \left(\sum_{\alpha=1}^{12} \left| \frac{s : d^\alpha}{\tau_y^\alpha} \right|^n \right)^{\frac{1}{n}} \tag{2.17}$$

where s is the deviatoric part of the stress tensor. According to this equation, material is at yield when the quantity in the parenthesis is one.

Following this approach, Zamiri and Pourboghrat [38] developed a method to define the yield function for crystals with multiple slip systems, where the yield function (with internal variables denoted by u) for a single slip system is described by:

$$f_\alpha(\sigma, u) = \frac{|\sigma : d^\alpha|}{\tau_y^\alpha} - 1 = 0 \tag{2.18}$$

where σ is the stress tensor. Dislocation glide on slip system α commences when the function $f_\alpha(\sigma, u)$ reaches zero. This equation is similar to the Darrieulat and Piot yield function in equation (2.17).

By summing the equation (2.18) for N slip systems, one can define a yield surface for a crystal. However, the yield surface defined this way is not smooth. As will be discussed later, the increment of plastic strain is parallel to the normal of yield surface. A non-smooth yield surface introduces ambiguity in calculation of the increment of plastic strain at the non-smooth conditions. To define a smooth yield surface, Zamiri and Pourboghrat [38] used the following equation to combine all yield surfaces for α slip systems into one yield function.

$$f(\sigma, u) = \frac{1}{\rho_f} \ln \left\{ \sum_{\alpha=1}^{n} \exp \left[\frac{\rho_f}{\mu} \left(\frac{|\sigma : d^\alpha|}{\tau_y^\alpha} - 1 \right) \right] \right\} \tag{2.19}$$

Where ρ_f is the so-called closeness factor, which determines the proximity of $f(\sigma, u)$ to the non-smooth yield surface, and μ is a parameter to further tune the yield surface. This equation was developed from a constraint optimization scheme and defines a smooth envelope inside the surfaces for each slip system defined by equation (2.18).

The model Zamiri and Pourboghrat developed accurately predicts the deformation behavior of FCC materials, however, it falls short of predicting the deformation behavior of BCC single crystals like Nb or α-Iron. This model does not account for the non-planar core of screw dislocation in BCC materials, which is among the reasons for this failure. The reasons for the failure of this model in predicting the deformation behavior of BCC single crystals are discussed in detail in Chapter 4.

2.2.2 Hardening rule

Yield criteria alone can only predict the onset of plastic deformation. To predict the plastic deformation behavior of the material beyond the initial yielding one needs a hardening model. These models predict how the yield surface expands, and the flow stress (yield stress) increases with the increase of strain.

Taylor's hardening rule suggests that the hardening is proportional to the total strain in a grain. In 1964, Hutchinson [34], used the incremental form of Taylor's hardening rule as:

$$\dot{\tau}_y^\alpha = h \sum_\alpha \dot{\gamma}^\alpha \tag{2.20}$$

in which h is the hardening moduli,$\dot{\gamma}^\alpha$ is the increment of shear strain and $\dot{\tau}_y^\alpha$ is the increment of shear stress on slip system α. With the above definition, the yield surface expands uniformly. This is inconsistent with the Bauschinger effect, which states hardening in the direction of plastic flow (e.g., tension) reduces yield strength in the reverse direction (e.g., compression). Thus, Taylor hardening model cannot predict reversed loading. It also cannot model the soft behavior of single slip as well as the high hardening rate of multiple-slip.

In 1966, Hill [39] suggested the following hardening law, based on Taylor's hardening rule.

$$\dot{\tau}^{\alpha} = \sum_{\beta} h^{\alpha\beta} \left| \dot{\gamma}^{\beta} \right| \tag{2.21}$$

Where $\dot{\gamma}^{\beta}$ is the increment of shear strain on slip system β. This equation reduces to Taylor's hardening rule, when all components of the hardening moduli matrix $h^{\alpha\beta}$ are equal.

Several authors defined relationships for $h^{\alpha\beta}$. In 1970, Hutchinson [40] suggested the following:

$$h^{\alpha\beta} = h^{m} + (h^{s} - h^{m})\delta^{\alpha\beta} \tag{2.22}$$

where h^{m} and h^{s} are the hardening rates for multiple and single slip, respectively. $\delta^{\alpha\beta}$ is the Kronecker delta.

In 1983, Asaro [41] summarized prior works and showed that the hardening moduli can be defined with the below equation.

$$h^{\alpha\beta} = h^{\beta} \left[q + (1-q)\delta^{\alpha\beta} \right] \quad \text{(no summation on } \beta) \tag{2.23}$$

In this equation, q is the latent-hardening ratio, which is defined as the ratio of latent-hardening to self-hardening rate and has values in the range of $1.0 \leq q \leq 1.4$. Diagonal components of $h^{\alpha\beta}$ are called self-hardening and off-diagonal components describe latent-hardening. h^{β} is a function that defines the hardening rate and is defined with the following equation.

$$h^{\beta} = h_0 \left| 1 - \frac{\tau_c^{\beta}}{\tau_s} \right|^{a} \cdot \operatorname{sgn}\left(1 - \frac{\tau_c^{\beta}}{\tau_s} \right) \tag{2.24}$$

where h_0 is the initial hardening rate, τ_c^{β} is the current slip resistance on slip system β, τ_s is the saturation value of the slip resistance, and finally a is the exponent controlling the hardening rate. Several other useful descriptions of h^{β} are described in the work of Brahme et al [42].

Shear stress vs. shear strain curves of single crystals that are initially orientated for single slip show three distinct hardening stages. These stages are shown in Figure 2.1.

The hardening rate just after yielding is low. Most of the deformation in this stage is accommodated by the primary slip system and the hardening is chiefly due to self-hardening. The low hardening rate corresponds to a large dislocation mean free path and few barriers. This stage is known as "easy glide" [43].

The second stage, which is known as "linear hardening", starts when other slip systems activate and interact with the primary slip system. This reduces the mean free path of dislocations and considerably increases the hardening rate. During this stage the dislocation density increases [43].

The hardening rate eventually decreases which signals the onset of the third stage, "exhaustion hardening". The high stress and dislocation density activate cross slip and dynamic recovery which in turn reduce the accumulation of dislocations in the material.

Although Hill's hardening rule, equation (2.21), is widely used in crystal plasticity, it can only model the stress-strain of the first stage of the deformation of single crystals, where the hardening rate does not change significantly during the deformation.

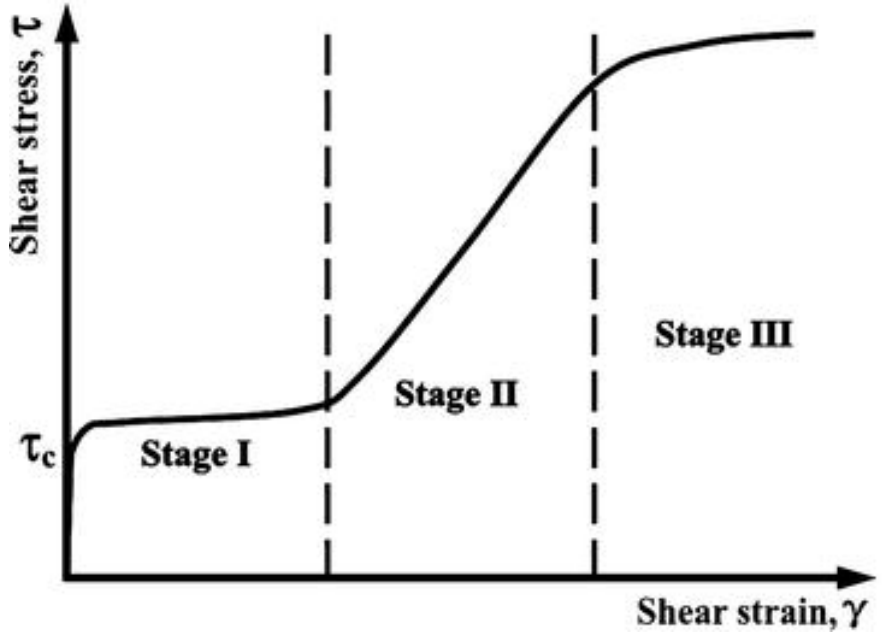

Figure 2.1: Shear stress - shear strain curves of single crystals that are initially orientated for single slip show three distinct stages. Each stage has a different hardening rate that is due to the different underlying mechanisms. Figure form [43].

2.2.3 Important aspects of crystal plasticity models

The crystal plasticity theory proposed by Taylor phenomenologically models the dislocation slip of a close-packed crystal structure. Therefore, it can only accurately model an FCC crystal that deforms just by dislocation slip. This type of crystal plasticity does not directly model grain boundaries or subgrain structure, and does not consider the temperature dependency of deformation. Moreover, this type of crystal plasticity model cannot accurately predict the behavior of metals that have deformation or transformation twinning, show a high temperature or strain rate sensitively, or do not have a close-packed crystal structure. The fundamental equations of crystal plasticity do not have any length scale parameters. Therefore, a crystal plasticity that gives accurate prediction for a microscale sample does not necessarily produce reasonable results for a macroscale sample of the same material.

Over the years, numerous crystal plasticity models have been developed to fix the short comings of the classical crystal plasticity theory and to increase the accuracy of predictions. Darrieulat and Piot [37], suggested an analytical formulation based on Schmid law to generate a yield surface for single crystal FCC metals. Buchheit et al. [44] developed a crystal plasticity model for FCC materials that tracks crystal orientation of grains and predicts the subgrain evolution. Geers et al. [45] developed an extended crystal plasticity scheme that models dislocation climb in addition to dislocation glide. Hansen et al. [46] developed a rate dependent dislocation density based crystal plasticity model that considers the temperature effects in the modeling of dislocation motion. Bittencourt [47] proposed a crystal plasticity model that considers dislocation slip and deformation as independent variables. He also included an artificial viscous effect. Depending on the value of the viscous term, the model can be rate dependent or rate independent. These areas form some of the most important aspects of the crystal plasticity theory. Therefore, some recent works in each of these areas are briefly reviewed below.

Rate-dependent vs. rate-independent crystal plasticity

Two stress update algorithms are used in crystal plasticity models, namely rate-independent and rate-dependent. The rate-independent crystal plasticity models, which are designed for low homologous temperature [48], assume that the dislocation slip is rate-independent. In this type of crystal plasticity, one needs to find the set of active slip systems. Often, the rate-independent crystal plasticity is ill-conditioned. The actives slip systems cannot be uniquely identified, because they are linearly dependent [48–50]. In other words, the yield surface defined in this type of crystal plasticity is not smooth [38], which cause ambiguity in finding the slip rate. One way to overcome this issue is to use rate-dependent crystal plasticity. This method does not distinguish between the active and inactive slip systems [50]. Instead, the slip rate at each slip system depends on the slip resistance on that slip system. Therefore, the activity of each slip system can be uniquely identified [48, 50].

Zhang and Li [51] used a rate-dependent crystal plasticity to calculate the lattice rotation and studied orientation stability in biaxial tension of magnesium alloy sheets. Li and Yang [52] worked on improving the efficiency of crystal plasticity. They used Taylor expansion to approximate the rate of shear strain with a set of linear equations and used them to develop an explicit integration algorithm. They showed that by implementing this model in parallel processing, the efficiency of the crystal plasticity could be improved. Zhang et al. [53] developed a semi-implicit integration algorithm. This algorithm facilitates the prediction of evolution of grain orientations. They implemented this algorithm in a rate-dependent crystal plasticity and simulated the earing profiles. The predictions of their model were in good agreement with experiments. Nguyen et al. [54] developed a rate-dependent crystal plasticity model for single crystals. This is a dislocation density based model and uses void growth dynamics to model damage. They proposed a scalar equivalent dislocation density parameter that models the effect of dislocation density on all slip systems in the crystal. Tajalli et al. [55] used a rate-dependent crystal plasticity to simulate micro-machining of copper. They included a thermal softening term in their crystal plasticity model to account

for the heat generated during the high strain rate micro-machining. They concluded that the initial orientation of the material affects the morphology of the chip.

Forest and Rubin [56] developed a rate-independent crystal plasticity. They compared their model with a quasi-rate-independent crystal plasticity for single crystals of a nickel based superalloy and single crystal copper. They argued that their model improves the computational efficiency and reduces the CPU time. Mohammed et al. [57] used a rate independent crystal plasticity model to predict the bulging of a three-phase advanced high strength steel. They started with a known volume fraction of each phase and assigned a phase distribution to each material point within the model. Thereofre, the overall volume fraction of all phases matches with experiment. They compared the prediction of their model with the Nakajima bulge test of an advanced high strength steel, and concluded that the model gives accurate predictions.

Phenomenological vs. dislocation density hardening rules

Many of the early crystal plasticity models used a phenomenological hardening rule [34, 39–41]. According to this hardening rule, which is presented in §2.2.2, the increase in the slip resistance of a slip system is a function of the shear strain on all slip systems. An alternative to this hardening rule is the dislocation density based hardening rule which models the evolution of dislocation density during the deformation [58–61]. This hardening rule, which is discussed in more detail in §3.2, defines the increase in the dislocation density of a slip system as a function of the shear strain on all slip systems.

Dislocation density based crystal plasticity models are widely used. For instance, Grilli et al. [62] proposed a crystal plastic model based on dislocation interactions for fatigue of FCC metals. They modeled the formation of dislocation junctions at a continuum level, and showed that this model can predict the formation of dislocation walls after cyclic loading. Gan et al. [63] proposed a rate-dependent elastic viscoplastic crystal plasticity for pure magnesium. In addition to dislocations slip, their model accounts for tensile and compressive

twinning. They studied the effect of each mechanism on deformation and concluded that for magnesium each twining system and its hardening law need to be individually modeled.

Modeling deformation twinning in crystal plasticity

Many researchers [64–70] haved studied and modeled deformation twinning in crystal plasticity. Tadano et al. [71] developed a crystal plasticity model for polycrystal magnesium. In this model they considered the deformation by twining in addition to the dislocation slip. They assumed at each material point only one twin system can be active and derived an equation for the evolution of volume fraction of deformation twining. Wong et al. [72] proposed a crystal plasticity model for twining induced plasticity (TWIP) and transformation induced plasticity (TRIP) of high manganese steel. They used a dislocation density based hardening model. In addition to twinning and dislocation slip, their model also accounts for phase transformation of martensite. This model uses the temperature dependence of stacking fault energy to distinguish the dominant deformation mode at each temperature. This model predicts the deformation to be dominated by martensitic phase transformation at low temperatures, twinning at mid-range temperatures, and dislocation slip at high temperatures.

Grain boundary and length scale in crystal plasticity

The crystal plasticity theory does not directly model the grain boundary. This is not an issue in modeling a single crystal, but the effect of grain boundaries needs to be considered for polycrystals. The effect of grain boundaries in materials behavior is indirectly accounted for in the material parameters (e.g., critical resolved shear stress) of crsytal plasticity. However, this means that material parameters will depend on the grain size. Consequently, a set of parameters that gives accurate predictions for a material may not be accurate for the same material with considerably different grain size. Thus, for a more accurate modeling of polycrystal behavior one needs to consider the effect of grain boundaries.

Many researchers have worked on modeling the grain boundary with crystal plasticity [73–78]. Benedetti et al. [79] proposed a method to model a 3D grain boundary using crystal plasticity. They modeled each grain as elasto-plastic domains. They used boundary integral equations and modeled the polycrystal as an aggregate of single crystals. Benedetti et al. formulated the grain boundary problem only in terms of boundary displacement and traction.

Ghorbani Moghadam et al. [80] proposed a framework for a grain-size dependent crystal plasticity, by defining core and mantle regions within a grain. The core is the inner part of the grain and the mantle is the region affected by the grain boundary where the resistance to dislocation pile up and nucleation is greater than the core. Such resistance increases the yield stress and reduces the modulus of strain hardening. Ghorbani Moghadam et al. validated their model by studying the relationship of yield stress and single crystal grain size. Their model produced similar results as the Hall-Petch relationship. They also modeled the deformation of a polycrystal copper sample and showed that their model could predict the grain-size dependent behavior of this material.

Many crystal plasticity models neglect the length scale. As with the grain boundary, the effect of length scale is indirectly incorporated in the material parameters. Therefore, a model that gives accurate predictions at one scale may need to be re-calibrated to work for a significantly different scale.

Many researchers have worked on incorporating the length scale in crystal plasticity [81–86]. Aoyagi et al [87] developed a crystal plasticity model that accounts for grain boundaries and dislocation sources. Thus, this model indirectly considers the effect of the grain size. Counts et al. [88] proposed a non-local integral method that accounts for grain size effects.

Liu et al. [89] developed a size-dependent crystal plasticity and studied the effect of sample size on the deformation of copper single crystals. They used a modified dislocation density hardening model that has a phenomenological size-depended term. They showed their model could predict the size effect in bending and compression.

Castelluccio and McDowell [90] argue that most crystal plasticity models only account for

dislocation interactions without considering the effect of length scale on dislocation structure at mesoscale. To address this issue, they propose a frame work for cyclic loading of metals that accounts for the dislocation evolution and structure at mesoscale. They introduced a method for calculating back stress that depends on the morphology of dislocation structure at mesoscale. They verified their model for single crystals and polycrystals of nickel.

Temperature dependence in Crystal Plasticity

Although the deformation behavior of metals is temperature dependent, the classical theory of crystal plasticity does not have a temperature dependent term. Therefore, a set of material parameters of a crystal plasticity model is only valid for a specific temperature range.

Many researchers have studied temperature-dependent crystal plasticity models [91–93]. He et al. [94] proposed a temperature and rate dependent constitutive model which is based on unified creep-plasticity theory. In this model the inelastic strain rate is defined as function of drag stress, which itself is a function of temperate and is rate dependent. He et al. simulated the uniaxial tensile test of high strength steel and solder alloys at various temperatures and strain rates with this model. The results showed that their model can accurately predict the experimental data.

Wang et al. [95] developed a temperature dependent crystal plasticity model based on the elastic visco-plastic self-consistent frame work. They defined the yield by modeling the dislocation de-pinning which itself is a function of temperature as well as the resolved shear stress. The model also predicts the rate sensitivity by defining the shear rate as function of activation energy of dislocation de-pinning.

Yu et al. [96] developed a rate dependent crystal plasticity to predict the cyclic deformation of super-elastic NiTi shape memory alloy. They accounted for the heat generated from inelastic dissipation and latent heat of transformation. Yu et al. compared the predictions of their model with experiments and concluded that the model matches with the experiment.

Liu et al. [97] developed a crystal plasticity model for temperature dependent behavior of

magnesium. Their model accounts for dislocation slip, twining and the interaction of these two. In this model both dislocation slip, and twining are temperature dependent. They argued that their model could capture the Hall-Petch effect in a range of temperatures, and concluded that the ductility of magnesium increases with temperature because of an increase in the non-basal slip activity.

Non-Schmid crystal plasticity

The Schmid law was developed for FCC materials based on the fact that they have a closed-packed crystal structure. Therefore, the slip plane and slip direction can be easily identified. BCC materials, however, do not have a close-packed structure. Finding the active slip system in BCC materials is more challenging than FCC materials [98–102], because slip in BCC materials can happen on multiple planes in the same slip direction. Additionally, dislocation slip in BCC materials may be affected by stresses other than the one resolved on the slip plane and long the slip direction [11, 103–105]. This is known as the non-Schmid behavior. Crystal plasticity models for BCC materials are usually more sophisticated than the FCC models, since the dislocation slip behavior of BCC materials is more complicated.

Many researchers have studied the non-Schmid behavior of BCC materials [11, 16, 98, 103–109]. For instance, Ghanbarpour et al. [110] studied the crystal plasticity modeling of a nickel based superalloy which was made through additive manufacturing. The model they used accounts for non-Schmid stresses and has a dislocation density based hardening rule. They also assumed that the initial slip resistance is size dependent and is affected by solid solution hardening and precipitates. They concluded that their model could predict a wide range of deformation response of this superalloy. More details on the non-Schmid modeling of BCC materials is presented in §3.1.

Multi-scale modeling

Crystal plasticity only models the behavior of materials at a crystal level. Often multiple material models at different length scales are connected to each other to make an Integrated Computational Materials Engineering (ICME) tool. Such multi-scale models can be used to develop new materials and processes. Some examples of the recent development in multi-scale modeling are discussed next.

Chandra et al. [111] created a multi-scale plasticity model for polycrystal copper that bridges the atomics scale to continuum level. They started with atomistic simulation; fed the results of that to a dislocation dynamic model; then found the parameters of a single crystal plasticity model using the results of the dislocation dynamic model. Finally, they simulated the tensile behavior of single crystal copper and used the results as inputs to a polycrystal plasticity model. They showed that their polycrystal model could predict tensile deformation behavior of polycrystal copper.

Kim et al. [112] developed a rate-dependent viscoplastic crystal plasticity model to predict the Forming Limit Diagram (FLD) of a ferritic stainless steel. They found the material parameters from experiments and used a multi-scale Marciniak-Kuczynski modeling scheme to find the FLD of this steel.

Mellbin et al. [113] developed a multi-scale model for polycrystals by combining a rate-dependent crystal plasticity and a vertex model of a polycrystal structure. The vertex method predicts evolution of grain boundaries. In this method each triple junction is modeled with a vertex and boundaries are defined by connecting the vertices. In addition, virtual vertices (extra nodes on the grain boundary) are defined to capture the curvature of grain boundaries. Mellbin et al. [114] implemented the crystal plasticity part of the model using GPU-parallelization. This type of parallelization improves computational efficiency of crystal plasticity models which use Taylor homogenization. In this type of homogenization, it is assumed that all grains in a polycrystal are subject to the same strain. Therefore, at each integration point stresses for a number of crystal orientation need to be calculated. These

calculations can be done in parallel. Mellbin et al. achieved up to two orders of magnitude reduction in the computation time by using GPU-parallelization.

Crystal plasticity models can be used to simulate a wide range of manufacturing processes, including deep drawing [6], hydrofroming [115], and machining [55]. Before using any model in predicting the deformation behavior of a material, however, one needs to find the parameters of the model for the material. This is often done by fitting the model to results of simple experiments like tensile tests. The predictions of the model need to be compared to a new set of experiments to confirm the validity of material parameters. In addition, a model that is fitted and validated only with tensile tests, cannot be safely used to predict a more complex stress state. The model needs to be verified for complex stress states before one can trust its predictions.

2.3 Hydroforming

Hydroforming is a process in which a sheet or a tube is deformed using fluid pressure. If a die is used, the fluid pressure will force the material to conform to the shape of the die. Hydroforming has been widely used for about half a century in the automobile industry [116, 117], aerospace [117] and sanitary uses [116, 117]. Many materials including steel [116, 118], aluminum alloys [118–121], magnesium alloys [118, 122] and fine grain Nb [20, 123–125] can be hydroformed.

Hydroforming interests many researchers. Asnafi [126] assumed the bulge of the tube has a straight shape and developed a model to predict the limits of tube hydroforming. Using this model, Asanfi and Skogsgardh [119] simulated the hydroforming of aluminum tubes. Hwang and Lin [127] assumed the bulge of the tube has an ellipsoid shape and proposed a model that considers non-uniform thinning of the material during the process. Koc and Altan [128] studied the limits of tube hydroforming and failure modes of the tube.

Hydroforming can be divided into two groups: sheet hydroforming and tube hydroforming. Tube hydroforming has many advantages over conventional stamping and welding tech-

niques. These advantages include consolidating stamped and welded parts into one piece, which can reduce the tooling cost, reduce weight by making more efficient designs possible to manufacture, and reduce waste [117]. Tube hydroforming can also improve the strength and stiffness of the parts [117, 118, 127, 129].

Advantages of sheet hydroforming over conventional deep drawing and welding include better surface quality and drawing ratio, fewer forming steps and the possibility of forming more complex shapes [130].

Disadvantages of hydroforming include the slow manufacturing process and the high cost of machinery [117]. Due to technological difficulties, sheet hydroforming has fewer industrial applications than tube hydroforming [130].

Common failure modes of tube hydroforming can be categorized as buckling, bursting and wrinkling. These modes are shown in Figure 2.2. Buckling happens when the axial compressive loading causes the material to yield. This often happens in long tubes with thick walls, at small strains at the beginning of the process. High compressive strain in thin-walled tubes causes wrinkling. Bursting takes place due to necking of the material, which is a result of high local tensile stress [128]. The ability to predict failure modes computationally is desirable and could expand the efficiency in designing hydroformed parts.

2.4 Exemplary BCC metals for examining crystal plasticity modeling

Two BCC materials were studied in this dissertation. These materials are ferrite (BCC Iron) and niobium. The reasons for choosing these materials are explained further below.

2.4.1 Ferrite

To improve the fuel economy of vehicles, manufacturers need to find ways to reduce the weight of vehicles. Materials optimization is one of the remaining options to reduce weight. This includes designing new steel alloys with a higher strength that can be used as thinner sheets while satisfying the safety and durability concerns. Adding new materials to the

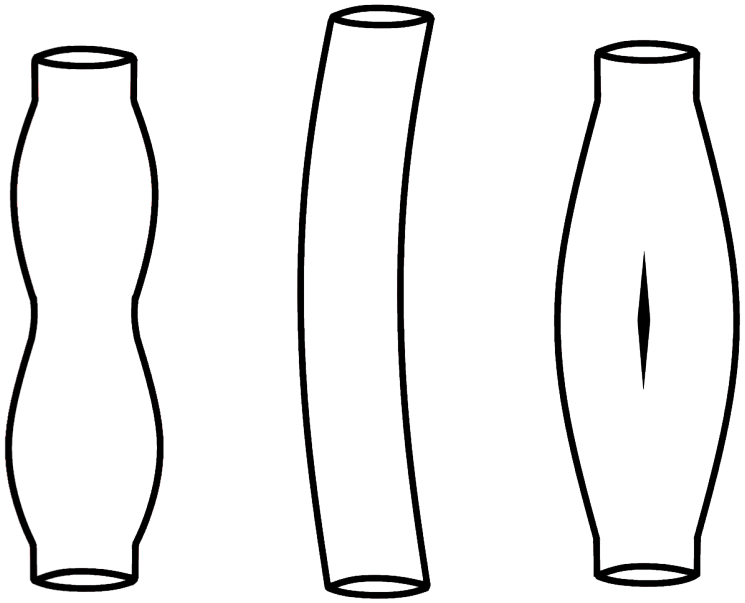

(a) Wrinkling (b) Buckling (c) Bursting

Figure 2.2: Common modes of failure in tube hydroforming. a) Wrinkling happens in thin-walled tubes b) buckling thick-walled long tubes c) bursting happens due to necking. Redrawn from [128].

current portfolio of hydroformable materials is desirable.

The current effort to model the deformation of ferrite is a part of a larger investigation that aims to develop a 3rd Generation Advanced High Strength Steel (3GAHSS) using an integrated computational materials engineering (ICME) tool. Models in multiple scales including atomistic, phase transformation, crystal plasticity, and performance models are being integrated to make a coordinated tool-set.

The 3GAHSS have complex microstructures comprised of different phases, such as ferrite, martensite, austenite, with different volume fractions, grain sizes, and crystal orientations distributed throughout the material. Therefore, the traditional models for steel with homogenized microstructure cannot predict the behavior of 3GAHSS. Consequently, crystal plasticity finite element (CPFE) modeling of 3GAHSS is becoming crucial for the development of lightweight structures.

Austenite has an FCC structure and can be modeled with available crystal plasticity

models. Martensite has a Body Centered Tetragonal (BCT) structure. The BCT martensite has the same slip systems as a BCC material [131]. Therefore, to enable modeling of the phases present in 3GAHSS steels, better modeling of ferrite is needed.

The goal of Chapter 4 is to model the deformation of ferrite single crystals. This Chapter explains the development of a rate-independent non-Schmid crystal plasticity model and compares the predictions of this model with that of a Schmid crystal plasticity. Before the models can be used, however, they need to be calibrated and verified. Therefore, Chapter 4 also explains the calibration and verification of both models using compression tests of ferrite micropillars.

2.4.2 Niobium

Superconducting Radio Frequency (SRF) cavities are the essential building blocks that make up the core of particle accelerators [20, 132]. These cavities are made from pure Niobium (Nb), which has the highest critical temperature for superconductivity ($T = 9.2K$) of the pure metals [133]. Pure Nb is very ductile. Tensile experiments show that Nb can deform more than 40% without necking [134]. Consequently, Nb is the preferred superconducting material for fabricating complex shaped cavities. Nonetheless, the large strain deformation behavior of pure Nb has not been thoroughly studied.

The mechanical behavior of Nb is anisotropic and shows a great directionality [134]. The topology arising from differential strains in neighboring grains on the surface degrade the SRF performance of Nb [135]. The deficiency in understanding the behavior of Nb makes use of fine grain sheets more desirable than large grain sheets, as fine grain sheets are less anisotropic.

As-cast ingots go through a series of steps including forging, milling, rolling, and intermediate annealing, to make fine grain ($25-50\mu m$) sheets. These sheets are then deep-drawn into a half-cell shape and subsequently electron beam welded together to make a cavity. Due to the Hall-Petch effect, fine grain materials have higher strength than large grain ones.

Nonetheless, fine grain sheets are easier to deform uniformly [136] than the more anisotropic large grain sheets. Therefore, most of Nb cavities are manufactured from fine grain Nb sheets.

Disks sliced from as-cast Nb ingots have large grains. These disks provide a cheaper path to cavity fabrication than fine grain sheets, because they go through fewer production steps and result in less waste. The lower number of grain boundaries in large grain Nb slices lead to a higher SRF performance, presumably due to having fewer defects or area per unit volume in the form of grain boundaries [135].

Achieving consistency in manufacturing of cavities from fine grain sheets is easier than large grain disks because anisotropy is less evident in deformation of non-textured fine grains. Although the combination of cost and performance makes large grain sheets a desirable candidate, the difficulties caused by their anisotropic deformation has restricted their application.

To use large grain disks instead of fine grain sheets in manufacturing of superconductive cavities, one needs to design a new manufacturing process. But the anisotropy complicates the designing process. Furthermore, the high price of pure Nb makes the trial-and-error design process costly. One way to overcome these difficulties and reduce the design costs is to use a constitutive model to predict the deformation behavior of single crystal Nb. A polycrystal can be modeled as an agglomerate of multiple single crystals. Therefore, a model capable of predicting the deformation behavior of single crystals is desirable to predict the behavior of polycrystals.

A model capable of predicting the deformation behavior of Nb can help facilitate designing a manufacturing process for large grain cavities. Such a model can be implemented in Computer Aided Design/Evaluation (CAD/CAE) software and be used to design a manufacturing process. Crystal plasticity is one of the modeling strategies that can be used to predict the deformation behavior of metals. Although conventional crystal plasticity models work relatively well for FCC materials and BCC polycrystals, their performance is not accurate enough for the highly anisotropic deformation behavior of single crystal BCC Nb.

The hardening rule of conventional crystal plasticity models does not accurately model the hardening of single crystals. To address this issue, Chapter 5 proposes a new hardening rule that improves the predictions of a Schmid-type crystal plasticity for single crystal Nb. This model needs to be calibrated and verified before it can be used. Therefore, Chapter 5 also discusses the calibrated and verification o the proposed model with tensile tests of single crystal Nb samples with distinct crystal orientations. Nonetheless, the model still needs to be verified for a more complex deformation path before it can be used to design manufacturing processes.

An alternative fabrication path to the current Nb cavity manufacturing process, is to make seamless cavities. This will eliminate the need to weld deep drawn cavity halves together. Hot spots that develop and degrade cavity performance are commonly found within the heat affected zone near the weld line. Also, the absence of a weld potentially decreases the cost of manufacturing in the long run. Moreover, the performance of a cavity potentially increases because the weld line is a possible source of contamination and other rare or random defects that arise from the complexities of welding.

Tube hydroforming can be used to make cavities from a tube. Singer et al [123, 125] made seamless polycrystalline Nb tubes by spinning and flow forming of a disk. The tubes were then hydroformed into single-cell, or up to three-cell units. The initial values for hydroforming parameters were found from FEM simulations and were further tuned in experiments. The processing and properties of the seamless tube are critical to the success of the hydroforming process. Variations in properties of the tube such as the yield strength, thickness and grain size can result in failure of the tube or irregular final shapes [125].

Thus, a number of issues have to be addressed before the hydroforming of large grain Nb could be industrialized. Large grain seamless Nb tubes are not readily available in the market. Therefore, Chapter 6 of this dissertation focuses on characterization of a large grain seamless Nb tube that was made for this study. This prototype tube provides essential data for comparing the experiment with numerical simulations of crystal plasticity models. Chapter

6 also investigates the forming behavior of the tube under the hydroforming conditions. Consequently, this dissertation work will provide the foundation for designing a seamless large grain tube hydroformed cavity.

CHAPTER 3

IMPROVEMENTS TO SCHMID CRYSTAL PLASTICITY MODEL

Traditional crystal plasticity models need improvement in multiple areas, like the yield function or hardening rule, before they can accurately predict the deformation response of many BCC materials. The current models are usually more accurate for FCC materials and polycrystals. FCC materials have close-packed planes and their active slip system can be determined without ambiguity. Randomly-orientated polycrystals are usually less anisotropic than single crystals. Hence, predicting the deformation of such polycrystals is easier than single crystals.

The deformation response of different BCC materials differs in nature and in many cases, cannot be accurately described with the Schmid law. For example, molybdenum, when loaded in compression, shows a twinning-antitwinning asymmetry, while tungsten shows none of this asymmetry [107]. The stress-strain of both materials deviates from the Schmid law. Gröger et al. [106] argued that the breakdown of the Schmid law in molybdenum is due to the combination of shear stresses perpendicular to slip direction and twinning-antitwinning asymmetry. In tungsten, however, the deviation from the Schmid law is only the effect of shear stresses perpendicular to slip direction. The extent of deviation from the Schmid law changes from one BCC material to another. Within a material, this deviation is also a function of crystal orientation.

Another area of the crystal plasticity theory that needs improvement is the hardening rule. Hill's power-law hardening rule cannot predict the varying hardening rate of single crystals. Instead, this model predicts a monotonic decrease in the hardening rate.

Dislocation density based crystal plasticity modeling is another method to improve the accuracy. For instance, Ma et al. [137] modified their model for FCC materials by considering the effect of the Peierls stress. Monnet [138] developed a dislocation density based crystal plasticity model for BCC materials that is valid over a wide range of temperatures and strain

rates.

Another approach is to modify the hardening moduli matrix. Madec and Kubin [139] studied the interactions of $1/2\langle 111\rangle\{1\bar{1}0\}$ and $1/2\langle 111\rangle\{11\bar{2}\}$ slip systems of BCC materials and found 17 distinct interaction types. This contrasts with the Hill-type hardening moduli matrix that only distinguishes between the self and latent-hardening. Following this idea, Queyreau et al. [140] studied the interactions of $1/2\langle 111\rangle\{1\bar{1}0\}$ slip systems in ferrite and calculated six independent hardening coefficients for possible interaction modes.

The rest of this chapter is organized as follows. The non-Schmid crystal plasticity model is explained in §3.1. The dislocation density hardening rule is presented in §3.2. The remaining sections in this chapter discuss the steps needed to implement a dislocation density based Schmid-type crystal plasticity model in the finite element scheme. §3.3 explains bridging the crystal level (crystal plasticity model) to the continuum level (finite element). §3.4 explains the derivation of a dislocation density based crystal plasticity model and §3.5 lays out a stress integration algorithm for this model.

3.1 Non-Schmid crystal plasticity model for BCC single crystals

The models introduced in §2.2, are mainly intended for FCC polycrystals. In the 1980s, researchers noticed that the deformation behavior of BCC single crystals does not obey the Schmid law. Many authors, including Qin and Bassani [11, 103], Bassani et al. [104], Gröger et al. [16, 106, 107] and Wang and Beyerlein [98] have worked on the modeling of this behavior, which is known as the non-Schmid behavior.

In BCC crystals the critical resolved shear stress (CRSS) is a function of the orientation of the crystal with respect to the loading axis, the sense of loading [11], as well as stresses on planes that are non-parallel and/or non-planar with respect to the slip direction [108]. These stresses are known as non-Schmid stresses.

The yielding asymmetry of BCC single crystals in tension and compression has long been associated with the twinning and antitwinning sense of the shear [141]. Recent studies,

however, show this may be only partially true, as non-Schmid stresses have a significant impact on the yielding asymmetry [107]. The non-Schmid stresses are also known as non-glide stresses because they affect the structure of the dislocation core and consequently the ease of dislocation slip, so they do not directly cause dislocation slip.

In BCC materials, the core of $1/2\langle 111\rangle$ screw dislocations spreads on three non-parallel $\{1\bar{1}0\}$ planes in the $\langle 111\rangle$ zone, which reduces their mobility, and in turn limits plastic flow [105]. The core spreading is controlled by the crystal symmetry [105]. This non-planar core leads to a violation of the Schmid law and also accounts for the strain rate sensitivity and temperature dependence of the flow stress [108].

To capture the effect of non-glide stresses on the non-planar core and subsequently on the yielding of BCC materials, Qin and Bassani [103] proposed the following yield criterion which is a generalization of Schmid law.

$$\tau^{\alpha} + \sum_{i=1}^{N_{ns}} a_i^{\alpha} \tau_i^{\alpha} = \tau_{cr}^{*\alpha} \tag{3.1}$$

Here α corresponds to the slip system, $\tau_{cr}^{*\alpha}$ is the critical resolved shear stress value in the non-Schmid case, τ_i^{α} and N_{ns} are the non-Schmid stresses and their identifying number, respectively. a_i^{α} are material parameters, and τ^{α} is the Schmid based resolved shear stress. The expanded form of the summation in equation (3.1) is:

$$\sum_{i=1}^{N_{ns}} a_i^{\alpha} \tau_i^{\alpha} = a_1 \sigma : [m^{\alpha} \otimes n_1^{\alpha}] + a_2 \sigma : [(n^{\alpha} \times m^{\alpha}) \otimes n^{\alpha}] + a_3 \sigma : [(n_1^{\alpha} \times m^{\alpha}) \otimes n_1^{\alpha}] \tag{3.2}$$

in which n_1^{α} is the plane normal of a $\{1\bar{1}0\}$ plane in the slip direction zone, that makes -60° with the slip plane normal n^{α}. The expanded non-Schmid yield criterion has the following form [107].

$$\tau_{cr}^{*\alpha} = \sigma : (m^{\alpha} \otimes n^{\alpha}) + a_1 \sigma : (m^{\alpha} \otimes n_1^{\alpha}) + a_2 \sigma : [(n^{\alpha} \times m^{\alpha}) \otimes n^{\alpha}] + a_3 \sigma : [(n_1^{\alpha} \times m^{\alpha}) \otimes n_1^{\alpha}] \tag{3.3}$$

Bassani et al. [104] combined all the geometric terms in a single parameter, $d^{*\alpha}$, that resembles the Schmid tensor in equation (2.16) as:

$$\sigma : d^{*\alpha} = \tau_{cr}^{*\alpha} \tag{3.4}$$

where

$$d^{*\alpha} = d^{\alpha} + \sum_{\eta} a_{\eta}^{\alpha} d_{\eta}^{\alpha} \tag{3.5}$$

in which d_{η}^{α} are the second rank tensors that represent the non-glide components of the applied stress.

Although BCC materials yield according to a non-Schmid rule, they still deform by dislocation motion (slip) on slip planes. This means that, similar to the Schmid-type crystal plasticity, the rate of plastic deformation D^p is proportional to the shear rate $\dot{\gamma}^{\alpha}$ [11].

$$D^p = \sum_{\alpha}^{N} d^{\alpha} \dot{\gamma}^{\alpha} \tag{3.6}$$

In the Schmid-type crystal plasticity model, d^{α} is used to define both the yield criterion and the flow potential [38]. This is known as the associated flow rule, and requires the increment of the plastic strain to be in the direction of the outward normal to the yield surface. A non-Schmid model, however, is based on the non-associated flow rule [142]. In non-associated plasticity, two functions need to be defined, one to estimate stresses that cause yielding, and another to define the direction of the plastic strain.

The non-Schmid model has been verified for several BCC materials including BCC iron, molybdenum, and tungsten, but there is still no consensus on the number of effective non-glide stress components. This number can vary for each material and may vary from one study to another. For instance, according to Gröger and Vitek [16], for tungsten the second term, and for molybdenum the third term, on the right-hand side of equation (3.3) vanishes. To model BCC iron, Chen et al. [109] used all terms in equation (3.3) while Koester et al. [108] proposed a more general non-Schmid model with an additional three non-glide normal stress terms included. This model is shown below.

$$\begin{aligned}\sigma : [m^{\alpha} \otimes n^{\alpha}] + a_1 \sigma : [m^{\alpha} \otimes n_1^{\alpha}] + a_2 \sigma : [(n^{\alpha} \times m^{\alpha}) \otimes n^{\alpha}] + a_3 \sigma : [(n_1^{\alpha} \times m^{\alpha}) \otimes n_1^{\alpha}] \\ + a_4 \sigma : [n^{\alpha} \otimes n^{\alpha}] + a_5 \sigma : [(n^{\alpha} \times m^{\alpha}) \otimes (n^{\alpha} \times m^{\alpha})] + a_6 \sigma : [m^{\alpha} \otimes m^{\alpha}] = \tau_{cr}^{*\alpha}\end{aligned} \tag{3.7}$$

The first term in this equation is the Schmid stress. The second to fourth terms incorporate the effect of shear stresses, and the fifth to seventh terms model the effect of normal

stresses. Parameters a_1 to a_6 are material constants. The planes on which these resolved stresses act are schematically shown in Figure 3.1. The red, green, and blue planes are three $\{1\bar{1}0\}$. The red plane is the slip plane. The gold and purple planes are drawn only to facilitate the illustration of non-Schmid normal stresses. The gray line is the slip direction and is along $\langle 111 \rangle$. The Schmid resolved shear stress is shown with a solid black line and is marked accordingly. The non-Schmid resolved shear stresses are shown with dashed lines, and normal stresses are shown with solid lines and are marked with their respective non-Schmid constants a_1-a_6.

The term including a_1 is the shear stress parallel to the slip direction on any $\{1\bar{1}0\}$ plane other than the slip plane (the blue and green planes in Figure 3.1). According to Gröger et al. [107], this stress causes the twinning-antitwinning effect. The term including a_2 is the shear stress normal to the slip direction acting in the slip plane; a_3 is the shear stress normal to slip direction acting on a $\{1\bar{1}0\}$ plane other than the slip plane (the red plane in Figure 3.1); a_4 is the normal stress perpendicular to slip plane (and therefore perpendicular to the slip direction) acting on the slip plane; a_5 is the normal stress perpendicular to slip direction acting on a plane perpendicular to the slip plane (the gold plane in Figure 3.1); and finally a_6 is the normal stress parallel to slip direction acting on a plane perpendicular to slip direction (the purple plane in Figure 3.1). According to Koester et al. [108], the last term makes the yield criterion independent of the hydrostatic stress. Many researchers [16, 35, 104–108, 142, 143] have used atomistic simulation to find the material constants used in the non-Schmid models.

3.2 The dislocation density hardening rule

An alternative to the Hill-type power-law hardening rule is a dislocation density based model, which directly models the slip and mutual intersection of dislocations.

Many researchers [17, 58–61, 137, 144, 145] have used a Taylor type equation to predict the increase of the flow stress with the evolution of the dislocation density. This hardening

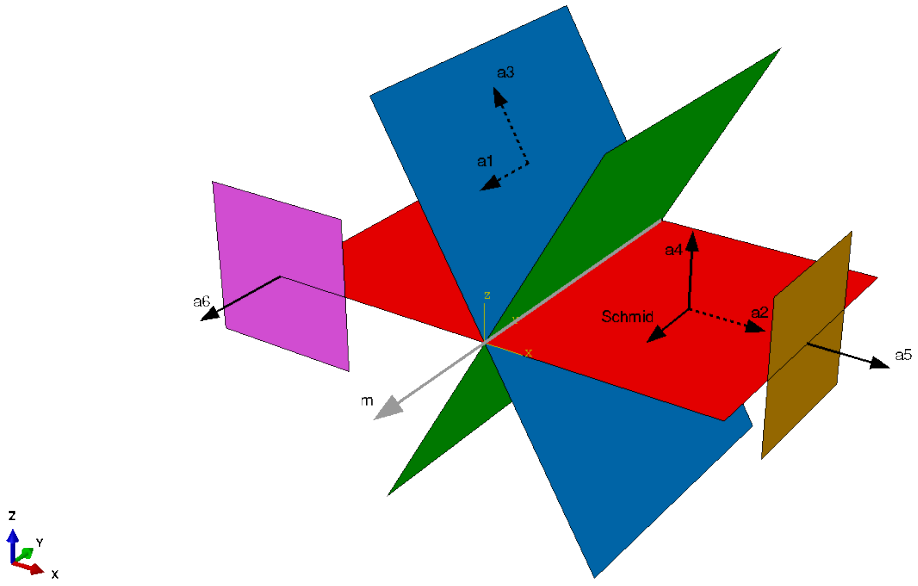

Figure 3.1: The non-Schmid planes and stresses that are considered in equation (3.7) are schematically shown here. The red, blue, and green planes are the $\{1\bar{1}0\}$ planes. Here the red plane is the slip plane. The slip direction is shown with a gray line along $\langle 111 \rangle$ direction. The Schmid resolved shear stress along the slip direction is shown with a solid black line on the red plane and in the slip direction. The non-Schmid resolved shear stresses are shown with dashed lines. For brevity, the resolved shear stresses a_1 and a_3 are only shown on the blue plane, however, similar shear stresses may be resolved on the green plane. The gold and purple planes are not planes and are only drawn to help with the visualization of the non-Schmid normal stresses. These stresses (a_4, a_5 and a_6) are drawn with solid lines and act normal to the red, gold and purple planes.

equation often has the following form [58, 145, 146]:

$$\tau_y^\alpha = \tau_0^\alpha + aGb\sqrt{\sum_{\beta=1}^{N} h_d^{\alpha\beta}\rho^\beta} \tag{3.8}$$

where τ_y^α is the current slip resistance on slip system α, and τ_0^α is the initial value of the CRSS on this slip system, a is a material parameter, b is the magnitude of the Burgers vector, G is the shear modulus, ρ^β is the dislocation density on slip system β, and $h_d^{\alpha\beta}$ is the dislocation density hardening moduli matrix.

Equation (3.8) assumes dislocations of every slip system β, which are denoted with ρ^β, interact with dislocations on slip system α and contribute to the increase of the flow stress.

The contribution of each slip system to hardening is defined through the hardening moduli matrix $h_d^{\alpha\beta}$ with the following equation [145].

$$h_d^{\alpha\beta} = n^{\alpha} \cdot f^{\beta} \tag{3.9}$$

In which n^{α} is the slip plane normal and f^{β} is the line direction of the forest dislocation corresponding to the moving dislocation. Therefore, the hardening contribution of the part of the dislocation forest that is co-planar with the slip system α is zero.

The line direction of the forest dislocation can be calculated by assuming that all immobile statistically stored dislocations (SSDs) are the product of mobile dislocation interaction. Therefore, one can find the line direction of the forest dislocation from the cross product of the slip plane normal and the dislocation slip direction [60].

$$f^{\beta} = n^{\beta} \times m^{\beta} \tag{3.10}$$

This, however, is only true for edge dislocations.

Several equations for the evolution of dislocation density are suggested and used in the literature [60, 144, 145]. For instance, the evolution of dislocation density can be defined with [145]:

$$\Delta\rho^{\alpha} = \left[\frac{1}{b\, k_a} \sqrt{\sum_{\beta=1}^{N} \rho^{\beta}} - \frac{k_b}{b} \rho^{\alpha} \right] |\Delta\gamma^{\alpha}| \tag{3.11}$$

where k_a and k_b are material constants for dislocation generation and annihilation. This approach is more physically realistic than the phenomenological model described in §2.2.2, but the computation cost of the dislocation density model is higher than the phenomenological model.

3.3 Implementation of crystal plasticity in finite element modeling

Crystal plasticity models are usually implemented as constitutive equations in finite element codes. To make the connection between the continuum mechanics (used in finite

element analysis) and dislocation slip (used in crystal plasticity theory), one needs to define the relationship between the slip rate as defined by each of these theories.

The velocity gradient tensor L that is applied to a material point can be additively decomposed.

$$L = D + W \tag{3.12}$$

The symmetric part D is known as the rate of deformation tensor and the antisymmetric part W is known as the spin tensor. Subsequently, each of these tensors can be decomposed into elastic (lattice rotation) and plastic parts.

$$D = D^e + D^p \tag{3.13}$$

$$W = \Omega + W^p \tag{3.14}$$

Where superscripts e and p denote elastic and plastic parts of the respective tensors. The elastic part of the spin tensor is the lattice spin rate tensor Ω which can be defined as follows:

$$\Omega = R\dot{R}^{\intercal} \tag{3.15}$$

where R is the rigid body lattice rotation.

Two coordinate systems are used in the crystal plasticity finite element model. One coordinate system is attached to the axes of a crystal and rotates with the crystal. This coordinate system is known as the crystal coordinate system. The second one is defined in the local material axes (a finite element) and rotates with the material. This coordinate system is called a material co-rotational coordinate system. The grain orientation matrix Q defines the orientation of the crystal coordinate system with respect to the material co-rotational coordinate system.

Let us assume for a slip system α, the slip direction, m^α, and the slip plane normal, n^α, are defined with respect to the material co-rotational coordinate system. The initial state of any slip system α in this coordinate system can be defined with the Schmid tensor.

$$P^\alpha = m^\alpha \otimes n^\alpha \tag{3.16}$$

One can write the Schmid tensor, P^α, as the sum of a symmetric and an antisymmetric tensor.

$$P^\alpha = d^\alpha + w^\alpha \tag{3.17}$$

Here d^α is the symmetric part of the Schmid tensor which is defined with equation (2.14). This equation is repeated below.

$$d^\alpha = \frac{1}{2}\left(m^\alpha \otimes n^\alpha + n^\alpha \otimes m^\alpha\right) \tag{3.18}$$

w^α is the antisymmetric part of the Schmid tensor and is defined with the following equation.

$$w^\alpha = \frac{1}{2}\left(m^\alpha \otimes n^\alpha - n^\alpha \otimes m^\alpha\right) \tag{3.19}$$

Crystal plasticity assumes that dislocation slip accommodates all deformation. Therefore, as discussed in §3.1, the rate of plastic deformation D^p needs to be accommodated by dislocation slip. This means that for a single crystal with N slip systems, D^p is proportional to the shear rate $\dot{\gamma}^\alpha$ [11]. This was modeled with equation (3.6), which for convenience is repeated here.

$$D^p = \sum_\alpha^N d^\alpha \dot{\gamma}^\alpha \tag{3.6}$$

From plasticity theory, the rate of deformation is parallel to the outward normal of the yield surface. Therefore, D^p can also be found from the following [38]:

$$D^p = \lambda \frac{\partial f\left(\sigma, u\right)}{\partial \sigma} \tag{3.20}$$

Here λ is a Lagrange multiplier, or as it is called in plasticity theory, the consistency parameter. By comparing equations (3.6) and (3.20), one can find the equation for $\dot{\gamma}^\alpha$.

The plastic spin rate is defined with the following equation [38].

$$W^p = \sum_\alpha^N w^\alpha \dot{\gamma}^\alpha \tag{3.21}$$

Therefore, one can find the lattice spin rate by plugging equation (3.21) in equation (3.14) and rearranging.

$$\Omega = W - \sum_\alpha^N w^\alpha \dot{\gamma}^\alpha \tag{3.22}$$

The increment of rigid body rotation can be written in the following form [115].

$$R_{t_0+\Delta t} = R_{t_0} + \dot{R}_{t_0+\Delta t} = \left[I + R_{t_0} \cdot \dot{R}_{t_0+\Delta t}\Delta t\right] R_{t_0} = \left[I + \Omega_{t_0+\Delta t}\Delta t\right] R_{t_0} \tag{3.23}$$

The grain orientation matrix Q can be updated in a similar fashion with the following equation [115].

$$Q_{t_0+\Delta t} = Q_{t_0} + \Delta Q = \left[I + \Omega_{t_0+\Delta t}\Delta t\right] Q_{t_0} \tag{3.24}$$

Where $\Omega_{t_0+\Delta t}$ is the increment of lattice spin rate tensor in the finite element coordinate system. More details on updating crystal orientation can be found in [147] and [115].

A general stress state applied on a crystal can induce a shear stress parallel to slip direction on the slip system α. This shear stress can be found from the Schmid resolved shear stress.

$$\sigma : d^{\alpha} = \tau^{\alpha} \tag{3.25}$$

Where σ is the stress tensor, and τ^{α} is the resolved shear stress (RSS).

According to the Schmid law, the dislocation motion starts when the in-plane shear stress parallel to the slip direction reaches a critical value. This is known as the critical resolved shear stress (CRSS). In FCC crystals, the CRSS is a material parameter and is independent of the crystal orientation and the sense of loading (compression or tension).

3.4 Derivation of a crystal plasticity model with a dislocation density based hardening rule

The details of derivation of a Schmid-type associate crystal plasticity model with a dislocation density based hardening rule are presented here. The flow stress and the yielding behavior in a Schmid-type crystal plasticity model are defined using a yield function. This translates to an associated plasticity model. Following Zamiri and Pourboghrat [38], equation (2.19) is used to define the yield function. This equation is repeated below.

$$f(\sigma, u) = \frac{1}{\rho_f} \ln \left\{ \sum_{\alpha=1}^{N} \exp \left[\frac{\rho_f}{\mu} \left(\frac{|\sigma : d^{\alpha}|}{\tau_y^{\alpha}} - 1 \right) \right] \right\} \tag{3.26}$$

Here ρ_f is termed the closeness factor and has an inverse relation with the distance between the smooth inner envelope and the original yield surface.

Next, the dislocation density hardening rule defined in §3.2 is used to complete the crystal plasticity model. Equation (3.8) calculates the slip resistance, τ_y^α, for each slip system based on the initial value of slip resistance and the current dislocation content. This equation is repeated here.

$$\tau_y^\alpha = \tau_0^\alpha + aGb\sqrt{\sum_{\beta=1}^{N} h_d^{\alpha\beta}\rho^\beta} \tag{3.8}$$

where ρ^β is the dislocation density on slip system β.

During the deformation dislocations interact and change the dislocation content of the material. This evolution is modeled with equation (3.11), which is repeated below.

$$\Delta\rho^\alpha = \left[\frac{1}{b\,k_a}\sqrt{\sum_{\beta=1}^{N}\rho^\beta} - \frac{k_b}{b}\rho^\alpha\right]|\Delta\gamma^\alpha| \tag{3.11}$$

The normality rule of plasticity states that the increment of plastic strain, $\Delta\varepsilon^p$, at yield is parallel to the outward normal of the yield surface. The normality rule can be expressed with the following equation [38].

$$\Delta\varepsilon^p = \Delta\lambda\frac{\partial f}{\partial\sigma} \tag{3.27}$$

Where $\Delta\lambda$ is the consistency parameter.

Using the normality rule and the chain rule, the increment of shear strain on slip system α can be written as:

$$\Delta\gamma^\alpha = \Delta\lambda\frac{\partial f}{\partial\tau^\alpha} = \Delta\lambda\frac{\partial f}{\partial\tau^\alpha}\sum_{\beta=1}^{N}\frac{\partial\tau^\alpha}{\partial\rho^\beta} \tag{3.28}$$

During the deformation the increment of total strain, $\Delta\varepsilon^t$, is known. But the amount of stress resulting form this strain needs to be calculated. The change in the stress can be found from elasticity theory.

$$\Delta\sigma = C^e : \Delta\varepsilon^e = C^e : (\Delta\varepsilon^t - \Delta\varepsilon^p) \tag{3.29}$$

Where C^e is the fourth-order stiffness tensor. $\Delta\varepsilon$ is the change in the strain and superscripts t, e, and p denote total, elastic and plastic strains, respectively. Substituting equation (3.27) in equation (3.29), the change in the stress as a result of plastic strain can be calculated as follows.

$$\Delta\sigma = C^e : (\Delta\varepsilon^t - \Delta\lambda\frac{\partial f}{\partial\sigma}) \tag{3.30}$$

Therefore, to calculate the change in the stress one needs to find the consistency parameter $\Delta\lambda$. This can be found at the yield point where the value of the yield function is $f = 0$.

The yield function can be linearized with Taylor expansion with respect to σ, τ^α and ρ^β.

$$\begin{aligned} f(\sigma^{(k)}, u^{(k)}) = 0 = f(\sigma^{(k-1)}, u^{(k-1)}) &+ \frac{\partial f(\sigma^{(k-1)}, u^{(k-1)})}{\partial\sigma} : \delta\Delta\sigma \\ &+ \sum_{\alpha=1}^{N} \frac{\partial f(\sigma^{(k-1)}, u^{(k-1)})}{\partial\tau^\alpha} \sum_{\beta=1}^{N} \frac{\partial\tau^\alpha}{\partial\rho^\beta}\delta\Delta\rho^\beta \end{aligned} \tag{3.31}$$

Here (k) and $(k-1)$ refer to the current and previous increment of deformation. To evaluate the above equation one needs to derive the differential terms on the right-hand-side. $f(\sigma^{(k-1)}, u^{(k-1)})$ can be calculated by plugging the values of $\sigma^{(k-1)}$ and $u^{(k-1)}$ in equation (3.26). Differentiating equation (3.26) with respect to σ and τ^α gives the following equations.

$$\frac{\partial f(\sigma, u)}{\partial\sigma} = \sum_{\alpha=1}^{N} \frac{\frac{\mathrm{sgn}(\sigma:d^\alpha)}{\tau_y^\alpha} \exp\left[\frac{\rho_f}{\mu}\left(\frac{|\sigma:d^\alpha|}{\tau_y^\alpha} - 1\right)\right]}{\mu\sum_{\beta=1}^{N}\exp\left[\frac{\rho_f}{\mu}\left(\frac{\left|\sigma:d^\beta\right|}{\tau_y^\beta} - 1\right)\right]} \tag{3.32}$$

$$\frac{\partial f(\sigma, u)}{\partial\tau^\alpha} = \frac{-\frac{|\sigma:d^\alpha|}{\tau_y^{\alpha 2}} \exp\left[\frac{\rho_f}{\mu}\left(\frac{|\sigma:d^\alpha|}{\tau_y^\alpha} - 1\right)\right]}{\mu\sum_{\beta=1}^{N}\exp\left[\frac{\rho_f}{\mu}\left(\frac{\left|\sigma:d^\beta\right|}{\tau_y^\beta} - 1\right)\right]} \sum_{\beta=1}^{N} \frac{\partial\tau^\alpha}{\partial\rho^\beta} \tag{3.33}$$

Rate of change of stress, $\delta\Delta\sigma^k$, can be found form the Taylor expansion of $\Delta\sigma^k$ with respect to the consistency parameter $\Delta\lambda$.

$$\Delta\sigma^{(k)} = \Delta\sigma^{(k-1)} + \left.\frac{\partial\Delta\sigma}{\partial\Delta\lambda}\right|^{(k-1)} \delta\Delta\lambda \tag{3.34}$$

Substituting $\Delta\sigma$ in the above equation with equation (3.30), one arrives at the following:

$$\Delta\sigma^{(k)} = \Delta\sigma^{(k-1)} - \delta\Delta\lambda C^e : \frac{\partial f}{\partial \sigma}\bigg|^{(k-1)} \tag{3.35}$$

By rearranging the above equation one can find the rate of change of stress.

$$\delta\Delta\sigma^{(k)} = \Delta\sigma^{(k)} - \Delta\sigma^{(k-1)} = -\,\delta\Delta\lambda C^e : \frac{\partial f}{\partial \sigma}\bigg|^{(k-1)} \tag{3.36}$$

Similarly, one can find the rate of change of shear strain.

$$\delta\Delta\gamma^{\alpha(k)} = \Delta\gamma^{\alpha(k)} - \Delta\gamma^{\alpha(k-1)} = \delta\Delta\lambda \frac{\partial f}{\partial \tau^\alpha} \sum_{\beta=1}^{N} \frac{\partial \tau^\alpha}{\partial \rho^\beta}\bigg|^{(k-1)} \tag{3.37}$$

To find the variation of the slip resistance, τ^α, with the change of dislocation density, ρ^β, one needs to differentiate equation (3.8) with respect to ρ^β.

$$\frac{\partial \tau^\alpha}{\rho^\beta} = \frac{a\,G\,b}{2} \frac{h_d^{\alpha\beta}}{\sqrt{\sum_{\beta=1}^{N} h_d^{\alpha\beta}\rho^\beta}} \tag{3.38}$$

The rate of change of the dislocation density, $\delta\Delta\rho^\alpha$, can be found by differentiating equation (3.11) with respect to $\Delta\gamma^\alpha$.

$$\delta\Delta\rho^\alpha = \left[\frac{1}{b\,k_a}\sqrt{\sum_{\beta=1}^{N}\rho^\beta} - \frac{k_b}{b}\rho^\alpha\right]|\delta\Delta\gamma^\alpha| \tag{3.39}$$

Finally, $\delta\Delta\lambda$ can be found by replacing equations (3.32) and (3.33), and equations (3.36) through (3.39) in the linearized form of the yield function (3.31). To simplify the notation in the following equation all occurrence of $f(\sigma^{(k-1)}, u^{(k-1)})$ are represented with $f^{(k-1)}$.

$$f^{(k-1)} + \frac{\partial f^{(k-1)}}{\partial \sigma} : \left(-\delta\Delta\lambda C^e : \frac{\partial f^{(k-1)}}{\partial \sigma}\right) + \sum_{\alpha=1}^{N} \frac{\partial f^{(k-1)}}{\partial \tau^\alpha} \sum_{\beta=1}^{N} \frac{aGb}{2} \frac{h_d^{\alpha\beta}}{\sqrt{\sum_{\theta=1}^{N} h_d^{\alpha\theta}\rho^\theta}}$$
$$\left[\frac{1}{b\,k_a}\sqrt{\sum_{\vartheta=1}^{N}\rho^\vartheta} - \frac{k_b}{b}\rho^\beta\right]\left|\delta\Delta\lambda \frac{\partial f^{(k-1)}}{\partial \tau^\beta} \sum_{\varpi=1}^{N} \frac{aGb}{2} \frac{h_d^{\beta\varpi}}{\sqrt{\sum_{\varsigma=1}^{N} h_d^{\beta\varsigma}\rho^\varsigma}}\right| = 0 \tag{3.40}$$

By rearranging this equation and factoring $\delta\Delta\lambda$ one arrives at the following equation.

$$f^{(k-1)} = \delta\Delta\lambda \left(\frac{\partial f^{(k-1)}}{\partial \sigma} : C^e : \frac{\partial f^{(k-1)}}{\partial \sigma} - \operatorname{sgn}(\delta\Delta\lambda) \left(\frac{aGb}{2}\right)^2 \sum_{\alpha=1}^{N}\sum_{\beta=1}^{N}\sum_{\varpi=1}^{N} \frac{\partial f^{(k-1)}}{\partial \tau^{\alpha}} \left| \frac{\partial f^{(k-1)}}{\partial \tau^{\beta}} \right| \right.$$
$$\left. \frac{h_d^{\alpha\beta}}{\sqrt{\sum_{\theta=1}^{N} h_d^{\alpha\theta}\rho^{\theta}}} \frac{h_d^{\beta\varpi}}{\sqrt{\sum_{\varsigma=1}^{N} h_d^{\beta\varsigma}\rho^{\varsigma}}} \left[\frac{1}{b\, k_a} \sqrt{\sum_{\vartheta=1}^{N} \rho^{\vartheta}} - \frac{k_b}{b}\rho^{\beta} \right] \right) \quad (3.41)$$

Dividing both sides of equation (3.41) by the term in the parenthesis gives one can find the rate of change of the consistency parameter.

$$\delta\Delta\lambda = \frac{f^{(k-1)}}{\frac{\partial f^{(k-1)}}{\partial \sigma} : C^e : \frac{\partial f^{(k-1)}}{\partial \sigma} - \operatorname{sgn}(\delta\Delta\lambda) \left(\frac{aGb}{2}\right)^2 \sum_{\alpha=1}^{N}\sum_{\beta=1}^{N}\sum_{\varpi=1}^{N} \frac{\partial f^{(k-1)}}{\partial \tau^{\alpha}} \left| \frac{\partial f^{(k-1)}}{\partial \tau^{\beta}} \right| \cdots}$$
$$\frac{}{\frac{h_d^{\alpha\beta}}{\sqrt{\sum_{\theta=1}^{N} h_d^{\alpha\theta}\rho^{\theta}}} \frac{h_d^{\beta\varpi}}{\sqrt{\sum_{\varsigma=1}^{N} h_d^{\beta\varsigma}\rho^{\varsigma}}} \left[\frac{1}{b\, k_a} \sqrt{\sum_{\vartheta=1}^{N} \rho^{\vartheta}} - \frac{k_b}{b}\rho^{\beta} \right]} \quad (3.42)$$

By summing $\delta\Delta\lambda$, over (k) increments of deformation one can find $\Delta\lambda$. Then, buy plugging this value in equation (3.30) one can find the change in the stress. This concludes development of the dislocation density based Schmid crystal plasticity model.

3.5 Stress-Integration algorithm of Schmid-type crystal plasticity with the dislocation density hardening

This section summarizes the algorithm for stress integration for schmid type crystal plasticity, which follows [115]. This algorithm is developed for the dislocation density hardening rule.

1. The following variables are assumed to be known at the beginning of a finite element increment i for a grain ($\hat{\sigma}_i$, g_i^{α},$\Delta\hat{\varepsilon}_i$,$Q_i$, ρ_i^{α}) in the element coordinate system. Parameter Q_i is the crystal orientation matrix and $g_i^{\alpha} = \tau_{y\,i}^{\alpha}$ is the critical resolved shear stress (slip resistance) of slip system α. Then, stress and strain tensors are rotated to the

crystal coordinate system as:

$$\sigma_i = Q_i \hat{\sigma}_i Q_i^T$$
$$\Delta\varepsilon_i = Q_i \Delta\hat{\varepsilon}_i Q_i^T$$

2. Initialize variables

   i: FEM increment

   k: Plasticity iteration

$$\sigma_{i+1}^{(0)} = \sigma_i + C^e : \Delta\varepsilon_i$$
$$\rho_{i+1}^{\alpha(0)} = \rho_i^\alpha$$
$$g_{i+1}^{\alpha(0)} = g_i^\alpha$$
$$\Delta\lambda_{i+1}^{(0)} = 0$$
$$k = 1$$

3. Evaluate the yield condition $f_{i+1}^{(k)}$

$$f_{i+1}^{(k)} = f\left(\sigma^{(k-1)}, u^{(k-1)}\right) = \frac{1}{\rho_f} \ln\left\{\sum_{\alpha=1}^{N} \exp\left[\frac{\rho_f}{\mu}\left(\frac{|\sigma : d^\alpha|}{\tau_y^\alpha} - 1\right)\right]\right\}$$
$$d^\alpha = \frac{1}{2}\left(m^\alpha \otimes n^\alpha + n^\alpha \otimes m^\alpha\right)$$

   If $f_{i+1}^{(k)} \leq 0$ go to step 9.

4. Calculate the correction to the plastic consistency parameter

$$\delta\Delta\lambda_{i+1}^{(k)} = \frac{f_{i+1}^{(k)}}{\frac{\partial f_{i+1}^{(k)}}{\partial\sigma} : C^e : \frac{\partial_{i+1}^{(k)}}{\partial\sigma} - \operatorname{sgn}(\delta\Delta\lambda)\left(\frac{aGb}{2}\right)^2 \sum_{\alpha=1}^{N}\sum_{\beta=1}^{N}\sum_{\varpi=1}^{N} \frac{\partial f_{i+1}^{(k)}}{\partial\tau^\alpha}\left|\frac{\partial f_{i+1}^{(k)}}{\partial\tau^\beta}\right| \cdots \frac{h_d^{\alpha\beta}}{\sqrt{\sum_{\theta=1}^{N} h_d^{\alpha\theta}\rho^\theta}} \frac{h_d^{\beta\varpi}}{\sqrt{\sum_{\varsigma=1}^{N} h_d^{\beta\varsigma}\rho^\varsigma}}\left[\frac{1}{b\,k_a}\sqrt{\sum_{\vartheta=1}^{N}\rho^\vartheta} - \frac{k_b}{b}\rho^\beta\right]}$$

5. Compute increment of stress, rate of change of shear strain, change of dislocation density and the critical resolved shear stress (slip resistance).

$$\Delta\sigma_{i+1}^{(k)} = \Delta\sigma_{i+1}^{(k-1)} - \delta\Delta\lambda_{i+1}^{(k)} C^e : \frac{\partial f\left(\sigma_{i+1}^{(k-1)}, u_{i+1}^{(k-1)}\right)}{\partial\sigma}$$

$$\delta\Delta\gamma_{i+1}^{\alpha(k)} = \delta\Delta\lambda_{i+1}^{(k)} \frac{a\,G\,b}{2} \sum_{\beta=1}^{N} \frac{\partial f\left(\sigma_{i+1}^{(k-1)}, u_{i+1}^{(k-1)}\right)}{\partial\tau^{\alpha}} \frac{h_d^{\alpha\beta}}{\sqrt{\sum_{\theta=1}^{N} h_d^{\alpha\theta}\rho^{\theta}}}$$

$$\delta\Delta\rho^{\alpha(k)} = \left[\frac{1}{b\,k_a}\sqrt{\sum_{\beta=1}^{N}\rho^{\beta}} - \frac{k_b}{b}\rho^{\alpha(k-1)}\right]\left|\delta\Delta\gamma^{\alpha(k-1)}\right|$$

$$\rho_{i+1}^{\alpha(k)} = \rho_{i+1}^{\alpha(k-1)} + \delta\Delta\rho_{i+1}^{\alpha(k)}$$

$$\Delta g_{(i+1)}^{\alpha(k)} = aGb\sqrt{\sum_{\beta=1}^{N} h_d^{\alpha\beta}\rho^{\beta(k)}}$$

$$g_{i+1}^{\alpha(k)} = g_{i+1}^{\alpha(k-1)} + \Delta g_{i+1}^{\alpha(k)}$$

6. Evaluate the yield function. If $f_{i+1}^{(k)} \leq$ Tolerance go to step 8, otherwise go to step 7.

7. Update the consistency parameter

$$\Delta\lambda_{i+1}^{\alpha(k)} = \Delta\lambda_{i+1}^{\alpha(k-1)} + \delta\Delta\lambda_{i+1}^{\alpha(k)}$$

$$k = k + 1$$

Then Go to 3.

8. Update the crystal orientation using equation (3.24).

9. Rotate the stress tensor back to the FEM coordinate system.

CHAPTER 4

DEVELOPMENT OF A NON-SCHMID CRYSTAL PLASTICITY MODEL AND A DIFFERENTIAL-EXPONENTIAL HARDENING RULE FOR FERRITE SINGLE CRYSTALS

Third generation advanced high strength steels (3GAHSS) are being developed for fabrication of lightweight automotive parts. These new steels have complex microstructures comprised of different phases, such as ferrite (BCC), martensite (BCT), austenite (FCC), etc., with different volume fractions, grain sizes, and crystal orientations distributed throughout the material. Crystal plasticity finite element (CPFE) modeling of 3GAHSS is, therefore, becoming crucial for the development of lightweight structures.

Accurate modeling of 3GAHSS using a CPFE model requires calibration of the hardening parameters of family of slip systems active in each phase (e.g., FCC and BCC). The calibration process involves repeated simulations of the uniaxial compression of a micropillar of a single phase (e.g., ferrite, martensite or austenite) with the CPFE model until there is a good match between predicted and experimentally measured force-displacement curves. The calibration could use just one or multiple experimental force-displacement curves. To assess the validity of the calibration, the calibrated CPFE model is used to simulate the uniaxial compression of the remaining micropillars that were not involved in the calibration process. In the case of 3GAHSS, the CPFE model gets calibrated separately for each phase in the bulk material, as explained above. The collection of calibrated CPFE models for FCC and BCC phases will then be used to predict the behavior of the bulk material. The focus of this Chapter, however, is on modeling of the ferrite phase, which has a BCC crystal structure.

Modeling the deformation of BCC materials is more challenging than FCC materials [98–102] due to the differences in the structure of dislocations. BCC materials have 48 slip systems but the slip planes are not ideally close-packed. The $1/2\langle 111\rangle$ screw dislocations in BCC metals have a non-planar core structure that spreads on three $\{1\bar{1}0\}$ planes. This

causes the non-Schmid behavior, in which stresses developing on planes and directions other than those on the primary slip system will influence dislocation motion.

The non-planar structure of the core of screw dislocations in BCC metals has been known for decades [148]. Studies of the effect of stresses other than the glide stress on this non-planar core can be traced back to the work of Duesbery [149, 150]. The first mechanistic model to capture the effect of the non-Schmid stresses, however, was proposed by Qin and Bassani [11, 103], which accounts for shear stresses affecting the core of screw dislocations. Terms for normal stresses affecting the core were later added to the model by Koester et al. [108]. The non-Schmid behavior has been studied in many BCC materials including molybdenum [16, 35, 104–107, 143, 151], tungsten [16, 35, 106, 107, 143, 152–154], tantalum [98], tantalum-tungsten alloy [155] and BCC iron [108, 109, 146, 156–158].

This Chapter will be only concerned with the calibration and verification of the CPFE for modeling of single crystal BCC metals. The primary goal is to examine the differences between CPFE models based on Schmid and a non-Schmid law to predict the deformation of the ferrite phase in three-phase quenched and partitioned QP980 steels.

Another important issue to consider when calibrating the CPFE model is related to the stage I and stage II hardening of single crystals during the deformation [43]. There is very little hardening in stage I, due to the lack of competing slip systems and barriers to pin dislocations in a single crystal. However, in stage II rate of hardening increases, which is attributed to dislocation entanglements and pile up caused by a combination of the primary slip system rotating away from the loading direction, and secondary slip systems becoming activated with increasing deformation.

In this Chapter, the CPFE models were calibrated with single crystal ferrite micropillars with different initial orientations. These micropillars were carved out of dual-phase DP980 and three-phase QP980 steels using Focused Ion Beam (FIB). The reason for using two different steels was two-fold, a) deformation of ferrite in these two steels show non-Schmid behavior [109, 146], and b) the ferrite phase was compressed to about 4% strain in QP980 and

only showed stage I hardening, while the strain reached double that amount in DP980 and showed both stage I and stage II hardening. Given that a conventional power-law hardening model could not represent the two-stage hardening of the ferrite phase, another important goal of this Chapter was to develop a novel phenomenological exponential hardening rule to be implemented into the CPFE model to predict the two-stage hardening of the ferrite phase. This new model, known as differential-exponential (DE) hardening, judiciously decides on the transitioning from stage I to stage II hardening when the following, a) the ratio of secondary to primary shear strain, and b) the ratio of the maximum shear stress to the saturation shear stress, are greater than the pre-specified values.

This Chapter is organized as follows. §4.1 reviews the materials and the sample preparation method of this study. §4.2 describes the development of a rate-independent non-Schmid crystal plasticity model. §4.3 proposes a new hardening rule to improve the predictions of the non-Schmid crystal plasticity model in cases when the hardening rate changes during deformation. This section also outlines the numerical implementation of the model for stress integration. §4.4 and §4.5 discuss the predictions of the CPFE model for uniaxial compression of ferrite micropillars obtained from QP980 and DP980 steels, respectively. The findings of this Chapter are summarized in §4.6. Various strategies used for calibrating the hardening parameters and the non-Schmid material parameters are explained in detail in Appendix B. The comparison between experimental force-displacement curves and those predicted by the CPFE model are also presented in this Appendix.

4.1 Materials and method - extraction of ferrite micropillars

Two advanced high strength steels (AHSS) were used in this study. A dual-phase DP980 and a three-phase QP980 steel. The chemical composition of these steels is shown in Table 4.1. All micropillar experiments were performed by Dr. Peng Chen and Dr. Hassan Ghassemi-Armaki at Brown University. The details of these experiments are presented in [109, 146] and reviewed below.

The microstructure of DP980 steel consists of ∼60% volume fraction martensite and ∼40% volume fraction ferrite. In uniaxial tensile tests of 1 inch gauge length samples performed at strain rate of $10^{-3}\,s^{-1}$, the yielding occurred at 350 MPa and the ultimate tensile strength was at $\sim 1050 \pm 50$ MPa.

Samples from the as-received 2 mm thick DP980 sheet were mechanically polished with 1 µm diamond paste. Next, to remove the damaged layer formed during the mechanical polishing, the samples were electropolished at 20 V at $-40\,^{\circ}C$ with 1 part perchloric acid in 9 parts ethanol solution.

Four ferrite micropillars were curved out of the polished samples using focused ion beam at 30 keV Ga ions. Final milling was performed at 9.7 pA. The microscope used for milling was a dual-beam FEI focused ion beam. The extracted micropillars had a diameter of 1.3 µm, a height to diameter ratio of between 2-4, and a taper angle of 4°. Each micropillar was extracted from the center of a single ferrite grain at least two diameters away from any boundary. The orientation of micropillars were the measured with Electron Back-Scattered Diffraction (EBSD). Finally, micropillars were uniaxially compressed using a flat punch nanoindenter [109].

The as received microstructure of QP980 sheet consists of ferrite, martensite and retained austenite. The volume fraction of martensite and retained austenite phases are $44 \pm 2\%$ and 8-10%, respectively. The reset of the microstructure is ferrite. The uniaxial tensile tests of this steel showed a yield stress of 400 MPa and an ultimate tensile strength of about 1000 MPa.

Six ferrite micropillars were extracted from the QP980 polished samples using the method that was explained above. The diameter of micropillars was in the range of 1 µm to 1.7 µm, had a height to diameter ratio of 2-3, and a taper angle of 4°. Orientation of these micropillars was also measured with EBSD. Then they were uniaxially compressed with a flat punch nanoindenter.

Table 4.1: Chemical composition of the steel sheets used in this study (wt%).

Chemical Composition	C	Mn	Si	P	Cr	Al	Fe
DP980	0.09	2.15	0.60	-	-	-	rest
QP980	0.2	1.8	1.5	0.02	0.024	0.04	rest

4.2 Developing the non-Schmid, non-associated crystal plasticity model

Crystal plasticity theory assumes that plastic deformation occurs as a result of dislocation motion on a slip plane. The current non-Schmid crystal plasticity model is developed following a Schmid-type crystal plasticity framework that Zamiri and Pourboghrat proposed [38]. The basic equations of this model are given in §3.3. Zamiri and Pourboghrat formulated the yield function for a single crystal with multiple slip systems as:

$$f_\alpha(\sigma, u) = \frac{|\sigma : d^\alpha|}{\tau_y^\alpha} - 1 \leq 0 \qquad \text{for} \qquad \alpha = 1 \dots N \tag{4.1}$$

where u represents the internal variables, α is the slip system, N is the total number of slip systems, d^α is the Schmid tensor defined in equation (2.14), and τ_y^α is the critical resolved shear stress for slip system α.

The yield surface defined with this equation is not smooth and may have sharp corners. Therefore, the outward normal to the yield surface at these points will not be unique and that implies that the plastic strain increment cannot be uniquely identified. To address this problem, Zamiri and Pourboghrat [38] used the following scheme.

$$G(\sigma, u) = \frac{1}{\rho} \ln \left\{ \sum_{\alpha=1}^{N} \exp \left[\frac{\rho}{\mu} \left(\frac{|\sigma : d^\alpha|}{\tau_y^\alpha} - 1 \right) \right] \right\} \tag{4.2}$$

This equation defines a smooth envelope inside the yield surface defined by equation (4.1). The parameter ρ is termed the closeness factor and has an inverse relation with the distance between the smooth inner envelope and the original yield surface. Parameter μ is used to further tune the yield function.

Assuming associated flow rule, the rate of the plastic deformation can be found from:

$$D^p = \lambda \frac{\partial G(\sigma, u)}{\partial \sigma} \tag{4.3}$$

where λ is the plastic consistency parameter.

For BCC materials, as discussed above, the Schmid law does not apply. This is one of the reasons why the crystal plasticity scheme that works well for FCC single crystals, such as aluminum, does not perform as well for BCC materials like Nb or BCC Iron.

Zamiri and Pourboghrat's combined constrained yield function is developed using the associated flow rule [38]. This rule mandates the plastic strain increment to be in the direction of the outward normal to the yield surface. While this is the case for FCC materials, it is not true for BCC materials.

To address this problem, and based on the above discussions, the authors developed a combined constrained non-associated (non-Schmid) crystal plasticity model by defining a yield function and an independent flow potential.

According to the non-Schmid rule, the material yields when the combined effect of the glide and non-glide resolved stresses, $\tau_y^* = \sigma : d^*$, reaches a critical value, τ_{cr}^*. For one slip system, the following function is used to indicate the onset of yielding. One can arrive at the below equation simply by rearranging equation (3.3).

$$\frac{\sigma : d^*}{\tau_{cr}^*} = 1 \tag{4.4}$$

The non-glide stresses do not cause dislocation slip. Only the glide stresses can initiate the dislocation motion. Therefore, the flow potential is modeled using the following equation.

$$\frac{\sigma : d}{\tau_{cr}^*} = 1 \tag{4.5}$$

Notice that the numerator in equation (4.4) is the non-Schmid resolved stress, and in equation (4.5) is the Schmid resolved shear stress.

Following Zamiri and Pourboghrat, a smooth *flow potential* is defined based on equation (4.5) as:

$$F(\sigma, u) = \frac{1}{\rho_1} \ln \left\{ \sum_{\alpha=1}^{N} \exp \left[\frac{\rho_1}{\mu_1} \left(\frac{|\sigma : d^\alpha|}{\tau_y^{*\alpha}} - 1 \right) \right] \right\} \tag{4.6}$$

where ρ_1 is the closeness factor and μ_1 is a parameter to tune the flow potential. Then, the rate of plastic strain is defined as:

$$D^p = \lambda \frac{\partial F(\sigma, u)}{\partial \sigma} \tag{4.7}$$

And the rate of slip (shear rate) as:

$$\dot{\gamma}^\alpha = \lambda \frac{\partial F(\sigma, u)}{\partial \tau^\alpha} \tag{4.8}$$

Finally, the rate of increase in the critical resolved shear stress (yield stress) is modeled with the hardening model by Hill [39].

$$\dot{\tau}_y^\alpha = \sum_{\beta=1}^{N} h^{\alpha\beta} \left| \dot{\gamma}^\beta \right| \tag{4.9}$$

The hardening moduli matrix, $h^{\alpha\beta}$, is defined as [41]:

$$h^{\alpha\beta} = h^\beta \left[q + (1 - q)\delta^{\alpha\beta} \right] \tag{4.10}$$

where $\delta^{\alpha\beta}$ is the Kronecker delta, and q is the latent-hardening ratio which is defined as the ratio of latent-hardening to self-hardening rate and has values in the range of $1 \leq q \leq 1.4$. Diagonal components of $h^{\alpha\beta}$ are called self-hardening, and off-diagonal components are latent-hardening. Parameter h^β is a function that defines the hardening rate and is defined using the following equation.

$$h^\beta = h_0 \left| 1 - \frac{\tau_c^\beta}{\tau_s} \right|^\eta \operatorname{sgn} \left(1 - \frac{\tau_c^\beta}{\tau_s} \right) \tag{4.11}$$

Here, h_0 is the initial hardening rate, τ_c^β is the current slip resistance on slip system β, τ_s is the saturation value of slip resistance, and η is the exponent controlling the hardening rate.

Equation (4.4) is then used to define the following smooth non-Schmid *yield function*,

$$Y(\sigma, u) = \frac{1}{\rho_2} \ln \left\{ \sum_{\alpha=1}^{N} \exp \left[\frac{\rho_2}{\mu_2} \left(\frac{|\sigma : d^{*\alpha}|}{\tau_y^{*\alpha}} - 1 \right) \right] \right\} \tag{4.12}$$

where ρ_2 is the closeness factor and μ_2 is a parameter to tune the yield function. Although, in general, BCC materials could have {110}, {112} and {123} slip planes, in the non-Schmid crystal plasticity model only $\{1\bar{1}0\}$ planes of $\langle 111 \rangle$ zone are considered. Table 4.2 lists the slip systems available in the non-Schmid model [107].

Table 4.2: This table lists the slip systems available in the non-Schmid crystal Plasticity model [107].

α	Reference system	m^α	n^α	n_1^α	α	Reference system	m^α	n^α	n_1^α
1	$(01\bar{1})[111]$	$[111]$	$[01\bar{1}]$	$[\bar{1}10]$	13	$(01\bar{1})[\bar{1}\bar{1}\bar{1}]$	$[\bar{1}\bar{1}\bar{1}]$	$[01\bar{1}]$	$[10\bar{1}]$
2	$(\bar{1}01)[111]$	$[111]$	$[\bar{1}01]$	$[0\bar{1}1]$	14	$(\bar{1}01)[\bar{1}\bar{1}\bar{1}]$	$[\bar{1}\bar{1}\bar{1}]$	$[\bar{1}01]$	$[\bar{1}10]$
3	$(1\bar{1}0)[111]$	$[111]$	$[1\bar{1}0]$	$[10\bar{1}]$	15	$(1\bar{1}0)[\bar{1}\bar{1}\bar{1}]$	$[\bar{1}\bar{1}\bar{1}]$	$[1\bar{1}0]$	$[0\bar{1}1]$
4	$(\bar{1}0\bar{1})[\bar{1}11]$	$[\bar{1}11]$	$[\bar{1}0\bar{1}]$	$[\bar{1}\bar{1}0]$	16	$(\bar{1}0\bar{1})[1\bar{1}\bar{1}]$	$[1\bar{1}\bar{1}]$	$[\bar{1}0\bar{1}]$	$[01\bar{1}]$
5	$(0\bar{1}1)[\bar{1}11]$	$[\bar{1}11]$	$[0\bar{1}1]$	$[101]$	17	$(0\bar{1}1)[1\bar{1}\bar{1}]$	$[1\bar{1}\bar{1}]$	$[0\bar{1}1]$	$[\bar{1}\bar{1}0]$
6	$(110)[\bar{1}11]$	$[\bar{1}11]$	$[110]$	$[01\bar{1}]$	18	$(110)[1\bar{1}\bar{1}]$	$[1\bar{1}\bar{1}]$	$[110]$	$[101]$
7	$(0\bar{1}\bar{1})[\bar{1}\bar{1}1]$	$[\bar{1}\bar{1}1]$	$[0\bar{1}\bar{1}]$	$[1\bar{1}0]$	19	$(0\bar{1}\bar{1})[11\bar{1}]$	$[11\bar{1}]$	$[0\bar{1}\bar{1}]$	$[\bar{1}0\bar{1}]$
8	$(101)[\bar{1}\bar{1}1]$	$[\bar{1}\bar{1}1]$	$[101]$	$[011]$	20	$(101)[11\bar{1}]$	$[11\bar{1}]$	$[101]$	$[1\bar{1}0]$
9	$(\bar{1}10)[\bar{1}\bar{1}1]$	$[\bar{1}\bar{1}1]$	$[\bar{1}10]$	$[\bar{1}0\bar{1}]$	21	$(\bar{1}10)[11\bar{1}]$	$[11\bar{1}]$	$[\bar{1}10]$	$[011]$
10	$(10\bar{1})[1\bar{1}1]$	$[1\bar{1}1]$	$[10\bar{1}]$	$[110]$	22	$(10\bar{1})[\bar{1}1\bar{1}]$	$[\bar{1}1\bar{1}]$	$[10\bar{1}]$	$[0\bar{1}\bar{1}]$
11	$(011)[1\bar{1}1]$	$[1\bar{1}1]$	$[011]$	$[\bar{1}01]$	23	$(011)[\bar{1}1\bar{1}]$	$[\bar{1}1\bar{1}]$	$[011]$	$[110]$
12	$(\bar{1}\bar{1}0)[1\bar{1}1]$	$[1\bar{1}1]$	$[\bar{1}\bar{1}0]$	$[0\bar{1}\bar{1}]$	24	$(\bar{1}\bar{1}0)[\bar{1}1\bar{1}]$	$[\bar{1}1\bar{1}]$	$[\bar{1}\bar{1}0]$	$[\bar{1}01]$

4.3 Modeling the hardening rate of a single crystal

Shear stress - shear strain curves for single crystals that are initially oriented for single slip show three distinct stages usually referred to as Stage I, II and Stage III hardening [43]. The hardening rate just after yielding is low. Most of the deformation in this stage is accommodated by the primary slip system and hardening is chiefly due to self-hardening. The low hardening rate corresponds to a large dislocation mean free path and few barriers. This stage I regime is also known as the "easy glide" [43].

The second stage, which is known as "linear hardening", starts when other slip systems become activated due to crystal rotation during deformation and interact with the primary

slip system. This reduces the mean free path of dislocations and considerably increases the hardening rate. During this stage the dislocation density increases [43]. The hardening rate eventually decreases which signals the onset of the third stage, "exhaustion hardening". The high stress and dislocation density activate cross slip and dynamic recovery which in turn softens the material.

Although the classical Hill-type hardening rule, equation (4.9), is widely used in crystal plasticity codes to model the hardening behavior of polycrystalline metals, it can only model the stress-strain behavior observed in the first stage of the deformation of a single crystal. The hardening rate predicted by equation (4.9) does not change significantly during the deformation.

As was discussed above, the hardening rate in each stage of the deformation of a single crystal is controlled by a different set of underlying mechanisms. Equation (4.11) effectively only models those mechanisms that are active in the first stage and predicts a rather uniform increase in hardening. To capture the variable hardening rate of a single crystal, a more sophisticated model is needed.

4.3.1 The Differential-Exponential (DE) hardening model

A single crystal oriented for single slip typically hardens linearly with a small slope in the first stage. In the second stage, the density of mobile dislocations decreases exponentially [159], which results in an exponential increase in the hardening of the material. To model this behavior, the authors propose the following exponential equation for the hardening rate.

$$h^{\beta}_{stage2} = h_{0DE} \exp\left[\gamma^{1st} + \left(1 + \gamma^{1st}\right)^{\nu}\right] \tag{4.13}$$

where h_0DE is the hardening rate of stage II, γ^{1st} is the accumulated shear strain on the most active (primary) slip system, and exponent ν is a material parameter. As will be discussed later in this section, the above equation successfully predicts the two-stage stress-

strain behavior of a single crystal. However, its definition is incomplete without some criteria for predicting the initiation of the second stage.

Based on the knowledge that second stage hardening occurs in single crystals when secondary slip systems become active, it became evident that criteria for the start of the second stage hardening must be a function of the ratio of the accumulated shear strain and critical resolved shear stresses in primary and secondary slip systems. The reason for the activation of secondary slip systems is the eventual rotation of the primary slip system away from the loading direction, caused by the evolution of texture induced by increased plastic deformation.

Using the definition of a step function:

$$\langle x \rangle = \begin{cases} 0, & x < 0 \\ 1, & x \geq 0 \end{cases} \tag{4.14}$$

the following hardening rate equation for stages I and II in a single crystal is proposed. Due to its ability to differentiate between active slip systems, as well as the use of the exponential function, this new hardening model was termed the Differential-Exponential (DE) hardening model.

$$h^{\beta}_{DE} = \left(h^{\beta}_{stage1} - h^{\beta}_{stage2} \right) \langle k_1 - \frac{\max(\tau^{\beta})}{\tau_s} \rangle \langle k_2 - \frac{\gamma^{2nd}}{\gamma^{1st}} \rangle + h^{\beta}_{stage2} \tag{4.15}$$

In this equation, k_1 and k_2 are material parameters to be fitted to the experimental stress-strain curve, τ^{β} is the slip resistance on a slip system β, and $\max(\tau^{\beta})$ is the largest slip resistance among all slip systems, τ_s is the saturation value, γ^{1st} and γ^{2nd} are the cumulative shear strains on the first and second most active slip systems. It should also be noted that at the start of deformation when the value of both step functions is equal to 1, equation (4.15) reduces to h^{β}_{stage1}, which is the Hill's hardening equation (4.9). However, as the plastic deformation increases and the value of either of those two step functions becomes zero, the second stage hardening, h^{β}_{stage2}, becomes activated. It should be pointed out that when the values of k_1 and k_2 are very large, the step functions become equal to 1, and equation (4.15) behaves similar to equation (4.11).

The hardening rate equation (4.11) was replaced by equation (4.15) in the non-Schmid crystal plasticity model, and implemented in the commercial FEM software Abaqus® as a user-defined material subroutine (VUMAT).

4.3.2 Stress-integration algorithm to solve for shear rate

This section summarizes the algorithm for stress integration which follows [115]. This algorithm is developed for the Differential-Exponential hardening rule.

1. The following variables are assumed to be known at the beginning of a finite element increment i for a grain ($\hat{\sigma}_i$, g_i^α,$\Delta\hat{\varepsilon}_i$,$Q_i$) in the element coordinate system. Parameter Q_i is the crystal orientation matrix and g_i^α is the slip resistance of slip system α. Then stress and strain tensors are rotated to the crystal coordinate system as:

$$\sigma_i = Q_i \hat{\sigma}_i Q_i^T$$
$$\Delta\varepsilon_i = Q_i \Delta\hat{\varepsilon}_i Q_i^T$$

2. Initialize variables

   i: FEM increment

   k: Plasticity iteration

$$\sigma_{i+1}^{(0)} = \sigma_i + C^e : \Delta\varepsilon_i$$
$$g_{i+1}^{\alpha(0)} = g_i^\alpha$$
$$\Delta\lambda_{i+1}^{(0)} = 0$$
$$k = 1$$

3. Evaluate the yield condition $Y_{i+1}^{(k)}$

$$Y_{i+1}^{(k)} = Y\left(\sigma^{(k-1)}, u^{(k-1)}\right) = \frac{1}{\rho_2}\ln\left\{\sum_{\alpha=1}^{N}\exp\left[\frac{\rho_2}{m_2}\left(\frac{|\sigma : d^{*\alpha}|}{g_y^{\alpha}} - 1\right)\right]\right\}$$

$$d^{*\alpha} = d^{\alpha} + \sum_{\eta} a_{\eta}^{\alpha} d_{\eta}^{\alpha}$$

$$d^{\alpha} = \frac{1}{2}\left(m^{\alpha}\otimes n^{\alpha} + n^{\alpha}\otimes m^{\alpha}\right)$$

$$\sum_{\eta} a_{\eta}^{\alpha} d_{\eta}^{\alpha} = a_1 m^{\alpha}\otimes n_1^{\alpha} + a_2(n^{\alpha}\times m^{\alpha})\otimes n^{\alpha} + a_3(n_1^{\alpha}\times m^{\alpha})\otimes n_1^{\alpha}$$

$$+ a_4 n^{\alpha}\otimes n^{\alpha} + a_5(n^{\alpha}\times m^{\alpha})\otimes(n^{\alpha}\times m^{\alpha}) + a_6 m^{\alpha}\otimes m^{\alpha}$$

If $Y_{i+1}^{(k)} \le 0$ go to step 10.

4. Compute the flow potential

$$F_{i+1}^{(k)} = F\left(\sigma^{(k-1)}, u^{(k-1)}\right) = \frac{1}{\rho_1}\ln\left\{\sum_{\alpha=1}^{N}\exp\left[\frac{\rho_1}{m_1}\left(\frac{|\sigma : d^{\alpha}|}{g_y^{\alpha}} - 1\right)\right]\right\}$$

$$d^{\alpha} = \frac{1}{2}\left(m^{\alpha}\otimes n^{\alpha} + n^{\alpha}\otimes m^{\alpha}\right)$$

5. Calculate the correction to the plastic consistency parameter

$$\delta\Delta\lambda_{i+1}^{(k)} = \frac{Y_{i+1}^{(k)}}{\frac{\partial Y_{i+1}^{(k)}}{\partial\sigma} : C^e : \frac{\partial F_{i+1}^{(k)}}{\partial\sigma} - \sum_{\alpha=1}^{N}\sum_{\beta=1}^{N} h^{\alpha\beta}\,\mathrm{sgn}(\delta\Delta\lambda)\frac{\partial Y_{i+1}^{(k)}}{\partial\tau^{\alpha}}\left|\frac{\partial F_{i+1}^{(k)}}{\partial\tau^{\beta}}\right|}$$

6. Compute stress, increment of shear strain, and slip resistance

$$\Delta\sigma_{i+1}^{(k)} = \Delta\sigma_{i+1}^{(k-1)} - \delta\Delta\lambda_{i+1}^{(k)} C^e : \frac{\partial F\left(\sigma_{i+1}^{(k-1)}, u_{i+1}^{(k-1)}\right)}{\partial\sigma}$$

$$\delta\Delta\gamma_{i+1}^{\alpha(k)} = \delta\Delta\lambda_{i+1}^{(k)}\frac{\partial F\left(\sigma_{i+1}^{(k-1)}, u_{i+1}^{(k-1)}\right)}{\partial\tau^{\alpha}}$$

If $k_1 > \frac{\max(\tau^\beta)}{\tau_s}\rangle$ and $\langle k_2 > \frac{\gamma^{2nd}}{\gamma^{1st}}\rangle$

$$\delta\Delta g_{i+1}^{\alpha(k)} = \sum_{\beta=1}^{N} h_0 \left|1 - \frac{g_{i+1}^{\beta(k-1)}}{\tau_s}\right|^{\eta} \operatorname{sgn}\left(1 - \frac{g_{i+1}^{\beta(k-1)}}{\tau_s}\right) \left[q + (1-q)\delta^{\alpha\beta}\right] \left|\delta\Delta\lambda_{i+1}^{(k)} \frac{\partial F\left(\sigma_{i+1}^{(k-1)}, u_{i+1}^{(k-1)}\right)}{\partial \tau^\alpha}\right|$$

Else,

$$\delta\Delta g_{i+1}^{\alpha(k)} = \sum_{\beta=1}^{N} h_{0DE} \exp\left[\gamma^{1st} + \left(1 + \gamma^{1st}\right)^{\nu}\right] \left[q + (1-q)\delta^{\alpha\beta}\right] \left|\delta\Delta\lambda_{i+1}^{(k)} \frac{\partial F\left(\sigma_{i+1}^{(k-1)}, u_{i+1}^{(k-1)}\right)}{\partial \tau^\alpha}\right|$$

Then

$$g_{i+1}^{\alpha(k)} = g_{i+1}^{\alpha(k-1)} + \delta\Delta g_{i+1}^{\alpha(k)}$$

7. Evaluate the yield function. If $Y_{i+1}^{(k)} \leq$ Tolerance go to step 9, otherwise go to step 8.

8. Update the consistency parameter

$$\Delta\lambda_{i+1}^{\alpha(k)} = \Delta\lambda_{i+1}^{\alpha(k-1)} + \delta\Delta\lambda_{i+1}^{\alpha(k)}$$

$$k = k + 1$$

Then Go to 3.

9. Update the crystal orientation using equation (3.24).

10. Rotate the stress tensor back to the FEM coordinate system.

4.4 CPFE modeling of uniaxial compression of QP980 ferrite micropillar

The models developed in §4.2 and §4.3 were used to predict the deformation behavior of ferrite micropillars of QP980 steel under uniaxial compression. First, the experimental results from compression of QP980 ferrite micropillars are presented, and then they are compared with the predictions of Schmid and non-Schmid crystal plasticity models.

4.4.1 Uniaxial compression of QP980 ferrite micropillars

Six ferrite micropillars were carved out of the bulk of QP980 steel using Focused Ion Beam (FIB), using the technique that was explained in §4.1.The micropillars were named 1-6, respectively. Each micropillar was extracted from a ferrite grain with a distinct initial orientation. Figure 4.8 shows the orientation of the compression axis of these micropillars in an inverse pole figure. Figure 4.1 shows a schematic of the cylindrical micropillar with a taper angle of 4°, a height to diameter ratio of 2-3, and a top surface diameter between 1.0 µm and 1.7 µm. The micropillar compression test was performed with a flat punch nanoindenter, and the force-displacement data was recorded for each experiment. More details on these experiments are given in [146].

Slip bands were observed at the end of the deformation of some of these micropillars. These bands changed the effective cross section of micropillars, which rendered calculation of engineering stress inappropriate. Therefore, the experimental data in this Chapter will be presented as force-displacement curves.

4.4.2 Modeling QP980 ferrite micropillars

The geometry of micropillars was modeled in Abaqus® commercial finite element software. The flat punch nanoindenter was modeled with a rigid surface. A friction coefficient of 0.5 was applied between the punch and the micropillar to prevent the slip between the surfaces [109]. The base of each micropillar was modeled with a perfectly elastic material to approximate

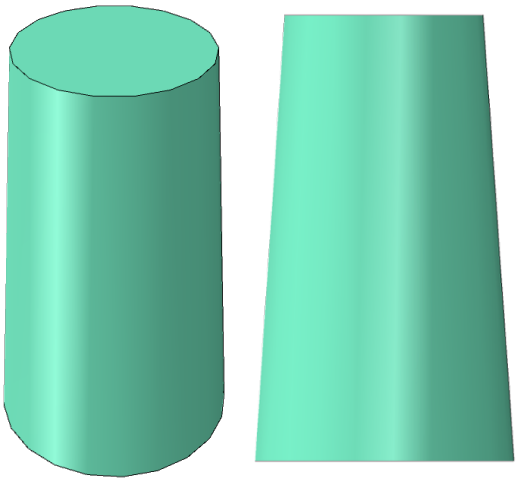

Figure 4.1: Schematic of the cylindrical micropillar with a taper angle of 4°, a height to diameter ratio of 2-3, and top surface diameter between 1.0 µm and 1.7 µm.

the elastic deformation of the bulk of the sheet underneath the micropillar [109].

Both Schmid and non-Schmid crystal plasticity models were implemented into Abaqus as user-defined material subroutines (UMAT) and were used to predict the deformation behavior of these micropillars. In the crystal plasticity finite element simulations, the typical 48 slip systems for BCC materials, i.e., {110}, {112}, {123} planes and $\langle 11\bar{1} \rangle$ slip directions, were used in the Schmid case. These will be referred to as slip family 1 to 3, respectively. In the non-Schmid case, the 24 slip systems (12 slip systems of $\{110\}\langle 11\bar{1} \rangle$ in positive and 12 in negative slip direction) shown in Table 4.2 were used. Since in this case the normal stresses also affect the yield stress, the positive and negative sense of the slip translates to tensile and compressive stresses, which in turn affect the onset of dislocation slip through the non-Schmid effect.

4.4.3 Material parameter fitting and evaluation

The criterion for evaluating the quality of the parameter fit was based on how accurately the calibrated CPFE model predicted the uniaxial compressive force-displacement curve of the remaining micropillars with distinct orientations. The metric used to quantify the

accuracy of the fit was based on the calculated error between experimental and predicted force-displacement curves, using equation (B.2) in Appendix B. The consistency of the fit was evaluated based on the variation in the calculated error for all available experimental data.

In the Schmid model, τ_{Si}, τ_{0i} and h_{0i} (where $i = 1 \dots 3$ refers to the slip family) were used as fitting parameters. These are the saturation shear stress, initial critical resolved shear stress and hardening rate, respectively. In the non-Schmid model, τ_S, τ_0, h_0 and a_i (where $i = 1 \dots 3$) were used as fitting parameters. Here, a_i are the non-Schmid constants. The hardening exponent η_i (where $i = 1 \dots 3$) in the Schmid model and η in the non-Schmid model were kept constant, $\eta_i = \eta = 3$. Also, the value of the initial hardening in the non-Schmid model was assumed to be a constant, $h_0 = 10$.

Material parameters for Schmid and non-Schmid models were fitted using one or more experimental force-displacement curves through an iterative procedure using commercial optimization software LS-OPT®. More details about the model calibration process are provided in Appendix B and in [160].

In the case of the non-Schmid model, it was found that a minimum of two experimental force-displacement curves (with different crystal orientations) are needed to get an accurate and consistent fit. When only one force-displacement curve was used, the fitted parameters were inconsistent and the non-Schmid CPFE model was unable to accurately predict the force-displacement curve for other micropillar orientations. Further improvement with using more than two experimental force-displacement curves was negligible. Also, it was found that the non-Schmid parameters, a_4, a_5 and a_6 have negligible effect on the predictions of the model, therefore, they were ignored and only a_1, a_2 and a_3 were considered in the non-Schmid model.

In the case of the Schmid model, it was discovered that the accuracy of this model's prediction is less than that of the non-Schmid model, regardless of how many experimental force-displacement curves were used for parameter calibration. The accuracy and consistency

of the Schmid model, however, improved when two or more experimental force-displacement curves were used in the calibration.

Material parameters fitted using various combinations of force-displacement curves are shown in Tables B.1 and B.3 for the non-Schmid model, and Tables B.5 and B.7 for the Schmid model, in Appendix B.

4.4.4 Predictions of calibrated models

In this section, only select number of CPFE simulation results will be presented and discussed. The summary of all numerical simulation results and their comparison with experimental data are given in Appendix B. Table 4.3 shows the fitted material parameters for the Schmid model using two micropillars (i.e., 1 and 4), and Table 4.4 shows the fitted material parameters for the non-Schmid model using three micropillar force-displacement curves (i.e., 1, 3 and 5). The CPFE simulation results based on these fitted parameters will be discussed next.

Figures 4.2 through 4.7 show the experimental force-displacement curves for micropillars 1-6. For comparison purposes, the force-displacement curves predicted by the Schmid model calibrated with micropillars 1 and 4, and those predicted by the non-Schmid model calibrated with micropillars 1, 3 and 5 are also shown in the same figures.

Overall, it can be seen from Figures 4.3, 4.4, 4.6 and 4.7, that the force-displacement predictions of the Schmid model for micropillars 2, 3, 5 and 6 are erratic. That is, in some cases the Schmid model overestimates, and in other cases, it underestimates the experimental curve. This erratic prediction by the Schmid model, however, is expected as ferrite has a BCC crystal structure, and its deformation is best described by the non-Schmid law. This will be discussed in more detail in the next section. Tables B.6 and B.8 in Appendix B show the magnitude of error and sign (i.e., over or underestimation) associated with different different calibrations of the Schmid model. For example, Table B.8 shows that the Schmid model calibrated with micropillars 1 and 4 underestimate the experimental curve for micropillar 5

Table 4.3: Material parameters found for the Schmid model (using QP980 Ferrite micropillars 1 and 4).

τ_{S1}	τ_{S2}	τ_{S3}	τ_{01}	τ_{02}	τ_{03}	h_{01}	h_{02}	h_{03}	η_1	η_2	η_3
650	650	720	195	205	330	110	110	110	3	3	3

Table 4.4: Material parameters found for the non-Schmid model (using QP980 Ferrite micropillars 1, 3 and 5).

τ_S	τ_0	h_0	η	a_1	a_2	a_3
537	249	10	3	0.0103	0.5748	0.0007

by 11.93% (see Figure 4.6), and overestimate that for micropillar 3 by 27.93% (see Figure 4.4). The worst overall prediction by the Schmid model is for micropillar 3 with an error of 47.75%, when the model was calibrated with the single force-displacement curve from micropillar 5 (Table B.6).

The non-Schmid model's predictions, however, are much more consistent and closer to experimental force-displacement curves. Table B.4 in Appendix B shows that the worst prediction of the non-Schmid model calibrated with micropillars 1, 3 and 5 is for micropillar 5 with an error value of -8.98, which implies that it underestimated the experimental curve by 8.98% (see Figure 4.6). Finally, Table B.2 shows that the non-Schmid model's worst overall error is for micropillar 3 with an error of 44.73%, when the model is calibrated with a single force-displacement curve from micropillar 6.

4.4.5 Further discussions on the Schmid versus non-Schmid law

As explained in §4.2, the non-Schmid model considers the effect of stresses that are applied on planes other than the slip plane or along directions other than the slip direction. Depending on the orientation of the material, these stresses can contract the dislocation core and reduce the critical stress needed for yielding. Similarly, for some other orientations, the combined effect of the non-Schmid stresses can expand the dislocation core and increase the stress needed for the initiation of dislocation slip and yielding. This is the reason why, compared

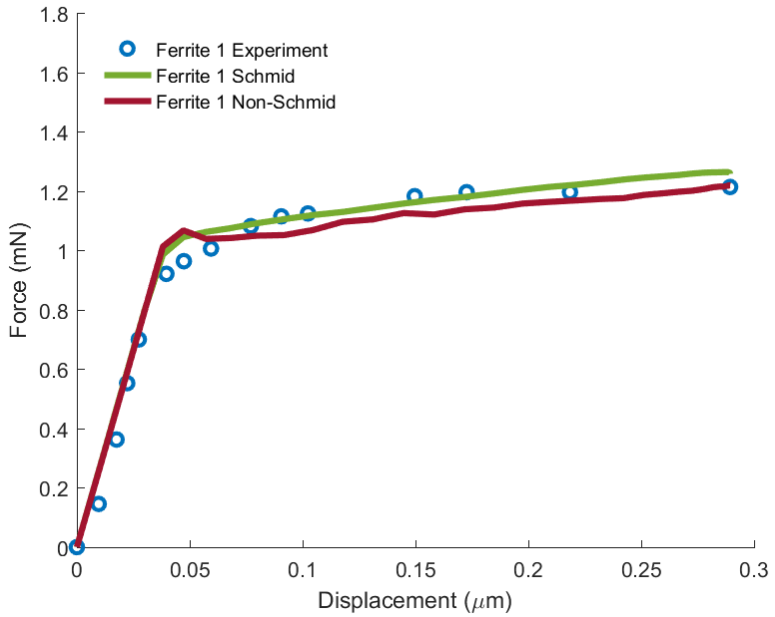

Figure 4.2: The green curve shows the Schmid and the red curve shows the non-Schmid models fit to ferrite micropillar 1. The Schmid model was simultaneously fitted to micropillars 1 and 4, while the non-Schmid model was calibrated with micropillars 1, 3 and 5. The blue circles represent the experimental measurements.

with the Schmid model, the non-Schmid model can more consistently and accurately predict the force-displacement curves of all micropillars.

The deviation from Schmid law can be further analyzed using the following equation which represents the ratio of the non-Schmid resolved shear stress, equation (3.3), to the Schmid resolved shear stress [157].

$$R_{ns} = \frac{\sigma : (m^\alpha \otimes n^\alpha) + a_1\sigma : (m^\alpha \otimes n_1^\alpha) + a_2\sigma : [(n^\alpha \times m^\alpha) \otimes n^\alpha] + a_3\sigma : [(n_1^\alpha \times m^\alpha) \otimes n_1^\alpha]}{\sigma : (m^\alpha \otimes n^\alpha)} \tag{4.16}$$

When this ratio is equal to 1.0, the material behaves according to Schmid law. In contrast, the more it deviates from 1.0, the more the material behavior deviates from the Schmid-type. Figure 4.8 shows the orientation of the compression axis for QP980 ferrite micropillars 1-6 mapped over the contour of R_{ns} as defined by equation (4.16). The calculated value of R_{ns} for each micropillar is also shown in Table 4.5.

When the Schmid model is calibrated with the force-displacement data of a material with

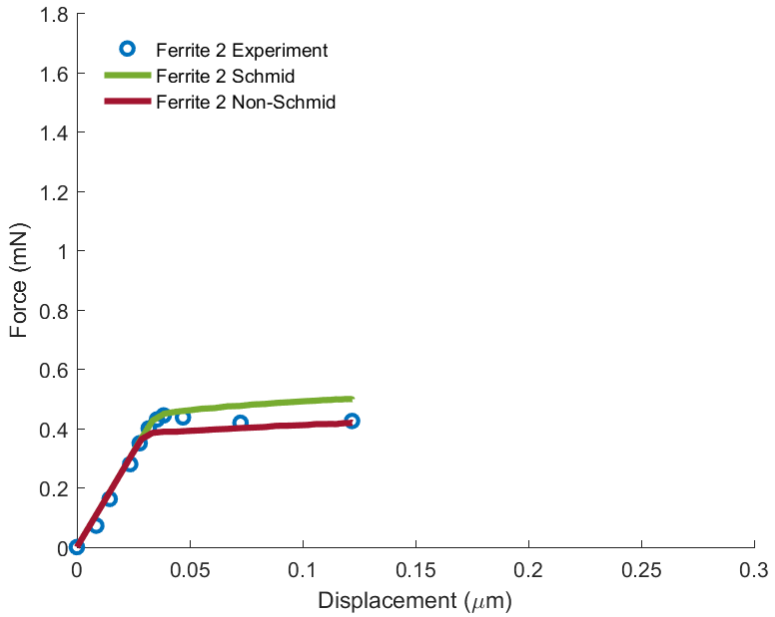

Figure 4.3: Comparing predictions of Schmid (green curve) and non-Schmid (red curve) models for ferrite micropillar 2 against the experiment. The Schmid model was simultaneously fitted to micropillars 1 and 4, while the non-Schmid model was calibrated with micropillars 1, 3 and 5.

a given R^*_{ns}, the model will overestimate the force-displacement of all other orientations with $R_{ns} > R^*_{ns}$, and underestimate those with $R_{ns} < R^*_{ns}$. For example, in Figures 4.2 through 4.7, the Schmid model was calibrated with micropillars 1 and 4, which have R_{ns} of 1.09 and 1.29, respectively. In comparison, micropillars 2 and 3 have higher R_{ns} of 1.33 and 1.78 (see Table 4.5), which means that the contribution of non-Schmid stresses to yielding for these micropillars is greater than those for micropillars 1 and 4. In contrast, micropillars 5 and 6 have lower R_{ns} of 0.96 and 0.94, which implies that the contribution of the non-Schmid stresses to their yielding is less than those for micropillars 1 and 4. Therefore, in the absence of non-Schmid stresses, the Schmid model calibrated with micropillars 1 and 4 will overestimate the required critical resolved shear stress (CRSS) to deform micropillars 2 and 3, and in turn overestimates their experimental force-displacement curve (as seen in Figures 4.3 and 4.4). On the other hand, given that micropillars 5 and 6 have smaller R_{ns} values, the same Schmid model underestimates their CRSS, and in turn underestimates their

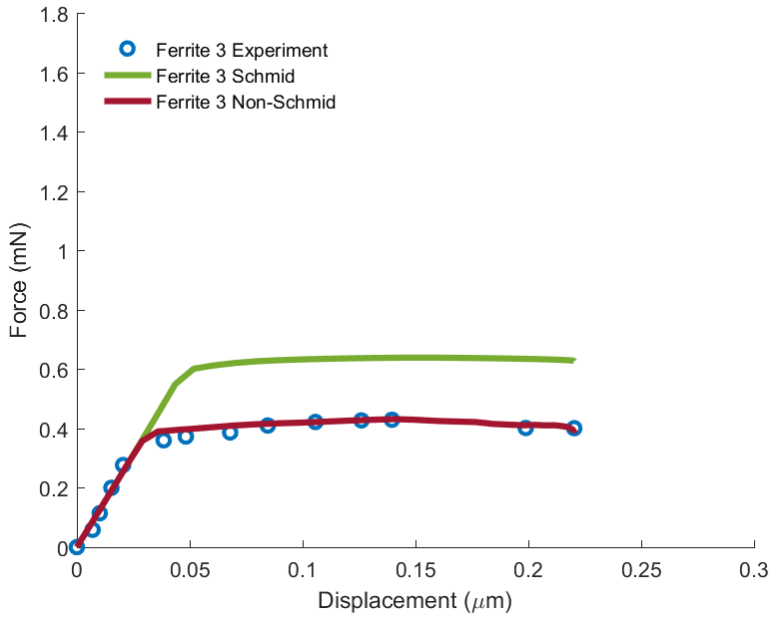

Figure 4.4: Calibration of the non-Schmid model (red curve) to micropillar 3. The non-Schmid model was simultaneously calibrated with micropillars 1, 3 and 5. This figure also compares the predictions of the Schmid model (green curve) for ferrite micropillar 3 against the experiment. The Schmid model was simultaneously fitted to micropillars 1 and 4.

Table 4.5: Value of deviation from Schmid-type behavior R_{ns} as defined in equation (4.16).

Micropillar	1	2	3	4	5	6
R_{ns}	1.09	1.33	1.78	1.29	0.96	0.94

experimental force-displacement curves (as seen in Figures 4.6 and 4.7).

Figure 4.9 further confirms this conclusion. This figure compares the predictions of the Schmid model for micropillar 2 when the model is calibrated with pairs of micropillars 1 and 6 and micropillars 4 and 5. The R_{ns} value for mircopillar 2 is greater than that for micropillars 1, 4, 5 and 6 which were used to calibrate the Schmid model. As expected, both calibrations overestimate the behavior of micropillar 2.

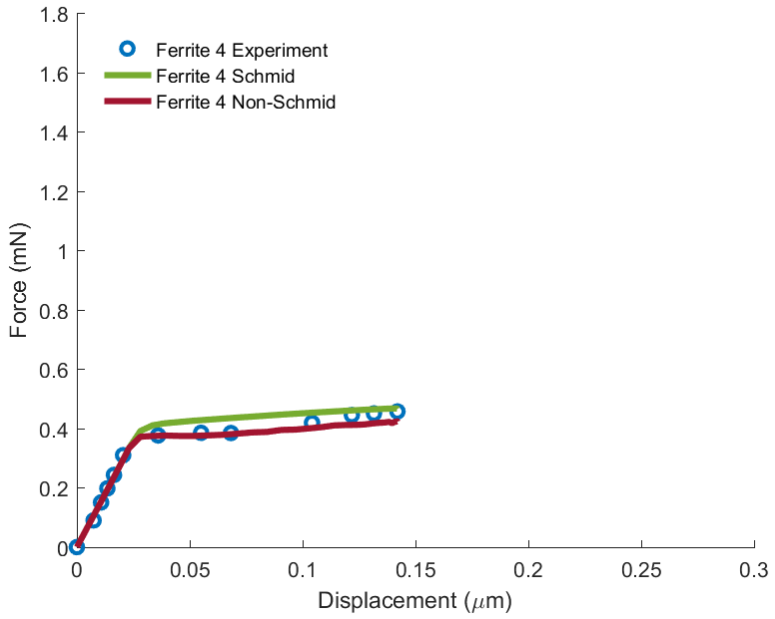

Figure 4.5: The green curve shows the calibration of the Schmid model to micropillar 4. The red curve shows the prediction of the non-Schmid model for ferrite micropillar 4 against the experiment. The Schmid model was simultaneously fitted to micropillars 1 and 4, while the non-Schmid model was calibrated with micropillars 1, 3 and 5.

4.5 CPFE modeling of uniaxial compression of DP980 ferrite micropillar

Four single crystal ferrite micropillars were machined out of a dual-phase DP980 steel sheet using the same FIB technique that was discussed in the §4.1. The modeling also followed the same procedure explained in that section. The samples were named A, B, C, and D. These micropillars have a height to diameter ratio of 2-4, a top surface diameter of about 1.3 µm and a taper angle of 4°. Figure 4.1 shows a schematic of the cylindrical micropillar. Each micropillar was uniaxially compressed using a flat punch nano-indentor. Figure 4.10 shows the orientation of these micropillars with respect to the loading axis. More details on the sample extraction and compression experiments can be found in [161].

It is noted here that after the first few percent of plastic deformation (strains $< 5\%$), these micropillars exhibit large slip steps and often deviate from the uniaxial loading due to bending and twisting.

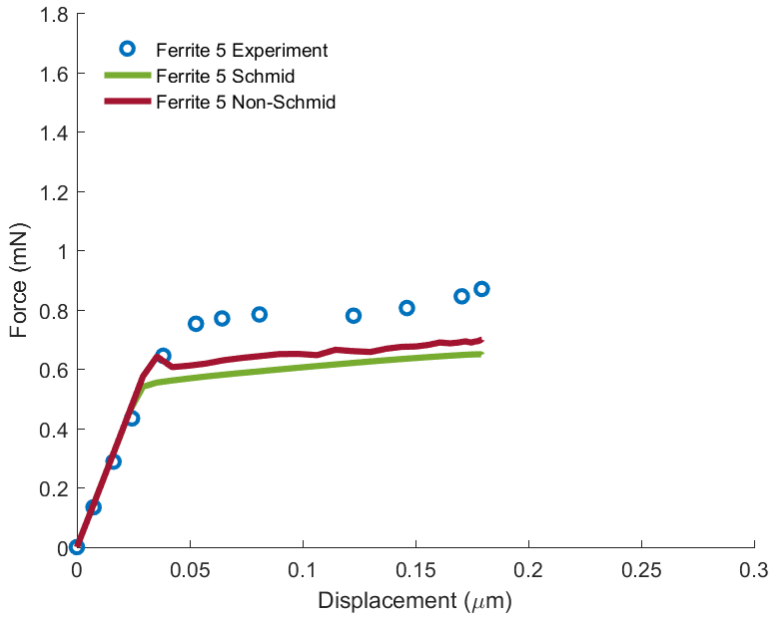

Figure 4.6: The red curve shows the fitting of the non-Schmid model to micropillar 5. This model was simultaneously calibrated with micropillars 1, 3 and 5. The green curve shows the prediction of the Schmid model for ferrite micropillar 5, based on material parameters fit to curves 1 and 4.

Unfortunately, the current test set-up and procedure do not lend themselves to interrupted testing or in-situ observations. Consequently, images of deformed micropillars were recorded at the end of each test using a scanning electron microscope (SEM). These images usually show significant micropillar distortion, as shown in Figure 4.13(a).

One of the most important parts of a crystal plasticity model is its hardening law, as it predicts the flow stress of each slip system. As mentioned before, the most commonly used hardening model is based on the pioneering work of Hill [39] and further development by authors like Hill and Rice [162], Havner and Baker [163, 164], Vause and Havner [165] and Asaro [41].

The main difference between these models is the definition of the hardening moduli matrix. The one defined by Asaro [41], equation (22), which is used in the simulation of QP980 micropillars only has two distinct parameters. One defines the self-hardening rate and the other defines the latent-hardening rate. This matrix, although convenient, only predicts

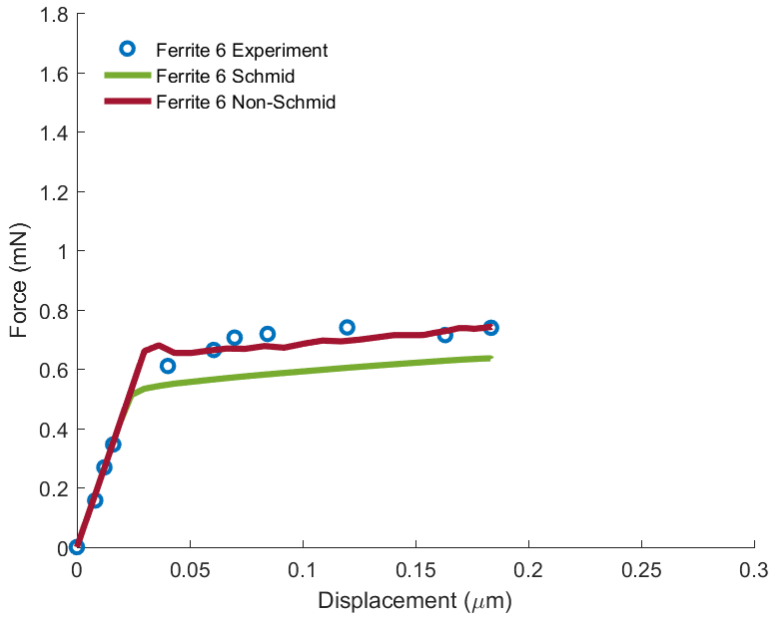

Figure 4.7: Comparing predictions of Schmid (green curve) and non-Schmid (red curve) models for ferrite micropillar 6 against the experiment. The Schmid model was simultaneously fitted to micropillars 1 and 4, while the non-Schmid model was calibrated with micropillars 1, 3 and 5.

good results until the end of stage I of deformation of a single crystal. Beyond this stage, the Asaro hardening moduli matrix is not accurate. The solid lines in Figures 4.11 and 4.12 compare the predictions of the non-Schmid crystal plasticity model with the conventional (Hill-type) hardening rule and the Asaro type hardening moduli matrix for deformation of DP980 ferrite micropillars A and B against the experiments.

To improve the predictions of the Hill-type hardening model, Madec and Kubin [139] studied the interactions of 12 slip systems of type $1/2\langle 111\rangle \{1\bar{1}0\}$ and 12 slip systems of type $1/2\langle 111\rangle \{11\bar{2}\}$ and found 17 distinct interaction types out of 144 possible binary interactions. The hardening moduli matrix they defined, therefore, has 17 distinct coefficients. Researchers like [140, 166, 167] used this matrix to model hardening. The dashed lines in Figures 4.11 and 4.12 compare the predictions of the non-Schmid model with the Hill-type hardening rule and Madec-Kubin (MK) type hardening moduli matrix for deformation of DP980 ferrite micropillars A and B against the experiments. As can be seen in these figures, the predictions

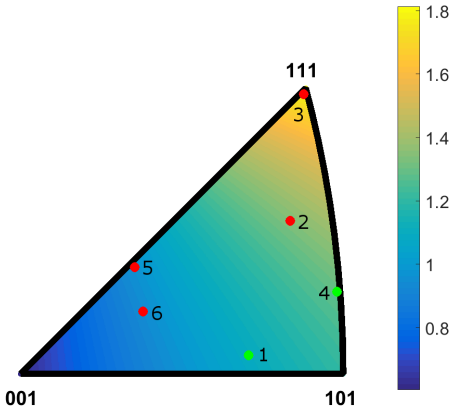

Figure 4.8: The contour shows the ratio of the non-Schmid resolved shear stress to the Schmid resolved shear stress equation (4.16). Circles show the orientation of compression axis of ferrite micropillars 1-6. Green circles denote the orientations for which predictions of both the Schmid and non-Schmid models are accurate. Red circles show the orientations for which only the non-Schmid model gives good predictions.

of the non-Schmid model with either of the hardening moduli are only accurate until the slope of the force-displacement curve changes and stage II begins.

Since the classical hardening model and moduli cannot accurately predict the deformation of single crystals past stage I, the deformation of DP980 micropillars was modeled with the non-Schmid model with the DE hardening rule described in §4.3.1. To ensure that FE simulation closely follows the complex deformation of the micropillar, care was taken to match the boundary conditions implemented in the CPFE model with those observed in the experiment. This allowed for qualitative comparison of the CPFE model results with the experimental curves beyond the uniform compression of the micropillar that was estimated to end around 5-6% strain.

Figure 4.13 shows the actual deformed shape and the prediction of the non-Schmid model with DE hardening rule for micropillar A. Qualitatively, the predicted deformed shape of the micropillar is similar to the experiment. Due to the lack of a damage criterion, however, the CPFE model is not equipped to predict slip bands and discontinuities which result in the slip step observed in the experiment. The predicted compressive strain contour levels shown

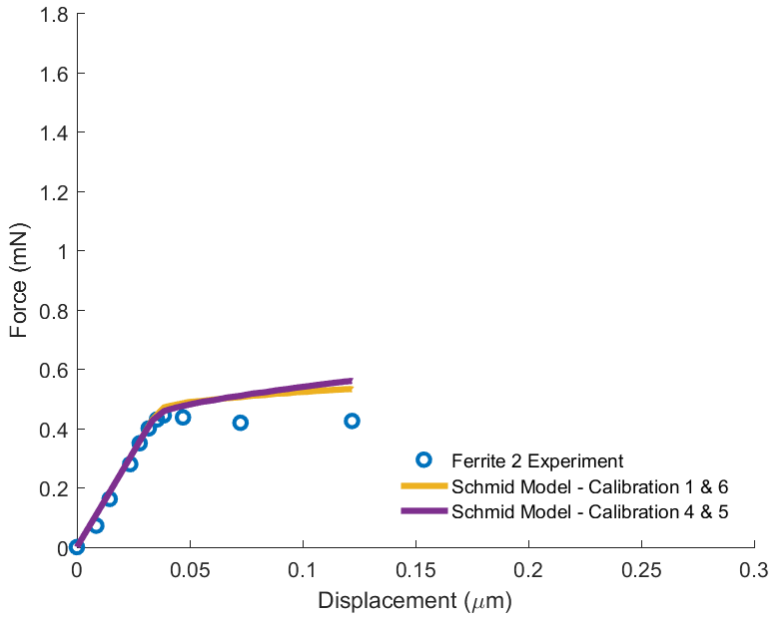

Figure 4.9: Comparing predictions of the Schmid model against the experiment when material parameters are calibrated using pairs of micropillars 1 and 6 (yellow curve) and micropillars 4 and 5 (purple curve).

in Figure 4.13(b) nonetheless, show similar shear bands forming in the same general area as in Figure 4.13(a).

Uchic [168] explained one needs to use a gradient based model to consider the size effect. Kuroda [169] compared a conventional and a gradient based model to predict the deformation of an FCC material and argued that to accurately predict the deformation mode of micropillars one should use a gradient based deformation model. He also points out that there is no significant difference between the yield stress predictions of the conventional and gradient based models. The non-Schmid crystal plasticity model developed in this Chapter is not a gradient-based model. However, given Kuroda's [169] findings, this model should still be able to accurately predict the yield stress of the uniaxially compressed ferrite micropillar. Given that the primary purpose of this study was to accurately match the force-displacement response of micropillars for parameter calibration, the use of the conventional CPFE model is well justified.

As mentioned earlier, equation (4.11) due to its two adjustable parameters can only predict the hardening rate of the first stage of deformation. However, the new hardening model in equation (4.15) has three extra material constants, i.e., k_1, k_2 and ν that can be calibrated with an experimental force-displacement curve. In this study, to reduce the total number of calibration parameters and increase the calibration speed, the non-Schmid parameters for DP980 ferrite micropillars, i.e., a_1, a_2 and a_3, were taken from the literature [157].

Commercial optimization software LS-OPT® was used to calibrate the model the compression test of ferrite micropillars A and B. Table 4.6 shows the material parameters found from this calibration. Figures 4.14 and 4.15 show the experimental and predicted force-displacement curves for these micropillars, which are in very good agreement.

Next, the compression response of the other two ferrite micropillars, i.e., C and D, were predicted with the calibrated non-Schmid crystal plasticity model using the Differential-Exponential (DE) hardening rule. Figures 4.16 and 4.17 compare predictions of the CPFE model with remaining two experiments (i.e., C and D) using the same hardening parameters shown in Table 4.6. As can be seen in these figures, predictions of the DE hardening model are in good agreement with the force-displacement curves of the DP980 ferrite micropillars. This confirms the validity of the DE hardening model and as a result, the corresponding criteria that were used to define the initiation of the stage II hardening. The black stars in Figures 4.14 through 4.16 indicate the point at which the DE hardening model switched the hardening rule from stage I to stage II. Figure 4.17 shows that for micropillar D, stage I hardening is dominant and stage II hardening never starts.

To study the mesh sensitivity of the DE hardening model, simulations for all micropillars were repeated with finer meshes. These are also shown in Figures 4.14 through 4.17 with a dashed line. As can be seen in these figures, the model is not mesh sensitive. The number of elements in each case is shown in Table 4.7.

As was discussed earlier, the second stage hardening commences when secondary slip sys-

tems become active and interact with the primary slip system. The activation of secondary slip systems is mainly caused by the crystal rotation which makes these systems more favorable, as well as the increase in the resolved shear stress beyond the CRSS value for secondary slip systems. This justifies the use of $\max(\tau^{\beta})$ as one of the criteria. Figure 4.18 shows the evolution of $\frac{\max(\tau^{\beta})}{\tau_s}$ parameter with the increasing engineering strain. The critical value k_1 is shown by a dashed black line. It is interesting to note that micropillars with different initial orientations reach the critical value at different engineering strain levels. It should be noted from Figure 4.17 that unlike micropillars A, B, and C, micropillar D never reaches the critical value for k_1.

The maximum slip resistance among all slip systems, however, cannot independently signal the onset of stage II hardening. Additionally, dislocations on secondary slip systems must start interacting and intersecting dislocations on the primary system. These dislocation interactions can act as barriers, thus increase the slip resistance, and harden the material. Therefore, the ratio $\frac{\gamma^{2nd}}{\gamma^{1st}}$ was also chosen as part of the criteria for the initiation of stage II hardening. Figure 4.19 shows the evolution of this criterion and the dashed black line represents the critical value. Figures 4.18 and 4.19 clearly show that these two conditions are met at different engineering strains for pillars A, B, C, and D. In other words, the stage II hardening occurs dynamically and is dependent on the loading direction and the crystal orientation.

Table 4.6: Material parameters found for the non-Schmid modeling of DP980 (calibrated to micropillars A and B).

τ_S	τ_0	h_0	h_{0DE}	η	k_1	k_2	ν	a_1	a_2	a_3
840	190	200	44060	3	0.2538	0.0700	3	0.0293	0.1727	0.3000

4.6 Summary

According to the Schmid law, only shear stresses resolved on the slip plane and parallel to the slip direction affect the dislocation motion. Although this is true for FCC materials,

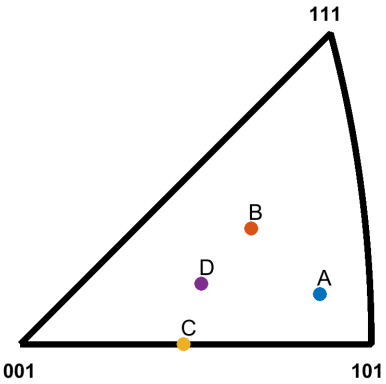

Figure 4.10: This inverse pole figure shows the orientation of compression axis of the DP980 ferrite micropillars A-D.

Table 4.7: The number of elements in coarse and fine mesh cases for DP980 ferrite micropillars.

Micropillar	Number of Elements in	
	Coarse Mesh	Fine Mesh
A	640	3276
B	640	3040
C	480	3217
D	480	3840

it does not represent the more complex deformation behavior of BCC materials. In these materials, other stresses that are not parallel and/or non-planar to the slip direction may also affect the dislocation motion.

In this study, the uniaxial compression of single crystal ferrite micropillars of QP980 steel was simulated with Schmid and non-Schmid crystal plasticity models, and their predicted force-displacement curves were compared with experimental curves. For some special orientations, predictions of both models were identical. Generally, however, only predictions of the non-Schmid-type crystal plasticity model accurately matched the experimental force-displacement curves of ferrite micropillars.

The Schmid model consistently overestimated the force-displacement of micropillars with orientations that had R_{ns} values greater than those used for the calibration, and underesti-

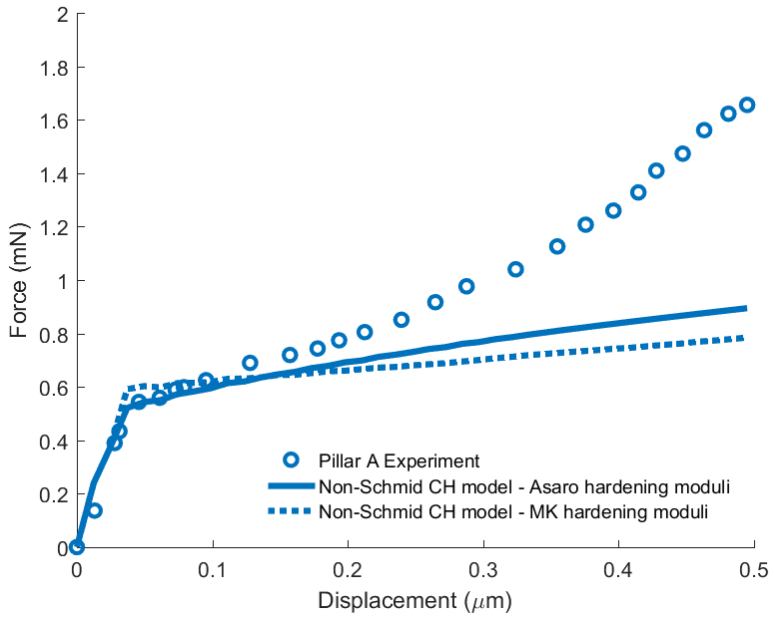

Figure 4.11: Comparing predictions of the non-Schmid model with classical hardening rule and two hardening moduli against the experiment of DP980 ferrite micropillar A. The circles show the experimental data, the solid line shows the predictions of the model with the Asaro hardening moduli and the dashed line represents the predictions of the model with the Madec-Kubin (MK) hardening moduli. As can be seen, the predictions are close to the experiment in stage I of deformation before the rate of hardening changes.

mated the force-displacement curves of those micropillars that had smaller R_{ns} values.

The classical Hill's power-law hardening used in crystal plasticity models can only predict the stage I hardening. In this study, an exponential hardening model was proposed to also model the stage II hardening. The accuracy of this model, termed as Differential-Exponential (DE) hardening, was verified against the uniaxial compression of single crystal ferrite micropillars of DP980 steel. It was shown that the DE hardening model can accurately predict stage I and stage II hardening in these single crystals.

Another important finding of this study was that calibrating the material parameters of the non-Schmid CPFE model using only one micropillar compression force-displacement curve will not be sufficient, and will result in invalid material parameters. This study shows that calibrating with two independent experimental force-displacement curves significantly improves the consistency of fitted parameters, and also increases the accuracy of the model's

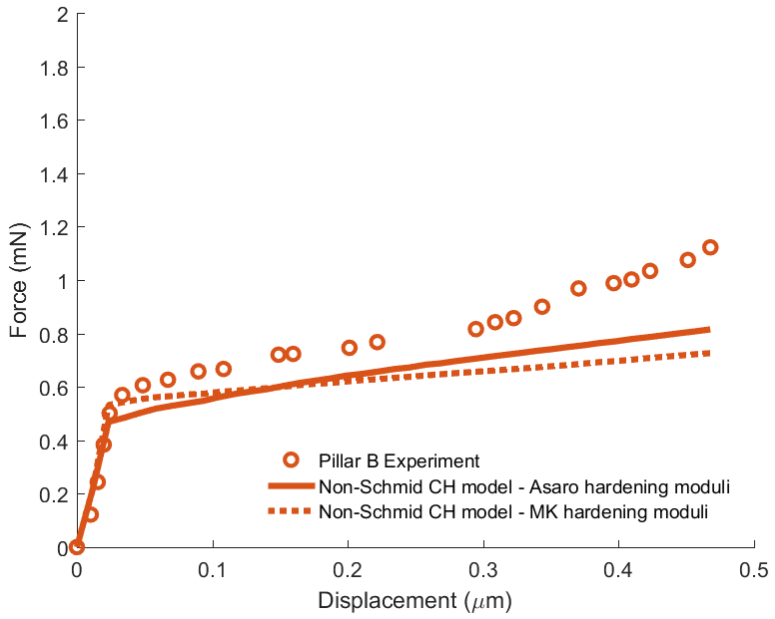

Figure 4.12: Comparing predictions of the non-Schmid model with classical hardening rule and two hardening moduli against the experiment of DP980 ferrite micropillar B. The solid line represents the predictions of the model with the Asaro hardening moduli and the dashed line shows the predictions of the model with the Madec-Kubin (MK) hardening moduli. The circles show the experimental data.

predictions.

According to the Schmid law, only shear stresses resolved on the slip plane and parallel to the slip direction affect the dislocation motion. Although this is true for FCC materials, it does not represent the more complex deformation behavior of BCC materials. In these materials, other stresses that are not parallel and/or non-planar to the slip direction may also affect the dislocation motion.

In this chapter, the uniaxial compression of single crystal ferrite micropillars of QP980 steel, which only show hardening stage I, were simulated with the Schmid and non-Schmid crystal plasticity models with the conventional Hill-type hardening rule. The force-displacement curves predicted by these models were compared with experimental curves. For some special orientations, predictions of both models were identical. Generally, however, only predictions of the non-Schmid type crystal plasticity model accurately matched the experimental

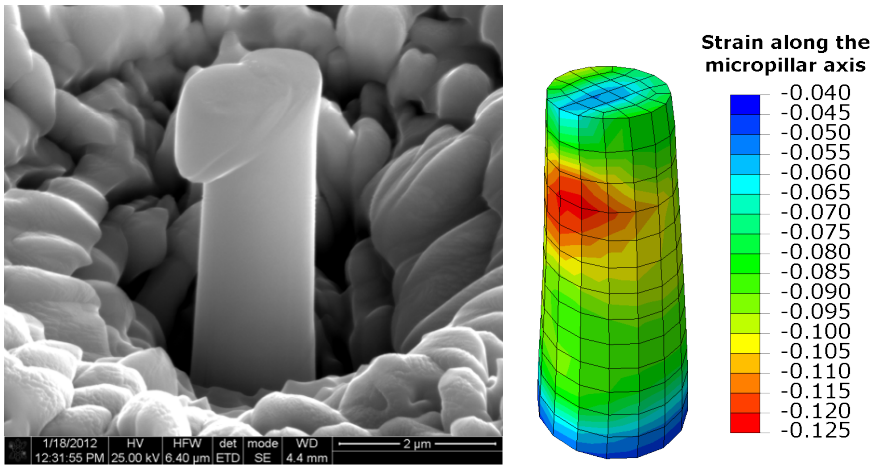

(a) Experiment (b) Simulation

Figure 4.13: This figure compares the geometry of the deformed ferrite A from (a) experiment with the (b) prediction of the non-Schmid model with DE hardening rule. The contour shows the compressive strain parallel to the axis of the micropillar. The current crystal plasticity model does not have a damage model. Therefore, it cannot show the slip steps. The contour levels, however, qualitatively match with the slip step observed in the experiment.

force-displacement curves of ferrite micropillars.

The Schmid model consistently overestimated the force-displacement of micropillars with orientations that had R_{ns} values greater than those used for the calibration, and underestimated the force-displacement curves of those micropillars that had smaller R_{ns} values.

The conventional Hill-type hardening rule can only predict the hardening stage I. An exponential hardening model was proposed in this Chapter to also model the hardening stage II. The accuracy of this model, termed as Differential-Exponential (DE) hardening, was verified against the uniaxial compression of single crystal ferrite micropillars of DP980 steel. It was shown that the DE hardening model can accurately predict stage I and stage II hardening in these single crystals.

Another important finding of this Chapter was that calibrating the material parameters of the non-Schmid CPFE model using only one experimental force-displacement curve will not be sufficient, and will result in invalid material parameters. The results presented in the current Chapter shows that calibrating the models with two independent experimental

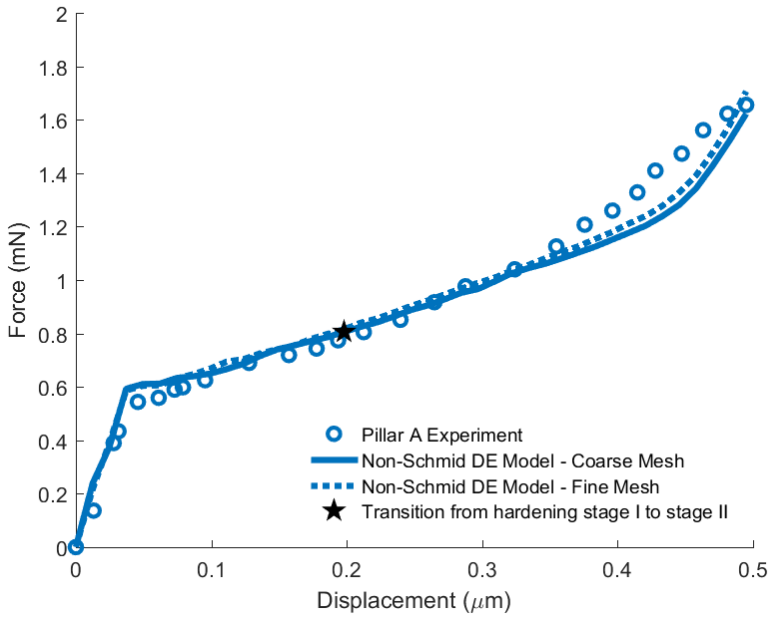

Figure 4.14: The Differential-Exponential non-Schmid crystal plasticity model was calibrated using DP980 single crystal ferrite micropillars A and B. The solid line shows the calibration of the model (with coarse mesh) against the experiment of DP980 ferrite micropillar A. The dashed line is the predictions of the model with a finer mesh. The black star represents the point at which the hardening rule switches from the stage I to stage II.

force-displacement curves significantly improves the consistency of fitted parameters, and increases the accuracy of the model predictions.

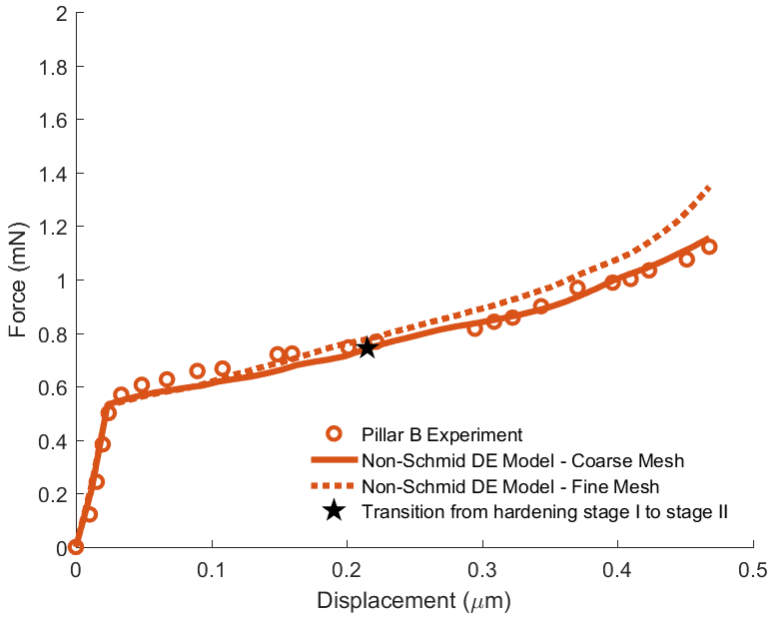

Figure 4.15: The Differential-Exponential non-Schmid crystal plasticity model was calibrated using DP980 single crystal ferrite micropillars A and B. The solid line shows the calibration of the model (with coarse mesh) against the experiment of ferrite micropillar B. The dashed line is the predictions of the model with a finer mesh. The black star represents the point at which the hardening rule switches from the stage I to stage II.

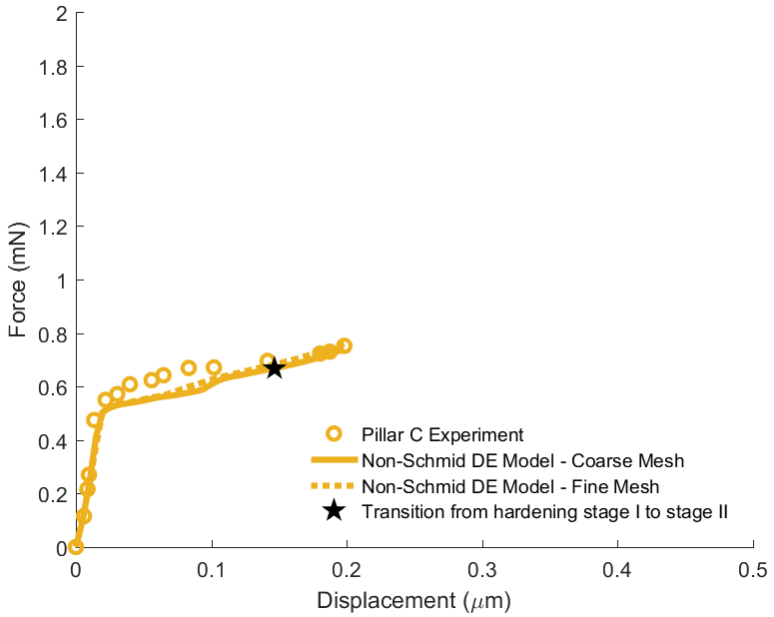

Figure 4.16: Comparing predictions of the Differential-Exponential non-Schmid crystal plasticity model for DP980 single crystal ferrite micropillar C against the experiment. The solid line shows the predicted behavior with the coarse mesh and the dashed line shows the predicted behavior with the fine mesh. The model is not mesh sensitive. The black star represents the point at which the hardening rule switches from the stage I to stage II.

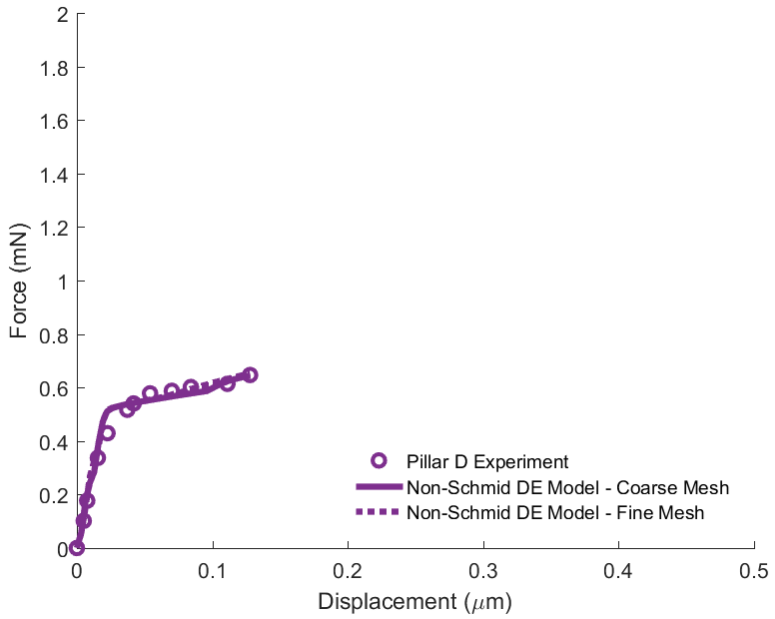

Figure 4.17: Comparing predictions of the Differential-Exponential non-Schmid crystal plasticity model for DP980 single crystal ferrite micropillar D against the experiment. The solid line shows the predicted behavior with the coarse mesh and the dashed line shows the predicted behavior with the fine mesh. The model is not mesh sensitive.

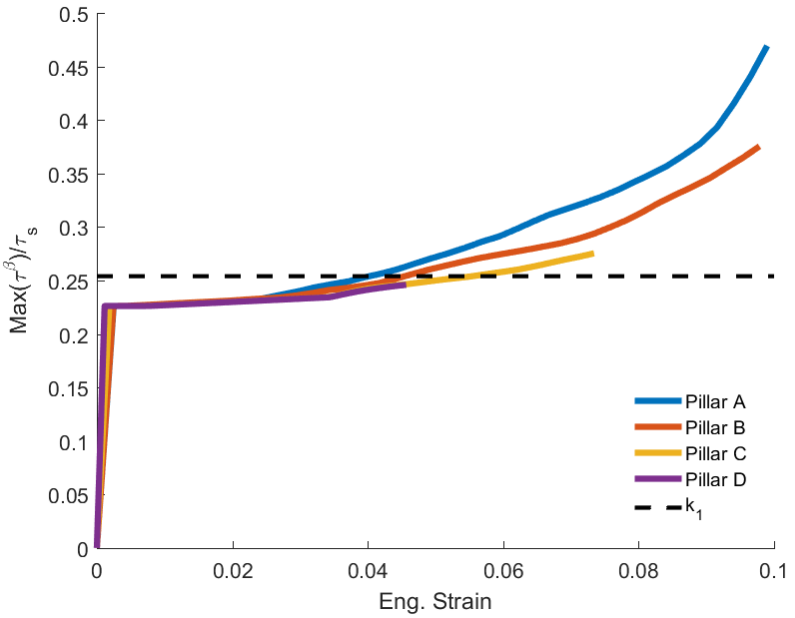

Figure 4.18: This plot shows the evolution of $\frac{\max(\tau^\beta)}{\tau_s}$ for each (coarse mesh) micropillar during the deformation. One of the conditions of the DE hardening model is met when this parameter reaches k_1, which is shown with the dashed black line.

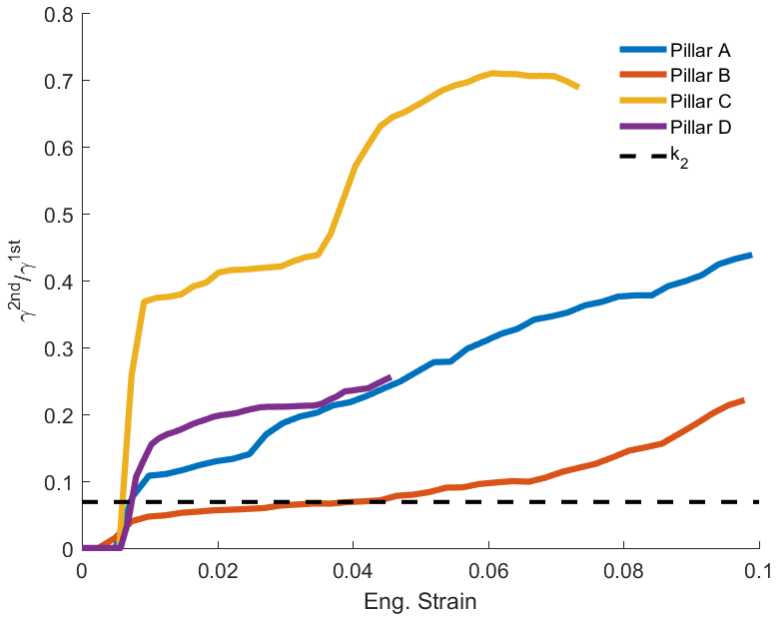

Figure 4.19: This plot shows the evolution of $\frac{\gamma^{2nd}}{\gamma^{1st}}$ for each (coarse mesh) micropillar during the deformation. One of the conditions of the DE hardening model is met when this parameter reaches k_2, which is shown with the dashed black line.

CHAPTER 5

A DYNAMIC HARDENING RULE FOR DEFORMATION OF BCC MATERIALS

In this Chapter, modeling the behavior of single crystal niobium (Nb) is explored. This BCC metal is the superconducting material of choice for particle accelerator cavities. Over the years, several Schmid-type crystal plasticity models have been developed [37, 44–47]. However, none of these models capture the behavior of BCC single crystals. Many researchers have tried to modify the classical crystal plasticity to make it capable of predicting the deformation behavior of BCC materials.

The non-Schmid crystal plasticity is one method to improve the prediction of the Schmid-type crystal plasticity for BCC materials. The non-Schmid modeling of deformation has been studied in many BCC materials including BCC iron [108, 156–158, 170], molybdenum [16, 35, 104–107, 143, 151], tantalum [98], tantalum-tungsten alloy [155], tungsten [16, 35, 106, 107, 143, 152–154]. Dislocation density based crystal plasticity modeling is another method to improve the accuracy [60, 137, 138, 145, 146].

The predictions of a crystal plasticity model can also be improved by modifying the hardening moduli matrix. Madec and Kubin [139] studied the interactions of $1/2\langle 111\rangle \{1\bar{1}0\}$ and $1/2\langle 111\rangle \{11\bar{2}\}$ slip systems of BCC materials and found 17 distinct interaction types. This contrasts with the Hill-type hardening moduli matrix that only distinguishes between the self and latent-hardening. Following this idea, Queyreau et al. [140] studied the interactions of $1/2\langle 111\rangle \{1\bar{1}0\}$ slip systems in ferrite and calculated six independent hardening coefficients for possible interaction modes.

Mapar et al. [100, 101] also devised schemes to modify these moduli. Their technique is based on multiplying the hardening moduli with a ratio of strain rate of the most active slip systems which changes with the deformation and alters the hardening rate of the material.

Fine grain (25 - 50 µm) niobium sheets are deep drawn and welded to make supercon-

ducting cavities. Disks sliced from as-cast Nb ingots have large grains. These disks provide a cheaper path to cavity fabrication than fine grain sheets because they go through fewer production steps and have less waste. Moreover, the large grain Nb cavities frequently provide higher superconducting performance, presumably due to having fewer grain boundaries [135]. Making a cavity consistently out of these disks however, is more challenging because deformation anisotropy is more evident in deformation of large grains. Reproducibility in making superconducting cavities can be improved if the formability of a particular slice from an ingot could be predicted. Subsequently, one can determine if the plastic anisotropy will cause undesirable flow behavior while forming.

To predict anisotropic deformation, a crystal plasticity model for BCC materials was derived based on the model of Zamiri and Pourboghrat [38]. A new hardening rule was developed and embedded in the BCC crystal plasticity model which was subsequently implemented as a user subroutine in commercial FEM software Abaqus®. This model was then used to predict the uniaxial response of nine Nb single crystal tensile specimens with distinct crystal orientations.

This Chapter is organized in the following order. §5.1 reviews the material and the experimental method used in this study. §5.2 discusses the development of the proposed Dynamic hardening rule. The details of the model calibration and the procedure for quantifying the quality of predictions are explained in §5.3. The boundary conditions implemented in the simulation are also explained in §5.3. The predictions of the Hill-type and the proposed Dynamic hardening rules are compared with experiments in §5.4. §5.5 explains how the Dynamic hardening rule improves the predictions of the classical Hill-Type hardening rule and §5.6 summarizes the findings of this Chapter.

5.1 Material and method - extraction of tensile specimens

The uniaxial tensile experiment data used in this study was a part of the Ph.D. research performed by Derek Baars and Di Kang. These experiments are explained in more details

below.

Residual Resistivity Ratio (RRR) is a measure that is used to roughly specify the purity of niobium [171]. This ratio is defined as the resistivity of a sample at room temperature (300 K) divided by its resistivity at 4.2 K. Since Nb is superconductive below 9.2 K and has no resistivity, the normal-state resistivity is extrapolated to define the resistivity at 4.2 K [172]. The residual resistivity (resistivity at 0 K) increases with the increase of impurity and reduces the RRR. Therefore, the higher the RRR, the higher the purity of Nb.

The material used in this study was pure niobium (RRR $>$ 300), which came from an as-cast ingot slice manufactured by "Ningxia Nonferrous Metals Import & Export Corporation". Table 5.1 shows the maximum acceptable impurity levels for RRR $>$ 300 and the impurity levels reported by the manufacturer for the production batch of the ingot slice used in this study.

A 3 mm-thick slice was cut from an ingot using electron discharge machining (EDM). The grain boundaries were visible on the as-cut slice. The orientation of the grains was measured using Laue camera. Nine sets of triplet uniaxial tensile specimens with distinct crystal orientations were cut from single grains using EDM. The geometry of these specimens follows the sub-size sample design of ASTM E8-04 which has a gauge length of 18 mm. The orientation of each set of tensile specimens was intentionally selected to favor dislocation slip on a single slip system or a known combination of multiple slip systems. More details on the selection of the sample orientation is given in [171].

One of each triplet samples were electropolished and annealed at 800 °C for 2 hours before being deformed using an Ernest Fullam in-situ tensile stage. The deformation was performed inside a Tescan Scanning Electron Microscope (SEM). The orientation of each sample was measured at three locations on the gauge length before the deformation, and at every 10% strain increment. The crystal orientation data and stress-strain curves from these experiments were used in the crystal plasticity modeling that is presented in the current Chapter.

Table 5.1: This table shows the acceptable impurity levels that was ordered to Ningxia and the actual impurity amounts of the batch from which the ingot slice was supplied.

Impurity Element	Ta	W	Ti	Fe	Si	Mo	Ni	O	N	H	C
Specification (less than ppm)	257	35	97	50	99	48	47	58	66	184	77
Ingot (ppm)	51	8	10	8	33	10	8	29	33	276	77

5.2 The Dynamic hardening model

The complete form of the classical Hill-type hardening rule consists of equations (2.21), (2.23), and (2.24). This form is summarized as follows.

$$\dot{\tau}^{\alpha} = \sum_{\beta} h^{\alpha\beta} \left| \dot{\gamma}^{\beta} \right| \tag{5.1a}$$

$$h^{\alpha\beta} = h^{\beta} \left[q + (1-q)\delta^{\alpha\beta} \right] \quad \text{(no summation on } \beta) \tag{5.1b}$$

$$h^{\beta} = h_0 \left| 1 - \frac{\tau_c^{\beta}}{\tau_s} \right|^{a} \cdot \operatorname{sgn}\left(1 - \frac{\tau_c^{\beta}}{\tau_s} \right) \tag{5.1c}$$

Where $\dot{\tau}^{\alpha}$ and $\dot{\gamma}^{\beta}$ are the increment of shear stress and shear strain on slip systems α and β, respectively. $h^{\alpha\beta}$ is the hardening moduli matrix, h^{β} defines the hardening rate, q is the latent-hardening ratio, and $\delta^{\alpha\beta}$ is the Kronecker delta. h_0 is the initial hardening rate, τ_c^{β} is the current slip resistance on slip system β, τ_s is the saturation value of the slip resistance, and finally a is the exponent controlling the hardening rate.

The classical hardening model cannot predict the rapid change of the hardening rate in the different stages of single crystal deformation (easy glide, hardening, saturation). The distinction between these three stages is more evident in BCC than FCC materials. The classical hardening model assumes that during the deformation, slip systems harden through self or latent-hardening. The rate of hardening of each slip system depends on the instantaneous slip rate of all slip systems and the ratio of the current resolved shear stress to the maximum shear stress on each slip system. This model has some shortcomings. For instance, at early stages of deformation when only one slip system is active, the model predicts increased shear resistance on all slip systems. Also, it does not account for the slip history and only considers

the instantaneous slip rate.

At the beginning of deformation of an annealed single crystal, mobile dislocations in the bulk can travel a long distance before encountering other dislocations. In addition, many and perhaps most of the dislocations can escape from a surface without encountering many obstacles, resulting in the easy glide first stage of deformation of a single crystal. As there is little accumulation of dislocations, the classical Hill-type hardening model overestimates the hardening of this stage, because it predicts hardening on all slip systems.

In the second stage of deformation of a single crystal, the hardening rate increases due to the activation of secondary slip systems which then interact with the primary slip systems resulting in dislocation multiplication mechanisms that cause hardening.

These two stages can be differentiated with the proposed Dynamic hardening rule defined with the below equations. This model is a generalization of the classical Hill-type hardening rule [100].

$$\dot{\tau}^{\alpha}_{DH} = \sum_{\beta} h^{\alpha\beta}_{DH} \left|\dot{\gamma}^{\beta}\right| \tag{5.2a}$$

$$h^{\alpha\beta}_{DH} = h^{\beta}_{DH} \left[q + (1-q)\delta^{\alpha\beta}\right] \quad \text{(no summation on } \beta) \tag{5.2b}$$

$$h^{\beta}_{DH} = h_0 \left|1 - \frac{\tau^{\beta}_c}{\tau_s}\right|^a \cdot \operatorname{sgn}\left(1 - \frac{\tau^{\beta}_c}{\tau_s}\right) \left[(1-w) + w\left(\frac{\gamma^{2nd}}{\gamma^{1st}}\right)^{\eta}\right] \tag{5.2c}$$

Here DH subscript signifies the "Dynamic Hardening" rule, γ^{1st} and γ^{2nd} are the total shear strain on the first and second most active slip systems (more specifically, the first and second most active slip directions that result in the opportunity for dislocation intersections), the exponent $\eta \geq 0$ is a material constant and $0 \leq w \leq 1$ is a weighting factor. The weighting factor, w, controls the deviation from the classical hardening and the exponent, η, controls the hardening rate. The Dynamic hardening rule thus considers the slip history in predicting the hardening of the material. This hardening rule can be expressed in terms of the classical hardening rule with the following equation.

$$\dot{\tau}^{\alpha}_{DH} = \sum_{\beta} h^{\alpha\beta}_{DH} \left|\dot{\gamma}^{\beta}\right| \left[(1-w) + w\left(\frac{\gamma^{2nd}}{\gamma^{1st}}\right)^{\eta}\right] \tag{5.3}$$

Depending on the value of w, the hardening rate predicted by the Dynamic hardening model will be less than or equal the hardening rate predicted by the classical hardening. In the extreme case when $w = 0$, the Dynamic hardening model reduces to the classical hardening. This also happens for $\eta = 0$.

When $w = 1$, the bracket on the right most part of the Dynamic hardening equation (5.3), simplifies to only $\left(\frac{\gamma^{2nd}}{\gamma^{1st}}\right)^{\eta}$. This ratio is always less than one, and consequently the hardening rate predicted by the model is less than the classical hardening rule. At the beginning of the deformation, when only the primary slip system is active, this ratio is nearly zero. Therefore, the Dynamic hardening model predicts no increase in the flow stress until other slip systems become active. At this point $\left(\frac{\gamma^{2nd}}{\gamma^{1st}}\right)^{\eta}$ becomes greater than zero and the model predicts hardening.

The hardening rate predicted by the model when $w = 1$ is only appropriate for a perfect crystal. For cases where the material has pre-existing dislocations, there will be dislocation multiplication and hardening that is based upon classical latent-hardening concepts. Hence, the weight parameter, w, reflects the initial dislocation density. To match experiments where there is a significant dislocation density, the weight factor is adjusted. For $w < 1$, the model predicts a non-zero hardening rate; even when only one slip system is active and $\left(\frac{\gamma^{2nd}}{\gamma^{1st}}\right)^{\eta}$ is zero.

5.3 Calibration of the crystal plasticity models

Nine tensile specimens were cut from differently oriented single crystals of a slice of a niobium ingot, as was explained in §5.1. The tensile experiments of these specimens were used to calibrate the BCC crystal plasticity models. Details underlying the motivation for choosing the orientations and the anticipated slip activity is summarized in [173, 174]. The samples were named alphabetically from “P” through ”X”. These samples were then annealed before going through 30 to 40% tensile deformation monitored in-situ in a scanning electron microscope. Figure 5.1(a) shows the initial orientation of the tensile axis of these

samples. Figure 5.1(b) shows the dimensions of the tensile dog-bone specimens and the model geometry that matches the tensile samples.

A plasticity model needs to be calibrated before its ability to accurately predict the behavior of a material can be assessed. Commercial optimization software LS-OPT® was used to fit the crystal plasticity models to the experiments and find the material parameters. This is an iterative process through which the optimization software generates a design (a set of several input parameters) based on the initial estimate of the parameters and within a pre-specified range for each parameter. The initial estimates can be found from literature or by trial and error. These initial estimates and ranges help constrain the design space so that an optimum design can be found with fewer iterations. Next, LS-OPT® runs the finite element crystal plasticity model through a user-defined script, which starts the simulation and extracts the results. Then the optimization software compares the simulation results with the experiment(s) and updates the design. The software continues the iterative process until the difference in the prediction error (objective function) in two consecutive iterations is less than a tolerance (in this case 0.01 which is the default value) and the difference between two consecutive parameter designs is less than another tolerance (again 0.01 which is the default value) or until a maximum number of iterations (20 iterations) is reached. The number of designs per iteration depends on the number of parameters to be fitted. For the details on the calibration process, see the Appendix B.

To calibrate the crystal plasticity model, at least one stress-strain curve is needed. To increase the accuracy, however, the crystal plasticity models with the classical ($w = 0$) and the Dynamic (w as a curve fitting parameter) hardening rules were calibrated against several sets of two and three stress-strain curves. The quality of each calibration was evaluated using a criterion that is presented below. Among the tested sets, the set of samples P, T and U provided the best calibration. The materials parameters resulting from these calibrations are shown in Table 5.2.

The normalized root-mean-square error (NRMSE) was used to evaluate the quality of

predictions. This is the mean-square error between the values of stress measured in the tensile test experiments and those predicted by the crystal plasticity models at specific strains which are then normalized by the maximum stress within each experiment. The NRMSE is formulated as below.

$$e = \sqrt{\frac{1}{N}\sum_{x=1}^{N}\left[\frac{P(x_n) - M(x_n)}{max\,|M(x_n)|}\right]^2} \times 100 \tag{5.4}$$

Where $M(x_n)$ is the n^{th} experimental stress measurement at strain x_n and $P(x_n)$ is predicted stress value at the same strain. N is the number of measurements per experiment. The mean-square error is then divided by the maximum value of $M(x_n)$ to normalize the error to make it dimensionless. For reasonable predictions, this normalized error is less than one. The error is then multiplied by 100 and expressed as percentage.

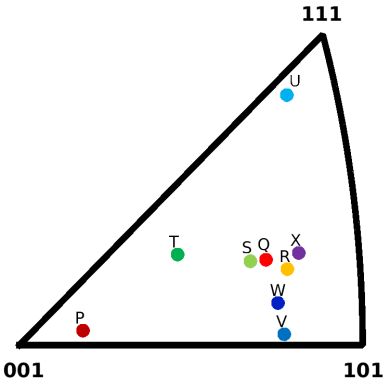

(a)

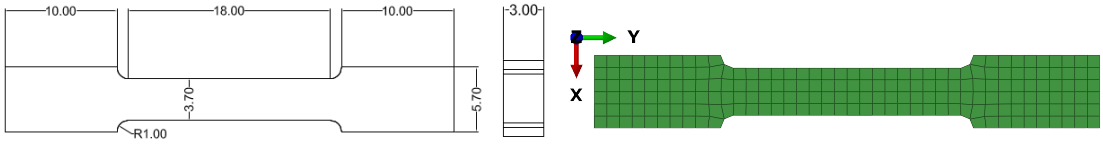

(b)

Figure 5.1: (a) The inverse pole figure shows the orientation of tensile axis of samples used in this study. (b) This figure shows the dimensions of the tensile dog-bone samples, and the model geometry that is used to simulate the tensile tests.

Table 5.2: Material parameters found from the calibrations to samples P, T and U for the crystal plasticity models with the classical hardening and the Dynamic hardening rules. The superscript denote the family of slip systems the parameter represents. For both models $\tau_0^{(123)} = 100$, $\tau_s^{(123)} = 1000$, and $h_0^{(123)} = 200$.

Parameters	$\tau_0^{(110)}$	$\tau_0^{(112)}$	$\tau_s^{(110)}$	$\tau_s^{(112)}$	$h_0^{(110)}$	$h_0^{(112)}$	a	w	η
Classical	15.42	18.17	100	171.68	10	339.65	3	0	0
Dynamic	15.34	16.51	444.63	545.90	10.92	224.41	3	0.702	8

5.4 Comparing predictions of the models with the experiments

Figures 5.2(a) through 5.4(a) show the calibration curves of the crystal plasticity model with the classical and Dynamic hardening rules against the tensile experiments of orientations P, T and U. These three orientations were chosen because they represent extremes of the material response. NRMSE values for these calibrations are presented in Table 5.3. As can be seen in this Table, the average error in the predictions of the Dynamic hardening model is less than that of the classical hardening rule. Therefore, the predictions of the Dynamic hardening model are generally more accurate than the classical hardneing model.

Calibrations were also done with other samples, including the set of P and R and the set of P and T. Results of these calibrations are presented in Tables 5.4 and 5.5. In both cases, the predictions of the dynamic hardening model are more accurate than the classical hardneing model. Nonetheless, the calibration of the Dynamic hardening model with P, T and U samples provided the least average error, thus it is presented in more details here.

The models calibrated with samples P, T and U were then used to predict the tensile stress-strain response of the remaining six (Q, R, S, V, W, and X) single crystal samples. Figures 5.5(a) through 5.10(a) compare the predictions of the classical and Dynamic hardening models with the results of tensile experiments of these six orientations. Open circle symbols in these figures show the results of experiments, dashed lines show the predictions of the Dynamic hardening, and solid lines show the predictions of the classical hardening models. Inspecting these figures, one can easily see that the predictions of the Dynamic

hardening model are better than the predictions of the classical hardening model. In Table 5.3, the average error in the predictions of the Dynamic hardening model is 6.76%, while the average error in the predictions of the classical hardening rule is larger by a factor of 1.32.

As can be seen in Figures 5.2(a) through Figure 5.10(a), the experimental slope of most of the stress-strain curves changes around 25% engineering strain. Neither of the classical and Dynamic hardening rules can predict this kind of change in the hardening rate of Nb single crystals. Therefore, the predictions of the crystal plasticity models deviate more strongly from the experiment after about 25% engineering strain. This indicates that the classical hardening assumption that the hardening is uniformly increased with increasing activity of the secondary slip system overestimates the rate of dislocation multiplication. It should be noted that neither of the models can predict the increase in slope that occurs with later strain.

Figures 5.2(b) through 5.10(b) show the geometry of the samples after straining. Figures 5.2(c)-(d) through 5.10(c)-(d) show contour plots of axial engineering stress on the deformed geometry of the samples as predicted by the simulation using the Dynamic hardening and the classical hardening model. The spatial distribution of stress (but not the magnitude) is similar for both models. The deformed geometry predicted by the models matches qualitatively with the experiment. Nevertheless, there are cases where the predictions and experiment are different. For instance, for specimen U, the deformed geometry shows macro shear bands that are not predicted by the models. These shear bands are a consequence of orientation splitting [from unpublished work of Di Kang, Ph.D. student at Michigan State University]. The crystal plasticity model has no means to identify localized dislocation reorganization, thus such features cannot be predicted.

The finite element model shown in Figure 5.1(b) has 600 elements. To study the mesh sensitivity of the prediction, the mesh was refined, which increased the number of elements to 21580. Figure 5.11 shows the effect of the mesh size on the predictions of the model for samples Q and X. As can be seen from these figures, the stress-strain curves of both mesh

sizes are similar. Therefore, the model is not mesh sensitive. The effect of the mesh size on the rest of the orientations was also minimal. Consequently, the stress-strain curves of other orientations with a finer mesh are not presented here.

The evolution of the texture during the tensile deformation is illustrated in Figures 5.12 through 5.20. Part "a" of these figures show the rotation of the tensile axis of the dog-bone samples during the deformation. Part "b" and "c" represent the evolution of crystal orientation as predicted by the crystal plasticity models with the Dynamic hardening and classical hardening rules, respectively. The contour shows the tensile strain. The predicted texture evolution is qualitatively accurate for all samples.

As was mentioned earlier, the tensile experiments were performed inside an electron microscope chamber using a specially designed tensile stage. The initial crystal orientation of the samples was measured before the deformation. Then the shoulders of the samples were secured between the grips of the tensile stage. One grip was fixed and the other one was moved in the tensile direction. The deformation was stopped at 10% engineering strain increments and the crystal orientation was measured. Samples were deformed up to 40% engineering strain.

In simulating the above tensile experiments, the grips were neglected and the deformation was imposed by boundary conditions. Neglecting the grips simplifies the model and makes the simulations less computationally expensive. The effect of the fixed grip was modeled with an encastre boundary condition. All the nodes on the left end of the left shoulder (the left-most nodes on the X-Z plane) in Figure 5.1(b) were pinned in their position. To model the moving grip, all the nodes on the right end of the right shoulder (the right-most nodes on the X-Z plane) in Figure 5.1(b) were moved in the positive Y direction.

The tensile stage recorded the force and displacement during the deformation. This data was used to calculate the engineering stress-strain curves. In simulations, the displacement at each finite element increment was extracted from the node at the top right corner of the right shoulder in Figure 5.1(b). The force was extracted from the encastre nodes of the

left shoulder. This data was used to plot the global engineering stress-strain curves of the simulation.

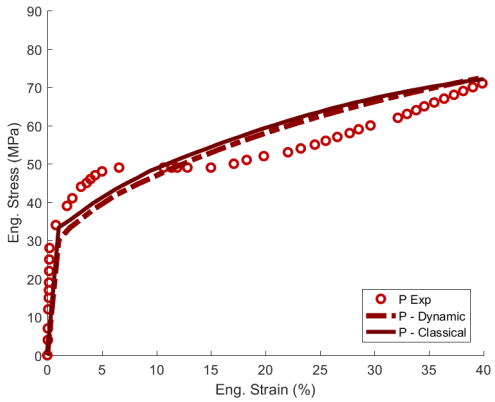

(a) Comparing the calibrations of the classical hardening and the Dynamic hardening rules against the stress-strain curve of the tensile test of sample P.

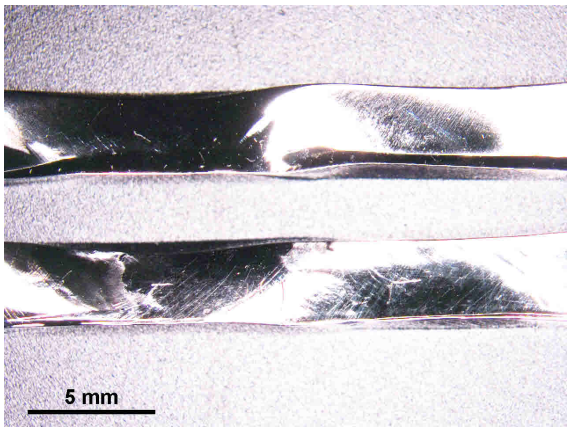

(b) Geometry of sample P after deformation.

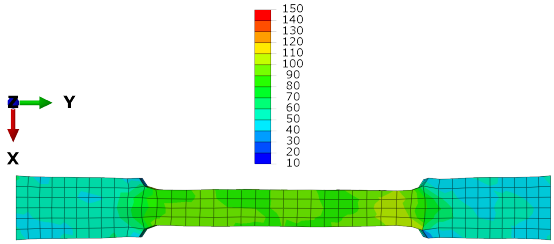

(c) Contour of axial stress for sample P as predicted by the Dynamic hardening rule.

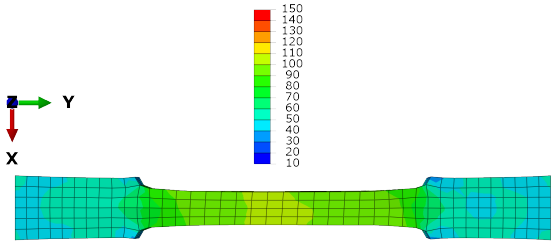

(d) Contour of axial stress for sample P as predicted by the classical hardening rule.

Figure 5.2: Each of the crystal plasticity models with the classical hardening and the Dynamic hardening rules was simultaneously calibrated against stress-strain curves of the experiments of P, T and U. (a) Compares the calibration of the Dynamic hardening and classical hardening rules to stress-strain curve of orientation P. In this plot, the experimental data is shown with circles, prediction of the Dynamic hardening model with a dashed line and prediction of the classical hardening rule with a solid line. (b) Shows the deformed P sample. (c) And (d) show the contour of the axial stress for sample P as predicted by the Dynamic hardening and the classical hardening rules, respectively.

5.5 Justifying the Dynamic hardening rule

As illustrated in Figures 5.2(a) through 5.10(d) and evident in Tables 5.3 through 5.5, the crystal plasticity model with the classical hardening rule cannot adequately predict

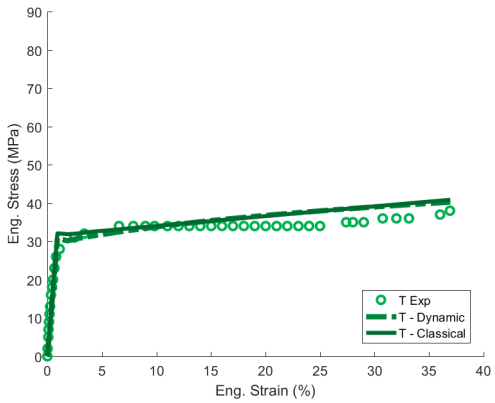

(a) Comparing the calibrations of the classical hardening and the Dynamic hardening rules against the stress-strain curve of the tensile test of sample T.

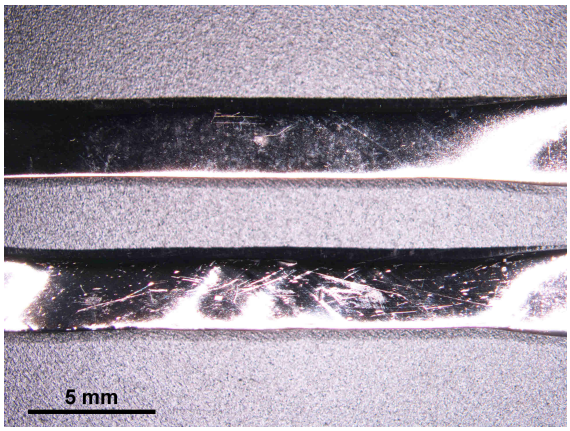

(b) Geometry of sample T after deformation.

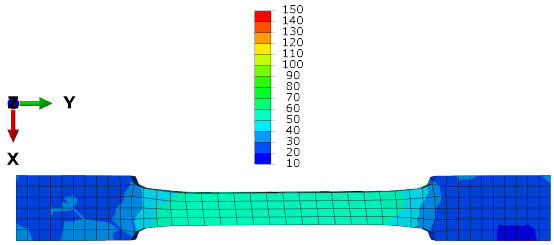

(c) Contour of axial stress for sample T as predicted by the Dynamic hardening rule.

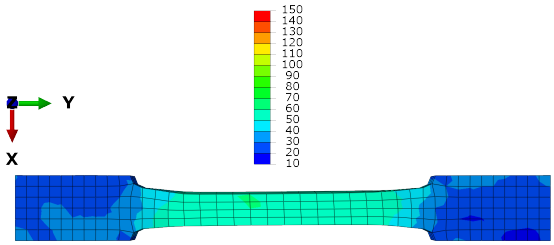

(d) Contour of axial stress for sample T as predicted by the classical hardening rule.

Figure 5.3: Each of the crystal plasticity models with the classical hardening and the Dynamic hardening rules was simultaneously calibrated against stress-strain curves of the experiments of P, T and U. (a) Compares the calibration of the Dynamic hardening and classical hardening rules to stress-strain curve of orientation T. In this plot, the experimental data is shown with circles, prediction of the Dynamic hardening model with a dashed line and prediction of the classical hardening rule with a solid line. (b) Shows the deformed T sample. (c) And (d) show the contour of the axial stress for sample T as predicted by the Dynamic hardening and the classical hardening rules, respectively.

the deformation behavior of Nb single crystals. One of the reasons for the failure of the classical model is that the definition of the hardening rate in this model does not accurately represent the physical processes taking place in a single crystal. The classical hardening model, equations (5.1), does not have an accumulated strain term. This model indirectly considers the effect of strain in calculation of the hardening rate, through the term $\frac{\tau_c^\beta}{\tau_s}$. This is the ratio of current critical shear stress (yield stress), τ_c^β, of slip system β to a saturation

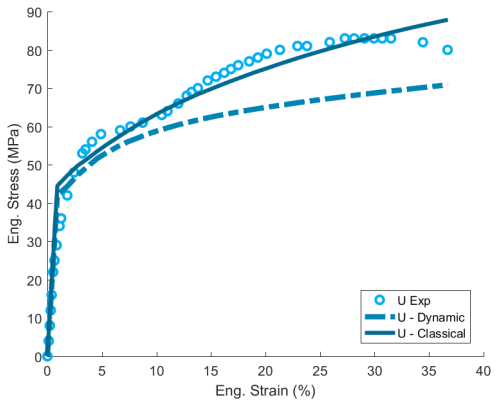

(a) Comparing the calibrations of the classical hardening and the Dynamic hardening rules against the stress-strain curve of the tensile test of sample U.

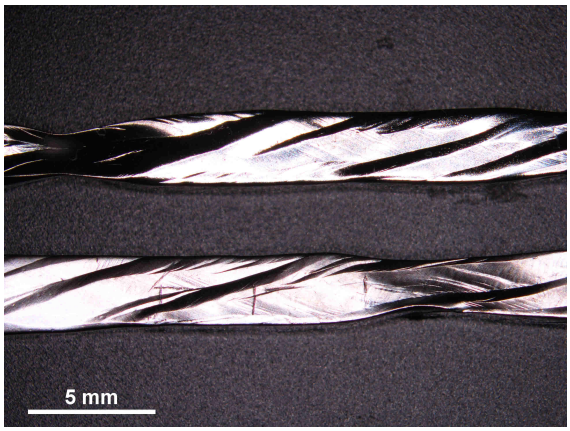

(b) Geometry of sample U after deformation.

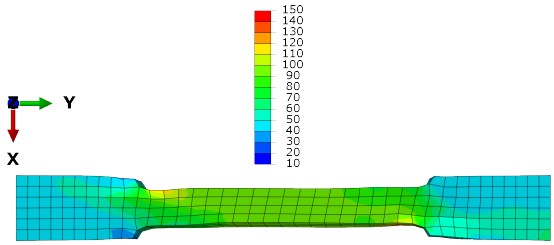

(c) Contour of axial stress for sample U as predicted by the Dynamic hardening rule.

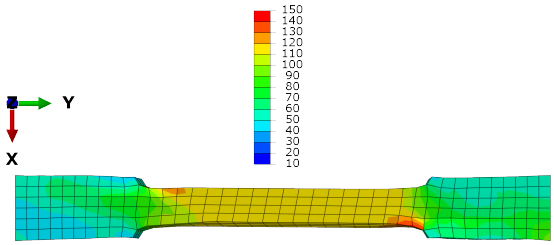

(d) Contour of axial stress for sample U as predicted by the classical hardening rule.

Figure 5.4: Each of the crystal plasticity models with the classical hardening and the Dynamic hardening rules was simultaneously calibrated against stress-strain curves of the experiments of P, T and U. (a) Compares the calibration of the Dynamic hardening and classical hardening rules to stress-strain curve of orientation U. In this plot, the experimental data is shown with circles, prediction of the Dynamic hardening model with a dashed line and prediction of the classical hardening rule with a solid line. (b) Shows the deformed U sample. (c) And (d) show the contour of the axial stress for sample U as predicted by the Dynamic hardening and theclassical hardening rules, respectively.

shear stress (the maximum allowed value), τ_s, which means that a slip system active at any moment hardens all other slip systems operating at different rate, unless its resolved shear stress reaches τ_s. In the single crystal deformation, no hardening occurs at the beginning as dislocation slip in only one direction dominates the deformation. At this stage, perhaps only one slip system is active, and there is no significant interaction with other slip systems to harden the material. This problem is addressed in the Dynamic hardening model.

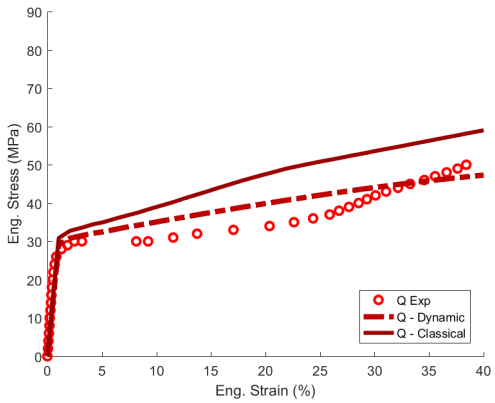

(a) Comparing the stress-strain curves predicted by the Dynamic hardening and the classical hardening rules against the experiment for Q orientation.

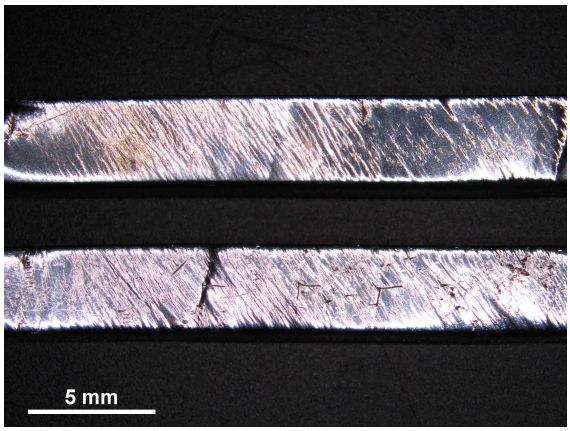

(b) Geometry of sample Q after deformation.

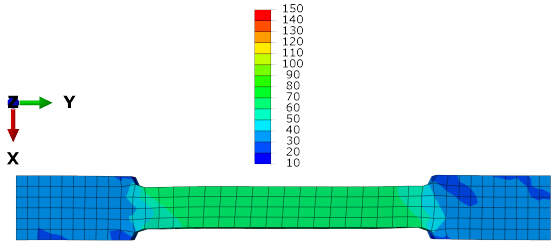

(c) Contour of axial stress for sample Q as predicted by the Dynamic hardening rule.

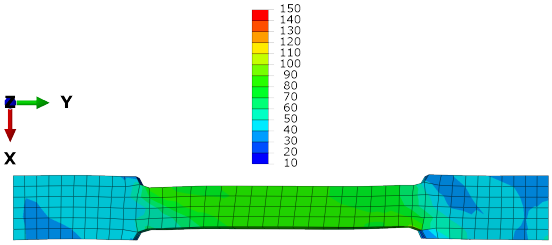

(d) Contour of axial stress for sample Q as predicted by the classical hardening rule.

Figure 5.5: (a) Comparing the stress-strain curves predicted by the Dynamic hardening and classical hardening rules against the experiments for sample Q. The experimental data is shown with circles, prediction of the Dynamic hardening model with a dashed line and prediction of the classical hardening rule with a solid line. (b) Shows the deformed Q sample. (c) And (d) show the contour of the axial stress for sample Q as predicted by the Dynamic hardening and the classical hardening rules, respectively.

To further discuss the Dynamic hardening model, equations (5.3) can be decomposed into two parts; the part modeling the hardening effect of the pre-existing barriers $\dot{\tau}^{\alpha}_{PE}$ and the part modeling the effect of interaction between active slip systems $\dot{\tau}^{\alpha}_{SSI}$.

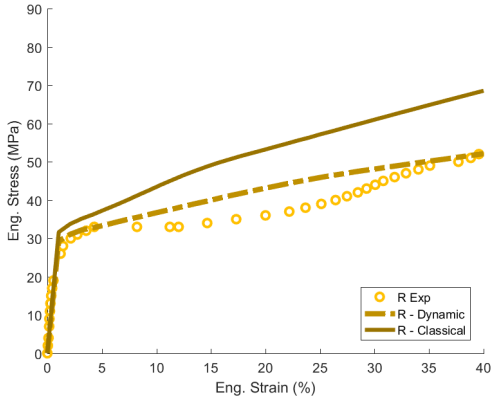

(a) Comparing the stress-strain curves predicted by the Dynamic hardening and the classical hardening rules against the experiment for R orientation..

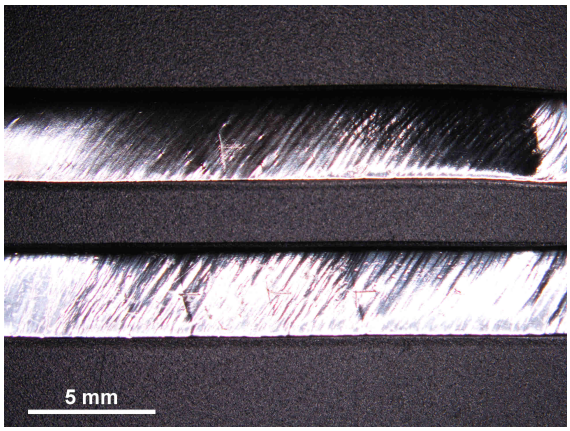

(b) Geometry of sample R after deformation.

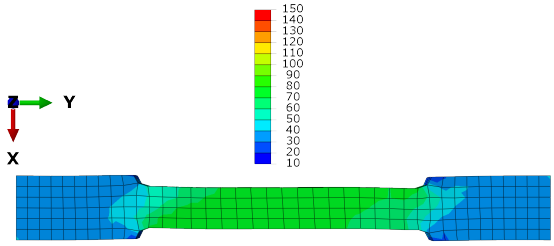

(c) Contour of axial stress for sample R as predicted by the Dynamic hardening rule.

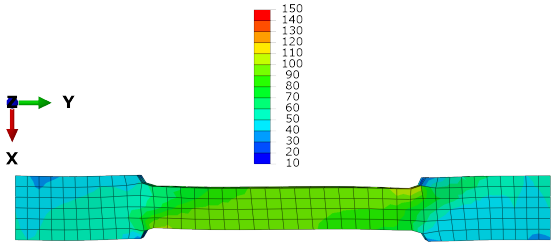

(d) Contour of axial stress for sample R as predicted by the classical hardening rule.

Figure 5.6: (a) Comparing the stress-strain curves predicted by the Dynamic hardening and classical hardening rules against the experiments for sample R. The experimental data is shown with circles, prediction of the Dynamic hardening model with a dashed line and prediction of the classical hardening rule with a solid line. (b) Shows the deformed R sample. (c) And (d) show the contour of the axial stress for sample R as predicted by the Dynamic hardening and the classical hardening rules, respectively.

$$\dot{\tau}^{\alpha}_{DH} = \sum_{\beta} h^{\alpha\beta}_{DH} \left|\dot{\gamma}^{\beta}\right| \left[(1-w) + w\left(\frac{\gamma^{2nd}}{\gamma^{1st}}\right)^{\eta}\right] = \dot{\tau}^{\alpha}_{PE} + \dot{\tau}^{\alpha}_{SSI} \tag{5.5a}$$

$$\dot{\tau}^{\alpha}_{PE} = \sum_{\beta} h^{\alpha\beta}_{DH} \left|\dot{\gamma}^{\beta}\right| (1-w) \tag{5.5b}$$

$$\dot{\tau}^{\alpha}_{SSI} = \sum_{\beta} h^{\alpha\beta}_{DH} \left|\dot{\gamma}^{\beta}\right| w\left(\frac{\gamma^{2nd}}{\gamma^{1st}}\right)^{\eta} \tag{5.5c}$$

At the beginning of the deformation when mainly one slip system is active; the total shear

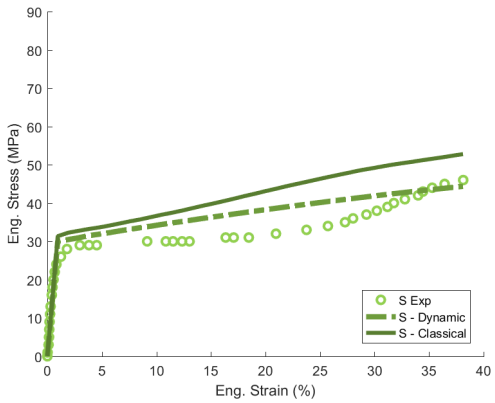

(a) Comparing the stress-strain curves predicted by the Dynamic hardening and the classical hardening rules against the experiment for S orientation.

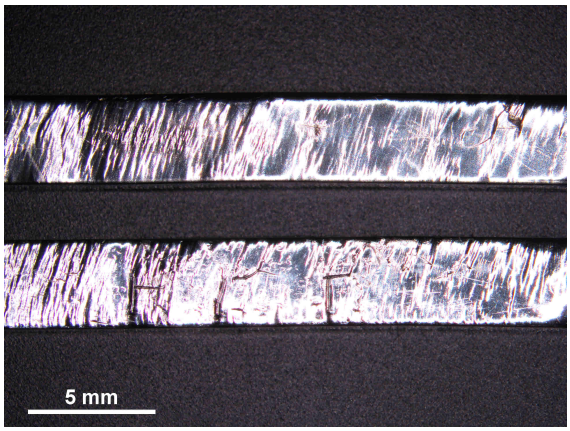

(b) Geometry of sample S after deformation.

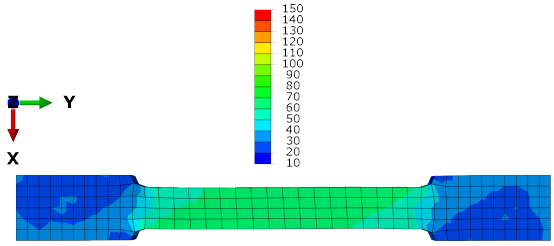

(c) Contour of axial stress for sample S as predicted by the Dynamic hardening rule.

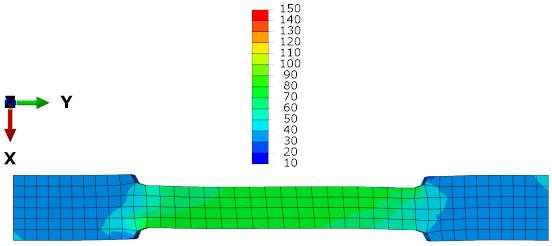

(d) Contour of axial stress for sample S as predicted by the classical hardening rule.

Figure 5.7: (a) Comparing the stress-strain curves predicted by the Dynamic hardening and classical hardening rules against the experiments for sample S. The experimental data is shown with circles, prediction of the Dynamic hardening model with a dashed line and prediction of the classical hardening rule with a solid line. (b) Shows the deformed S sample. (c) And (d) show the contour of the axial stress for sample S as predicted by the Dynamic hardening and the classical hardening rules, respectively.

strain on the second most active slip system γ^{2nd} is very small in comparison to total shear strain of the most active system γ^{1st}. Therefore, the term $w\left(\frac{\gamma^{2nd}}{\gamma^{1st}}\right)^{\eta}$ in equation (5.5c) is very small which effectively shuts down the increment in hardening, due to the lack of barriers such as grain boundaries and forest dislocations. The material, nevertheless, hardens slightly through the interaction of the active slip systems with the pre-existing obstacles. Equation (5.5b) models this effect. Any active slip system can run into pre-existing barriers and cause hardening. The term w adjusts this contribution to the overall hardening behavior. In the

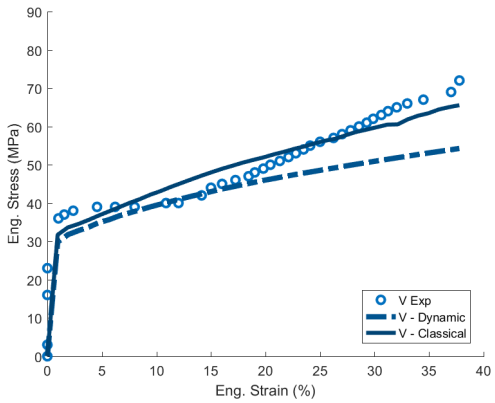

(a) Comparing the stress-strain curves predicted by the Dynamic hardening and the classical hardening rules against the experiment for V orientation.

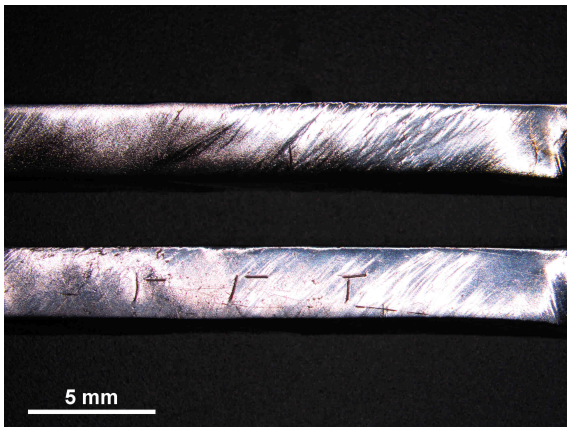

(b) Geometry of sample V after deformation.

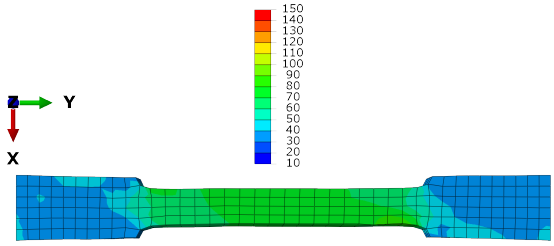

(c) Contour of axial stress for sample V as predicted by the Dynamic hardening rule.

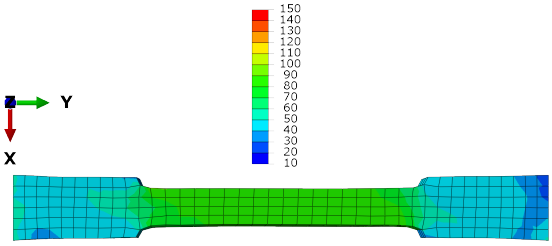

(d) Contour of axial stress for sample V as predicted by the classical hardening rule.

Figure 5.8: (a) Comparing the stress-strain curves predicted by the Dynamic hardening and classical hardening rules against the experiments for sample V. The experimental data is shown with circles, prediction of the Dynamic hardening model with a dashed line and prediction of the classical hardening rule with a solid line. (b) Shows the deformed V sample. (c) And (d) show the contour of the axial stress for sample V as predicted by the Dynamic hardening and the classical hardening rules, respectively.

experiments, the pre-existing dislocation content is not known. It is likely that pre-existing dislocations may be more effective in hardening some orientations than others, given that the samples were extracted from 4 distinct grains in an ingot slice. Consequently, a single value for w is not likely to be descriptive of the particular interactions between activated and existing dislocations in the experiments.

As seen in Figures 5.2(a) through 5.10(d), the Dynamic hardening model adequately predicts the deformation behavior of single crystal Nb. This confirms the validity of the

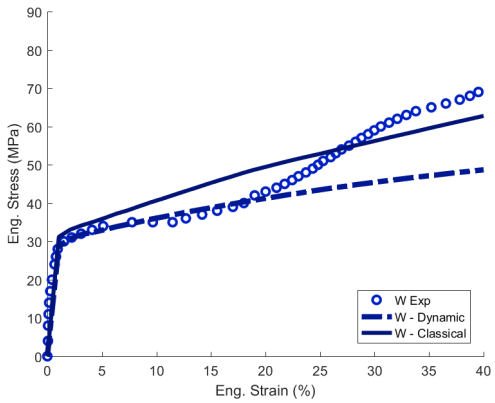

(a) Comparing the stress-strain curves predicted by the Dynamic hardening and the classical hardening rules against the experiment for W orientation.

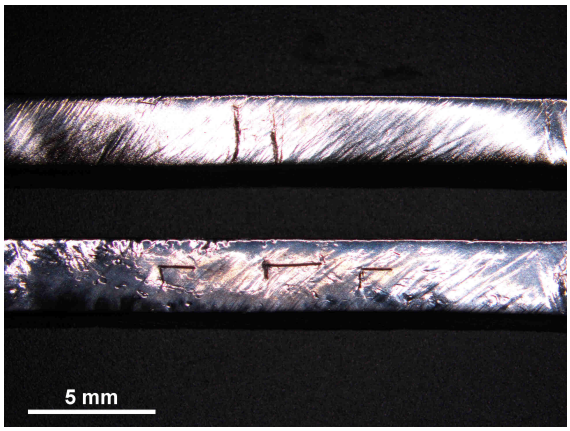

(b) Geometry of sample W after deformation.

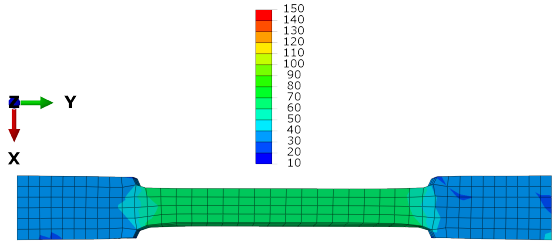

(c) Contour of axial stress for sample W as predicted by the Dynamic hardening rule.

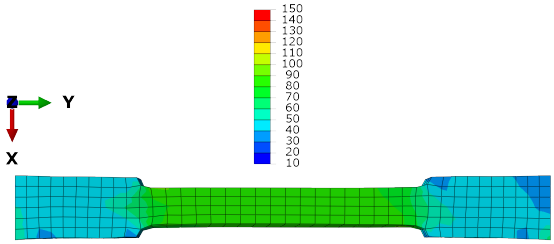

(d) Contour of axial stress for sample W as predicted by the classical hardening rule.

Figure 5.9: (a) Comparing the stress-strain curves predicted by the Dynamic hardening and classical hardening rules against the experiments for sample W. The experimental data is shown with circles, prediction of the Dynamic hardening model with a dashed line and prediction of the classical hardening rule with a solid line. (b) Shows the deformed W sample. (c) And (d) show the contour of the axial stress for sample W as predicted by the Dynamic hardening and the classical hardening rules, respectively.

Dynamic hardening model and is consistent with the underlying physical metallurgy of dislocation behavior.

The texture evolution predicted by both hardening model qualitatively matches with experiments. Although the tensile samples are single crystals, their orientation slightly varies from one side to the other. In addition, the initial dislocation density might vary slightly from one sample to other. The model, though, considers only one orientation throughout each sample and assumes an identical initial state for all samples. These can affect the

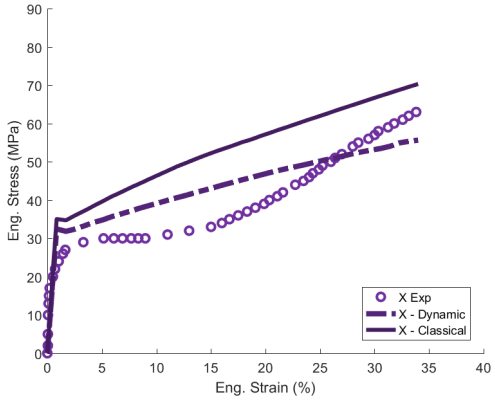

(a) Comparing the stress-strain curves predicted by the Dynamic hardening and the classical hardening rules against the experiment for X orientation.

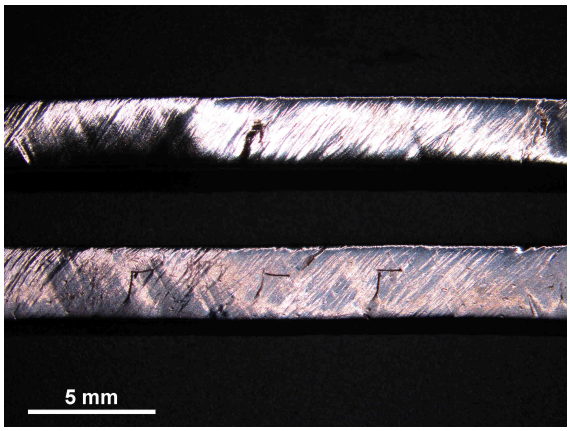

(b) Geometry of sample X after deformation.

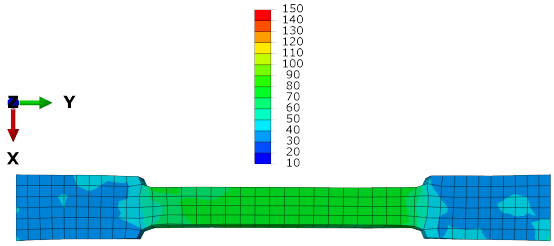

(c) Contour of axial stress for sample X as predicted by the Dynamic hardening rule.

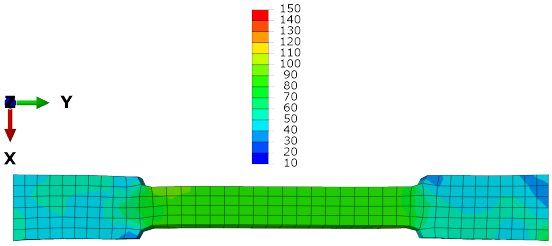

(d) Contour of axial stress for sample X as predicted by the classical hardening rule.

Figure 5.10: (a) Comparing the stress-strain curves predicted by the Dynamic hardening and classical hardening rules against the experiments for sample X. The experimental data is shown with circles, prediction of the Dynamic hardening model with a dashed line and prediction of the classical hardening rule with a solid line. (b) Shows the deformed X sample. (c) And (d) show the contour of the axial stress for sample X as predicted by the Dynamic hardening and the classical hardening rules, respectively.

prediction of the texture evolution as well as the stress-strain curves.

The current model is based on a Schmid law for activation of a slip system. The deformation behavior of BCC materials, however, may be more accurately modeled with non-Schmid-type models [170], which provides a potential improvement to the Dynamic hardening approach. Given the uncertainties in initial dislocation content and their effect on hardening, the non-Schmid effects may be hidden behind effects from the initial dislocation content. Furthermore, the mathematical construction of the model still results in flow curves

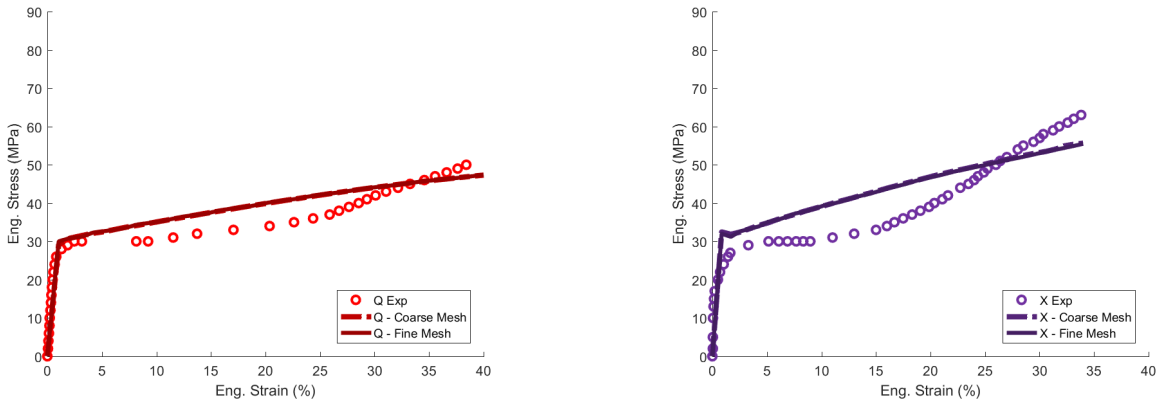

(a) (b)

Figure 5.11: Comparing the stress-strain curves predicted by the Dynamic hardening model for coarse (600 elements - shown with dashed lines) and fine mesh (21580 elements - shown with solid lines) models of (a) Q and (b) X. As can be seen in these figures the crystal plasticity model is not mesh sensitive.

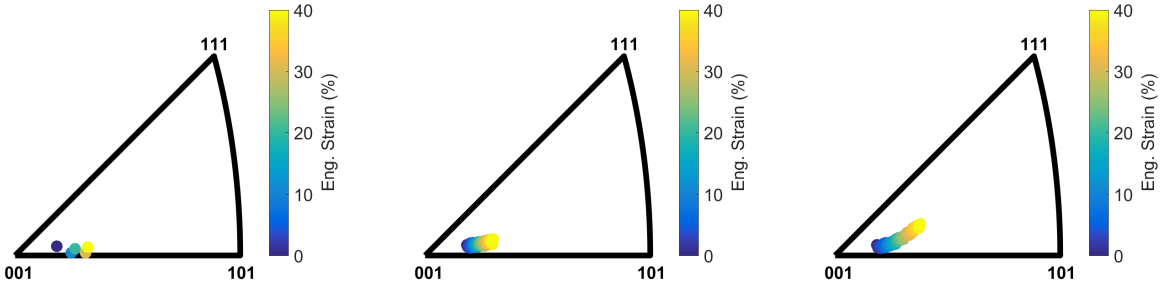

(a) Experiment - P (b) Dynamic hardening - P (c) Classical hardening - P

Figure 5.12: Inverse pole figures show the results of (a) experiment, (b) the Dynamic hardening and (c) the classical hardening rule for the evolution of texture during 40% tensile deformation of P orientation. The contour shows the engineering strain. The orientation data in the experiment was recorded at 10% increments while the simulation data was recorded at 1% increments.

with downward curvature, so inflection leading to upward curvature cannot be captured by the Dynamic hardening rule. Thus, the source of this more pronounced hardening effect requires models that can generate flow behavior with upward curvature and is the subject of continuing research efforts.

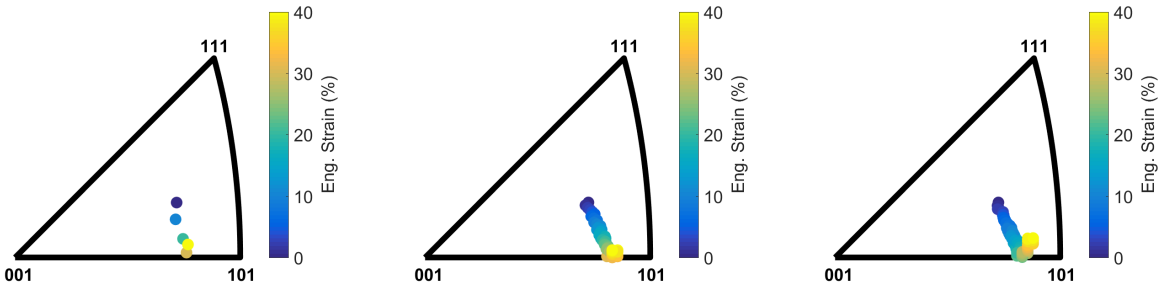

(a) Experiment - Q (b) Dynamic hardening - Q (c) Classical hardening - Q

Figure 5.13: Inverse pole figures show the results of (a) experiment, (b) the Dynamic hardening and (c) the classical hardening rule for the evolution of texture during 40% tensile deformation of Q orientation. The contour shows the engineering strain. The orientation data in the experiment was recorded at 10% increments while the simulation data was recorded at 1% increments.

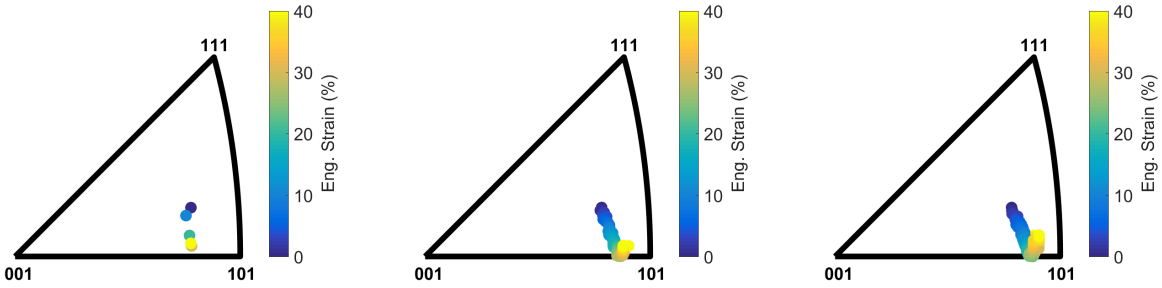

(a) Experiment - R (b) Dynamic hardening - R (c) Classical hardening - R

Figure 5.14: Inverse pole figures show the results of (a) experiment, (b) the Dynamic hardening and (c) the classical hardening rule for the evolution of texture during 40% tensile deformation of R orientation. The contour shows the engineering strain. The orientation data in the experiment was recorded at 10% increments while the simulation data was recorded at 1% increments.

5.6 Summary

Another approach taken to improve the predictions of the Schmid-type crystal plasticity model was presented in this Chapter. This approach proposes a generalization to the classical hardening rule (which is termed the Dynamic hardening rule) to model the hardening of single crystal BCC materials more accurately. The Dynamic hardening rule, equations (5.2), reduces to the classical form, equations (5.1), when either $w = 0$ or $\eta = 0$.

The classical hardening model cannot accurately predict the deformation behavior of Nb.

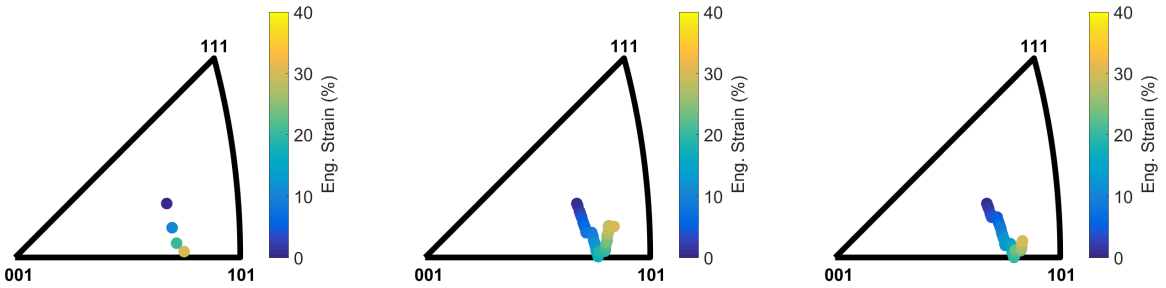

(a) Experiment - S (b) Dynamic hardening - S (c) Classical hardening - S

Figure 5.15: Inverse pole figures show the results of (a) experiment, (b) the Dynamic hardening and (c) the classical hardening rule for the evolution of texture during 30% tensile deformation of S orientation. The contour shows the engineering strain. The orientation data in the experiment was recorded at 10% increments while the simulation data was recorded at 1% increments.

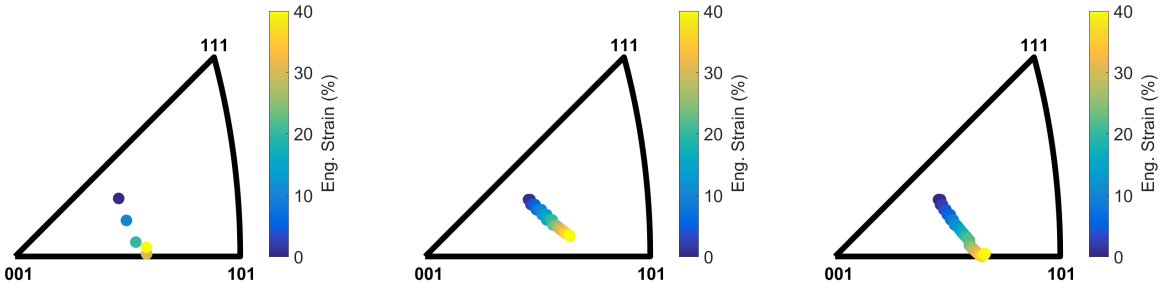

(a) Experiment - T (b) Dynamic hardening - T (c) Classical hardening - T

Figure 5.16: Inverse pole figures show the results of (a) experiment, (b) the Dynamic hardening and (c) the classical hardening rule for the evolution of texture during 40% tensile deformation of T orientation. The contour shows the engineering strain. The orientation data in the experiment was recorded at 10% increments while the simulation data was recorded at 1% increments.

The Dynamic hardening model, however, significantly improves the ability of the Schmid-type crystal plasticity model to predict the flow behavior of BCC single crystal niobium. This is done by introducing a simplified concept based on the physical processes of dislocation behavior. The Dynamic hardening model assumes at the beginning of the deformation and during the single slip stage, dislocation accumulation is minimal and the material does not harden significantly. This model can be easily implemented into the existing crystal plasticity codes.

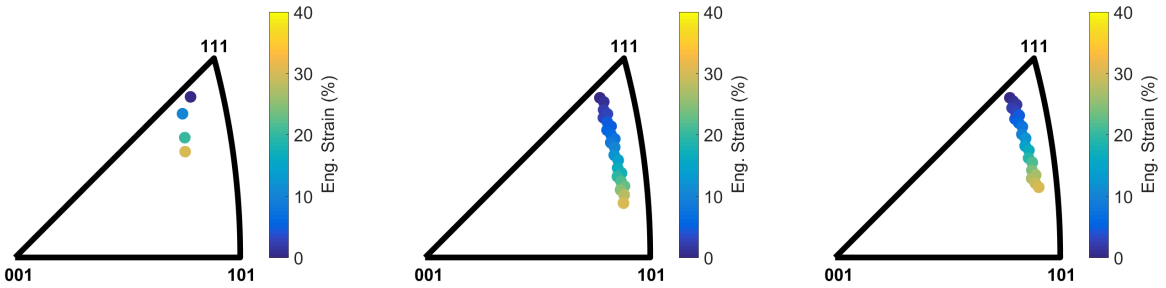

(a) Experiment - U (b) Dynamic hardening - U (c) Classical hardening - U

Figure 5.17: Inverse pole figures show the results of (a) experiment, (b) the Dynamic hardening and (c) the classical hardening rule for the evolution of texture during 30% tensile deformation of U orientation. The contour shows the engineering strain. The orientation data in the experiment was recorded at 10% increments while the simulation data was recorded at 1% increments.

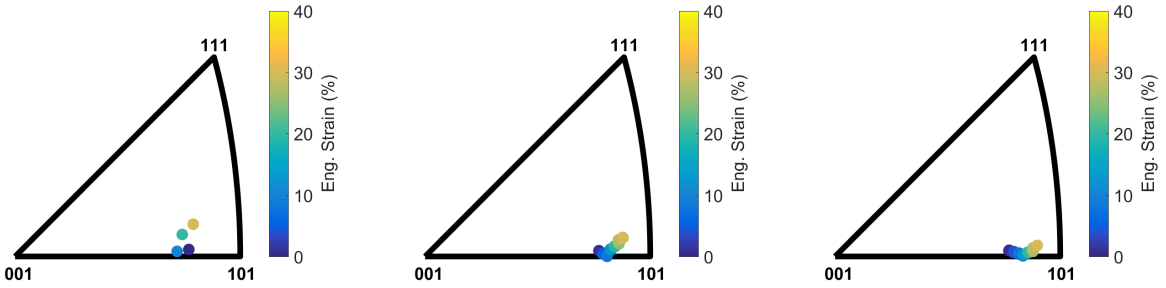

(a) Experiment - V (b) Dynamic hardening - V (c) Classical hardening - V

Figure 5.18: Inverse pole figures show the results of (a) experiment, (b) the Dynamic hardening and (c) the classical hardening rule for the evolution of texture during 30% tensile deformation of V orientation. The contour shows the engineering strain. The orientation data in the experiment was recorded at 10% increments while the simulation data was recorded at 1% increments.

In the current Chapter and Chapter 4, the normalized root means-square error (NRMSE) was used as a metric to compare the quality of model predictions throughout the deformation process. NRMSE is a scalar measure of error between predictions of simulations and the respective experimental data. A model fit to the experiment is acceptable when NRMSE value is small. Therefore, the model calibration process was defined as an optimization problem to minimize this error.

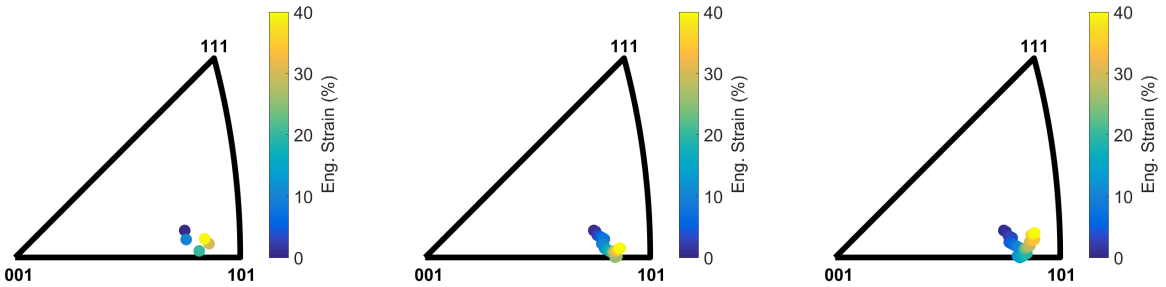

(a) Experiment - W (b) Dynamic hardening - W (c) Classical hardening - W

Figure 5.19: Inverse pole figures show the results of (a) experiment, (b) the Dynamic hardening and (c) the classical hardening rule for the evolution of texture during 40% tensile deformation of W orientation. The contour shows the engineering strain. The orientation data in the experiment was recorded at 10% increments while the simulation data was recorded at 1% increments.

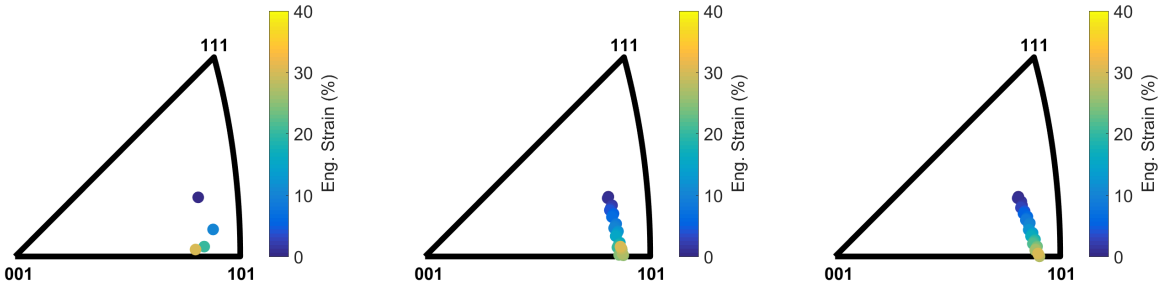

(a) Experiment - X (b) Dynamic hardening - X (c) classical hardening - X

Figure 5.20: Inverse pole figures show the results of (a) experiment, (b) the Dynamic hardening and (c) the classical hardening rule for the evolution of texture during 30% tensile deformation of X orientation. The contour shows the engineering strain. The orientation data in the experiment was recorded at 10% increments while the simulation data was recorded at 1% increments.

Table 5.3: NRMSE for predictions of crystal plasticity models with the classical and the Dynamic hardening rules calibrated simultaneously with stress-strain curves of samples P, T, and U. The lower error values are in bold font.

Sample	NRMSE (%) for crystal plasticity model	
	Classical hardening	Dynamic hardening
P	**6.93**	7.16
Q	11.29	**4.17**
R	16.30	**5.92**
S	11.94	**5.17**
T	4.88	**4.49**
U	**4.62**	8.60
V	**5.32**	8.77
W	4.76	10.04
X	14.31	**6.89**
Average error	8.93	**6.76**

Table 5.4: NRMSE for predictions of crystal plasticity models with the classical and the Dynamic hardening rules calibrated simultaneously with stress-strain curves of samples P and R. The lower error values are in bold font.

Sample	NRMSE (%) for crystal plasticity model	
	Classical hardening	Dynamic hardening
P	7.85	**7.81**
Q	6.68	**4.16**
R	15.41	**3.78**
S	6.38	**5.96**
T	**3.51**	5.65
T	22.53	**21.02**
V	7.16	**5.54**
W	**5.44**	10.10
X	15.93	**8.26**
Average error	10.10	**8.03**

Table 5.5: NRMSE for predictions of crystal plasticity models with the classical and the Dynamic hardening rules calibrated simultaneously with stress-strain curves of samples P, T. The lower error values are in bold font.

Sample	NRMSE (%) for crystal plasticity model	
	Classical hardening	Dynamic hardening
P	**5.92**	6.47
Q	14.03	**5.50**
R	20.87	**4.60**
S	13.20	**7.15**
T	5.17	**4.82**
T	**7.70**	13.74
V	**5.24**	7.26
W	**4.75**	11.38
X	19.88	**8.24**
Average error	10.75	**7.68**

CHAPTER 6

CRYSTAL PLASTICITY MODELING OF TUBE HYDROFORMING

A major industrial application of pure polycrystalline niobium (Nb) sheet metal is for particle accelerator cavities. The International Linear Collider (ILC) project will require a very large amount of Nb to fabricate cavities in a limited time. This large future demand has stimulated alternative cavity fabrication strategies such as directly slicing disks out of as-cast Nb ingots [175] which eliminates the costly Nb sheet rolling process [176] and reduces waste for axisymmetric parts. It has been shown that cavities manufactured from large grain (grains larger than 5-10 mm) sheets often have a better superconducting radio frequency (SRF) performance than the fine grain (grain size in range of 50 µm) sheets [135, 176]. This increase in performance is correlated with the presence of fewer grain boundaries in the material. Also, the sheet rolling process can introduce impurities to the material. Slices that are cut form from an ingot potentially have fewer defects per unit volume.

Nb ingots are manufactured by electron beam melting of a Nb feedstock. This molten Nb drips into a continuous casting mold. The ingot made with this process has a nearly columnar grain structure. As single crystal ingots are routinely fabricated in other materials, it may be possible to fabricate ingots with a preferred orientation [175]. However, the intrinsic plastic anisotropy of Nb single crystals will lead to non-uniform forming, which must be anticipated.

Figure 6.1 schematically shows a particle accelerator cavity. These cavities are traditionally made from deep drawing of a Nb sheet into bowl shapes having a hole in the center. Two bowls are welded together to make an elliptical cavity. Then a tube with the inner diameter equal to the diameter of the holes is welded to each end to make a single cell cavity.

Although the above is the standard manufacturing process for these cavities, it is not an optimal one. A manufacturing process like tube hydroforming has the potential to fabricate a cavity from a single piece of tube, and the lack of welding could lead to better reproducibility and improve the performance of the cavity while reducing the manufacturing costs. Tube

hydroforming is a forming process in which an internal hydraulic pressure applies the deformation force. If an outer die is used, the material conforms to it. Figure 6.2 schematically shows the steps of the tube hydroforming process. The ultimate goal of this research is to make a particle accelerator cavity from the large grain tube that was previously made. The current study uses a crystal plasticity model with Dynamic hardening rule described in Chapter 5 to predict the hydroforming of a large grain Nb tube.

The rest of this Chapter is organized as follows. §6.1 reviews the process for fabrication of the seamless large grain Nb tube that was hydroformed in this study. To verify the microstructure of the tube, crystal orientation was systematically measured at several locations around the tube. The results of these measurements are presented in §6.2. Next, the tube was hydroformed. Details of this experiment are explained in §6.3. Then, the hydroforming experiment was simulated with the Schmid-type crystal plasticity model with the Dynamic hardening rule. §6.4 compares the predictions of the model with the experiment. §6.5 discusses the tube making process, the hydroforming experiment and the crystal plasticity modeling in more details. Findings of this Chapter are summarized in §6.6.

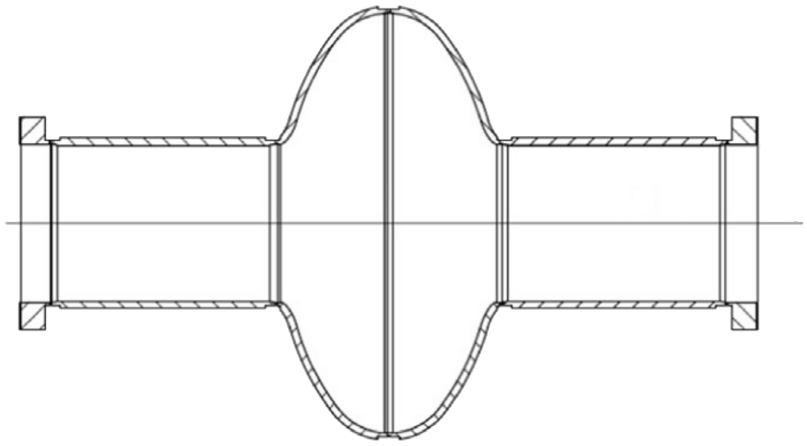

Figure 6.1: Cross section of a single-cell particle accelerator cavity. Figure from [132].

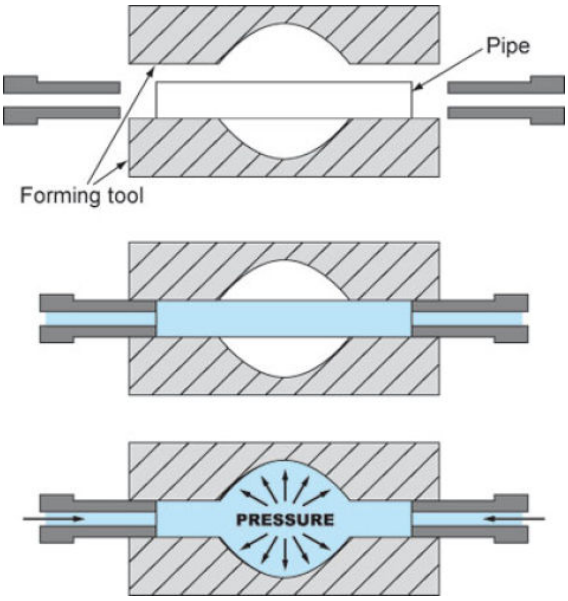

Figure 6.2: This figures shows the schematics of a tube hydroforming process. The tube is secured between the rams and die (if available). The fluid pressure brings the material to yield. Rams can be moved axially to assist in the forming process. Figure from [177].

6.1 Material and method - fabrication of a large grain niobium tube

To provide the means to examine effects of large grain material on hydroforming, a seamless large grain Nb tube with an outer diameter of 38 mm was made from a 2 mm-thick polycrystal Nb sheet. The tube manufacturing process was done by Dr. Jim Murphy at University of Nevada, Reno.

A rectangular Nb sheet was bent into a 38 mm (1.5 inches) outer diameter tube and arc welded. To grow the crystals and convert the initial microstructure to a large grain structure, the tube was locally heated to a very high temperature (near the melting temperature) in a high vacuum ($\sim 5 \times 10^{-6}$ torr) furnace. The vacuum reduced impurities that have a lower melting point and a higher vapor pressure. The heat was created with a radio frequency local hot zone. This technique quickly heated up a small section of the tube. The hot zone was then moved along the length of the tube with a fixed velocity, which encouraged recrystallization and grain growth parallel to the tube axis. The tube was fixed between

water-cooled copper plates in the furnace, that did not allow thermal expansion in the axial direction. Therefore, the tubes that came out of this process were not perfectly straight.

The most successful tube is shown in Figure 6.3(a). The surface of the tube shows some grooves and ledges, the deepest of which are traced with black lines in Figure 6.3. As will be demonstrated later, these black lines (often) mark the grain boundaries. Some shallower grooves represent the location of finer grain boundaries that were present before the large grain growth. These grooves are evident in an enlarged part of the tube image in Figure 6.3(b).

(a)

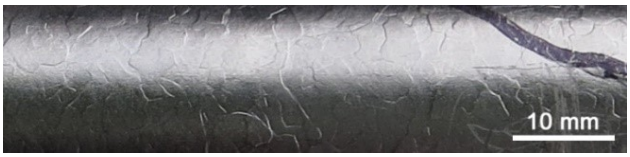

(b)

Figure 6.3: (a) The large grain Nb tube made for this study. The tube is not fully straight because it was fixed between two rigid cooling plates in the furnace. The black lines mark the current grain boundaries. (b) An enlarged section from the center of the tube shows visible grooves and ledges showing the grain boundaries prior to forming the large grains.

6.2 Characterization of the tube

After the heat treatment, the orientation of the tube was examined with a Laue camera. Laue measurement is an X-ray diffraction based technique and does not need to be performed in a vacuum. This contrasts with Orientation Imaging Microscopy (OIM) measurement,

which is extracted from Electron Back Scatter Diffraction (EBSD) data and is done in an electron microscope chamber under a vacuum. Laue camera samples can be larger than OIM samples because they do not have to fit into a microscope chamber.

Figure 6.4 shows the arrangement of the large grain boundary lines unrolled into a sheet. The white dashed lines show the location of the original weld line. The black lines correspond to the dominant surface groove features of the tube. Each color in this figure represents an individual grain, but the colors are arbitrary.

To examine the visible ledges on the surface of the tube more closely, grain orientations on either side of selected ledges were measured using Laue camera at locations denoted with A1-A4, B1-B4, and C1-C6 in Figure 6.4. Crystal orientations were also measured around the weld line at locations that are labeled with D1-D3 in Figure 6.4. The orientations measured at locations A through D are shown in pole figures in Figure 6.5. The B measurements were made parallel to the length of the tube, so they were directly measured in a common coordinate system. Measurements made at locations A, C, and D required rotation around the tube axis. Each orientation shown in Figure 6.5(a), (c) and (d) is measured with respect to a separate coordinate system. Each coordinate system is rotated around the tube axis with respect to other orientations within the same plots.

As can be seen in Figure 6.5(a), the measurements A2 and A3 represent the same grain orientation but with a rotation around the tube axis. By rotating A3 around the tube axis by approximately 50°, one gets to the A2 orientation. Hence, A2 and A3 are from the same grain. By rotating A4 around the tube by approximately 80°, it gets close to the orientation of A2, but there is still a misorientation between them. There is also a misorientation between grains A1 and A2.

By inspecting B1 through B4 in Figure 6.5(b), one can easily conclude that the ledge between B2 and B3 is a grain boundary. B1 and B2 have the same grain orientation and B3 and B4 have another orientation.

The measurements at locations C1 through C6 were performed to check three visible

ledges in that section of the tube. The orientation was measured on either side of each boundary. Results shown in Figure 6.5(c) confirm that these ledges are grain boundaries.

The heat treatment was designed to remove the weld line and the heat affected zone (HAZ). To verify that grain growth consumed the weld line, measurements D1 through D3 were performed below, on, and above the weld line, as shown in Figure 6.4. The orientation of these measurements is shown in Figure 6.5(d). Orientations D2 and D3 match the orientation D1 when rotated by the approximately 30° and 50° around the tube axis that was imposed. Therefore, the heat treatment fully recrystallized the heat affected zone and the initial grain structure to a new grain that covers the middle section of the tube. This grain is represented by the light green area in the middle of Figure 6.4 .

Next, the orientations of grains were measured systematically using a grid. The grid lines are on the surface of the tube, parallel to the tube axis and approximately 60° apart. The orientation was measured at eight points along each axial line. The points are 25.4 mm (1 inch) apart from each other and the ends. The Laue camera stage on which the tube was placed, moves in X-Z plane (left-right and up-down directions). This machine, however, does not have the capability of turning the tube around its axis. Therefore, the measurements along the axis of the tube were made on the exact 25.4 mm intervals; while the rotation around the axis of the tube was manual and approximately 60°. Figure 6.4 schematically shows the grid defined by outside longitudinal locations 25.4 mm apart (P-W) and circumferential markings (approximately 60° apart, 1-6) at which the orientation was measured. The axis of the tube is horizontal (Y-direction). Red circles show the approximate locations of X and Z axis. The commercial software "Orient Express" was used to index the Laue patterns and identify the crystal orientation.

Since orientations were measured on the surface of the tube; each measurement around the circumference was with respect to a separate coordinate system. Therefore, to express all the measured orientations in a common reference coordinate system the measurements around the axis of the tube (on lines 1-6) were rotated by 0°, 71°, 152°, 213°, 263° and 315°,

respectively.

The three ⟨100⟩ directions for each set of circumferential measurements (at positions P through W after rotating the orientations to the 0° common reference) are plotted on pole figures shown in Figure 6.6. At positions P and Q, two distinct ⟨100⟩ orientations are apparent. This means that there are two grains in these locations. At positions R, S, and T, the three ⟨100⟩ directions coincide, indicating that the central grain has the same orientation with respect to the reference coordinate system. Three distinct orientations can be seen in U and V and four orientations are seen in position W.

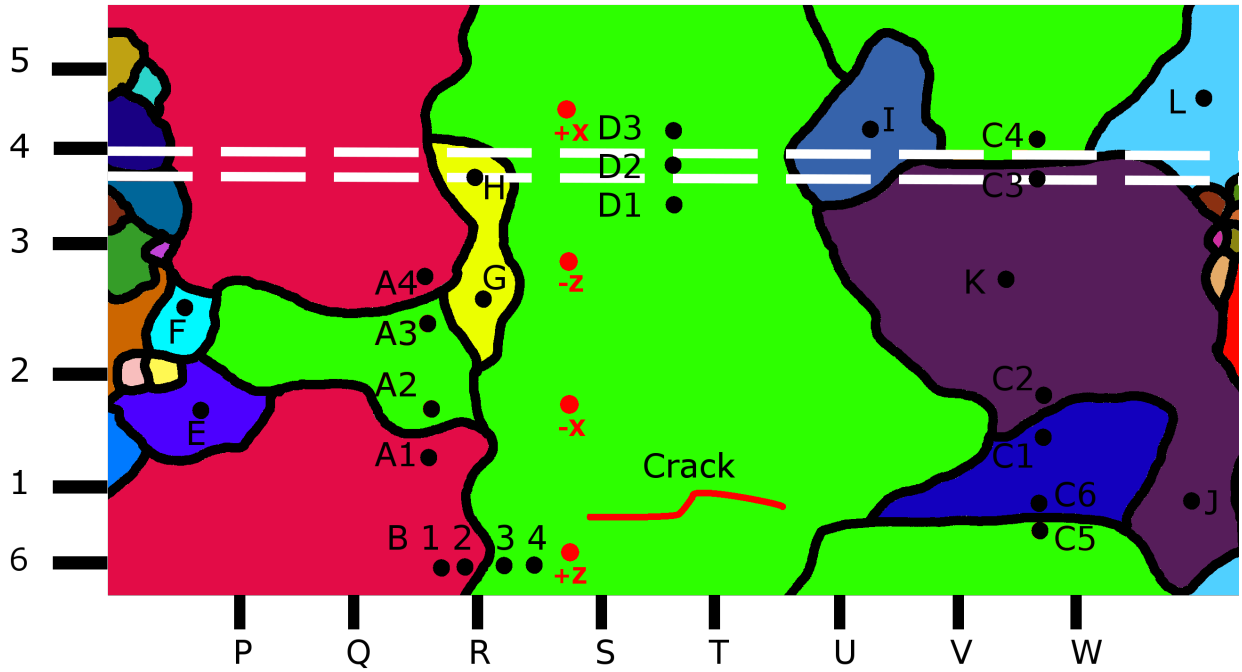

Figure 6.4: This map shows the grain structure of the large grain Nb tube. Major grain boundaries are shown with black lines and the weld is shown with the white dashed lines. The red line shows the location of crack after hydroforming. Each color represents one grain. The axis of the tube is horizontal (Y-direction). Red circles show the approximate locations of X and Z axis.

6.3 Tube bulging with pressurized water

A standard approach to the tube hydroforming process was used to study the deformation of the large grain tube and as a first step towards designing a tube hydroforming manufac-

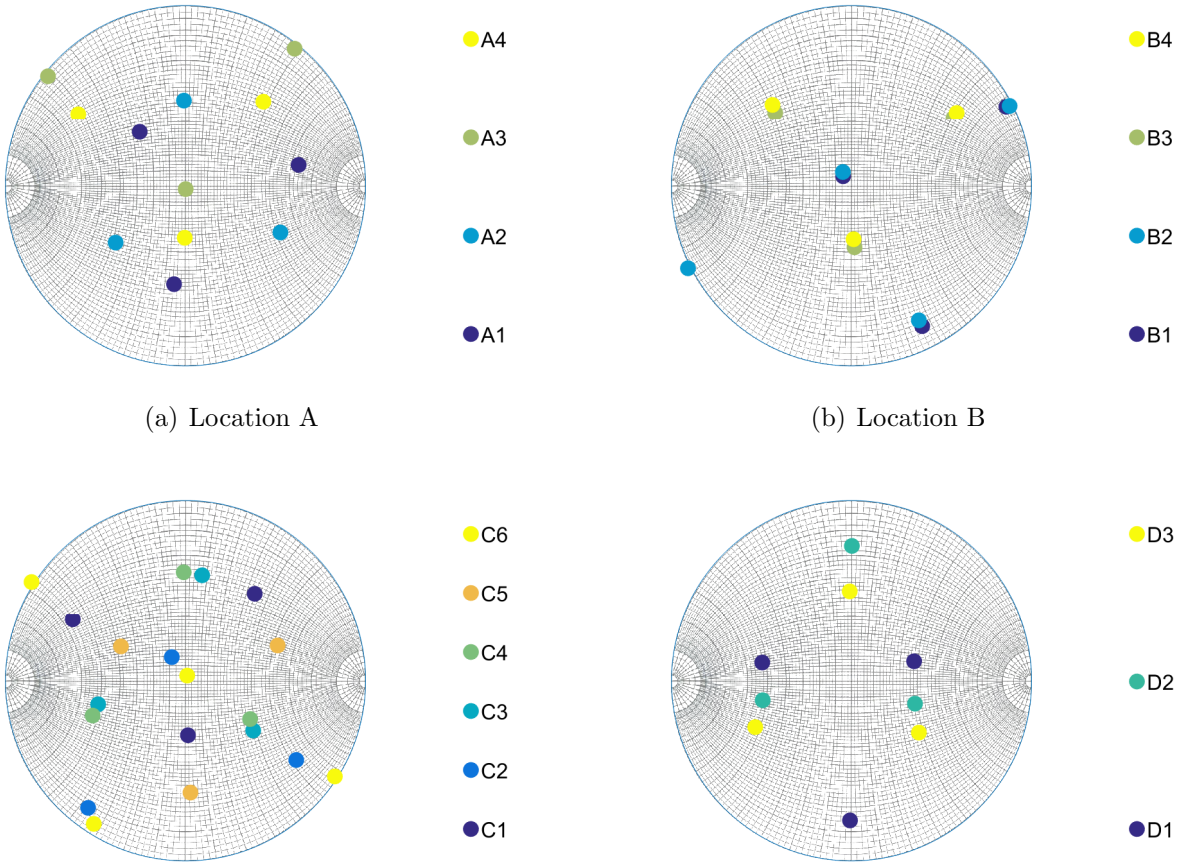

(a) Location A

(b) Location B

(c) Location C

(d) Location D

Figure 6.5: These Pole figures show the Laue camera measurements of crystal orientations at locations A through D. The orientation of these measurements was not corrected for the rotation of the tube.

turing process. A square-circle grid was put on the tube to facilitate the measurement of local strains after deformation.

The tube was mounted in a custom-built tube hydroforming machine. A clamp fixture was used to secure the tube between the rams and create a seal. The clamp system design includes a pair of collars that have an inner diameter equal to the outer diameter of the tube. They have a negative conical shape that matches the conical shape of the rams. These collars were put on the tube; then the tube was compressed between the conical shape rams to flare out the ends. The collars are designed to compress the flare of the tube against the rams. The clamp system compresses the flared ends of the tube between the rams and the

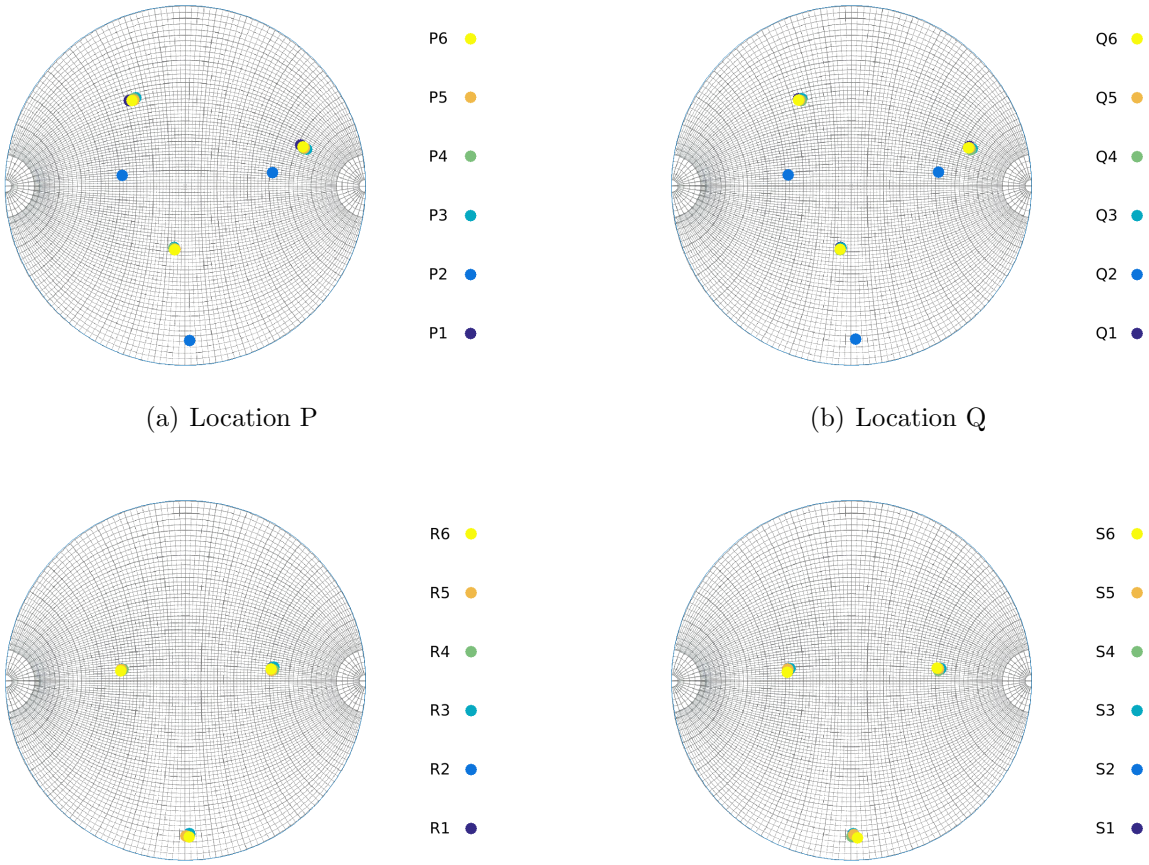

(a) Location P

(b) Location Q

(c) Location R

(d) Location S

Figure 6.6: Pole figures show the Laue camera measurements of crystal orientation. Each pole figure shows 6 measurements made around the tube at positions P-W shown in Figure 6.4. The crystal orientations plotted in these pole figures are rotated back to a common reference orientation by 0°, 71°, 152°, 213°, 263° and 315°, respectively for circumferential positions 1-6 shown in Figure 6.4.

collars to establish the seal.

The inner surfaces of the flared parts of the tube were lightly grounded circumferentially to remove the grain boundary ledges and grooves. Because the tube was not straight, it bent slightly due to the compressive force of the flaring process. To make the tube nearly straight again, the fixing clamps were put around the tube and the rams (but they were not tightened) to allow pulling the tube back to nearly straight. The clamps were then tightened. Figure 6.7 shows the final assembly.

Figure 6.6: (cont'd)

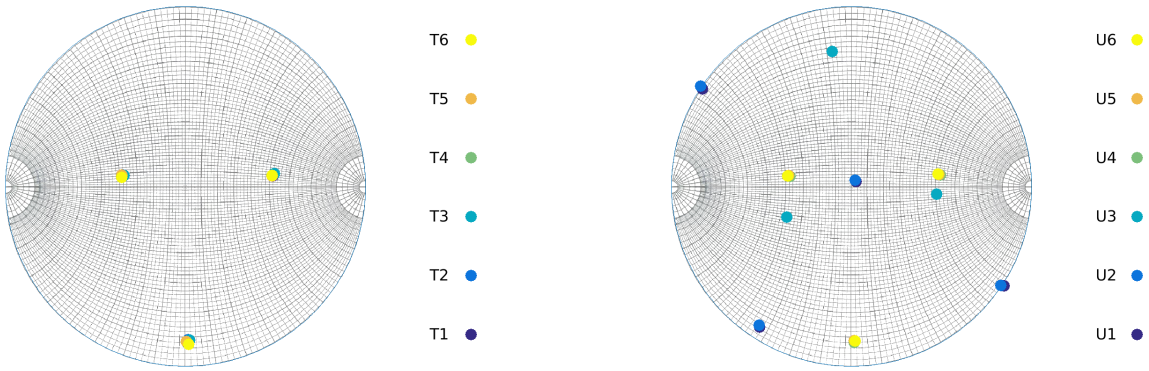

(e) Location T

(f) Location U

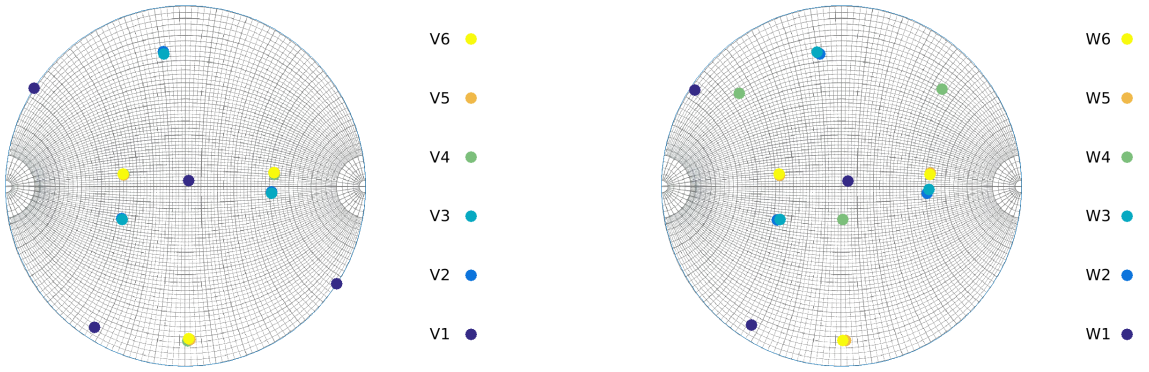

(g) Location V

(h) Location W

The tube bulging process started with incrementally increasing the fluid pressure. The left ram was also incrementally moved along the tube axis to maintain an approximately constant compressive load. Both fluid pressure and axial load were incrementally increased until the tube cracked. The tube cracked in the middle of a bulged section within the center single crystal region, about 10 mm from grain boundaries, and far from the prior weld line. The crack is shown in Figure 6.8(a) and schematically presented in Figure 6.4. A side view of the deformed tube is shown in Figure 6.8(b).

The data acquisition software recorded the fluid pressure, ram displacement and reaction force. Figure 6.9 shows the value of these parameters during the deformation. The hydro-forming process was monitored with a "GoPro Hero3+ dual-camera system" at two-second

intervals.

As can be seen in Figure 6.9, at the beginning of the process the left ram was moved 0.025 mm to apply an axial force on the tube. Then the fluid pressure was increased to about 600 kPa. This resulted in a drop in the axial force. Next, at second 54, the ram was moved to the 0.305 mm location, which increased the compressive load to about 4300 N. The fluid pressured was then incrementally increased. The tube bulged with increasing of the pressure which caused a contraction in the length of the tube and a drop in the compressive load. At second 237, after the fluid pressure reached about 5000 kPa and the compressive load dropped to about 500 N, the left ram was moved to the position of 0.635 mm. This increased the compressive load to the maximum of ∼5460 N. The pressure was then increased to the maximum of ∼5400 kPa. The material became unstable under these conditions and eventually cracked at about second 280.

After the deformation, the change in the dimensions of the square grid (which was previously put on the tube) was measured and the local strains were calculated at each of the locations in the longitudinal and circumferential positions. Figure 6.10 shows the distribution of the measured local circumferential (hoop) strain. The white regions are where the grid was damaged or incomplete and no reliable measurements could be made. The location of the crack is shown with a purple arrow.

6.4 Crystal plasticity modeling of the tube hydroforming

As was mentioned before, the large grain tube that came out of the heat treatment process was not straight. To capture the geometry of the tube in the simulation, the company "Laser Design" created a CAD model from a 3D scan of the tube with a target accuracy of ±0.001 inch. The CAD model was then meshed with 60012 solid eight-node brick elements with reduced integration (C3D8R). The mesh is composed of three layers with 20004 elements each.

While the geometry of the model matches closely with the physical tube, the finite

element mesh does not show any of the surface features of the tube, such as the curved grain boundaries, ledges, and grooves. The complex grain boundary shapes were not easily mapped onto the finite element mesh of the tube. Therefore, as a first approximation, smaller grains were neglected and the boundaries were modeled with straight lines using the grid shown in Figure 6.11.

In the experiment, the clamp system constrained the smaller grains near the ends of the tube, so they did not contribute to the overall deformation. The implemented boundary conditions in the model similarly limit the deformation of these grains. Therefore, the smaller grains were ignored in modeling without compromising the results. The colored blocks were filled with the corresponding Laue camera measurement orientation data from the pole figures shown in Figure 6.6. Figure 6.12 shows the model of the tube with the grain orientations mapped.

Next, mechanical boundary conditions were imposed on the model of the tube. The rams and the clamps were ignored, but the boundary condition imposed by the collars were modeled. To do so, the nodes within $\sim$25 mm of each end were constrained to only move in the axial direction. The tube flaring process which resulted in the slight bending of the tube was modeled with an axial 12.7 mm compressive displacement on each end of the tube. This was applied on the end nodes (nodes perpendicular to the axis of the tube). The applied displacement is equal to the flaring displacement that was done in the experiment. An equal displacement but in the reverse directions was then applied to simulate the straightening of the tube. Then the nodes on the right end of the tube (nodes perpendicular to the axis of the tube) were fixed. Next, the left ram was displaced incrementally to 0.635 mm, and the pressure was incrementally increased to 5400 kPa. These values of applied pressure and the compressive displacement are similar to the experiment.

A tensor visualization technique was used to process the simulation data. Therefore, the basics of this technique need to be explained before presenting the simulation results. This method is named Superquadric Tensor Glyphs [178] and visualizes tensors using their

eigenvectors and eigenvalues. In a strain tensor, the principal directions (eigenvectors) of the tensor define the spatial orientation of the glyph and the principal strains (eigenvalues) convey the dimensions of a glyph. Therefore, for a plane strain state the glyph has a plate shape; for a uniaxial strain the glyph has a bar shape, and for a hydrostatic pressure the glyph is a sphere. A larger hydrostatic strain will be presented by a larger sphere. The color of each glyph signifies the von Mises strain value of the element from which the strain tensor was extracted. The details of the visualization method are explained in [178] and a range of glyph shapes are shown in Figure 6.13.

The Schmid-type crystal plasticity model with the Dynamic hardening rule was used to predict the deformation of the tube. This model was previously calibrated with single crystal Nb tensile specimens described in the Chapter 5. The deformed geometry predicted by this model is shown in Figure 6.14. The color bar on the left of this figure represents the equivalent plastic strain of the top surface of the tube. In Figure 6.14(a), the location that corresponds with the location of the crack in the experiment is shown with a purple ellipse. This area has a light blue strain contour.

The colors used to illustrate plastic strain contours are set to discern the strain gradients in the bulged center of the tube most easily. The gradient occurs in the equivalent strain range of 0-0.3. As will be shown with strain glyphs, the gray and red parts of the contour are mainly compressive strain, which arose due to the axial compressive displacement applied during the deformation. Most of the hoop strain happens in the mid-section of the tube, where the tube has bulged the most. The spatial orientation of the tube is the same as the deformed tube shown in Figure 6.8(b).

Although the equivalent plastic strain in the mid-section of the tube is less than other parts, the bulging happened in this section. Therefore, the type of strain experienced by elements in the center is different from the strain experienced by elements closer to the ends (in red and gray parts of the contour). To study the variation of strain, two lines of elements parallel to the axis of the tube were selected and highlighted in Figure 6.14. These lines

are also shown with two purple arrows. The line in Figure 6.14(a) corresponds to the line where the crack developed in the experiment. The line in Figure 6.14(b) is a location with significant hoop strain. The location of the crack in Figure 6.14(b) is marked with a purple ellipse.

Plastic strain tensors were extracted from elements highlighted in Figure 6.14 and visualized using glyphs. The glyphs on either end have a plate shape, which means that they represent a plane strain state. The orientation of the glyphs in the center, which have a bar shape, indicate the direction of maximum tensile hoop strain. The glyphs closer to the ends are approximately parallel to the axis of the tube, which means that they have a principal component parallel to the axis of the tube. This component is a longitudinal compressive strain that was applied during the deformation. On the other hand, the glyphs in the center are perpendicular to the axis of the tube. This means that neither of their two principal strain directions is a compressive strain along the axis of the tube.

6.5 Further analysis of the experiments and crystal plasticity simulation

The goal of the initial heat treatment was to obtain a seamless large grain tube. The Laue camera investigations confirm that this goal was achieved. During the heat treatment, the fine grains grew and formed large grains. A few of these large grains grew and consumed most of the remaining microstructure. The tube was supported on each end by water-cooled copper plates. The high thermal gradient limited the grain growth at the ends. Therefore, the grains close to each end were smaller and were not consumed by the larger grains. The Laue camera measurements showed, however, that the grain growth fully consumed the weld line and the heat affected zone. If the small grains at the ends of the tube are ignored, one can argue that the heat treatment was successful in creating a seamless large grain tube. Thus, this method can be used as a baseline for designing a manufacturing process of such large grain tubes.

The tube hydroforming method has been used in automotive industry for decades. Prior

to the current hydroforming experiment, several practice experiments were performed with annealed polycrystalline copper tubes. Figure 6.15 shows a copper tube before and after tube hydroforming. While pure niobium is exceptionally ductile, the tube burst with a much smaller bulge than was formed in the copper tubes. This is evident when comparing Figures 6.8(b) and 6.15(a). Clearly, more research is needed before this process can be used to form large grain Nb cavities. Future research should focus on developing optimal tubes with strategic crystal orientations that do not form preferential strain conditions (light blue to yellow regions in Figure 6.10 and light blue regions in Figure 6.14).

During the hydroforming process, the tube deformed inhomogeneously and asymmetrically and eventually cracked in the large grain in the middle of the tube and away from the grain boundaries. This is the largest grain of the tube. It has the same crystal orientation with respect to an external coordinate frame for every point around the circumference of the tube. This effect can be illustrated with a counter-example. The crystal orientation for every point on a single crystal sheet is the same. But if such a sheet is rolled into a tube, every point around the circumference will have a different crystal orientation with respect to a fixed external frame, which is the opposite condition of the present experiment.

The applied internal fluid pressure exerts a radial stress normal to the interior wall of the tube. Consequently, the crystal has a varying orientation at each point around the tube with respect to the radial stress exerted by the internal fluid pressure. Thus, the resolved shear stress and the active slip systems are different at each location around the circumference of the tube. This is evident in Figure 6.16 which shows the variation of Schmid factor for $\langle 111\rangle\{1\bar{1}0\}$ and $\langle 111\rangle\{11\bar{2}\}$ slip systems around the tube for the large grain in the middle of the tube. As can be seen in this figure, the maximum Schmid factor (or resolved shear stress on a slip system) varies with azimuthal location. There are four regions with high values and four regions between them with low values. Two of the regions with higher values have multiple peaks from different slip systems near each other, while the other two have only two peaks with two slip directions. In most azimuthal locations of the grain, there is at least

one slip system that is favorably oriented for dislocation slip and will yield with increasing fluid pressure. The positions with the highest Schmid factor (resolved shear stress) yield earlier than other locations, resulting in thinning the material locally. This increases the stress in that location and makes it more susceptible to further strain and eventual cracking. It should be noted that such thinning did not happen at the prior weld line since it had become a part of the large grain.

As can be seen in Figure 6.10, the circumferential (hoop) strain in the tube is very inhomogeneous. The location of the crack is shown with a purple arrow. At the crack and a few other areas, the strain grid was damaged and unmeasurable. Since no data is available in these areas, they are shown with white blocks. Some locations in Figure 6.10 show highly localized deformation. Locations immediately around the crack show a relatively small localized hoop strain. Therefore, another reason for the failure of the tube in the center of a large grain could be the arrangement of the grain orientations and boundaries, and the distribution of the strain in the in the vicinity of a boundary dividing soft and hard orientations. Based on the contour levels around the crack, it seems to have developed in a soft region adjacent to harder regions.

Figure 6.17(a) and (b) show the distribution of circumferential (hoop) strain as predicted by the model. The strain distribution in these figures is shown with two contour scales. In Figure 6.17(a) the contour levels are adjusted so that the variation is visible. The contour levels of Figure 6.17(b) match with Figure 6.10. The detailed contour levels in Figure 6.17 are different from the contour levels in Figure 6.10, but the location of the highest strain in Figure 6.17 matches with the location of the crack in Figure 6.10. The simulation data has a higher resolution because the element size of the model is smaller than the grid size in the experiment. The bright yellow areas in Figure 6.17(a) match approximately with the locations of maximum Schmid factor in Figure 6.16. Both figures predict highly localized deformation at four locations (areas near angles 0°, 90°, 180° and 270°).

As can be seen in Figure 6.14, the center of the tube bulged the most. The reason for

the chosen strain range in the plot is to show the variation of the strain in the mid-section of the tube. The equivalent plastic strain predicted for this part of the tube is less than other parts. When a larger contour scale range is used, the variations in the center are not as apparent.

One can argue that the green to red strain contours in Figure 6.14 show a different type of strain than the navy to light blue areas because most of the bulging is accommodated by the smaller strains in the central region. Strain tensor glyphs in Figure 6.14 show that the sense of the strain at the ends and in the center of the tube are quite different. By inspecting Figure 6.13, one can conclude in each element (or glyph) the deformation is almost plane strains. In other words, the minimum principal strain is very small in comparison to the two other principal directions. Otherwise, the glyphs would have been thicker. For the glyphs on either side, the angle between at least one of the mid or maximum principal directions and the axis of the tube (which is horizontal) is small. Many of these glyphs are nearly coplanar with the axis of the tube. On the other hand, the mid and maximum principal directions for glyphs extracted from the center of the tube are approximately perpendicular to the axis of the tube. These glyphs still have a plate shape, but because they are perpendicular to the axis of the tube, they appear as a bar. The middle part of the tube bulged the most, which confirms that most of the strain in this part of the tube is hoop strain. The glyphs closer to ends are nearly perpendicular to the glyphs extracted from the center. Therefore, strain away from the center is mostly longitudinal stress.

In Figure 6.14(a), the horizontal light blue area noted with a purple arrow shows the highest circumferential strain. This is also the area where the tube cracked in the experiment. As can be seen in Figure 6.14(b), the predicted deformed geometry of the tube matches qualitatively with the experiment. Moreover, the location of the light blue contour in this figure, which is another area that shows large circumferential strain, approximately matches with the white block at the bottom of Figure 6.10. Therefore, the Dynamic hardening crystal plasticity model can predict the location of significant circumferential deformation and the

potential location of the crack.

Nb is a very anisotropic BCC material. Therefore, forming or modeling of large grain Nb sheets and tubes is challenging. For that reason, fine grain Nb sheets are traditionally used in making particle accelerator cavities, although cavities made from large grain Nb often have a better performance. Nonetheless, the crystal plasticity model with the Dynamic hardening rule, which was developed in Chapter 5, gives satisfactory predictions of deformation of large grain Nb tube. One can use this model to find an optimum grain orientation for forming a large grain tube. This information can be used as a guide to identify desirable orientation as an experimental goal.

6.6 Summary

The possibility of making a large grain Nb cavity was explored in this Chapter. To do so, a Nb tube was made from bending and arc welding a Nb polycrystal sheet. The tube then went through a heat treatment cycle that was designed for grain growth. The Laue camera measurement of the tube showed that the heat treatment successfully favored the growth of a few grains that consumed the weld line and created a large grain tube.

The tube was hydroformed until it cracked in the middle grain. This is the only grain in the mid-section of the tube and spans the entire circumference of the middle section. Due to variation of the crystal orientation with respect to the hoop stress resulting from the applied pressure, slip systems at different material points around the tube experienced different resolved shear stresses and have regions of distinctly favored dislocation slip activity. Such anisotropy is one of the reasons for the failure of the tube in the middle of a large grain. Another reason may be the deformation characteristics of the neighboring grains that may have been softer or harder, and influenced the magnitude of hoop strain where the failure occurred.

The Schmid-type crystal plasticity model with the Dynamic hardening rule, that was developed and calibrated in Chapter 5, was used to simulation the tube hydroforming process.

The location of the crack predicted by this model matches with the experiment. Therefore, this model can be used to give insight in designing new manufacturing processes for large grain Nb cavities.

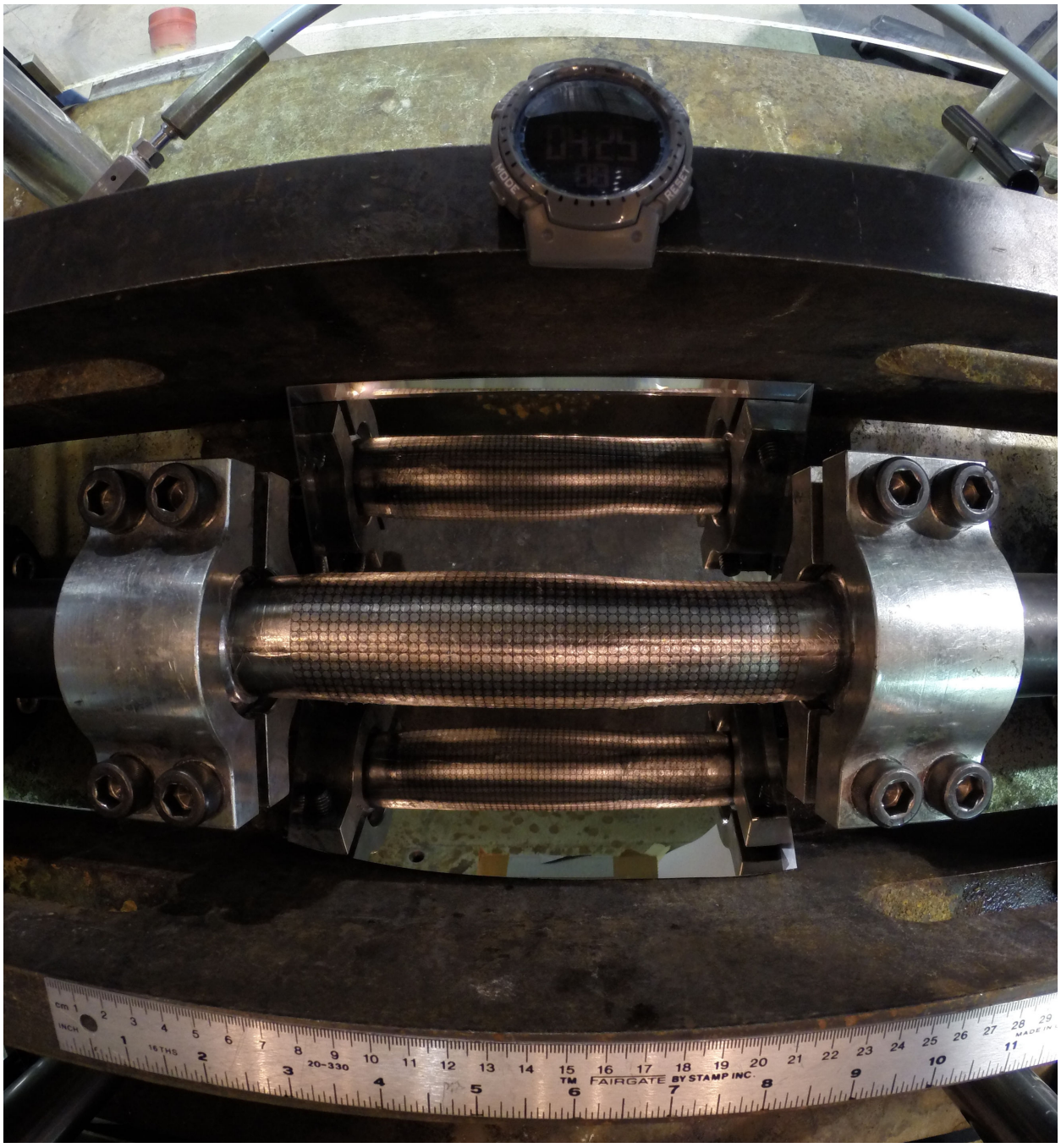

Figure 6.7: This picture shows the assembly of the tube in the hydroforming machine. The tube was clamped to the rams to ensure a seal. The ram heads have a conical shape. The tube ends were flared with the rams, so the seal could be established. This picture was taken with a "GoPro Hero3+" camera which has a wide angle lens.

(a)

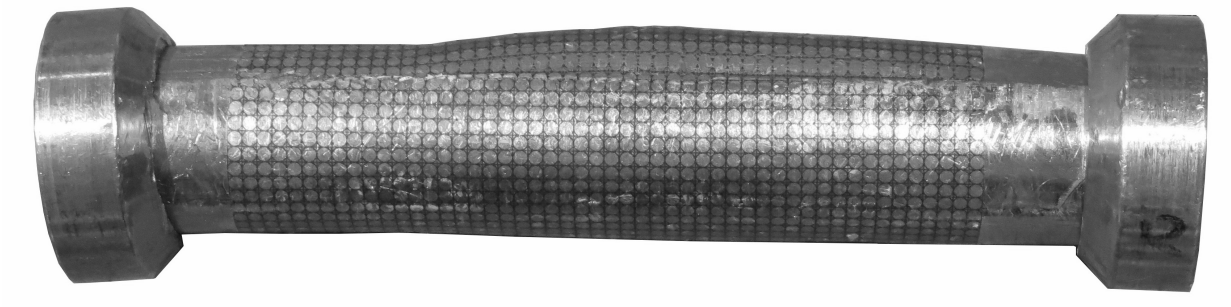

(b)

Figure 6.8: The tube was hydroformed until it cracked. (a) The cracked region is shown in the enlarged image looking down to the top of the tube. (b) The side view of the tube shows the bulge. The location of the crack is at the top of this image. The crack location is schematically shown in Figure 6.4. The collars shown at either end are a part of the clamp design.

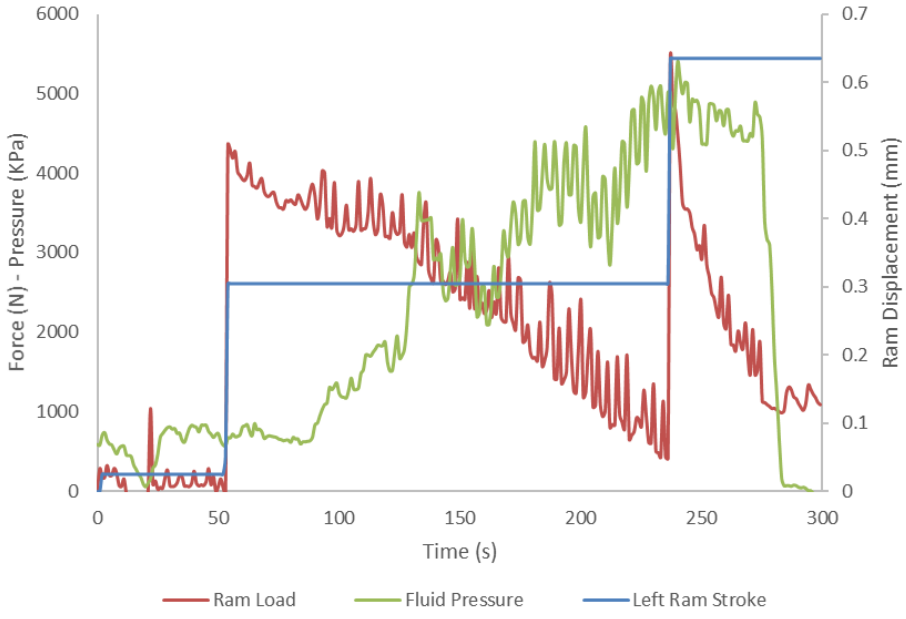

Figure 6.9: Variation of hydroforming fluid pressure, ram load and displacement recorded during the experiment. All three parameters were incrementally increased.

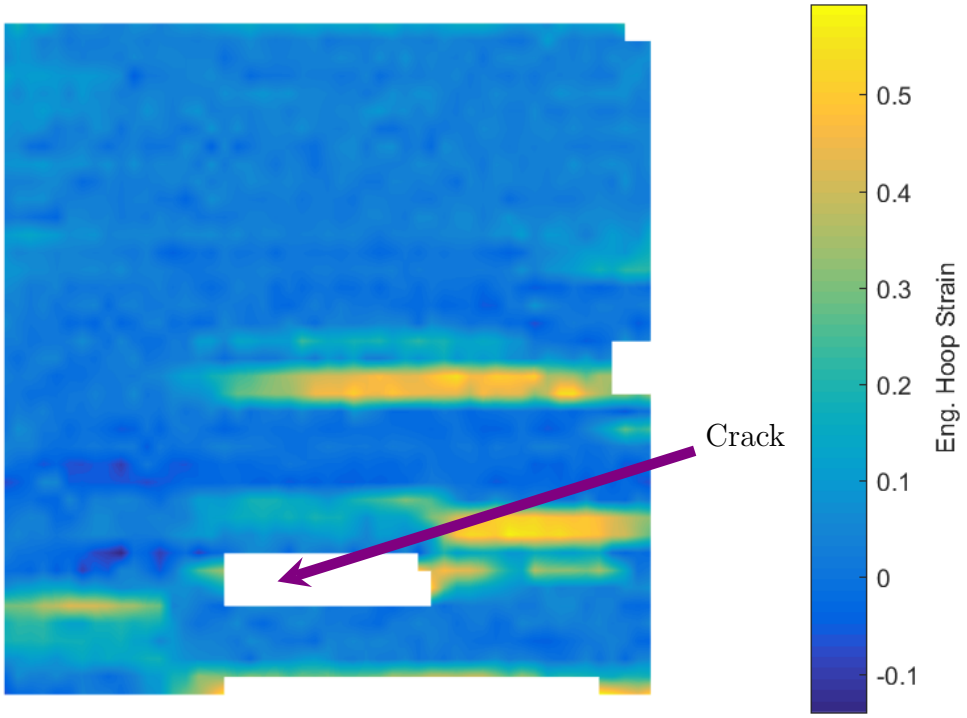

Figure 6.10: Distribution of the circumferential (hoop) strain on the length of the tube. The strains were measured from the change in the dimensions of the square grid that was put on the tube before deformation. The grid has 39 rows along the length of the tube and 50 columns wrapping around the tube. The white blocks are where the grid was damaged and unmeasurable. The crack is shown with a purple arrow.

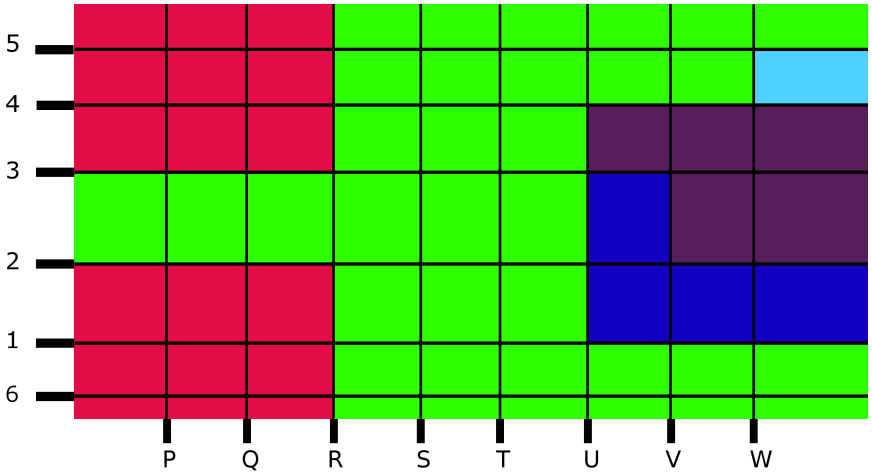

Figure 6.11: This figure shows the grid that was created from the orientations measured with the Laue camera. Each color represents a distinct grain orientation, but the colors are arbitrary. The smaller grains were neglected. This grid was then mapped on the model of the tube, as can be seen in Figure 6.12.

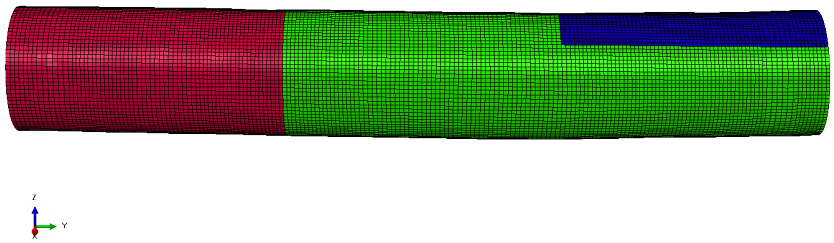

Figure 6.12: This figure shows the grain distribution as implemented in the finite element model. Each color represents one grain orientation and corresponds with the grain orientation grid shown in Figure 6.11. The spatial orientation of the tube is the same as the spatial orientation of the deformed in Figure 6.8.

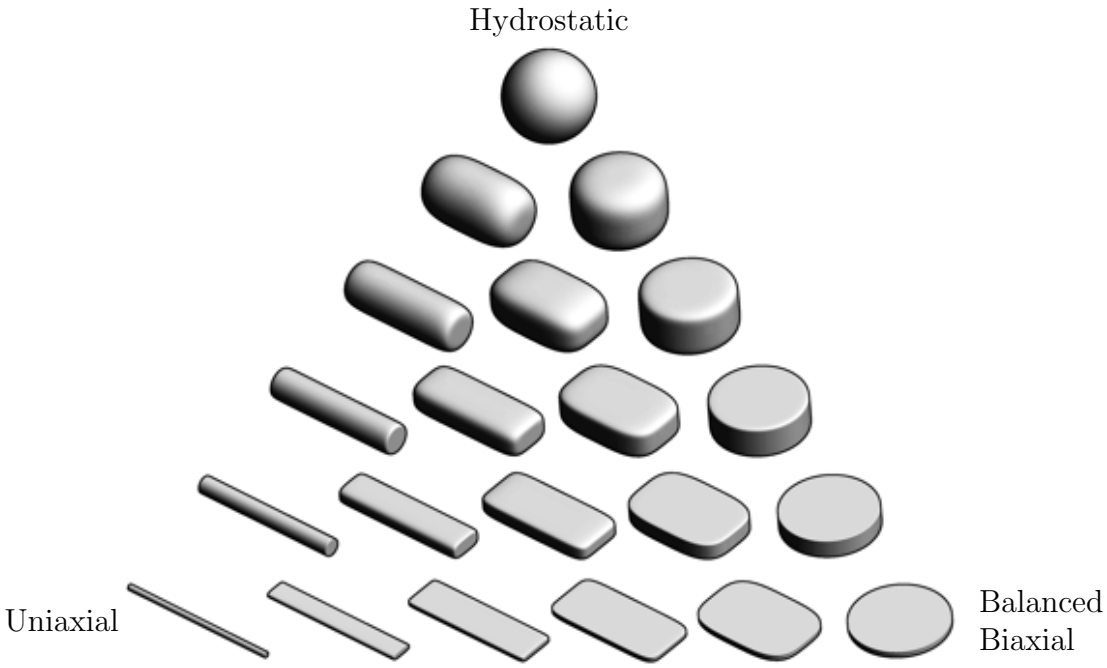

Figure 6.13: This figure shows how tensors can be visualized in 3D space using Superquadric Tensor Glyphs method described in [178]. In this technique, the principal directions (eigenvectors) of a tensor are used to define the orientation of the glyph in 3D space. The principal values (eigenvalues) convey the dimensions of a glyph. Therefore, for plane strain, the glyph has a plate shape; while for a hydrostatic pressure the glyph is a sphere. The glyph representation of uniaxial strain is a bar. Any other strain state will be visualized by a unique glyph between these three extreme shapes. The details of the visualization method are explained in [178].

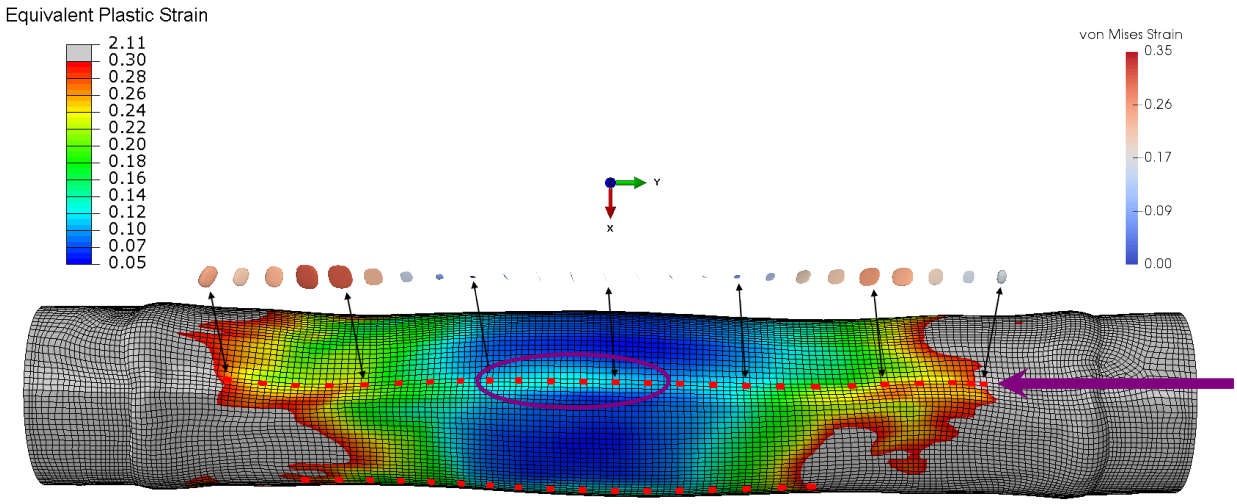

(a) Top view

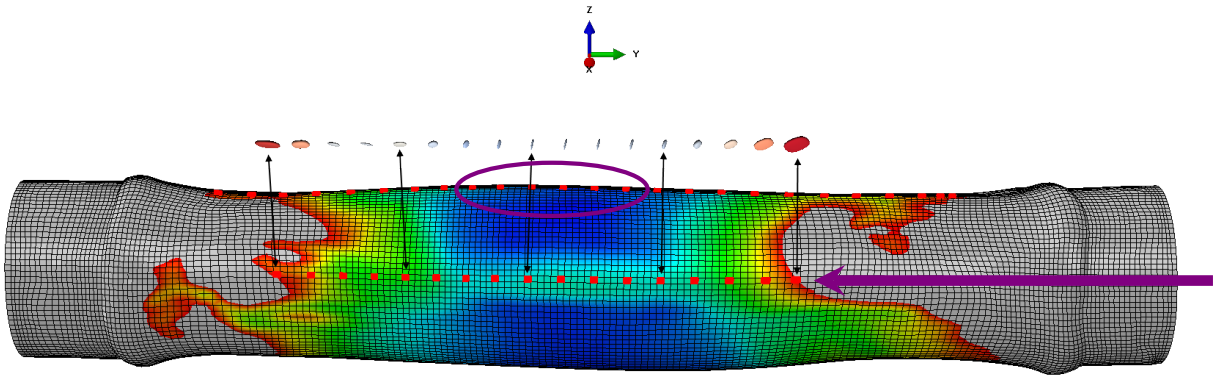

(b) Side view

Figure 6.14: Contours of the equivalent plastic strain of the deformed tube. The glyphs above the tube represent strain tensors extracted from highlighted elements for (a) top view and (b) side view of the tube. The black arrows are guidelines and connect the tensor glyphs to the elements from which they were extracted. The purple ellipses show the location of the crack. The color bar on the left shows the contour of the equivalent plastic strain of the tube. The light blue area along the purple arrow in the center of (a) is where the tube cracked and (b) is another area where the tube bulged significantly. This high strain area is located where a white block is visible along the bottom edge of Figure 6.10. The strain tensor was extracted from the highlighted elements along the purple arrows and visualized as tensor glyphs which are shown above the tube. These glyphs represent the orientation of the stress tensor at the locations indicated by the thin black arrows. The color bar on the right represents the contour of von Mises strain in the glyphs. All the glyphs have a plate shape, but the ones in the center appear as bars due to their orientation. Therefore, highlighted elements in the center experience a different strain state than the highlighted elements on the ends.

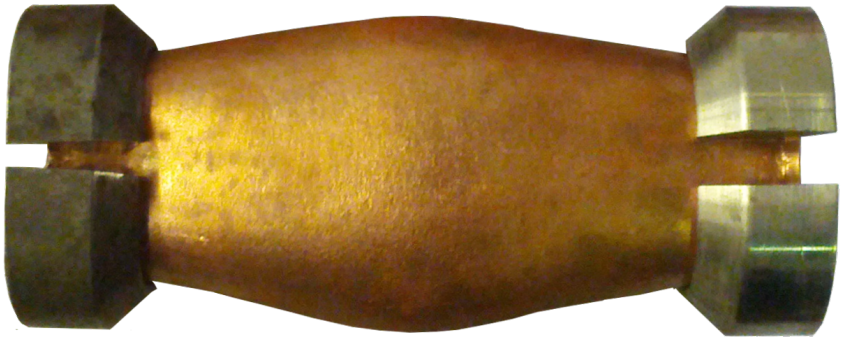

(a)

(b)

Figure 6.15: (a) Shows a hydroformed annealed commercial polycrystal copper tube. Practice copper tubes bulged considerably more than the large grain Nb tube shown in Figure 6.8(b). The collars shown at either end of the tube are a part of the clamp design. (b) The copper tube before deformation.

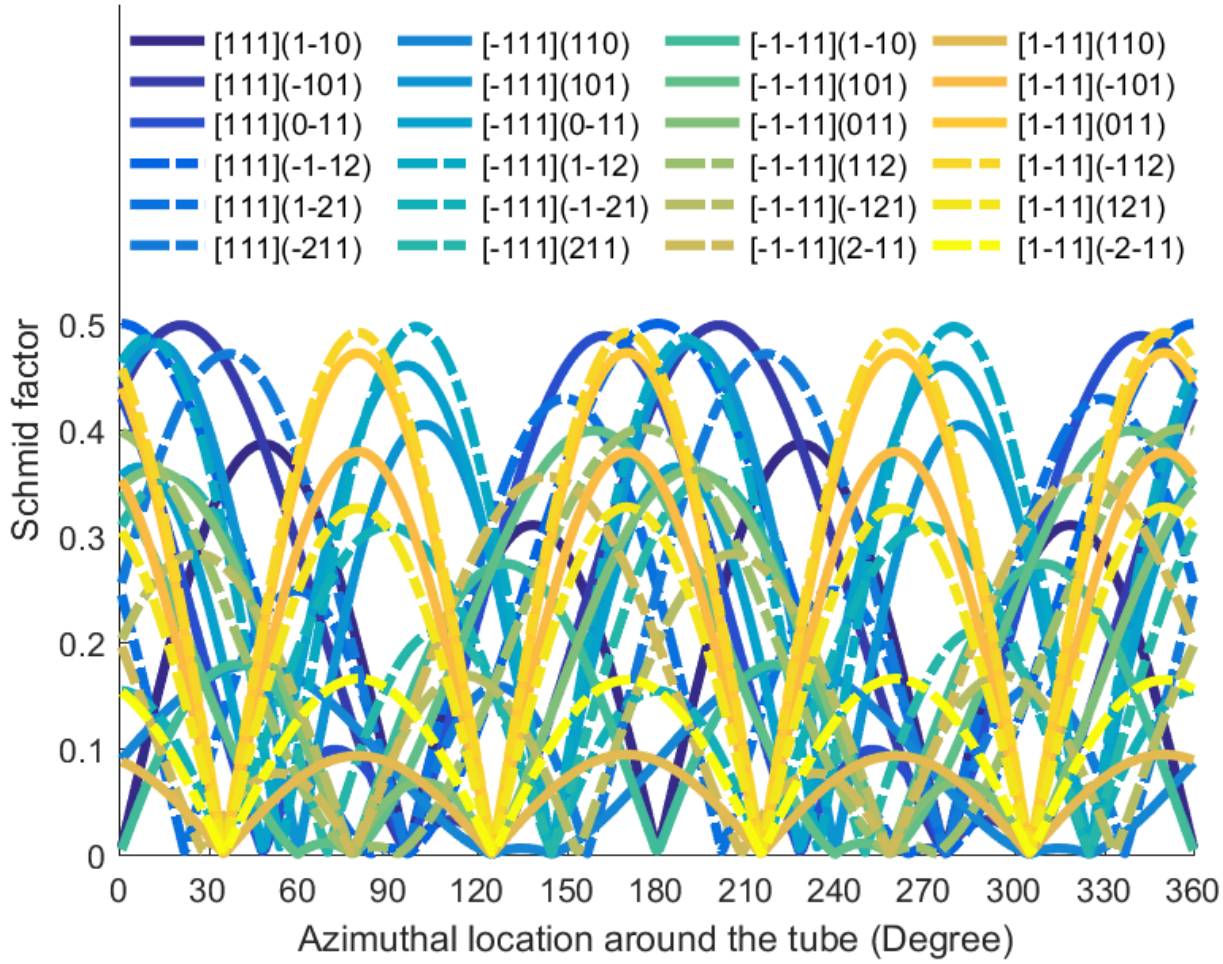

Figure 6.16: Variation of the absolute value of Schmid factor around the tube for slip systems $\langle 111\rangle\{1\bar{1}0\}$ and $\langle 111\rangle\{11\bar{2}\}$.This plot only shows the slip systems of the large single crystal in the middle of the tube.

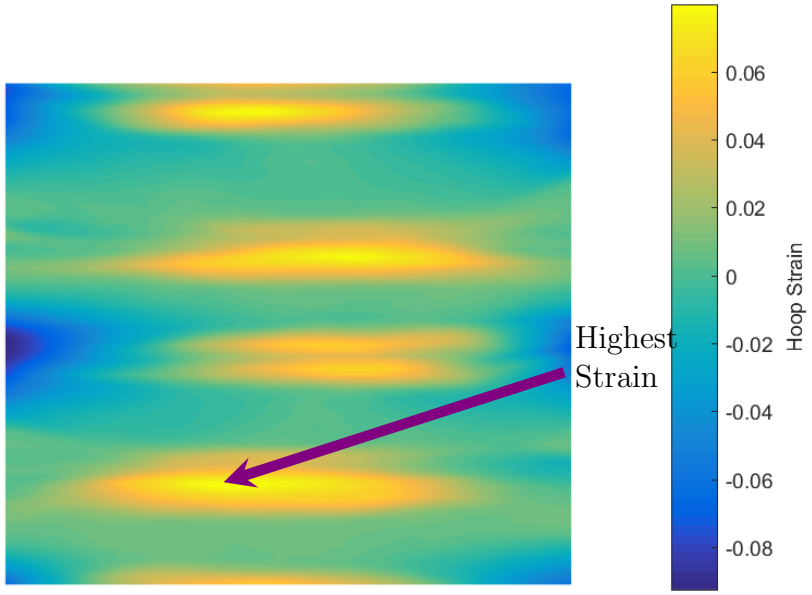

(a)

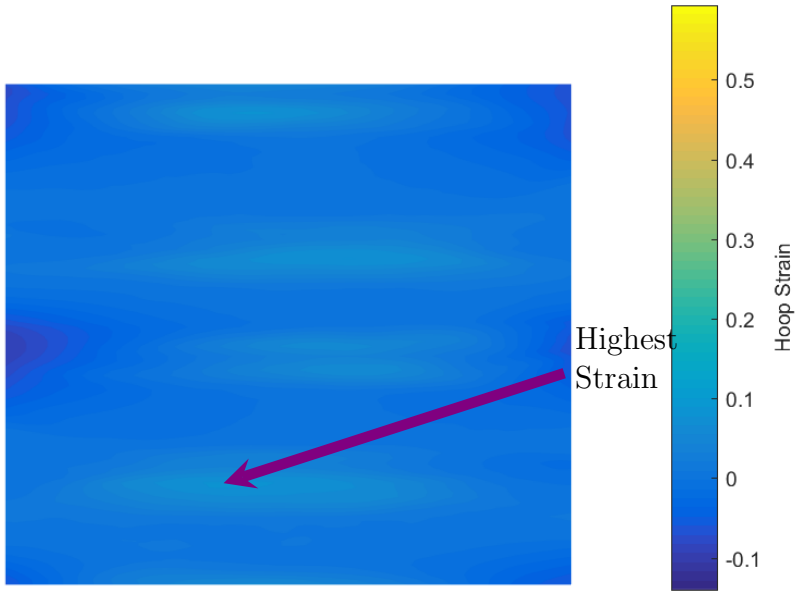

(b)

Figure 6.17: Predicted distribution of the circumferential (hoop) strain along the length of the tube as extracted from the model. This figure is shown with two contour scales. In (a) contour levels are adjusted to make the gradient visible. In (b) the same data is plotted on the same scale as Figure 6.10. The grid has 104 rows along the length of the tube and 54 columns wrapping around the tube. The location with the highest strain is shown with a purple arrow. The contour is qualitatively similar to the experiment in Figure 6.10, although the contour levels are different.

CHAPTER 7

DISCUSSION

This dissertation focuses on improving conventional crystal plasticity model to make it capable of predicting the deformation of single crystals of BCC. To that end, two parts of the crystal plasticity theory were explored: the yield function and the hardening rule. The crystal plasticity models with these improvements were verified for single crystal ferrite micropillars and single crystal Nb tensile dog-bone samples. Finally, the crystal plasticity model that was developed for Nb was used to predict the tube hydroforming of a large grain Nb Tube. The simulation results qualitatively match with the experiment. Each of the above subjects is discussed in more details in the following sections.

7.1 Non-Schmid crystal plasticity modeling of BCC single crystals

Conventional crystal plasticity is based on the associated flow rule of plasticity. This rule states that the increment of plastic strain is in the direction of the outward normal of the yield surface. This flow rule is not correct for some BCC materials, which yield according to the non-Schmid law. In such materials, the flow behavior and yield behavior are defined with separate functions. The non-Schmid model defines yielding by considering the effect of stresses resolved on planes and directions in additions to the ones calculated by the Schmid model. Nonetheless, in the non-Schmid crystal plasticity, deformation is accommodated by dislocation slip which happens on slip planes and along slip directions. Therefore, the outward normal of the non-Schmid yield function will not be parallel to the direction of plastic strain increment. In this case, a flow potential is used to find the direction of this increment. This kind of flow behavior is known as the non-associated flow rule. This method was implemented in the crystal plasticity model, and was compared against the classical crystal plasticity for ferrite and Nb. The results showed that ferrite behaves according to the non-Schmid rule.

The efforts to fit the non-Schmid model to the tensile tests of single crystal Nb was not successful. The Schmid model, however, could predict the deformation of Nb. Nonetheless, this does not necessarily mean that Nb behaves according to the Schmid law. Nb may still show non-Schmid behavior in other stress states like compression. Gröger et al. [106] studied the deformation of molybdenum and tungsten, and observed that in pure shear tungsten follows the Schmid law and molybdenum shows the non-Schmid behavior. In tension and compression, however, both materials show the non-Schmid effect.

All the Nb tensile experiments were performed at room temperature. However, the effect of non-Schmid stresses decrease with the increase of temperature [157, 179]. Christian [179] reported that the tension-compression asymmetry of Nb is very small at room temperature, but it is considerable at 77 K. Therefore, the non-Schmid model needs to be verified for other stress states and temperature ranges before a strong argument could be made for or against the validity of the Schmid model in Nb.

As was explained in §3.1, the core of screw dislocations in BCC materials simultaneously spread on three $\{1\bar{1}0\}$ planes that share a $\langle 111 \rangle$ direction. The non-Schmid model considers the effect of shear and normal stresses that are applied on all three planes, because these stresses can affect the dislocation core. Depending on the orientation of the material with respect to the imposed load, the resolved shear stress on the slip plane and parallel to the slip direction (RSS) needed for yield will change. If the material is orientated so that the non-Schmid stresses contract the dislocation core, the RSS needed for yielding will decrease. This is mathematically modeled by adding the value of non-Schmid stresses to the value of the Schmid RSS. For some other orientations, the combined effect of the non-Schmid stresses can expand the dislocation core and increase the RSS needed for the initiation of yielding. This change in the critical shear stress with the orientation improves the accuracy of the non-Schmid model with respect to the Schmid model.

As was shown in Figures 4.2 through 4.7 the Schmid model that was calibrated simultaneously with micropillars 1 and 4 over estimates the force-displacement of micropillars 2

and 3 and underestimates the behavior of micropillars 5 and 6. The reason is that in the Schmid model the RSS must reach the same critical value (CRSS) for all orientations.

In §4.4.5 the ratio of non-Schmid to Schmid stress (R_{ns}), equation (4.16), was defined. The variation of this ratio with the orientation of the material is shown in Figure 4.8. This ratio can be used to predict if the Schmid model will overestimate or underestimate the behavior of some orientations, based on the orientations that were used for the calibrations.

A CRSS value is found when the Schmid model is calibrated with an orientation with a given R^*_{ns}. For other orientations with $R_{ns} > R^*_{ns}$, the combined contribution of non-Schmid stresses contracts the dislocation core, thus a smaller RSS is needed for this material to deform. Therefore, the Schmid model will overestimate the behavior of this orientation. On the other hand, for orientations with $R_{ns} < R^*_{ns}$, the non-Schmid stresses expand the dislocation core, which means a higher RSS will be needed to initiate the dislocation motion. The previously calibrated Schmid model will underestimate the behavior of these orientations.

The range of values of the ratio of non-Schmid to Schmid stress (R_{ns}) depend on the non-Schmid constants a_1 through a_3 in equation (4.16). These constants are found from the calibration of the non-Schmid model to experiments and vary for different BCC materials. For materials with very small non-Schmid constants, variation of this ratio with the crystal orientation is small. In this case, non-Schmid stresses do not significantly affect the yielding, and a Schmid model can predict the behavior of the material accurately. The larger the non-Schmid constants, the more the predictions of the Schmid model will deviate from the predictions of the non-Schmid model.

7.2 Improving the hardening rule of the conventional crystal plasticity

The hardening model predicts how the flow stress increases during the deformation. This is an essential part of the crystal plasticity model and significantly impacts the predictions of the model beyond initial yielding. Conventional crystal plasticity models often use a Hill-type hardening rule. This study showed that the Hill-type hardening rule cannot accurately

predict the behavior of BCC single crystals such as Nb and ferrite. This model is only correct for early stages of deformation when the hardening rate is low, and fails to predict the deformation of BCC single crystals at higher strains.

The stress-strain curves predicted by the classical Hill-type hardening rule have negative curvatures. Experimentally, though, as the switch from the stage I to stage II of the hardening of single crystal happens, the slope of stress-strain changes considerably. The classical hardening rule, however, has no means to model such a change in the stress-strain curves.

To address the shortcomings of the Hill-type hardening rule for BCC single crystals, two novel hardening rules were developed and verified for Nb and ferrite. These models are discussed in more details below.

7.2.1 The Differential-Exponential (DE) hardening rule

Shear stress - shear strain curves for single crystals that are initially oriented for single slip show three distinct stages usually referred to as Stage I, II and Stage III hardening [43]. Stage I is known as the "easy glide", stage II as "linear hardening", and stage II as "exhaustion hardening".

Most of the deformation in stage I is accommodated by the primary slip system, and hardening is chiefly due to self-hardening. The low hardening rate in stage I corresponds to a large dislocation mean free path and few barriers. Stage II starts when other slip systems become activated due to crystal rotation during deformation and they interact with the primary slip system. This reduces the mean free path of dislocations and considerably increases the hardening rate. During this stage, the dislocation density increases significantly [43].

The classical Hill-type hardening rule can model the hardening rate at stage I but not the stage II and III, because different underlying mechanisms control each hardening stage. Nonetheless, the classical hardening rule only considers some of the underlying mechanism of deformation. This model accounts for self and latent-hardening, but the rate of hardening

it predicts cannot change significantly. Therefore, the classical hardening model can only predict the behavior of the materials that show a monotonic increase in the flow stress.

The classical hardening rule does not change as the hardening mechanisms change. To capture the variable hardening rate of a single crystal, the Differential-Exponential (DE) hardening rule, equation (4.15), was proposed in §4.3.1. This hardening rule models each stage of hardening with a separate hardening rate equation.

A single crystal oriented for single slip typically hardens with a small slope in the first stage. Therefore, in the DE hardening model, stage I is modeled with the Hill-type hardening rate, equation (2.24). In the second stage, the density of mobile dislocations decreases exponentially [159], which results in an exponential increase in the hardening rate of the material. Therefore, in the DE hardening rule, an exponential equation is used to model the rate of hardening of stage II.

Since the DE hardening model has two hardening rate equations, some criteria are needed for the model to switch between the hardening rate equations. Stage II of the hardening of single crystals occurs when secondary slip systems become active. The reason for the activation of secondary slip systems is the eventual rotation of the primary slip system away from the loading direction, caused by the evolution of texture induced by increased plastic deformation. Thus, the criteria for the start of the second stage hardening was defined as a function of the ratio of the accumulated shear strain and critical resolved shear stresses in primary and secondary slip systems. This model successfully predicted the deformation of ferrite single crystals.

The Hill-type hardening rate equation, equation (2.24), has only two adjustable parameters. However, the DE hardening model in equation (4.15) has three extra material constants, that can be calibrated with an experimental force-displacement curve.

The compression response of DP980 ferrite micropillars was simulated with the non-Schmid crystal plasticity model using the Differential-Exponential (DE) hardening rule. Predictions of the DE hardening model are in good agreement with the force-displacement

curves of the experiments. This confirms the validity of the DE hardening model, and as a result, the corresponding criteria that were used to define the initiation of the stage II hardening.

7.2.2 The Dynamic hardening rule

As illustrated in Figures 5.2(a) through 5.10(a), the Schmid-type crystal plasticity model with the classical hardening rule cannot adequately predict the deformation behavior of Nb single crystals. The Dynamic hardening rule was developed as another way to improve the Hill hardening rule [100–102]. The Dynamic hardening rule reduces the rate of hardening predicted by the Hill-type hardening model for single slip deformation and increases the hardening rate as other slip systems activate.

At the beginning of deformation of an annealed single crystal, mobile dislocations in the bulk can travel a long distance before interacting other dislocations. Furthermore, some dislocation can escape from the surface without encountering many obstacles. Thus, there is little accumulation of dislocations at the beginning of the deformation. The classical Hill-type hardening model overestimates the hardening behavior of single crystals at the beginning of the deformation, because it assumes hardening on all slip systems throughout the deformation.

As the strain increases, the hardening rate increases due to the activation of secondary slip systems which then interact with the primary slip systems. This interaction results in dislocation multiplication mechanisms that cause hardening.

The classical hardening model, equations (5.1), does not have an accumulated strain term and predicts the hardening rate of a slip system α based on the summation of the instantaneous shear rate ($\dot{\gamma}^{\beta}$) of every slip system. This model indirectly considers the effect of total strain on a slip system in calculation of the hardening rate, through the term $\frac{\tau_c^{\beta}}{\tau_s}$. This is the ratio of current critical shear stress (yield stress) of slip system β to a saturation shear stress (the maximum allowed value). In addition to this ratio, the Dynamic hardening

model, equations (5.2), also uses the strain the ratio $\left(\frac{\gamma^{2nd}}{\gamma^{1st}}\right)^{\eta}$ in modeling hardening rate. This ratio contains the history of deformation and increases the rate of hardening with the activity of secondary slip systems. The Dynamic hardening model has two parameters more than the classical hardening model, which provides more control over the rate of hardening. One of these parameters is a weight factor, w, that reflects the initial dislocation density and controls the deviation from the classical hardening rule. The other parameter is the exponent, η, which controls the hardening rate.

As seen in Figures 5.2(a) through 5.10(a), the Schmid-type crystal plasticity with the Dynamic hardening model adequately predicts the deformation behavior of single crystal Nb. After about 25% strain the curvature of some of the stress-strain curve becomes positive; but neither the Dynamic nor classical hardening models can predict a positive curvature.

The Dynamic hardening model is a generalization of the Hill-type hardening rule. Therefore, some of the issues of this model are inevitably inherited by the Dynamic hardening model. The existence of the term $\frac{\tau_c}{\tau_s}^{\beta}$ forces the hardening rate to saturate and the stress-strain curve to eventually plateau. Nonetheless, the Dynamic hardening model considerably increases the overall accuracy of the classical hardening for single crystal Nb.

The texture evolution predicted by the Dynamic hardening model qualitatively matches with experiments. Although the tensile samples are single crystals, their orientation slightly varies from one side to the other. In addition, the initial dislocation density might vary slightly from one sample to another. The model, though, considers only one orientation throughout each sample and assumes an identical initial state for all samples. This difference in the orientation between the experiment and simulation can affect the predictions of the texture evolution, as well as the predictions of the stress-strain curves.

The current model is based on the Schmid law for activation of a slip system. As was discussed earlier the deformation behavior of some BCC materials may be more accurately modeled with the non-Schmid crystal plasticity model. The non-Schmid model that was developed in Chapter 4, was used to predict the deformation behavior of Nb. The results,

that are not presented here, showed that the behavior of the Nb in tension is closer to the Schmid-type behavior. However, one needs to test the Nb in other stress states including compression and shear before concluding that it behaves according to the Schmid law.

At room temperature, the non-Schmid effect in Nb is small [179]. This means that the core of screw dislocations are only weakly affected by stresses other than the resolved shear stress on the slip plane and parallel to the slip direction. Christian [179] studied the deformation of single crystals of Nb and found that the orientations near the [101] − [111] edge of the inverse pole figure show a small tension-compression asymmetry at room temperature. The orientations near the center of the inverse pole figure, however, did not show any asymmetry at room temperature. As the temperature decreases the non-Schmid effect become more evident [156, 157, 179]. Therefore, the Schmid-type crystal plasticity model, that was developed in Chapter 5, could accurately predict the behavior of Nb single crystals at room temperature, where the non-Schmid effect is negligible.

The Schmid-type crystal plasticity with the Dynamic hardening rule that was verified for the single crystal tensile dog-bones of Nb was used to predict the deformation behavior of a large grain Nb tube. The next section discusses the results of the latter study in more detail.

7.3 Tube hydroforming of a large grain Nb tube

Grain boundaries and the weld line are sources of defects in the crystal and can affect the superconductive performance of a particle accelerator cavity. Therefore, the performance of cavities could potentially increase, if they could be made by hydroforming of a seamless large grain tube.

A large grain tube was made from rolling, welding and heat treatment of a fine grain Nb sheet. The Laue camera measurements showed that the heat treatment successfully recrystallized the prior microstructure to large grains. The recrystallization also consumed the prior weld line and made the tube seamless. Although the current process can be used

to create large grain sheets, more research is needed to find ways to control the resulting microstructure. As will be discussed later, due to the spatial orientation of the large grains around the tube, preferential thinning and premature failure can occur. Therefore, finding orientations that are less susceptible to localized-thinning is of interest.

While pure niobium is exceptionally ductile, the large grain tube burst with a much smaller bulge than was formed in practice copper tubes. The large grain structure of the tube is one of the reasons for the early failure. Due to the spatial orientation of the large grains with respect to the axis of the tube, the Schmid factor is maximum at a few azimuthal locations around the tube. Figure 6.16 shows the variation of the Schmid factor around the tube. This variation is likely the reason behind the highly localized deformation and early failure of the tube during the hydroforming experiment. Other researchers [123, 125] have performed tube hydroforming on fine grain Nb sheets, and have successfully made cavities. The randomly oriented fine grains reduce the strong anisotropy of Nb. Thus, fine grain sheets can be uniformly hydroformed with less difficulty than large grain ones.

As can be seen in Figure 6.10, the circumferential (hoop) strain in the tube is very inhomogeneous. Locations immediately around the crack show a relatively small localized hoop strain. Therefore, another reason for the failure of the tube in the center of a large grain could be the arrangement of the grain orientations and boundaries, and the distribution of the strain in the vicinity of a boundary dividing soft and hard orientations. Based on the contour levels around the crack, it developed in a soft region adjacent to harder regions.

As can be seen in Figure 6.14, the predicted deformed geometry of the tube matches qualitatively with the experiment. Moreover, the location of the light blue contour in this figure, which is another area that shows large circumferential strain, matches with the white block at the bottom of Figure 6.10. Therefore, the Dynamic hardening crystal plasticity model can effectively predict the location of significant circumferential deformation and the potential location of the crack.

The crystal plasticity model with the Dynamic hardening rule that was developed in

Chapter 5 gives satisfactory predictions of the deformation of the large grain Nb tube, even with a highly-simplified representation of the grain shapes. One can use this model to find an optimum grain orientation for forming a large grain tube. This information can be used as a guide to identify desirable orientation as an experimental goal.

CHAPTER 8

CONCLUSION AND FUTURE WORK

8.1 Conclusions

The classical crystal plasticity model cannot accurately predict the deformation of single crystal BCC materials like ferrite and niobium. One method to improve the accuracy of such models is to use the non-Schmid law. This type of crystal plasticity, in addition to resolved shear stresses on the slip plane and parallel to the slip direction, considers the effect of resolved stresses on other planes and directions in predicting the yielding of materials. Since more than one stress is used to calculate the yield criterion of non-Schmid crystal plasticity, the yield behavior predicted by this model is different from the Schmid model. The non-Schmid crystal plasticity model that was developed in this study successfully predicted the deformation of ferrite micropillars, while the predictions of the Schmid model for this material were less accurate.

The rate of hardening predicted by the Hill-type hardening rule, does not match with the hardening rate of ferrite and niobium single crystals. Another way to increase the accuracy of the classical crystal plasticity is to adjust the hardening rule. In this study two novel hardening models were developed and verified for BCC materials. These two are the Differential-Exponential hardening rule and the Dynamic hardening rule .

The Differential-Exponential hardening rule uses two different equations to define the hardening rate of "easy glide" and "linear hardening" parts of the stress-strain curve for ferrite micropillars. A criterion is used to distinguish the onset of stage II of the deformation. This model accurately predicts the yielding behavior and the change in the hardening rate of ferrite, which confirms the validity of the model and the criteria used for distinguishing the onset of stage II hardening.

The Hill-type hardening rule overestimates the hardening rate of niobium. The Dynamic

hardening rule reduces the hardening rate at early stages of the deformation, and increases the hardening rate once multiple slip systems become activated. This hardening rule accurately predicts the deformation of single crystal niobium.

A large grain niobium tube was hydroformed until it cracked. The deformation of the tube was modeled with the Dynamic hardening crystal plasticity that was previously calibrated with the tensile test of niobium single crystals. The predictions of the model qualitatively matched with the experiments, which confirms the potential of this crystal plasticity model as a useful tool in developing a large grain superconducting Nb cavity.

The models developed in this study can be used to predict the deformation behavior of BCC materials. Some BCC materials like ferrite show a non-Schmid behavior. Deformation of some other BCC materials like niobium is better explained with the Schmid law. In either case the rate of hardening predicted by the Hill-type hardening rule is usually unsatisfactory. The hardening models proposed in this study significantly increase the accuracy of the Schmid and non-Schmid crystal plasticity models.

8.2 Recommendations for future work

Although Nb is a BCC material, the efforts to model the its behavior with the non-Schmid crystal plasticity model was not successful. The experimental data used for the calibrations was only from tensile experiments. Nb may show non-Schmid behavior under other stress states, like compression or pure shear. Moreover, Christian [179] showed that at room temperature the non-Schmid effect in Nb is very small. The non-Schmid behavior becomes more pronounced as the temperature decreases [179]. Therefore, the deformation behavior of Nb under other stress states and at lower temperatures needs to be investigated, to be able to make a strong argument about the validity of non-Schmid behavior in Nb.

The Differential-Exponential hardening model that was developed in Chapter 4 was only verified for ferrite micropillars. Some of the Nb tensile tests that were studied in this research show the stage II hardening. Future research should focus on verifying the Differential-

Exponential hardening model for Nb.

The tube hydroforming of seamless large grain Nb tube needs to be further investigated. Only one large grain tube was created for this study. Therefore, only one tube hydroforming experiment was performed. Future hydroforming experiment could benefit from the experience gained from the experiment that was performed in this study. For instance, the loading paths of future tests can be adjusted to capture a larger bulge.

The Dynamic hardening model was verified with the only available tube hydrofroming experiment. The model should be verified with multiple hydroforming experiments to make sure it can consistently predict the area of failure. Hydroforming and modeling more Nb tubes can help improve the model and advance the understanding of deformation of large grain structures.

The current mapping of the grain boundary on the tube is an approximation. Implementing a more realistic grain map on the tube may increase the accuracy of the simulation.

APPENDICES

APPENDIX A

EINSTEIN NOTATION

Einstein notation, also known as index notation or indicial notation, is briefly reviewed here. Familiarity of the reader with this subject is essential, because many of the equations presented in this dissertation are written with this notation. This is a notation convention that is often used in continuum mechanics to deal with mathematics and especially linear algebra. Using this notation increases the brevity of the equations.

According to this convention, a summation is implied when an index is repeated (only) twice in a single term. For example:

$$Y = \sum_{i=1}^{n} c_i x_i \tag{A.1}$$

Under the Einstein notation the summation sign is removed and the above can be written as:

$$Y = c_i x_i \tag{A.2}$$

which means (for a known range of i, for instance $i = 1 \dots n$):

$$Y = c_1 x_1 + c_2 x_2 + c_3 x_3 + \cdots + c_n x_n \tag{A.3}$$

Here no distinction is made between a subscript and a superscript, however, they can be of significance in other contexts.

Next, some of the most common operations in linear algebra are presented in the index notation.

Dot product

The dot product of two vectors u and v produces a scalar.

$$u \cdot v = u_i v_i \tag{A.4}$$

Double dot products of matrices

This product operates on matrices and reduces the order of the product matrix by two. Therefore, if double dot product operates on two second-order matrices, it produces a scalar. This product is denoted with ":" and for matrices A_{ij} and B_{ij} is defined as below:

$$c = A : B = A_{ij}B_{ij} \tag{A.5}$$

Cross product of vectors

Cross product of two vectors u and v produces a vector. In Einstein notation the cross product is defined as:

$$u \times v = u_j v_k \epsilon_{ijk} e_i \tag{A.6}$$

where e_i is the basis and ϵ_{ijk} is the Levi-Civita symbol. In three dimensions, ϵ_{ijk} is 0 if any of (i, j, k) is repeated, it is 1 if (i, j, k) is an even permutation of $(1, 2, 3)$ like $(3, 1, 2)$ and if it is an odd permutation like $(3, 2, 1)$ then the value is -1.

Outer product of vectors

This is a product of two vectors which is denoted by $\otimes$ and results in a matrix. For two vectors u and v this product can be defined is as follows:

$$C_{ij} = u \otimes v = uv^T = u_i v_j \tag{A.7}$$

Matrix multiplication

Matrix product of matrices A_{ij} and B_{jk} in index notation is shown as below:

$$C_{ik} = AB = A_{ij}B_{jk} \tag{A.8}$$

Trace of a matrix A_{ij}

Trace of a of a matrix A_{ij} in index notation is defined as follows:

$$Trace(A) = A_{ii} \tag{A.9}$$

APPENDIX B

CRYSTAL PLASTICITY FINITE ELEMENT MODEL CALIBRATION METHOD

This appendix explains the method that was used in Chapter 4 to fit the Schmid and non-Schmid crystal plasticity models to the force-displacement curves of ferrite micropillar compression experiments. A similar approach was taken in Chapter 5 to fit the Schmid-type crystal plasticity model to the stress-strain curves of tensile tests of Nb single crystals. The fitting of a model to the experimental data is called model calibration and is the process through which the unknown parameters of the model are found.

To start, microscale experiments were conducted where the Focused Ion Beam (FIB) was used to carve out single crystal ferrite micropillars with different initial orientations from the ferrite phase of a three-phase quenched and partitioned QP980 commercial steel sheet. These micropillars were uniaxially compressed with a flat punch nanoindenter to determine their force-displacement response. It was found that beyond a certain displacement, micropillars were no longer deforming under uniaxial compression, rather they were experiencing a three-dimensional deformation. This was an important observation since it became obvious that the micropillar compression test has to be modeled with three-dimensional geometry and boundary conditions.

Given there were 6 micropillar compression force-displacement experiments for QP980 ferrite with distinct initial orientations, the first question to answer was how many forces-displacement curves would be sufficient to accurately calibrate the Crystal Plasticity Finite Element (CPFE) model for the ferrite phase. In this section, the results from the non-Schmid CPFE model calibrated with different number of force-displacement curves are qualitatively and quantitatively compared. The approach taken is based on first calibrating parameters of the CPFE model using a set number of force-displacement curves (e.g., 1, 2, 3), then using the calibrated model to predict the force-displacement curves for remaining orien-

tations. A quantitative measure of the quality of calibrations was determined based on the normalized root-mean-square error (NRMSE) between the experimental and predicted force-displacement data.

B.1 Calibrating the non-Schmid CPFE model with LS-OPT®

The calibration of crystal plasticity models presented in dissertation was done using commercial design optimization and probabilistic analysis software LS-OPT®. This is a standalone package developed as a part of LS-Dyna® family which can interface with many other packages and user-defined codes.

The calibration was defined as an optimization problem to minimize the normalized mean-square error (NMSE) between the values of force measured in the micropillar compression experiments and those predicted by the CPFE model at specific displacements. The below equation shows the objective function as implemented in LS-OPT® [180].

$$e = \frac{1}{N}\sum_{n=1}^{N}\left[\frac{f_n(u,x) - g_n(x)}{\max|g_n(x)|}\right]^2 \tag{B.1}$$

In this equation, N is the number of experimental measurements, $g_n(x)$ (where $n = 1 \dots N$) is the value of each measurement, $f_n(u,x)$ is the corresponding predicted value and u is the vector of design parameters (in this case material parameters). $g_n(x)$ is independent of this vector. x is an independent state variable and depending on the problem can represent time, strain, or any other type of response. In this study x, represents the displacement. The mean-square error is then normalized by $\max|g_n(x)|$ which is the maximum of the absolute value of $g_n(x)$. The result e is a dimensionless scalar of order unity.

LS-OPT®was used to loop through the iterative process of running simulations, extracting the force-displacement, finding the mean-square error and refining input parameters. To do so a user-defined script was developed to run the simulations and extract the force-displacement data. In each iteration, depending on the size of the problem (number of parameters to optimize), a number of designs were evaluated. LS-OPT®then compared the NMSE for all designs within the iteration, chose the best design, made a new set of designs

for the next iteration and started the simulations over. The termination criteria were either reaching a maximum number of iterations or when the difference between the two consecutive designs was less than a tolerance and the change in the two consecutive objective functions was less than another tolerance [180].

The NMSE gives the square of error. The metric used in Chapter 4 to quantify the quality of calibrations is the signed normalized root-mean-square error (S-NRMSE) which is defined by the following equation.

$$e_s = \text{sgn}\left(\frac{1}{N}\sum_{n=1}^{N}\left[f_n(u,x) - g_n(x)\right]\right)\sqrt{\frac{1}{N}\sum_{n=1}^{N}\left[\frac{f_n(u,x) - g_n(x)}{\max|g_n(x)|}\right]^2} \times 100 \tag{B.2}$$

The term in the sign function is the average error between the model prediction and the experiment. A positive value means the model overestimates the force, while a negative value implies the model underestimates the force. The term inside the square root is the NMSE as defined by equation (B.1). Taking the square root and multiplying it by 100 gives the percentage error for each prediction and makes the results easier to understand. When the signs are neglected, results of equations (B.1) and (B.2) are consistent

In calibrations presented in Chapter 5, however, the absolute value of equation B.2 is used. This absolute value is referred to as normalized root-mean-square error (NRMSE) throughout Chapter 5.

B.2 Comparing model calibrations with different sets of experimental data

In the non-Schmid model, there are seven material parameters (τ_S, τ_0, h_0, η, a_1, a_2 and a_3) that can be fitted. In this study, $h_0 = 10$ and $\eta = 3$ were kept constants and the remaining five parameters were found from the calibrations.

At first, the non-Schmid CPFE model was calibrated with only one micropillar at a time. The material parameters for each individual calibration are shown in Table B.1. Table B.2 shows the matrix of S-NRMSE values calculated based on this calibration. For example, the value of 37.68 appearing at the intersection of row 3 and column 1 implies that there

was a 37.68% error when the CPFE model calibrated with micropillar 1 was used to predict the force-displacement of micropillar 3. The positive sign of S-NRMSE implies that the predicted force-displacement curve overestimated the experimental curve (see Figure B.2).

Figure B.1 shows the non-Schmid model calibrated to QP980 ferrite micropillar 1. Although the model closely predicts the behavior of micropillar 1, Table B.2 shows that its prediction for micropillars 3, 5 and 6 are inaccurate. Figure B.2 shows the predictions of the non-Schmid CPFE model for QP980 ferrite micropillars 3 and 4 when the model is calibrated with micropillar 1. As can be seen in Table B.2, the same model has the largest S-NRMSE for micropillar 3 (i.e., 37.68%), and the second smallest S-NRMSE for micropillar 4 (i.e., 8.36%).

The last row of Table B.2 shows the sum of absolute error (SAE) for each calibration. This sum was used as a criterion to compare the quality of calibrations. According to Table B.2, calibration of the non-Schmid CPFE model using micropillar 4 results in the best total performance, since it has the smallest SAE of 26.95. While using only one micropillar to calibrate the CPFE model might seem ideal, according to Table B.2, only 1 out of 6 calibrations resulted in the accurate prediction of other force-displacement curves, which is statistically insignificant.

Given the low rate of success when using just one micropillar, it was decided to calibrate the non-Schmid CPFE model with two and three micropillars. Table B.3 shows the material parameters found for a select number of calibrations using combinations of 2 and 3 micropillar force-displacement curves. Table B.4 shows the matrix of S-NRMSE values when the calibrated non-Schmid CPFE model was used to predict the force-displacement curves of the remaining micropillars. By inspecting Table B.4, it is apparent that calibrations with 2 and 3 micropillars consistently produce small errors, with the smallest error being for micropillar 2, and the largest error being for micropillar 5. Figure B.3 shows the result of the non-Schmid CPFE model simultaneously calibrated to QP980 ferrite micropillar 1 and 4. Figure B.4 shows the force-displacement predictions of the same calibrated non-Schmid

CPFE model for micropillars 2 (best) and 5 (worse).

Figure B.5 shows the calibration of the non-Schmid CPFE model with several distinct pairs. These figures show how closely each calibration matches with the experiments and present the best and worst predictions of each calibration.

Figure B.6 shows the calibration with micropillars 1, 4 and 5, and. Figure B.7 shows the predictions of the same model for micropillars 2 and 3, which show very good agreement with the experiment. Finally, according to Table B.4, calibration to micropillars 1, 3 and 5 produced results similar to calibration with 1, 4 and 5, with a slightly smaller sum of absolute error.

The total sum of absolute error in calibrating the non-Schmid model with only one micropillar varies between 27% and 114% (Table B.2). The accuracy of the calibration highly depends on the orientation of the material used for the calibration. On the other hand, using two micropillars for calibration of the CPFE model produces maximum total error of about 28%, regardless of which pair is used for calibration (Table B.4). Adding a third micropillar to the calibration only negligibly improves the results (Table B.4).

The same process was repeated for the Schmid modeling of QP980 ferrite micropillars. Tables B.5 and B.7 show the calibrated material parameters. According to Table B.6, the total prediction error when the Schmid model was calibrated with only one micropillar ranged from 58.4% to 109.29%. Table B.8 shows that the range of the sum of absolute error for calibrating with pairs of micropillars was improved 60.62% to 79.54%, and for sets of three micropillars, the errors were 63.46% and 67.17%. It can be concluded that the accuracy of the Schmid model calibrated with sets of three micropillars did not improve as much as it did for the non-Schmid model.

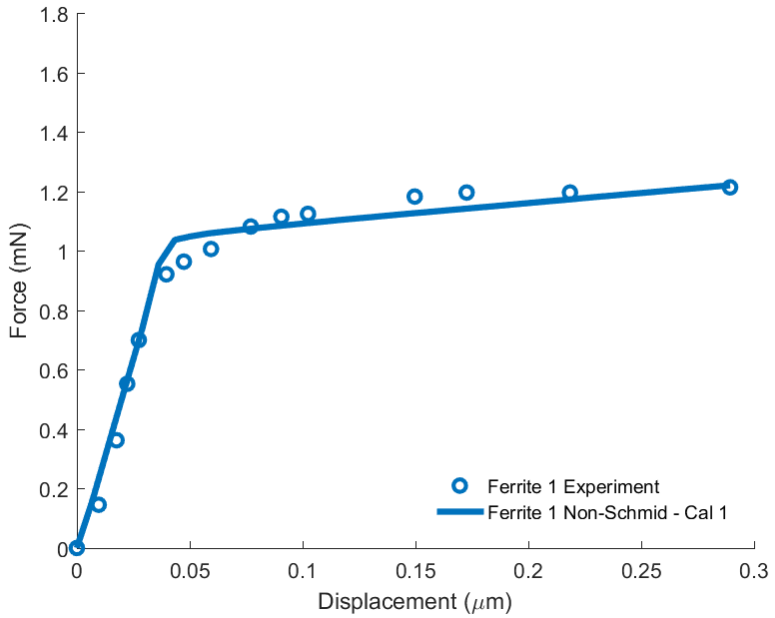

Figure B.1: Calibrating the non-Schmid model with QP980 ferrite micropillar 1. The circles show the force-displacement values measured in the micropillar compression test. The line shows the fitting of the model to the experiment.

Table B.1: Material parameters found for the non-Schmid modeling of QP980 ferrite micropillar when the model was calibrated with one micropillar. In these calibrations $h_0 = 10$ and $\eta = 3$.

Material Parameters	Calibration of the non-Schmid model to micropillar					
	1	2	3	4	5	6
τ_s	562	716	1000	945	814	886
τ_0	224	261	204	294	395	383
a_1	0.1931	0.4109	0.8736	0.1343	0.5092	0.0821
a_2	0.0062	0.5261	0.3319	0.9585	0.7091	0.4543
a_3	0.2432	0.4841	0.4157	0.0718	0.1441	0.9938

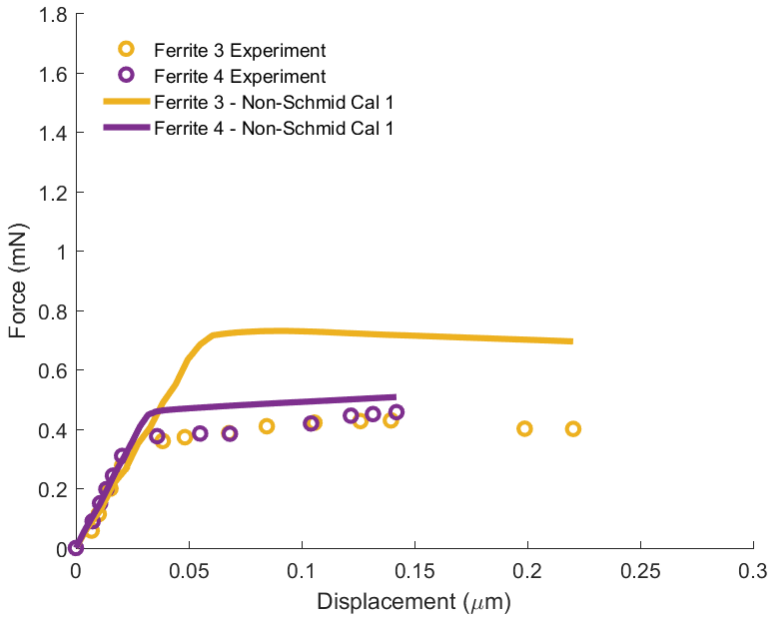

Figure B.2: The best and worst predictions of the non-Schmid model calibrated with QP980 micropillar 1. The circles show the force-displacement values measured in the experiments. The yellow and purple lines show the predictions of the model for deformation micropillar 3 and 4, respectively.

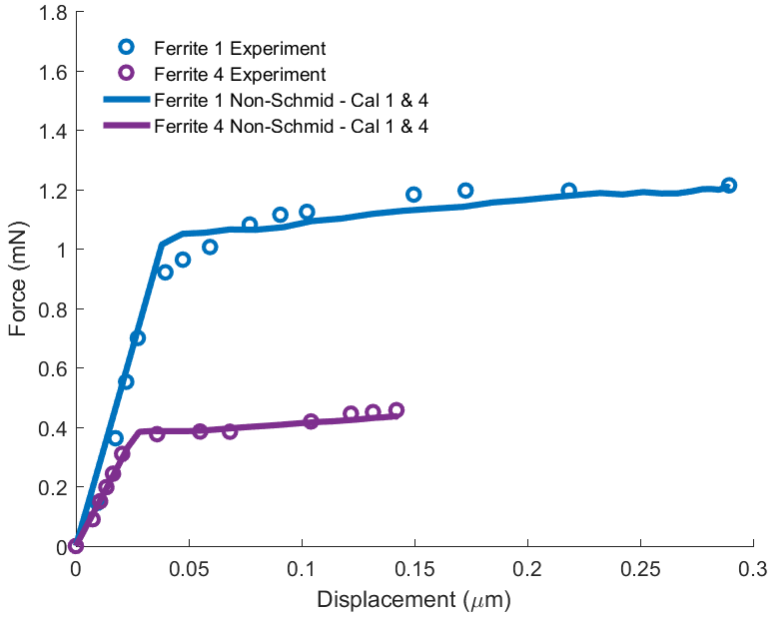

Figure B.3: Calibration of the non-Schmid model simultaneously to micropillars 1 and 4. The circles show the force-displacement values measured in the experiments, and the solid lines represent the fitting of the models.

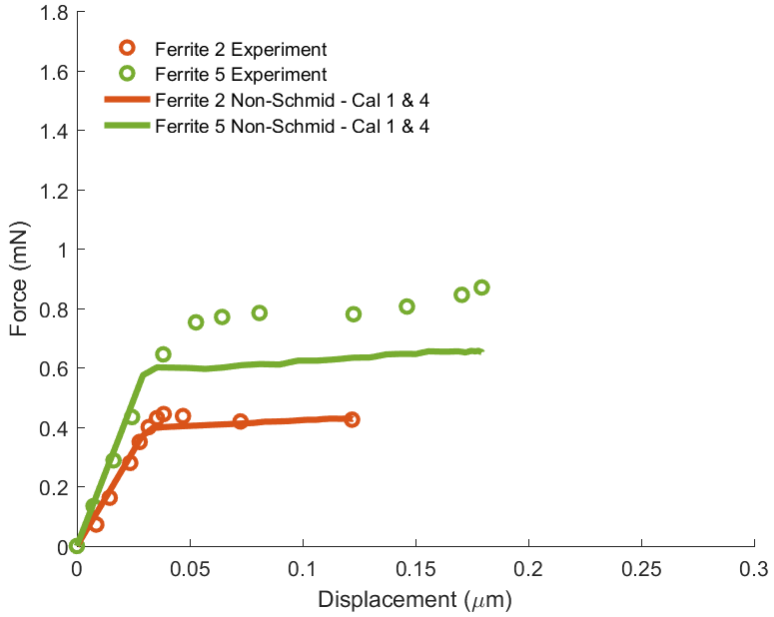

Figure B.4: The best and worst predictions of the non-Schmid model calibrated with micropillars 1 and 4. The circles show the experimental measurements, and the solid lines show the force-displacement predictions of the model.

Table B.2: S-NRMSE for non-Schmid model calibrated to a single micropillar experiment at a time. A negative number represents the underestimation and a positive number indicates the overestimation of experimental data.

Predicting Micropillar	S-NRMSE for calibration of the non-Schmid model to micropillar (%)					
	1	2	3	4	5	6
1	2.97	-4.85	-19.88	4.09	12.19	14.63
2	8.50	3.02	-16.84	-4.13	8.79	18.09
3	37.68	15.29	-2.57	4.43	23.82	44.73
4	8.36	2.43	-17.13	-2.07	10.95	27.59
5	-16.51	-18.43	-29.40	-9.62	2.93	-6.85
6	-13.31	-14.48	-27.68	-2.61	8.00	2.10
Sum of absolute error	87.33	58.50	113.49	26.95	66.68	114.00

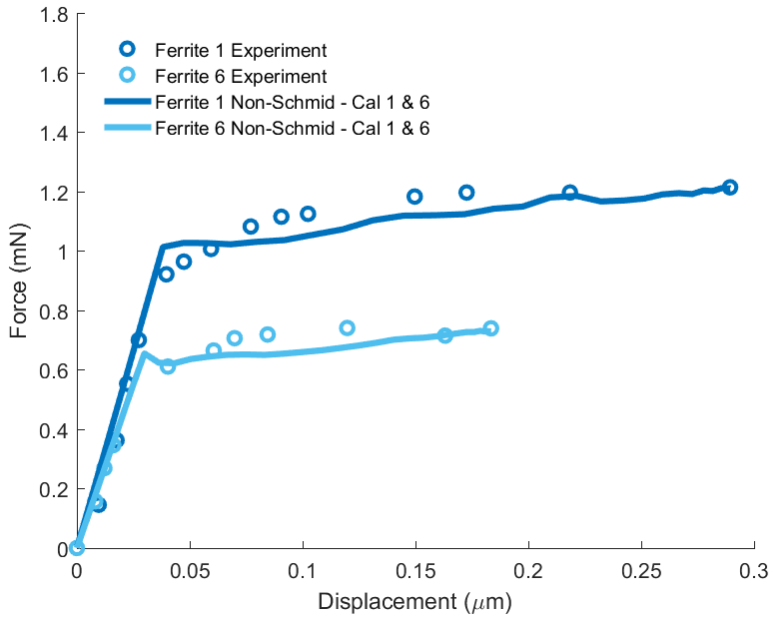

(a)

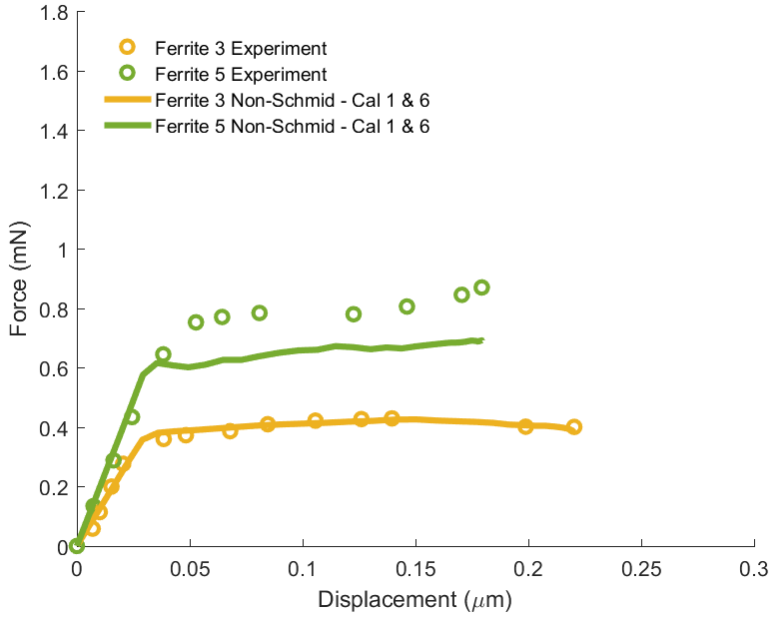

(b)

Figure B.5: a) The non-Schmid model simultaneously calibrated to micropillars 1 and 6, b) the best and worst predictions with this calibration. c) The non-Schmid model simultaneously calibrated to micropillar 2 and 5, d) the best and worst predictions with this calibration. e) The non-Schmid model simultaneously calibrated to micropillar 4 and 5, f) the best and worst predictions with this calibration.

Figure B.5: (cont'd)

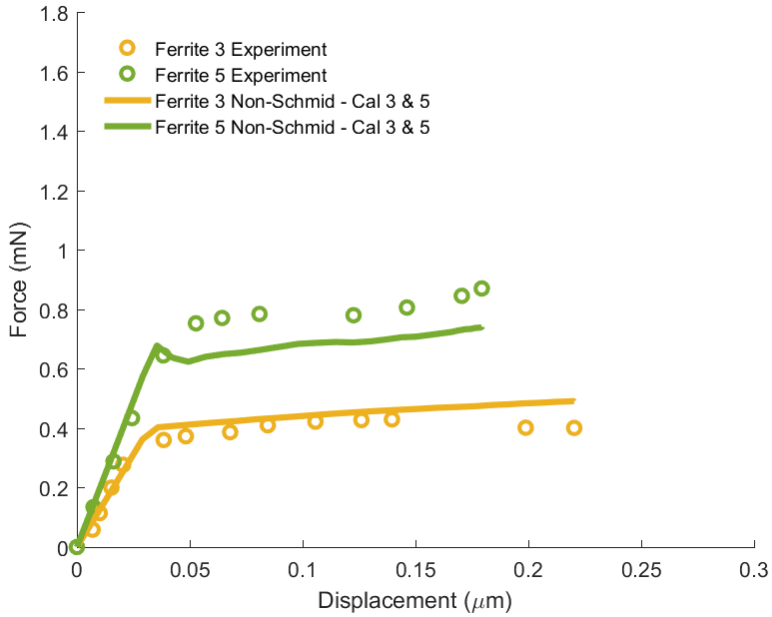

(c)

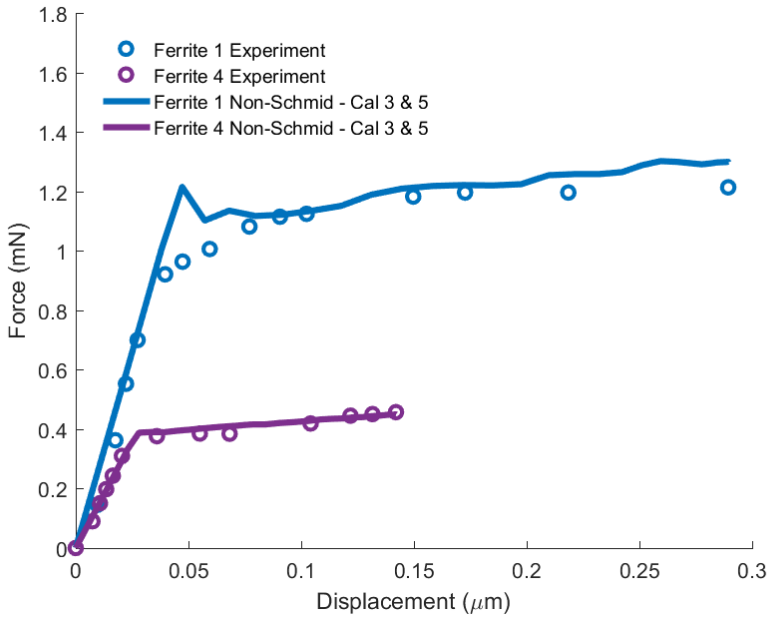

(d)

Figure B.5: (cont'd)

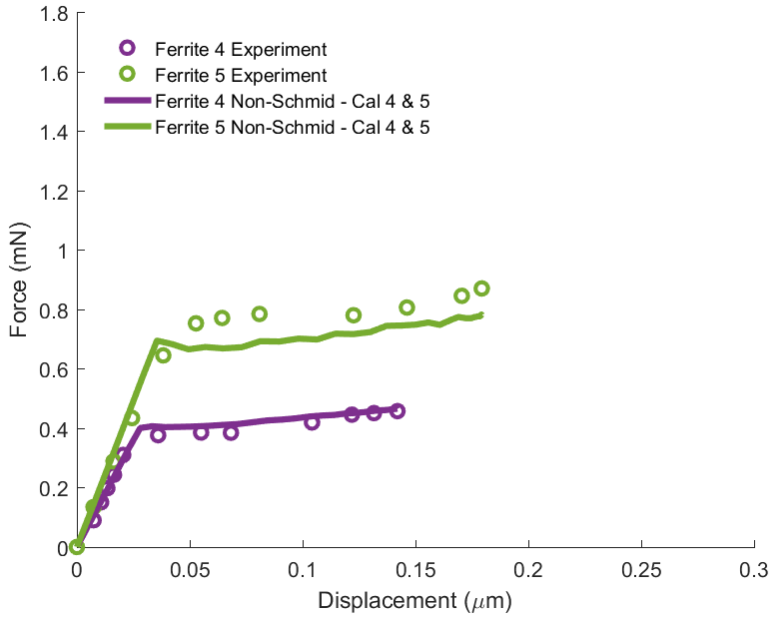

(e)

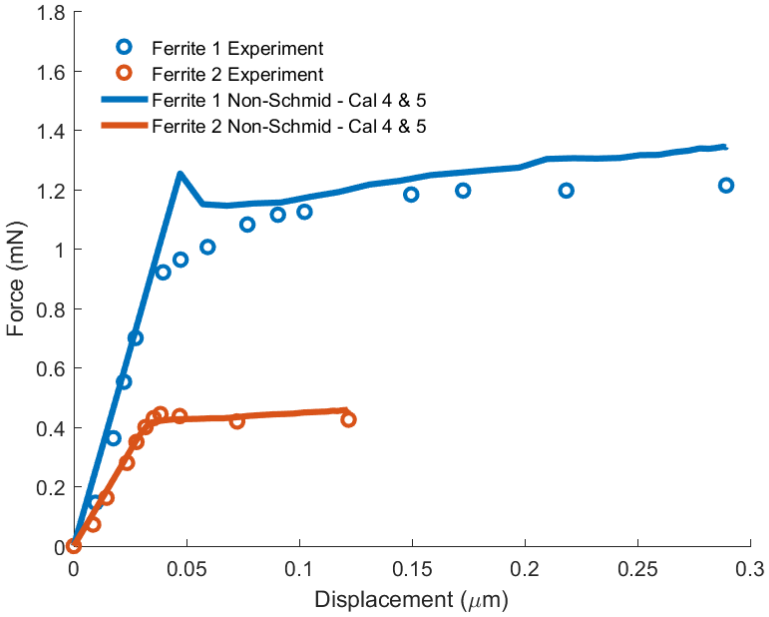

(f)

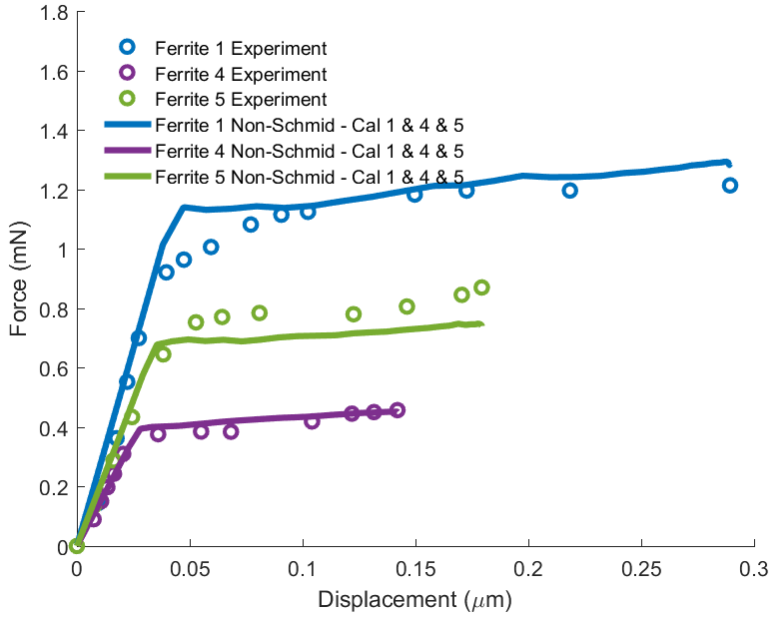

Figure B.6: Calibration of the non-Schmid model simultaneously to micropillars 1, 4 and 5. The circles show the force-displacement values measured in the experiments and the solid lines represent the fitting of the models.

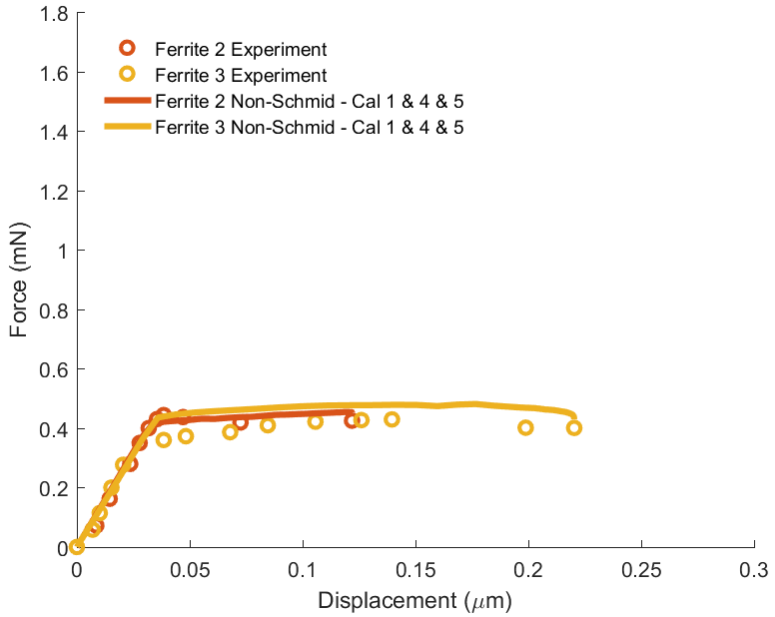

Figure B.7: The best and worst predictions of the non-Schmid model calibrated with micropillars 1, 4 and 5. The circles show the experimental measurements and the solid lines show the force-displacement predictions of the model.

Table B.3: Material parameters found for the non-Schmid modeling of QP980 ferrite micropillar when the model was simultaneously calibrated with multiple micropillars. In these calibrations $h_0 = 10$ and $\eta = 3$.

Material Parameters	Calibration of the non-Schmid model to micropillar						
	1 & 3	1 & 4	1 & 6	3 & 5	4 & 5	1 & 3 & 5	1 & 4 & 5
τ_s	570	760	880	400	555	537	445
τ_0	257	280	276	300	306	249	269
a_1	0.0034	0.1454	0.0297	0	0.0045	0.0103	0.0618
a_2	0.8814	0.9204	0.9993	1	0.9646	0.5748	0.7022
a_3	0.3442	0.2546	0.1250	0	0.0127	0.0007	0.0084

Table B.4: S-NRMSE for non-Schmid model simultaneously calibrated to multiple micropillar experiments at a time. A negative number indicates the underestimation and a positive number represents the overestimation of experimental data.

Predicting Micropillar	S-NRMSE for calibration of the non-Schmid model to micropillars (%)						
	1 & 3	1 & 4	1 & 6	3 & 5	4 & 5	1 & 3 & 5	1 & 4 & 5
1	-4.18	3.52	3.74	5.36	6.58	3.80	4.74
2	-5.93	-3.92	-5.36	-3.74	3.26	-4.86	3.15
3	-2.56	4.50	2.52	6.78	6.09	2.79	8.30
4	-3.89	-1.96	-3.29	1.85	2.41	-2.81	2.52
5	-11.09	-10.97	-9.30	-7.28	-5.35	-8.98	-5.67
6	-3.72	-3.72	-3.27	2.87	5.65	-2.69	3.16
Sum of absolute error	31.38	28.59	27.48	27.88	29.35	25.92	27.54

Table B.5: Material parameters found from calibration of the Schmid model to single micropillars of QP980 ferrite. In these calibrations $h_01 = h_02 = h_03$ and $\eta_1 = \eta_2 = \eta_3 = 3$.

Material Parameters	Calibration of the Schmid model to micropillar					
	1	2	3	4	5	6
τ_{s1}	615	400	881	400	944	557
τ_{s2}	615	400	881	400	944	557
τ_{s3}	685	470	951	470	1014	627
τ_{01}	185	191	113	183	260	238
τ_{02}	195	201	123	193	270	248
τ_{03}	305	311	233	303	380	358
h_{01}	272	10	66	10	98	66

Table B.6: S-NRMSE for Schmid model calibrated to one micropillar experiment at a time. A negative number represents the underestimation and a positive number indicates the overestimation of experimental data.

Predicting Micropillar	S-NRMSE for calibration of the Schmid model to micropillars (%)					
	1	2	3	4	5	6
1	2.71	-3.26	-20.15	-4.34	15.56	10.29
2	4.52	3.80	-16.83	3.17	15.62	11.76
3	28.18	24.56	2.56	22.14	47.75	39.57
4	2.46	2.54	-16.28	-2.36	17.37	12.17
5	-12.35	-13.85	-27.43	-15.25	2.59	-5.33
6	-9.35	-10.39	-26.04	-11.97	5.66	2.13
Sum of absolute error	59.56	58.40	109.29	59.22	104.56	81.26

Table B.7: Material parameters found from calibration of the Schmid model to single micropillars of QP980 ferrite. In these calibrations $h_{01} = h_{02} = h_{03}$ and $\eta_1 = \eta_2 = \eta_3 = 3$.

Material Parameters	Calibration of the Schmid model to micropillars						
	1 & 3	1 & 4	1 & 6	3 & 5	4 & 5	1 & 3 & 5	1 & 4 & 5
τ_{s1}	400	650	751	400	1000	400	1000
τ_{s2}	400	650	751	400	1000	400	1000
τ_{s3}	470	720	821	470	1070	470	1070
τ_{01}	150	195	207	159	200	173	185
τ_{02}	160	205	217	169	210	183	195
τ_{03}	270	330	327	279	320	293	330
h_{01}	10	110	154	10	400	10	400

Table B.8: S-NRMSE for Schmid model simultaneously calibrated to multiple micropillar experiments at a time. A negative number indicates the underestimation and a positive number represents the overestimation of experimental data.

Predicting Micropillar	S-NRMSE for calibration of the Schmid model to micropillars (%)						
	1 & 3	1 & 4	1 & 6	3 & 5	4 & 5	1 & 3 & 5	1 & 4 & 5
1	-11.70	3.23	5.34	-9.49	6.84	-6.36	4.47
2	-7.91	5.18	7.56	-5.87	8.42	3.68	6.56
3	10.82	27.93	33.01	13.91	38.35	18.37	34.53
4	-8.55	3.84	6.81	-6.47	7.85	-3.70	4.91
5	-21.49	-11.93	-9.11	-19.73	-7.41	-17.18	-9.75
6	-19.07	-8.51	-5.54	-17.08	-4.56	-14.17	-6.95
Sum of absolute error	79.54	60.62	67.36	72.55	73.42	63.46	67.17

BIBLIOGRAPHY

BIBLIOGRAPHY

[1] Ferdinand P. Beer et al. *Mechanics of Materials*. 6, illustr. McGraw-Hill Education, 2011, p. 832. ISBN: 0073380288.

[2] Arbind Kumar Singh. *Mechanics of Solids*. PHI Learning, 2007, p. 452. ISBN: 9788120331907.

[3] R. v. Mises. "Mechanik der festen Körper im plastisch-deformablen Zustand". In: *Nachrichten von der Gesellschaft der Wissenschaften zu Göttingen, Mathematisch-Physikalische Klasse* 1913 (1913), pp. 582–592.

[4] John H. Hollomon. "Tensile Deformation". In: *Metals Technoloogy* 1879 (1945), pp. 268–290.

[5] F J Nye. *Physical properties of crystlas*. Oxford: Oxford University Press, 1967, p. xiii.

[6] M Grujicic and S Batchu. "Crystal plasticity analysis of earing in deep-drawn OFHC copper cups". In: *Journal Of Materials Science* 37 (2002), pp. 753–764.

[7] R. Hill. "A Theory of the Yielding and Plastic Flow of Anisotropic Metals". In: *Proceedings of the Royal Society A: Mathematical, Physical and Engineering Sciences* 193.1033 (May 1948), pp. 281–297. ISSN: 1364-5021. DOI: 10.1098/rspa.1948.0045.

[8] D. Peirce, R. J. Asaro, and A. Needleman. "An Analysis of nonuniform and localized deformation in ductile single crystals". In: *Acta Metallurgica* (1982).

[9] Robert J. Asaro and A. Needleman. "Overview Texture Development And Strain Hardening In Rate Dependent Polycrystals". In: 33.6 (1985), pp. 923–953.

[10] F. Barlat. "Crystallographic Texture, Anisotropic Yield Surfaces and Forming Limits of Sheet Metals". In: *Materials Science and Engineering* 91 (1987), pp. 55–72.

[11] Qing Qin and John L. Bassani. "Non-Associated Plastic Flow In Single Crystals". In: *Journal of the Mechanics and Physics of Solids* 40.4 (1992), pp. 835–862.

[12] Sia Nemat-Nasser and Tomoo Okinaka. "A new computational approach to crystal plasticity: fcc single crystal". In: *Mechanics of Materials* 24.1 (Sept. 1996), pp. 43–57. ISSN: 01676636. DOI: 10.1016/0167-6636(96)00020-8.

[13] W. Gambin and F. Barlat. "Modeling of deformation texture development based on rate independent crystal plasticity". In: *International Journal of Plasticity* 13.1-2 (Jan. 1997), pp. 75–85. ISSN: 07496419. DOI: 10.1016/S0749-6419(97)00001-6.

[14] S Kalidindi. "On the prediction of yield surfaces by the crystal plasticity models for fcc polycrystals". In: *Materials Science and Engineering A* 293.1-2 (Nov. 2000), pp. 120–129. ISSN: 09215093. DOI: 10.1016/S0921-5093(00)01048-0.

[15] F Roters. "Application of crystal plasticity FEM from single crystal to bulk polycrystal". In: *Computational Materials Science* 32.3-4 (Mar. 2005), pp. 509–517. ISSN: 09270256. DOI: 10.1016/j.commatsci.2004.09.014.

[16] R. Gröger and V. Vitek. "Multiscale modeling of plastic deformation of molybdenum and tungsten. III. Effects of temperature and plastic strain rate". In: *Acta Materialia* 56.19 (Nov. 2008), pp. 5426–5439. ISSN: 13596454. DOI: 10.1016/j.actamat.2008.07.027.

[17] T. M. Hatem and M. a. Zikry. "Dislocation density crystalline plasticity modeling of lath martensitic microstructures in steel alloys". In: *Philosophical Magazine* 89.33 (2009), pp. 3087–3109. ISSN: 1478-6435. DOI: 10.1080/14786430903185999.

[18] Jerzy Gawad et al. "An evolving plane stress yield criterion based on crystal plasticity virtual experiments". In: *International Journal of Plasticity* (2015), pp. 1–29. ISSN: 07496419. DOI: 10.1016/j.ijplas.2015.02.011.

[19] Haiming Zhang et al. "A virtual laboratory using high resolution crystal plasticity simulations to determine the initial yield surface for sheet metal forming operations". In: *International Journal of Plasticity* 80 (2016), pp. 111–138. ISSN: 0749-6419. DOI: 10.1016/j.ijplas.2016.01.002.

[20] H. S. Kim et al. "Development of a multi-scale simulation model of tube hydroforming for superconducting RF cavities". In: *Materials Science and Engineering A* 679.October 2016 (2017), pp. 104–115. ISSN: 09215093. DOI: 10.1016/j.msea.2016.10.022.

[21] Oana Cazacu, Benoit Revil-Baudard, and Nitin Chandola. "A yield criterion for cubic single crystals". In: *International Journal of Solids and Structures* (2017). ISSN: 00207683. DOI: 10.1016/j.ijsolstr.2017.04.006.

[22] R. Hill. "Theoretical plasticity of textured aggregates". In: *Mathematical Proceedings of the Cambridge Philosophical Society* 85.01 (Oct. 1979), pp. 179–191. ISSN: 0305-0041. DOI: 10.1017/S0305004100055596.

[23] Roger W. Logan and William F. Hosford. "Upper-Bound Anisotropic Yield Locus Calculations Assuming < 111 >-Pencil Glide". In: *International Journal of Mechanical Science* 22 (1980), pp. 419–430.

[24] F. Barlat and J. Lian. "Plastic Behavior And Stretchability Of Sheet Metals. Part I: A Yield Function For Orthotropic Sheets Under Plane Stress Conditions". In: *International Journal of Plasticity* 5 (1989), pp. 51–66.

[25] Frédéric Barlat, Daniel J. Lege, and John C. Brem. "A six-component yield function for anisotropic materials". In: *International Journal of Plasticity* 7.7 (1991), pp. 693–712. ISSN: 07496419. DOI: 10.1016/0749-6419(91)90052-Z.

[26] F. A C M Habraken and J. H. Dautzenberg. "Some Applications of the Barlat 1991 Yield Criterion". In: *CIRP Annals - Manufacturing Technology* 44.1 (1995), pp. 185–188. ISSN: 17260604. DOI: 10.1016/S0007-8506(07)62303-8.

[27] F Barlat et al. "Plane stress yield function for aluminum alloy sheets-part 1: theory". In: *International Journal of Plasticity* 19.9 (2003), pp. 1297–1319. ISSN: 07496419. DOI: http://dx.doi.org/10.1016/S0749-6419(02)00019-0.

[28] Jeong Whan Yoon et al. "Plane stress yield function for aluminum alloy sheets - Part II: FE formulation and its implementation". In: *International Journal of Plasticity* 20.3 (2004), pp. 495–522. ISSN: 07496419. DOI: 10.1016/S0749-6419(03)00099-8.

[29] F. Barlat et al. "Linear transfomation-based anisotropic yield functions". In: *International Journal of Plasticity* 21.5 (2005), pp. 1009–1039. ISSN: 07496419. DOI: 10.1016/j.ijplas.2004.06.004.

[30] F. Grytten et al. "Evaluation of identification methods for YLD2004-18p". In: *International Journal of Plasticity* 24.12 (2008), pp. 2248–2277. ISSN: 07496419. DOI: 10.1016/j.ijplas.2007.11.005.

[31] N Souto, A Andrade-campos, and S Thuillier. "Material parameter identification within an integrated methodology considering anisotropy , hardening and rupture". In: *Journal of Materials Processing Tech.* 220 (2015), pp. 157–172. ISSN: 0924-0136. DOI: 10.1016/j.jmatprotec.2015.01.017.

[32] G. I. Taylor. "Plastic strain in metals". In: *Twenty-Eighth May Lecture to the Institute of Metals* (1938).

[33] Henry R Piehler. "Crystal-Plasticity Fundamentals". In: *ASM Handbook Volume 22A: Fundamentals of Modeling for Metals Processing* 22.Ref 2 (2009), pp. 232–238.

[34] J. W. Hutchinson. "Plastic Stress-Strain Relations Of F.C.C Polycrystalline Metals Hardening According To Taylor's Rule". In: *Journal of the Mechanics and Physics of Solids* 12 (1964), pp. 11–24.

[35] Christopher R. Weinberger et al. "Incorporating atomistic data of lattice friction into BCC crystal plasticity models". In: *International Journal of Plasticity* 37 (Oct. 2012), pp. 16–30. ISSN: 07496419. DOI: 10.1016/j.ijplas.2012.03.012.

[36] Laszlo S. Toth, Paul Van Houtte, and Albert Van Bael. "Analytical Representation Of Polycrystal Yield Surfaces". In: *Anisotropy and Localization of Plastic Deformation, Plasticity 1991*. 1991, pp. 183–186.

[37] Michel Darrieulat and David Piot. "A method of generating analytical yield surfaces of crystalline materials". In: *International Journal of Plasticity* 12.5 (1996), pp. 575–610.

[38] Amir R. Zamiri and Farhang Pourboghrat. "A novel yield function for single crystals based on combined constraints optimization". In: *International Journal of Plasticity* 26.5 (May 2010), pp. 731–746. ISSN: 07496419. DOI: 10.1016/j.ijplas.2009.10.004.

[39] R. Hill. "Generalized Relations For Incremental Deformation Of Metal Crystals". In: *Journal of the Mechanics and Physics of Solids* 14 (1966), pp. 95–102.

[40] J. W. Hutchinson. "Elastic-Plastic Behaviour of Polycrystalline Metals and Composites". In: *Proceedings of the Royal Society A: Mathematical, Physical and Engineering Sciences* 319.1537 (Oct. 1970), pp. 247–272. ISSN: 1364-5021. DOI: 10.1098/rspa.1970.0177.

[41] Robert J. Asaro. "Crystal Plasticity". In: *Journal of Applied Mechanics* 50.December (1983), pp. 921–934.

[42] Abhijit P. Brahme et al. "A new strain hardening model for rate-dependent crystal plasticity". In: *Computational Materials Science* 50.10 (2011), pp. 2898–2908. ISSN: 09270256. DOI: 10.1016/j.commatsci.2011.05.006.

[43] Xiao-Wu Li. *Encyclopedia of Tribology*. Ed. by Q. Jane Wang and Yip-Wah Chung. Boston, MA: Springer US, 2013, pp. 2313–2323. ISBN: 978-0-387-92896-8. DOI: 10.1007/978-0-387-92897-5.

[44] T Buchheit. "Investigating the limits of polycrystal plasticity modeling". In: *International Journal of Plasticity* 21.2 (Feb. 2005), pp. 221–249. ISSN: 07496419. DOI: 10.1016/j.ijplas.2003.10.009.

[45] M.G.D. Geers et al. "Coupled glide-climb diffusion-enhanced crystal plasticity". In: *Journal of the Mechanics and Physics of Solids* 70 (Oct. 2014), pp. 136–153. ISSN: 00225096. DOI: 10.1016/j.jmps.2014.05.007.

[46] B.L. Hansen et al. "A dislocation-based multi-rate single crystal plasticity model". In: *International Journal of Plasticity* 44 (May 2013), pp. 129–146. ISSN: 07496419. DOI: 10.1016/j.ijplas.2012.12.006.

[47] E. Bittencourt. "Numerical solution of crystal plasticity problems by a mixed formulation". In: *Computational Materials Science* 63 (Oct. 2012), pp. 145–153. ISSN: 09270256. DOI: 10.1016/j.commatsci.2012.06.003.

[48] Manish Kothari. "Rate Independent Crystal Plasticity". PhD thesis. Massachusetts Institute of Technology, 1995.

[49] J. Schröder and C. Miehe. "Aspects of computational rate-independent crystal plasticity". In: *Computational Materials Science* 9.1-2 (1997), pp. 168–176. ISSN: 09270256. DOI: 10.1016/S0927-0256(97)00072-4.

[50] Christian Miehe and Jörg Schröder. "Comparative study of stress update algorithms for rate-independent and rate-dependent crystal plasticity". In: *International Journal for Numerical Methods in Engineering* 50.2 (2001), pp. 273–298. ISSN: 00295981. DOI: 10.1002/1097-0207(20010120)50:2<273::AID-NME17>3.0.CO;2-Q.

[51] Donghong Zhang and Saiyi Li. "A Rate-Dependent Crystal Plasticity Analysis of Orientation Stability in Biaxial Tension of Magnesium". In: *Journal of Materials Science and Technology* 27.2 (2010), pp. 175–182. ISSN: 10050302. DOI: 10.1016/S1005-0302(11)60045-5. URL: http://dx.doi.org/10.1016/S1005-0302(11)60045-5.

[52] Hongwei Li and He Yang. "An efficient parallel-operational explicit algorithm for Taylor-type model of rate dependent crystal plasticity". In: *Computational Materials Science* 54.1 (2012), pp. 255–265. ISSN: 09270256. DOI: 10.1016/j.commatsci.2011.10.018. URL: http://dx.doi.org/10.1016/j.commatsci.2011.10.018.

[53] Haiming Zhang et al. "An effective semi-implicit integration scheme for rate dependent crystal plasticity using explicit finite element codes". In: *Computational Materials Science* 54.1 (2012), pp. 208–218. ISSN: 09270256. DOI: 10.1016/j.commatsci.2011.10.011. URL: http://dx.doi.org/10.1016/j.commatsci.2011.10.011.

[54] Thao Nguyen, D. J. Luscher, and J. W. Wilkerson. "A dislocation-based crystal plasticity framework for dynamic ductile failure of single crystals". In: *Journal of the Mechanics and Physics of Solids* 108 (2017), pp. 1–29. ISSN: 00225096. DOI: 10.1016/j.jmps.2017.07.020. URL: http://dx.doi.org/10.1016/j.jmps.2017.07.020.

[55] S. A. Tajalli, M. R. Movahhedy, and J. Akbari. "Simulation of orthogonal microcutting of FCC materials based on rate-dependent crystal plasticity finite element model". In: *Computational Materials Science* 86 (2014), pp. 79–87. ISSN: 09270256. DOI: 10.1016/j.commatsci.2014.01.016. URL: http://dx.doi.org/10.1016/j.commatsci.2014.01.016.

[56] Samuel Forest and M. B. Rubin. "A rate-independent crystal plasticity model with a smooth elastic-plastic transition and no slip indeterminacy". In: *European Journal*

of Mechanics, A/Solids 55 (2016), pp. 278–288. ISSN: 09977538. DOI: 10.1016/j.euromechsol.2015.08.012. URL: http://dx.doi.org/10.1016/j.euromechsol.2015.08.012.

[57] Bassam Mohammed et al. "Multiscale crystal plasticity modeling of multiphase advanced high strength steel". In: *International Journal of Solids and Structures* 0 (2017), pp. 1–19. ISSN: 00207683. DOI: 10.1016/j.ijsolstr.2017.05.007.

[58] P Franciosi, M Berveiller, and A Zaoui. "Latent hardening in copper and aluminium". In: *Acta Materialia* 28 (1979), pp. 273–283.

[59] H. Mughrabi. "A two-parameter description of heterogeneous dislocation distributions in deformed metal crystals". In: *Materials Science and Engineering* 85 (1987), pp. 15–31. ISSN: 00255416. DOI: 10.1016/0025-5416(87)90463-0.

[60] A. Ma, F. Roters, and D. Raabe. "A dislocation density based constitutive model for crystal plasticity FEM including geometrically necessary dislocations". In: *Acta Materialia* 54.8 (May 2006), pp. 2169–2179. ISSN: 13596454. DOI: 10.1016/j.actamat.2006.01.005.

[61] T. M. Hatem and M. a. Zikry. "Shear pipe effects and dynamic shear-strain localization in martensitic steels". In: *Acta Materialia* 57.15 (Sept. 2009), pp. 4558–4567. ISSN: 13596454. DOI: 10.1016/j.actamat.2009.06.028.

[62] N. Grilli et al. "Multiple slip dislocation patterning in a dislocation-based crystal plasticity finite element method". In: *International Journal of Plasticity* 100 (2017), pp. 104–121. ISSN: 07496419. DOI: 10.1016/j.ijplas.2017.09.015.

[63] Yuanchao Gan et al. "An elastic-viscoplastic crystal plasticity modeling and strain hardening for plane strain deformation of pure magnesium". In: *Mechanics of Materials* 92 (2016), pp. 185–197. ISSN: 01676636. DOI: 10.1016/j.mechmat.2015.09.012.

[64] Hamidreza Abdolvand, Mark R. Daymond, and Charles Mareau. "Incorporation of twinning into a crystal plasticity finite element model: Evolution of lattice strains and texture in Zircaloy-2". In: *International Journal of Plasticity* 27.11 (2011), pp. 1721–1738. ISSN: 07496419. DOI: 10.1016/j.ijplas.2011.04.005. URL: http://dx.doi.org/10.1016/j.ijplas.2011.04.005.

[65] Chao Yu, Guozheng Kang, and Qianhua Kan. "Crystal plasticity based constitutive model of NiTi shape memory alloy considering different mechanisms of inelastic deformation". In: *International Journal of Plasticity* 54 (2014), pp. 132–162. ISSN: 07496419. DOI: 10.1016/j.ijplas.2013.08.012. URL: http://dx.doi.org/10.1016/j.ijplas.2013.08.012.

[66] Milan Ardeljan et al. "Explicit incorporation of deformation twins into crystal plasticity finite element models". In: *Computer Methods in Applied Mechanics and Engineering* 295 (2015), pp. 396–413. ISSN: 00457825. DOI: 10.1016/j.cma.2015.07.003. URL: http://dx.doi.org/10.1016/j.cma.2015.07.003.

[67] Milan Ardeljan, Irene J. Beyerlein, and Marko Knezevic. "Effect of dislocation density-twin interactions on twin growth in AZ31 as revealed by explicit crystal plasticity finite element modeling". In: *International Journal of Plasticity* 99 (2017), pp. 81–101. ISSN: 07496419. DOI: 10.1016/j.ijplas.2017.09.002. URL: https://doi.org/10.1016/j.ijplas.2017.09.002.

[68] Jiahao Cheng and Somnath Ghosh. "A crystal plasticity FE model for deformation with twin nucleation in magnesium alloys". In: *International Journal of Plasticity* 67 (2015), pp. 148–170. ISSN: 07496419. DOI: 10.1016/j.ijplas.2014.10.005. URL: http://dx.doi.org/10.1016/j.ijplas.2014.10.005.

[69] Jiahao Cheng and Somnath Ghosh. "Crystal plasticity finite element modeling of discrete twin evolution in polycrystalline magnesium". In: *Journal of the Mechanics and Physics of Solids* 99.July 2016 (2017), pp. 512–538. ISSN: 00225096. DOI: 10.1016/j.jmps.2016.12.008. URL: http://dx.doi.org/10.1016/j.jmps.2016.12.008.

[70] C. Y. Sun et al. "Modeling of slip, twinning and transformation induced plastic deformation for TWIP steel based on crystal plasticity". In: *International Journal of Plasticity* 76 (2016), pp. 186–212. ISSN: 07496419. DOI: 10.1016/j.ijplas.2015.08.003.

[71] Yuichi Tadano, Yui Yoshihara, and Seiya Hagihara. "A crystal plasticity modeling considering volume fraction of deformation twinning". In: *International Journal of Plasticity* 84 (2015), pp. 88–101. ISSN: 07496419. DOI: 10.1016/j.ijplas.2016.05.002. URL: http://dx.doi.org/10.1016/j.ijplas.2016.05.002.

[72] Su Leen Wong et al. "A crystal plasticity model for twinning- and transformation-induced plasticity". In: *Acta Materialia* 118 (2016), pp. 140–151. ISSN: 13596454. DOI: 10.1016/j.actamat.2016.07.032. URL: http://dx.doi.org/10.1016/j.actamat.2016.07.032.

[73] A. Ma, F. Roters, and D. Raabe. "On the consideration of interactions between dislocations and grain boundaries in crystal plasticity finite element modeling - Theory, experiments, and simulations". In: *Acta Materialia* 54.8 (2006), pp. 2181–2194. ISSN: 13596454. DOI: 10.1016/j.actamat.2006.01.004.

[74] P. R.M. Van Beers et al. "Grain boundary interface mechanics in strain gradient crystal plasticity". In: *Journal of the Mechanics and Physics of Solids* 61.12 (2013), pp. 2659–2679. ISSN: 00225096. DOI: 10.1016/j.jmps.2013.08.011. URL: http://dx.doi.org/10.1016/j.jmps.2013.08.011.

[75] Marko Knezevic et al. “Three dimensional predictions of grain scale plasticity and grain boundaries using crystal plasticity finite element models”. In: *Computer Methods in Applied Mechanics and Engineering* 277 (2014), pp. 239–259. ISSN: 00457825. DOI: 10.1016/j.cma.2014.05.003. URL: http://dx.doi.org/10.1016/j.cma.2014.05.003.

[76] V. Doquet and B. Barkia. “Combined AFM, SEM and crystal plasticity analysis of grain boundary sliding in titanium at room temperature”. In: *Mechanics of Materials* 103 (2016), pp. 18–27. ISSN: 01676636. DOI: 10.1016/j.mechmat.2016.09.001. URL: http://dx.doi.org/10.1016/j.mechmat.2016.09.001.

[77] Y. Su et al. “Quantifying deformation processes near grain boundaries in α titanium using nanoindentation and crystal plasticity modeling”. In: *International Journal of Plasticity* 86 (2016), pp. 170–186. ISSN: 07496419. DOI: 10.1016/j.ijplas.2016.08.007.

[78] Habib Pouriayevali and Bai Xiang Xu. “Decomposition of dislocation densities at grain boundary in a finite-deformation gradient crystal-plasticity framework”. In: *International Journal of Plasticity* 96 (2017), pp. 36–55. ISSN: 07496419. DOI: 10.1016/j.ijplas.2017.04.010. URL: http://dx.doi.org/10.1016/j.ijplas.2017.04.010.

[79] I. Benedetti, V. Gulizzi, and V. Mallardo. “A grain boundary formulation for crystal plasticity”. In: *International Journal of Plasticity* 83 (2016), pp. 202–224. ISSN: 07496419. DOI: 10.1016/j.ijplas.2016.04.010. URL: http://dx.doi.org/10.1016/j.ijplas.2016.04.010.

[80] Masoud Ghorbani Moghaddam et al. “Grain size-dependent crystal plasticity constitutive model for polycrystal materials”. In: *Materials Science and Engineering A* 703.July (2017), pp. 521–532. ISSN: 09215093. DOI: 10.1016/j.msea.2017.07.087. URL: http://dx.doi.org/10.1016/j.msea.2017.07.087.

[81] Douglas J. Bammann. “A model of crystal plasticity containing a natural length scale”. In: *Materials Science and Engineering A* 309-310 (2001), pp. 406–410. ISSN: 09215093. DOI: 10.1016/S0921-5093(00)01614-2.

[82] G. Venkatramani, S. Ghosh, and M. Mills. “A size-dependent crystal plasticity finite-element model for creep and load shedding in polycrystalline titanium alloys”. In: *Acta Materialia* 55.11 (2007), pp. 3971–3986. ISSN: 13596454. DOI: 10.1016/j.actamat.2007.03.017.

[83] Sinisa Dj Mesarovic, Raghuraman Baskaran, and Alexander Panchenko. “Thermodynamic coarsening of dislocation mechanics and the size-dependent continuum crystal plasticity”. In: *Journal of the Mechanics and Physics of Solids* 58.3 (2010), pp. 311–

329. ISSN: 00225096. DOI: 10.1016/j.jmps.2009.12.002. URL: http://dx.doi.org/10.1016/j.jmps.2009.12.002.

[84] Peng Lin et al. "A stochastic crystal plasticity model with size-dependent and intermittent strain bursts characteristics at micron scale". In: *International Journal of Solids and Structures* 69-70 (2015), pp. 267–276. ISSN: 00207683. DOI: 10.1016/j.ijsolstr.2015.05.024. URL: http://dx.doi.org/10.1016/j.ijsolstr.2015.05.024.

[85] Xiazi Xiao et al. "A size-dependent tensorial plasticity model for FCC single crystal with irradiation". In: *International Journal of Plasticity* 65 (2015), pp. 152–167. ISSN: 07496419. DOI: 10.1016/j.ijplas.2014.09.004. URL: http://dx.doi.org/10.1016/j.ijplas.2014.09.004.

[86] Masoud Ghorbani Moghaddam et al. "Development of a precipitate size-dependent crystal plasticity constitutive model for two-phase materials and its implementation on a multi-scale computational framework". In: *Materials Science and Engineering A* 651 (2016), pp. 893–903. ISSN: 09215093. DOI: 10.1016/j.msea.2015.11.042. URL: http://dx.doi.org/10.1016/j.msea.2015.11.042.

[87] Y. Aoyagi, T. Tsuru, and T. Shimokawa. "Crystal plasticity modeling and simulation considering the behavior of the dislocation source of ultrafine-grained metal". In: *International Journal of Plasticity* 55 (Apr. 2014), pp. 43–57. ISSN: 07496419. DOI: 10.1016/j.ijplas.2013.09.009. URL: http://linkinghub.elsevier.com/retrieve/pii/S0749641913001897.

[88] William a. Counts et al. "Predicting the Hall-Petch effect in fcc metals using non-local crystal plasticity". In: *International Journal of Plasticity* 24.7 (July 2008), pp. 1243–1263. ISSN: 07496419. DOI: 10.1016/j.ijplas.2007.09.008.

[89] Qiang Liu, Anish Roy, and Vadim V. Silberschmidt. "Size-dependent crystal plasticity: From micro-pillar compression to bending". In: *Mechanics of Materials* 100 (2016), pp. 31–40. ISSN: 01676636. DOI: 10.1016/j.mechmat.2016.06.002. URL: http://dx.doi.org/10.1016/j.mechmat.2016.06.002.

[90] "Mesoscale cyclic crystal plasticity with dislocation substructures". In: *International Journal of Plasticity* 98 (Nov. 2017), pp. 1–26. ISSN: 07496419. DOI: 10.1016/j.ijplas.2017.06.002. URL: http://dx.doi.org/10.1016/j.ijplas.2017.06.002%20http://linkinghub.elsevier.com/retrieve/pii/S0749641917301705.

[91] Hojun Lim et al. "A physically based model of temperature and strain rate dependent yield in BCC metals : Implementation into crystal plasticity". In: *Journal of the Mechanics and Physics of Solids* 74 (2015), pp. 80–96. ISSN: 0022-5096. DOI: 10.1016/j.jmps.2014.10.003.

[92] Milan Ardeljan et al. "Strain rate and temperature sensitive multi-level crystal plasticity model for large plastic deformation behavior: Application to AZ31 magnesium alloy". In: *International Journal of Plasticity* 83 (2016), pp. 90–109. ISSN: 07496419. DOI: 10.1016/j.ijplas.2016.04.005. URL: http://dx.doi.org/10.1016/j.ijplas.2016.04.005.

[93] David Cereceda et al. "Unraveling the temperature dependence of the yield strength in single-crystal tungsten using atomistically-informed crystal plasticity calculations". In: *International Journal of Plasticity* 78 (2016), pp. 242–265. ISSN: 07496419. DOI: 10.1016/j.ijplas.2015.09.002. arXiv: 1506.02224. URL: http://dx.doi.org/10.1016/j.ijplas.2015.09.002.

[94] Xu He, Yao Yao, and Leon M. Keer. "A rate and temperature dependent unified creep-plasticity model for high strength steel and solder alloys". In: *Mechanics of Materials* 106 (2017), pp. 35–43. ISSN: 01676636. DOI: 10.1016/j.mechmat.2017.01.005.

[95] H. Wang et al. "A crystal plasticity model based on transition state theory". In: *International Journal of Plasticity* 93 (2017), pp. 251–268. ISSN: 07496419. DOI: 10.1016/j.ijplas.2016.05.003.

[96] Chao Yu, Guozheng Kang, and Qianhua Kan. "Study on the rate-dependent cyclic deformation of super-elastic NiTi shape memory alloy based on a new crystal plasticity constitutive model". In: *International Journal of Solids and Structures* 51.25-26 (2014), pp. 4386–4405. ISSN: 00207683. DOI: 10.1016/j.ijsolstr.2014.09.006. URL: http://dx.doi.org/10.1016/j.ijsolstr.2014.09.006.

[97] Qiang Liu, Anish Roy, and Vadim V. Silberschmidt. "Temperature-dependent crystal-plasticity model for magnesium: A bottom-up approach". In: *Mechanics of Materials* 113 (2017), pp. 44–56. ISSN: 01676636. DOI: 10.1016/j.mechmat.2017.07.008. URL: http://dx.doi.org/10.1016/j.mechmat.2017.07.008.

[98] Z.Q. Wang and I.J. Beyerlein. "An atomistically-informed dislocation dynamics model for the plastic anisotropy and tension-compression asymmetry of BCC metals". In: *International Journal of Plasticity* 27 (Oct. 2011), pp. 1471–1484. ISSN: 07496419. DOI: 10.1016/j.ijplas.2010.08.011.

[99] Marko Knezevic and Daniel J. Savage. "A high-performance computational framework for fast crystal plasticity simulations". In: *Computational Materials Science* 83 (Feb. 2014), pp. 101–106. ISSN: 0927-0256. DOI: 10.1016/j.commatsci.2013.11.012.

[100] Aboozar Mapar et al. "Crystal Plasticity Finite Element Modeling of Single Crystal Niobium Tensile Tests with Weighted Dynamic Hardening Rule". In: *2nd World Congress on Integrated Computational Materials Engineering*. Ed. by Mei Li et al. TMS (The Minerals, Metals & Materials Society), 2013, pp. 255–258.

[101] A. Mapar et al. “Dynamic hardening rule; a generalization of the classical hardening rule for crystal plasticity”. In: *16th International Conference on RF Superconductivity*. Paris, France, 2013, pp. 499–503. ISBN: 9783954501434.

[102] A. Mapar et al. “Crystal plasticity modeling of single crystal niobium”. In: *17th International Conference on RF Superconductivity*. Ed. by Robert E. Laxdal, Jana Thomson, and Volker RW Schaa. Whistler, British Columbia, Canada: JACoW, Geneva, Switzerland, 2015, pp. 228–232. DOI: 10.18429/JACoW-SRF2015-MOPB057.

[103] Qing Qin and John L. Bassani. “Non-Schmid Yield Behavior in Single Crystals”. In: *Journal of the Mechanics and Physics of Solids* 40.4 (1992), pp. 813–833.

[104] J.L. Bassani, K. Ito, and V. Vitek. “Complex macroscopic plastic flow arising from non-planar dislocation core structures”. In: *Materials Science and Engineering: A* 319-321 (Dec. 2001), pp. 97–101. ISSN: 0921-5093. DOI: 10.1016/S0921-5093(00)02008-6.

[105] R. Gröger and V. Vitek. “Breakdown of the Schmid Law in BCC Molybdenum Related to the Effect of Shear Stress Perpendicular to the Slip Direction”. In: *Materials Science Forum* 482 (2005), pp. 123–126. ISSN: 1662-9752. DOI: 10.4028/www.scientific.net/MSF.482.123.

[106] R. Gröger, A.G. Bailey, and V. Vitek. “Multiscale modeling of plastic deformation of molybdenum and tungsten: I. Atomistic studies of the core structure and glide of $1/2 < 111 >$ screw dislocations at 0K”. In: *Acta Materialia* 56.19 (Nov. 2008), pp. 5401–5411. ISSN: 13596454. DOI: 10.1016/j.actamat.2008.07.018.

[107] R. Gröger et al. “Multiscale modeling of plastic deformation of molybdenum and tungsten: II. Yield criterion for single crystals based on atomistic studies of glide of $1/2 < 111 >$ screw dislocations”. In: *Acta Materialia* 56.19 (Nov. 2008), pp. 5412–5425. ISSN: 13596454. DOI: 10.1016/j.actamat.2008.07.037.

[108] Aenne Koester, Anxin Ma, and Alexander Hartmaier. “Atomistically informed crystal plasticity model for body-centered cubic iron”. In: *Acta Materialia* 60.9 (May 2012), pp. 3894–3901. ISSN: 13596454. DOI: 10.1016/j.actamat.2012.03.053.

[109] Peng Chen et al. “Microscale-calibrated modeling of the deformation response of dual-phase steels”. In: *Acta Materialia* 65 (Feb. 2014), pp. 133–149. ISSN: 13596454. DOI: 10.1016/j.actamat.2013.11.036.

[110] Saeede Ghorbanpour et al. “A crystal plasticity model incorporating the effects of precipitates in superalloys: Application to tensile, compressive, and cyclic deformation of Inconel 718”. In: *International Journal of Plasticity* 99 (2017), pp. 162–185. ISSN: 07496419. DOI: 10.1016/j.ijplas.2017.09.006. URL: https://doi.org/10.1016/j.ijplas.2017.09.006.

[111] Sagar Chandra et al. "Modeling the Mechanical Behavior of Dynamically Deformed Cu using the Theories of Crystal Plasticity". In: *Procedia Engineering* 173 (2017), pp. 1203–1208. ISSN: 18777058. DOI: 10.1016/j.proeng.2016.12.119. URL: http://dx.doi.org/10.1016/j.proeng.2016.12.119.

[112] Ji Hoon Kim et al. "Crystal plasticity finite element analysis of ferritic stainless steel for sheet formability prediction". In: *International Journal of Plasticity* 93 (2017), pp. 26–45. ISSN: 07496419. DOI: 10.1016/j.ijplas.2017.04.007. URL: http://linkinghub.elsevier.com/retrieve/pii/S0749641917301948.

[113] Ylva Mellbin, Håkan Hallberg, and Matti Ristinmaa. "An extended vertex and crystal plasticity framework for efficient multiscale modeling of polycrystalline materials". In: *International Journal of Solids and Structures* 125 (2017), pp. 150–160. ISSN: 00207683. DOI: 10.1016/j.ijsolstr.2017.07.009.

[114] Y. Mellbin, H. Hallberg, and M. Ristinmaa. "Accelerating crystal plasticity simulations using GPU multiprocessors". In: *International Journal for Numerical Methods in Engineering* 100.2 (Oct. 2014), pp. 111–135. ISSN: 00295981. DOI: 10.1002/nme.4724. arXiv: 1010.1724. URL: http://doi.wiley.com/10.1002/nme.4724%20http://arxiv.org/abs/1010.1724.

[115] A. Zamiri, F. Pourboghrat, and F. Barlat. "An effective computational algorithm for rate-independent crystal plasticity based on a single crystal yield surface with an application to tube hydroforming". In: *International Journal of Plasticity* 23.7 (July 2007), pp. 1126–1147. ISSN: 07496419. DOI: 10.1016/j.ijplas.2006.10.012.

[116] F. Dohmann and C. Hartl. "Tube hydroforming-research and practical application". In: *Journal of Materials Processing Technology* 71.1 (1997), pp. 174–186. ISSN: 09240136. DOI: 10.1016/S0924-0136(97)00166-0.

[117] M Ahmetoglu et al. "Tube hydroforming: current research, applications and need for training". In: *Journal of Materials Processing Technology* 98.2 (2000), pp. 224–231. ISSN: 09240136. DOI: 10.1016/S0924-0136(99)00203-4.

[118] L. H. Lang et al. "Hydroforming highlights: Sheet hydroforming and tube hydroforming". In: *Journal of Materials Processing Technology* 151.1-3 SPEC. ISS. (2004), pp. 165–177. ISSN: 09240136. DOI: 10.1016/j.jmatprotec.2004.04.032.

[119] Nader Asnafi and Anders Skogsgardh. "Theoretical and experimental analysis of stroke-controlled tube hydroforming". In: *Materials Science and Engineering* 279 (2000), pp. 95–110.

[120] Yabo Guan and Farhang Pourboghrat. "Fourier series based finite element analysis of tube hydroforming-Generalized plane strain model". In: *Journal of Materi-*

als Processing Technology 197.1-3 (Feb. 2008), pp. 379–392. ISSN: 09240136. DOI: 10.1016/j.jmatprotec.2007.06.044.

[121] Lorenzo Iorio, Ernesto Maspero, and Matteo Strano. "Hydroforming of locally heat treated tubes". In: *Journal of Manufacturing Processes* 16.2 (2014), pp. 157–165. ISSN: 1526-6125. DOI: 10.1016/j.jmapro.2014.01.002.

[122] Gang Liu et al. "Warm hydroforming of magnesium alloy tube with large expansion ratio". In: *Transactions of Nonferrous Metals Society of China (English Edition)* 20.11 (2010), pp. 2071–2075. ISSN: 10036326. DOI: 10.1016/S1003-6326(09)60419-2.

[123] X Singer et al. "Hydroforming of Multi-Cell Niobium and Nbcu-Clad Cavities". In: *Proceedings of the 23rd Particle Accelerator Conference*. 2009, pp. 3–5.

[124] H. S. Kim et al. "Analysis of Materials Properties of Niobium tube from the results of a virtual bulge test". In: 305 (2012), pp. 305–312. DOI: 10.1063/1.4712110.

[125] W. Singer et al. "Hydroforming of elliptical cavities". In: *Physical Review Special Topics - Accelerators and Beams* 18.2 (2015), pp. 1–22. ISSN: 1098-4402. DOI: 10.1103/PhysRevSTAB.18.022001.

[126] Nader Asnafi. *Analytical modelling of tube hydroforming*. Vol. 34. 4. Aug. 1999, pp. 295–330. ISBN: 4612212487. DOI: 10.1016/S0263-8231(99)00018-X.

[127] Yeong-Maw Hwang and Yi-Kai Lin. "Analysis and finite element simulation of the tube bulge hydroforming process". In: *Journal of Materials Processing Technology* 125-126 (Sept. 2002), pp. 821–825. ISSN: 09240136. DOI: 10.1016/S0924-0136(02)00381-3.

[128] Muammer Koc and Taylan Altan. "Prediction of forming limits and parameters in the tube hydroforming process". In: *International Journal of Machine Tools and Manufacture* 42.1 (2002), pp. 123–138. ISSN: 0890-6955. DOI: 10.1016/S0890-6955(01)00048-7.

[129] M. Ahmetoglu and T. Altan. "Tube hydroforming: State-of-the-art and future trends". In: *Journal of Materials Processing Technology* 98.1 (2000), pp. 25–33. ISSN: 09240136. DOI: 10.1016/S0924-0136(99)00302-7.

[130] S. H. Zhang et al. "Recent developments in sheet hydroforming technology". In: *Journal of Materials Processing Technology* 151.1-3 SPEC. ISS. (2004), pp. 237–241. ISSN: 0924-0136. DOI: 10.1016/j.jmatprotec.2004.04.054.

[131] Hassan Ghassemi-Armaki et al. "Microscale-calibrated modeling of the deformation response of low-carbon martensite". In: *Acta Materialia* 61.10 (June 2013), pp. 3640–3652. ISSN: 13596454. DOI: 10.1016/j.actamat.2013.02.051.

[132] G Ciovati et al. "Mechanical properties of niobium radio-frequency cavities". In: *Materials Science & Engineering A* 642 (2015), pp. 117–127. ISSN: 0921-5093. DOI: 10.1016/j.msea.2015.06.095.

[133] M. Peiniger and H. Piel. "A superconducting Nb3Sn coated multicell accelerating cavity". In: *IEEE Transactions on Nuclear Science* NS-32.5 (1985), pp. 3610–3612.

[134] D. Kang et al. "Study of slip and deformation in high purity single crystal nb for accelerator cavities". In: *17th International Conference on RF Superconductivity*. Ed. by Robert E. Laxdal, Jana Thomson, and Volker RW Schaa. Whistler, British Columbia, Canada: JACoW, Geneva, Switzerland, 2015. DOI: https://doi.org/10.18429/JACoW-SRF2015-MOPB045.

[135] P.J. Lee et al. "Grain boundary flux penetration and resistivity in large grain niobium sheet". In: *Physica C: Superconductivity* 441.1-2 (July 2006), pp. 126–129. ISSN: 09214534. DOI: 10.1016/j.physc.2006.03.027.

[136] L. Lilje et al. "Achievement of 35 MV/m in the superconducting nine-cell cavities for TESLA". In: *Nuclear Instruments and Methods in Physics Research Section A: Accelerators, Spectrometers, Detectors and Associated Equipment* 524.1-3 (May 2004), pp. 1–12. ISSN: 01689002. DOI: 10.1016/j.nima.2004.01.045.

[137] A. Ma, F. Roters, and D. Raabe. "A dislocation density based constitutive law for BCC materials in crystal plasticity FEM". In: *Computational Materials Science* 39.1 (Mar. 2007), pp. 91–95. ISSN: 09270256. DOI: 10.1016/j.commatsci.2006.04.014. URL: http://linkinghub.elsevier.com/retrieve/pii/S0927025606001376.

[138] Ghiath Monnet, Ludovic Vincent, and Benoit Devincre. "Dislocation-dynamics based crystal plasticity law for the low- and high-temperature deformation regimes of bcc crystal". In: *Acta Materialia* 61.16 (Sept. 2013), pp. 6178–6190. ISSN: 13596454. DOI: 10.1016/j.actamat.2013.07.002.

[139] R Madec and L.P. P Kubin. "Dislocation Interactions and Symmetries in BCC Crystals". In: *IUTAM Symposium on Mesoscopic Dynamics of Fracture Process and Materials Strength: Proceedings of the IUTAM Symposium held in Osaka, Japan, 6–11 July 2003*. Ed. by H Kitagawa and Y Shibutani. January 2004. Dordrecht: Springer Netherlands, 2004, pp. 69–78. ISBN: 978-1-4020-2111-4. DOI: 10.1007/978-1-4020-2111-4_7.

[140] Sylvain Queyreau, Ghiath Monnet, and Benoît Devincre. "Slip systems interactions in α-iron determined by dislocation dynamics simulations". In: *International Journal of Plasticity* 25.2 (Feb. 2009), pp. 361–377. ISSN: 07496419. DOI: 10.1016/j.ijplas.2007.12.009.

[141] Derek Hull and D. J. Bacon. *Introduction to Dislocations*. 3rd. Oxford [Oxfordshire]: Pergamon Press, 1984, p. 121.

[142] J.L. Bassani and V. Racherla. "From non-planar dislocation cores to non-associated plasticity and strain bursts". In: *Progress in Materials Science* 56.6 (Aug. 2011), pp. 852–863. ISSN: 00796425. DOI: 10.1016/j.pmatsci.2011.01.010.

[143] Thomas E. Buchheit et al. "Multi-scale modeling of low-temperature deformation in b.c.c. metals". In: *JOM* 63.11 (Nov. 2011), pp. 33–36. ISSN: 1047-4838. DOI: 10.1007/s11837-011-0188-x.

[144] T. M. Hatem and M. a. Zikry. "Dynamic shear-strain localization and inclusion effects in lath martensitic steels subjected to high pressure loads". In: *Journal of the Mechanics and Physics of Solids* 58.8 (2010), pp. 1057–1072. ISSN: 00225096. DOI: 10.1016/j.jmps.2010.04.009.

[145] M.G. Lee et al. "A dislocation density-based single crystal constitutive equation". In: *International Journal of Plasticity* 26.7 (July 2010), pp. 925–938. ISSN: 07496419. DOI: 10.1016/j.ijplas.2009.11.004.

[146] Ankit Srivastava et al. "Micromechanics of plastic deformation and phase transformation in a three-phase TRIP-assisted advanced high strength steel: Experiments and modeling". In: *Journal of the Mechanics and Physics of Solids* 78 (2015), pp. 46–69. ISSN: 00225096. DOI: 10.1016/j.jmps.2015.01.014.

[147] Y. Guan, F. Pourboghrat, and F. Barlat. "Finite element modeling of tube hydroforming of polycrystalline aluminum alloy extrusions". In: *International Journal of Plasticity* 22.12 (Dec. 2006), pp. 2366–2393. ISSN: 07496419. DOI: 10.1016/j.ijplas.2006.04.003.

[148] V. Vítek, R. C. Perrin, and D. K. Bowen. "The core structure of 1/2(111) screw dislocations in B.C.C. crystals". In: *Philosophical Magazine* 21.173 (1970), pp. 1049–1073.

[149] M. S. Duesbery. "On Non-Glide Stresses and Their Influence on the Screw Dislocation Core in Body-Centred Cubic Metals. I. The Peierls Stress". In: *Proceedings of the Royal Society A: Mathematical, Physical and Engineering Sciences* 392.1802 (Mar. 1984), pp. 145–173. ISSN: 1364-5021. DOI: 10.1098/rspa.1984.0027.

[150] M. S. Duesbery. "On Non-Glide Stresses and Their Influence on the Screw Dislocation Core in Body-Centred Cubic Metals II. The Core Structure". In: *Proceedings of the Royal Society A: Mathematical, Physical and Engineering Sciences* 392.1802 (Mar. 1984), pp. 175–197. ISSN: 1364-5021. DOI: 10.1098/rspa.1984.0028.

[151] V. Vitek et al. "Effects of non-glide stresses on the plastic flow of single and polycrystals of molybdenum". In: *Materials Science and Engineering: A* 387-389 (Dec. 2004), pp. 138–142. ISSN: 09215093. DOI: 10.1016/j.msea.2004.04.066.

[152] K. Srivastava et al. "Dislocation motion in tungsten: Atomistic input to discrete dislocation simulations". In: *International Journal of Plasticity* 47.0 (Feb. 2013), pp. 1–17. ISSN: 0749-6419. DOI: 10.1016/j.ijplas.2013.01.014.

[153] Alexander Stukowski et al. "Thermally-activated non-Schmid glide of screw dislocations in W using atomistically-informed kinetic Monte Carlo simulations". In: *International Journal of Plasticity* 65 (2015), pp. 108–130. ISSN: 07496419. DOI: 10.1016/j.ijplas.2014.08.015.

[154] David Cereceda et al. "Unraveling the temperature dependence of the yield strength in single-crystal tungsten using atomistically-informed crystal plasticity calculations". In: *International Journal of Plasticity* (2015). ISSN: 07496419. DOI: 10.1016/j.ijplas.2015.09.002. arXiv: 1506.02224.

[155] Marko Knezevic et al. "A strain-rate and temperature dependent constitutive model for BCC metals incorporating non-Schmid effects: Application to tantalum-tungsten alloys". In: *International Journal of Plasticity* 62 (2014), pp. 93–104. ISSN: 0749-6419. DOI: 10.1016/j.ijplas.2014.07.007.

[156] H Lim et al. "Application of generalized non-Schmid yield law to low-temperature plasticity in bcc transition metals". In: *Modelling and Simulation in Materials Science and Engineering* 21 (2013), p. 045015. ISSN: 0965-0393. DOI: 10.1088/0965-0393/21/4/045015.

[157] Anirban Patra, Ting Zhu, and David L. McDowell. "Constitutive equations for modeling non-Schmid effects in single crystal bcc-Fe at low and ambient temperatures". In: *International Journal of Plasticity* 59 (Apr. 2014), pp. 1–14. ISSN: 07496419. DOI: 10.1016/j.ijplas.2014.03.016.

[158] H Lim et al. "A multi-scale model of dislocation plasticity in α-Fe: Incorporating temperature, strain rate and non-Schmid effects". In: *International Journal of Plasticity* 73 (2015), pp. 100–118. ISSN: 07496419. DOI: 10.1016/j.ijplas.2014.12.005. URL: http://www.sciencedirect.com/science/article/pii/S0749641914002356.

[159] John Joseph Gilman. *Micromechanics of flow in solids*. New York: McGraw-Hill, 1969, p. 195.

[160] Nielen Stander et al. "Multi-scale Material Parameter Identification Using LS-DYNA® and LS-OPT®". In: *10th European LS-DYNA Conference*. Würzburg, Germany: DYNAmore GmbH, 2015.

[161] H. Ghassemi-Armaki et al. "Deformation response of ferrite and martensite in a dual-phase steel". In: *Acta Materialia* 62.1 (Jan. 2014), pp. 197–211. ISSN: 1359-6454. DOI: 10.1016/j.actamat.2013.10.001.

[162] R. Hill and J.R. Rice. "Constitutive analysis of elastic-plastic crystals at arbitrary strain". In: *Journal of the Mechanics and Physics of Solids* 20.6 (Dec. 1972), pp. 401–413. ISSN: 00225096. DOI: 10.1016/0022-5096(72)90017-8.

[163] K. S. Havner and G. S. Baker. "Theoretical latent hardening in crystals - I General equations for tension and compression with application to FCC crystals in tension". In: *Journal of the Mechanics and Physics of Solids* 27.4 (1979), pp. 285–314. ISSN: 00225096. DOI: 10.1016/0022-5096(79)90031-0.

[164] K. S. Havner and G. S. Baker. "Theoretical latent hardening in crystals - II BCC crystals in tension and compression". In: *Journal of the Mechanics and Physics of Solids* 27.4 (1979), pp. 285–314. ISSN: 00225096. DOI: 10.1016/0022-5096(79)90031-0.

[165] R. F. Vause and K. S. Havner. "Theoretical latent hardening in Crystals - III FCC Crystals in Compression". In: *J. Mech. Phys. Solids* 27 (1979), pp. 393–414.

[166] B. Liu et al. "Dislocation interactions and low-angle grain boundary strengthening". In: *Acta Materialia* 59.19 (2011), pp. 7125–7134. ISSN: 13596454. DOI: 10.1016/j.actamat.2011.07.067.

[167] C. Gérard, G. Cailletaud, and B. Bacroix. "Modeling of latent hardening produced by complex loading paths in FCC alloys". In: *International Journal of Plasticity* 42 (2013), pp. 194–212. ISSN: 07496419. DOI: 10.1016/j.ijplas.2012.10.010.

[168] Michael D Uchic. "Sample Dimensions Influence Strength and Crystal Plasticity". In: *Science* 305.5686 (Aug. 2004), pp. 986–989. ISSN: 0036-8075. DOI: 10.1126/science.1098993.

[169] Mitsutoshi Kuroda. "Higher-order gradient effects in micropillar compression". In: *Acta Materialia* 61.7 (2013), pp. 2283–2297. ISSN: 1359-6454. DOI: 10.1016/j.actamat.2012.12.038.

[170] A. Mapar et al. "A differential-exponential hardening law for non-Schmid crystal plasticity finite element modeling of ferrite single crystals". In: *International Journal of Plasticity* 91 (Apr. 2017), pp. 268–299. ISSN: 07496419. DOI: 10.1016/j.ijplas.2016.11.009. URL: http://linkinghub.elsevier.com/retrieve/pii/S0749641916302984.

[171] Derek Baars. "Investigation Of Active Slip Systems In High Purity Single Crystal Niobium". PhD thesis. Michigan State University, 2013.

[172] J. D. Splett, D. F. Vecchia, and L. F. Goodrich. "A Comparison of Methods for Computing the Residual Resistivity Ratio of High-Purity Niobium". In: *Journal of Research of the National Institute of Standards and Technology* 116.1 (2011), pp. 489–504.

[173] T. R. Bieler et al. "Physical and mechanical metallurgy of high purity Nb for accelerator cavities". In: *Physical Review Special Topics - Accelerators and Beams* 13.3 (Mar. 2010), p. 031002. ISSN: 1098-4402. DOI: 10.1103/PhysRevSTAB.13.031002.

[174] Thomas R Bieler et al. "Deformation mechanisms, defects, heat treatment, and thermal conductivity in large grain niobium". In: *AIP Conference Proceedings*. Vol. 020002. AIP Publishing, 2015. ISBN: 9780735413344. DOI: 10.1063/1.4935316.

[175] H Umezawa et al. "Single Crystal Niobium Development Multi-Wire Saw Slicing". In: *Proceedings of IPAC'10*. Kyoto,Japan, 2010, pp. 438–440.

[176] P Kneisel et al. "Preliminary Results From Single Crystal and Very Large Crystal Niobium Cavities". In: *Proceedings of 2005 Particle Accelerator Conference*. Knoxville, Tennessee, 2005, pp. 3991–3993. ISBN: 0780388593.

[177] *Schematic image of tube hydroforming*. URL: http://www.designlight.se/files/ror01.jpg.

[178] Gordon Kindlmann. "Superquadric Tensor Glyphs". In: *Joint Eurographics - IEEE TCVG Symposium on Visualization* (2004), pp. 1–8. DOI: 10.2312/VisSym/VisSym04/147-154.

[179] J. W. Christian. "Some surprising features of the plastic deformation of body-centered cubic metals and alloys". In: *Metallurgical Transactions A* 14.7 (July 1983), pp. 1237–1256. ISSN: 0360-2133. DOI: 10.1007/BF02664806.

[180] Nielen Stander et al. *LS-OPT ® User's Manual - A Design Optimization and Probabilistic Analysis Tool*. Version 5. December. Livermore Software Technology Corporation, 2015. ISBN: 9254492507.